

Studies on ceramics and glass-ceramics for immobilization of high-level nuclear wastes

Caurant^a, D.; Loiseau^a, P.; Aubin-Chevaldonnet^a, V.; Gourier^a, D.; Majerus^a, O.; Bardez^a, I.; Advocat^b, T.

a: CNRS, Ecole Nationale Supérieure de Chimie de Paris (ENSCP, Paristech), Laboratoire de Chimie de la Matière Condensée de Paris (UMR-CNRS 7574), 11 rue Pierre et Marie Curie, 75231 Paris cedex 05, France

b: CEA Marcoule, Laboratoire d'Etude de Base sur les Verres, 30207 Bagnols-sur-Cèze, France

ABSTRACT

The reprocessing of nuclear spent fuel generates highly radioactive liquid wastes (HLW) that must be isolated from biosphere in very durable solid matrices. In the first part of this chapter, generalities are presented on the radionuclides occurring in HLW and on the main characteristics and preparation methods of waste forms (glasses, ceramics, glass-ceramics) for the immobilization of separated or non-separated wastes. In the second part of this chapter, the characteristics of two categories of long-lived radionuclides (¹³⁵Cs and minor actinides Np, Am, Cm) and the main matrices proposed for their specific immobilization are reviewed. Results are presented on ceramic and glass-ceramic matrices developed for the conditioning of Cs (hollandite) and minor actinides (zirconolite, zirconolite-based glass-ceramic) and studied in our laboratories. For cesium, Ba_xCs_yTi_(8-z)M_zO₁₆ hollandite ceramics (M: Al³⁺, Cr³⁺, Fe³⁺, Ga³⁺) prepared by oxide route are characterized by different methods. The effect of M on the single phase character of hollandite and on its capacity to incorporate Cs is studied. External electron irradiation experiments performed on a simple hollandite composition (Ba_{1.16}Ti_{5.68}Al_{2.32}O₁₆) to simulate the effect of β-irradiation due to radioactive Cs decay are presented. Structural changes and defects formation are studied by different spectroscopic techniques such as Electron Paramagnetic Resonance (EPR). The stability with temperature of titanium (Ti³⁺) and oxygen (O₂) paramagnetic defects is studied. For selective immobilization of minor actinides, results concerning both zirconolite ceramic (nominally CaZrTi₂O₇) and a zirconolite-based glass-ceramic are presented. Rare earths (mainly neodymium)

and Th are used as minor actinide surrogates. Structural and microstructural results concerning the incorporation of Nd^{3+} ions in $\text{Ca}_{1-x}\text{Nd}_x\text{ZrTi}_{2-x}\text{Al}_x\text{O}_7$ ($x \leq 0.6$) zirconolite ceramics prepared by oxide route are presented. The local environment of Nd^{3+} ions in zirconolite ceramic samples is studied by EPR and optical absorption spectroscopy. A zirconolite-based glass-ceramic consisting of small zirconolite crystals homogeneously dispersed in its bulk and prepared by controlled crystallization of a parent glass belonging to the $\text{SiO}_2\text{-Al}_2\text{O}_3\text{-CaO-TiO}_2\text{-ZrO}_2\text{-Nd}_2\text{O}_3$ system is studied. The effect of different parameters such as the crystallization temperature on the nature of the crystals (bulk + surface), their structure and their microstructure is developed. Glass composition changes are performed in order to increase the amount of zirconolite in the glass-ceramic samples and to incorporate preferentially minor actinide surrogate in the zirconolite crystals (double containment principle).

I. INTRODUCTION

Today more than 7% of all the energy consumed in the world is produced by nuclear power reactors (440 reactors were in activity in 2004 around the world). Nuclear energy is essentially used to produce electricity and represents about 16% of the electricity produced in the world. For this application, about 50 000 tons of natural uranium are consumed every year producing 11 000 tons of nuclear spent fuel [1]. For several countries (France, Belgium, Lithuania), the contribution of nuclear energy to electricity production is higher than 50% (e.g. nearly 80% for France) [2]. Even if a few number of countries in Western Europe have made the choice not to develop nuclear energy (Italy, Austria) or to give up progressively their nuclear power activity (Germany, Sweden, Belgium) for political reasons, other countries have decided either to continue to use nuclear reactors (France, Finland, Switzerland) or to significantly increase the part of nuclear energy in their electricity production (China, Japan, United States, Russia, South Korea, India). The rising demand for energy, the risks of losing oil and gas sources of procurement and the need to reduce green-house gas emissions are among the reasons of current and future nuclear energy development. Moreover, the building of a new type of nuclear reactor (EPR, European Pressurized water Reactor) more efficient than current PWR (Pressurized Water Reactor) is in progress in Finland and is envisaged in France. As for PWR, this new kind of reactor -belonging to the third generation- will use UOX (uranium oxide, UO_2) and MOX (mixed uranium and plutonium oxides) fuels. All these considerations about nuclear energy demonstrate that increasing amounts of highly radioactive nuclear wastes will be produced in the future. Today, according to each country, two options exist concerning nuclear spent fuel:

- (i) Reprocessing with the Purex process to extract Pu and remaining U for reuse in new fuel and conditioning of residual wastes that contain fission products (FP) and minor actinides (MA: Np, Am, Cm) in highly durable glasses (closed nuclear fuel cycle) [3] followed by interim storage and then disposal of waste forms in deep geological formations [4].
- (ii) Direct disposal in deep geological formations of spent fuel without reprocessing (opened nuclear fuel cycle).

Today, about 30% of the nuclear spent fuel is reprocessed in the world [1]. The high level radioactive liquid wastes (HLW) produced after reprocessing are made of a complex mixture of both radioactive (fission products, minor actinides) and non-radioactive elements (for more details see §II). As they contain long-lived radionuclides (and/or long-lived daughter products) for which half-lives can reach thousands to millions years [5] (MA, ^{135}Cs , ^{99}Tc , ^{93}Zr ..., **Table I**), HLW must be isolated from the biosphere for very long times (from thousands to hundreds of thousands years), at least until their radiotoxicity level drops back to the radiotoxicity level of the initial uranium ore (**Figure 1**). For instance HLW obtained after UOX1 (UO_2 with 3.5% ^{235}U) spent fuel reprocessing, decay to return to a level close to the original fuel after approximately 2 000 years (**Figure 1a**).

For a very efficient immobilization, a multi-barrier concept is envisaged (waste-form < container < engineered barrier < geological barrier) around the radioactive waste to limit the release of radionuclides into the environment through the action of the underground water. The increasing need for fundamental and applied studies on HLW and nuclear waste forms for their conditioning is thus obvious. This last point is the main topic of this Chapter.

Currently, after water evaporation and calcination of HLW solutions, wastes are incorporated by dissolution into the structure of glasses¹ (mainly calcium alkali borosilicate glasses but alumino-phosphate glasses are also used in Russia [6,7]) melted in metallic² or ceramic melters³ at temperature not exceeding 1100-1150°C for technical reasons. Borosilicate glassy matrices are also used to immobilize the defence wastes obtained after the reprocessing of military spent fuel [7]. Moreover, new glassy matrices are also envisaged to immobilize old HLW solutions stored in stainless steel tanks and HLW solutions that will be produced in the future in commercial reactors after reprocessing of new spent fuels. For instance, in France, in order to improve reactors performance, the proportion of ^{235}U fissile isotope in fuel will grow in the future (high burn up UO_2 fuel) [1]. Today in France, uranium oxide fuel used in PWR contains 3.5 or 3.7 % ^{235}U (UOX1 and UOX2 fuels respectively). In the future, the concentration of ^{235}U will reach 4.7-4.9 % (UOX3 fuel) [1]. As a consequence, new glass

¹ Due to the lack of long range order in glassy matrices, glasses are the best waste forms for immobilization of complex waste mixtures.

² Such as the AVH process (see §III) used in France (La Hague) and in United Kingdom (Sellafield).

compositions are under development to efficiently incorporate and immobilize the highly concentrated HLW solutions that will be obtained after reprocessing of these new spent fuels [8]. For instance, a new rare earth-rich glass composition which enables greater waste volume reduction than current borosilicate nuclear glasses has recently been proposed to immobilize these new wastes [9,10,11]. Indeed, as rare earths represent the most abundant family of FP [12] (**Table III**), their concentration in these new wastes will be high and rare earth-rich glassy waste forms appeared as the best candidate for their immobilization. Another example of glassy matrix has been recently developed for the immobilization of old HLW solutions containing high Mo and P concentrations. These solutions were recovered after the reprocessing -in the seventies in France- of UMo⁴ spent fuel [13]. The new waste form developed for UMo HLW conditioning must be more properly called glass composite material rather than glass because the melt partly crystallizes on cooling (see **Figure 5** in §III). The use in the future of a new melting technology with cold crucible melter in vitrification nuclear plants will enable to melt glass compositions with higher refractory character than current borosilicate nuclear glasses [14,15,16]. Thus, new glassy waste forms that could not be melted in classical metallic or ceramic melters (such as the waste forms envisaged above to immobilize concentrated HLW and (Mo,P)-rich wastes) can be now envisaged.

To minimize the potential long-term impact of HLW solutions, investigations are currently in progress in several countries such as in France⁵ on the enhanced separation of several long-lived radionuclides (MA, ¹³⁵Cs, ¹²⁹I, ⁹⁹Tc) from HLW followed by their transmutation (into short-lived radionuclides or stable elements) or their immobilization in specific host matrices such as ceramics and glass-ceramics [17,18,19,20,21] more durable than current nuclear glasses (**Figure 2**). These long-lived radionuclides may have a major contribution to the long term potential radiotoxicity⁶ of HLW. This is the case for MA which are long-lived α -emitting radionuclides and that will be mainly responsible for the potential

³ LFCM (Liquid-Fed Ceramic Melter) are in use in Russia, United States and Japan.

⁴ UMo is a metallic alloy containing U and Mo that was used in gas cooled reactors in France in 1960's.

⁵ Research programs are in progress in France since 1991 (following the French Act of December 1991) to reduce the toxicity and quantity of nuclear wastes recovered after spent fuel reprocessing, their conditioning, storage and deep disposal.

⁶ The potential radiotoxicity of radionuclides corresponds to their activity multiplied by ingestion dose factors.

radiotoxicity of HLW after 2-3 hundred years disposal (**Figure 1**). Even if experiments have shown the possibility to transmute MA in neutron reactors [22] to reduce the radiotoxic inventory, the specific immobilization of MA is still considered as a possible alternative to transmutation. For MA immobilization, several ceramics such as zirconates, titanates and phosphates may incorporate higher amounts of MA in their structure than glasses and also exhibit better chemical resistance against water [18,19,23]. Similarly, highly durable matrices have also been developed for the conditioning of other highly radiotoxic actinide-rich wastes such as Pu-rich military wastes in United States and Russia [7]. Other long-lived radionuclides (fission products) such as ^{135}Cs , ^{129}I and ^{99}Tc have a lower contribution to the long-term radiotoxicity of spent fuel than MA but are more soluble in water and more mobile in geologic media [24,25,26] (**Table II**). Their selective separation and immobilization in specific and highly durable matrices (hollandite, apatite...) would thus reduce the risks of migration towards biosphere during disposal. After enhanced separation of the most problematic radionuclides occurring in HLW, it is planned to immobilize the remaining wastes (consisting of non radioactive elements, short-lived radionuclides and long-lived radionuclides with low mobility and very slightly soluble in water) in glassy matrices (**Figure 2**). These glassy waste forms will lose their radiotoxicity relatively rapidly in comparison with current nuclear glasses. Indeed, after a few centuries, their radiotoxicity level will drop to that of the initial fuel. Radioactive ^{90}Sr is known to have one of the main contribution (with ^{137}Cs) to the radiotoxicity and radioactivity of HLW during the first centuries (^{90}Sr , 28.5 years half-life), is highly water soluble and may have a strong impact on biosphere [27]. However, because of the lack of long-lived strontium isotopes its separation from radioactive solutions followed either by transmutation or specific immobilization is not envisaged contrary to Cs. Studies on enhanced separation, transmutation or specific immobilization of other long-lived FP such as ^{93}Zr occurring in HLW (**Table I**) have not been performed because these radionuclides are not mobile in geological environment (**Table II**) and have only very low solubility in water.

In this Chapter, we will firstly present generalities about the HLW recovered after nuclear spent fuel reprocessing (§II). The principles of their immobilization in different kinds of waste forms (ceramics, glass-ceramics and glasses) for mixed or separated radionuclides will be presented in §III. Results concerning ceramic

and glass-ceramic matrices developed for the specific immobilization of Cs and MA that have been studied in our laboratories will be then presented (§IV):

- $\text{Ba}_x\text{Cs}_y(\text{M},\text{Ti})_8\text{O}_{16}$ hollandite ceramics (M: trivalent cation) for Cs immobilization.
- $\text{CaZrTi}_2\text{O}_7$ zirconolite ceramics for MA immobilization.
- Zirconolite-based glass-ceramics containing small zirconolite crystals homogeneously dispersed in a glass for MA immobilization.

II. Composition of HLW recovered after spent fuel reprocessing

During the burning of nuclear fuel in nuclear reactors to produce electricity or military Pu, different elements (radioactive or not) considered as wastes are produced under the flux of neutrons:

- Fission products (FP), produced by fission of ^{235}U and fissile Pu isotopes (^{239}Pu , ^{241}Pu). More than 300 radionuclides (which are β -emitters and sometimes also γ -emitters) were identified, but more than 60 % of them will have disappeared several times after spent fuel discharge. These different FP correspond to nearly 40 elements of the Mendeleev classification from Ge to Dy and belong to different families (**Table III**). They are all considered as wastes. An example of composition of HLW recovered after UOX1 reprocessing that illustrates this chemical diversity is shown **Table IV** [28]. However, the majority of FP are stable isotopes (for instance all Mo isotopes and the majority of rare earth isotopes occurring in significant amounts in HLW are stable) and will thus not contribute to radioactivity. Nevertheless, radioactive FP (among which ^{137}Cs , ^{90}Sr and ^{99}Tc) will represent -during the first centuries- the main source of radioactivity and radiotoxicity of HLW solutions after Pu and U separation (**Figure 1**). The main long-lived FP are given in **Table I**. Studies have been performed concerning the possibility to isolate and transmutate the more mobile of these long-lived FP (I, Cs, Tc) or to find very durable specific waste forms to immobilize them.

- Pu and MA isotopes produced by neutron captures mainly by ^{238}U . They are all long-lived α -emitters and sometimes also γ -emitters. MA are all considered as wastes. This is not the case for Pu in countries which reprocess their spent fuel to extract Pu and produce MOX fuel. If civil spent fuel is not reprocessed, it is

considered as a waste and Pu will be the main responsible for spent fuel long-term radiotoxicity (**Figure 1**). More details about MA in HLW and their specific immobilization are given in §IV.

- Activation products are radioactive elements (such as ^{55}Fe , ^{60}Co , ^{59}Ni , ^{63}Ni , ^{93}Zr , ^{14}C) [1] produced by transmutation of non radioactive elements present in the fuel or in surrounding structures. The amount of activation products is very small in comparison with the two previous kinds of wastes (FP, MA).

Even if FP and MA occurred in all nuclear spent fuels, their composition may strongly depend on:

- The isotopic composition of the fuel, i.e. the level of ^{235}U enrichment before its introduction in reactors (from 0.7 % for natural U to about 4.5-4.9 % in the future). Classically, the amount of ^{235}U in the UOX fuel used nowadays in PWR is about 3.5-3.7 %.

- The chemical composition of the fuel (UO_2 , U metal, metallic alloys with U).

- The burn-up level when spent fuel is discharged from the reactor.

- The time after discharge.

Consequently, the composition of HLW solutions that are recovered after reprocessing of spent fuel by the Purex process, will strongly depend on these different parameters. For instance, the concentrations of FP and MA are relatively low in HLW solutions originating from the reprocessing of military spent fuels or civil spent fuels with natural uranium because of their low burn up in comparison with the HLW solutions originating from PWR reactors [7]. Indeed, the amount of FP increases proportionally with the burn-up of UO_2 fuel. However, the amount of MA increases more rapidly than the amount of FP (compare the compositions of UOX1 (**Table IV**) and UOX3 (**Table V**) spent fuels and see **Table VI**). The concentrations of short live radionuclides (for instance ^{134}Cs) will strongly decrease several years after spent fuel discharge and become negligible. For instance, UOX1 spent fuel is generally reprocessed 3 years after discharge. The time before reprocessing also enables to reduce the heat power of spent fuel. In the future, for high burn up spent fuels, this time will increase (**Table VI**). The chemical composition of nuclear fuel has also a strong impact on HLW composition. For instance, the high quantity of molybdenum in UMo fuel is mixed with FP and MA in HLW solutions.

In the Purex (Plutonium Uranium Refining by Extraction) process, the spent fuel is dissolved in hot nitric acid. U and Pu are then isolated from FP, MA and impurities by solvent extraction using tributyl phosphate (TBP). This process initially developed in the United States, is used industrially for more than 50 years. During dissolution of the spent fuel in hot nitric acid, several volatile FP evaporated among which I, Kr and Xe [12]. Xe is non radioactive. ^{85}Kr is a short live β -emitter (half-life 10.7 years). Kr and Xe are discharged in the atmosphere. ^{127}I (19.4 %) is non radioactive but the majority of iodine (80.6 %) occurs as the long-lived radioactive isotope ^{129}I (half-life $1.57 \cdot 10^7$ years). Iodine is a volatile element that can be incorporated with difficulty in classical glassy matrices. Moreover, it is highly mobile in geological environment (**Table II**) and soluble in ground water. During spent fuel dissolution, I_2 gas evaporates, is purified as iodide salt and is then discharged into the sea (principle of isotopic dilution with ^{127}I occurring in sea water). However, this solution is now regarded as unacceptable for instance in Japan and in France. This is the reason why studies have been performed concerning iodine transmutation or its specific incorporation in highly durable matrices. As ^{129}I transmutation does not appear as technically possible [22], its immobilization in ceramic matrices [19,29,30] or by encapsulation in a metallic matrix [31] have been envisaged. For instance, it was shown that a composite apatitic ceramic made of $\text{Pb}_{10}(\text{VO}_4)_{4.8}(\text{PO}_4)_{1.2}\text{I}_2$ encapsulated in a $\text{Pb}_3(\text{VO}_4)_{1.6}(\text{PO}_4)_{0.4}$ matrix prepared by hot pressing at 580°C exhibited good chemical durability [19]. It is interesting to notice that a flux of about 184 kg of iodine is produced every year in France during spent fuel reprocessing [32].

It must be underlined that the proportions of FP and MA in spent fuels are relatively small in comparison with the quantity of uranium remaining after burning. For instance, the evolution of the composition of UO_2 fuel (enriched with 3.5% ^{235}U) after 3 years in a PWR reactor is shown in **Figure 3** [33]. In this case, it appears that the amounts of FP and MA in spent fuel are respectively about 4 wt% and 0.1 wt%. MA represent only 2-3 wt% of the wastes (FP + MA) in HLW solutions. Moreover, non radioactive but relatively abundant additional or corrosion elements also occurred in the radioactive solutions such as P, Na, Fe,

Ni, Cr and Zr⁷ (**Tables IV and V**). These elements originate from the Purex process (P, Na) or from the corrosion of the tanks (Fe, Ni, Cr) in which are kept HLW solutions before conditioning.

Because of the risks of diffusion in the biosphere of the highly radiotoxic and toxic elements occurring in HLW solutions that are kept in metallic tanks⁸, these wastes must be conditioned in solid and highly durable matrices before deep underground disposal. Due to both its low chemical durability, its very high thermal power (produced by the high concentration of thermal radionuclides) and its high specific area, the calcine that is obtained after evaporation and calcination of HLW solutions cannot be considered as a good waste form. We will see below that calcine can only be considered as an intermediate product during vitrification processes for instance. In the next paragraph we will present the different kinds of matrices that can be envisaged to immobilize HLW solutions and separated long-lived radionuclides.

III. Immobilization of non-separated or separated HLW: principles and examples.

III.A. Principles of immobilization.

Concerning the immobilization of both non-separated wastes (HLW solutions) and separated long-lived radionuclides, two kinds of waste forms are generally proposed in literature [7]. Firstly, waste forms can be envisaged in which wastes are dissolved in the atomic structure of glassy or (single phase or multiphase) crystalline matrices (**Figure 4a**). In these conditions, the elements of the wastes are immobilized at atomic scale and the matrix act as a solvent. This is the case of the majority of specific and non-specific waste forms that have been studied in literature. It must be notice that all the nuclear glasses produced industrially belong to this category⁹. Secondly, waste forms can be envisaged in which the totality or at least a high fraction of wastes is encapsulated as particles in highly

⁷ Additional zirconium originates from zircalloy cladding but the majority of zirconium occurring in HLW is produced during fission reactions (**Tables IV and V**).

⁸ After several years, leaks of radioactive solutions may appear due to tanks corrosion. Moreover, as it is necessary to evacuate continuously the hydrogen gas formed in tanks by water radiolysis and to permanently cool the solution in order to avoid explosion risks, the storage of HLW solutions in metallic tanks can only be considered as temporary.

⁹ It must be indicated that even if the high majority of elements of HLW solutions are dissolved in the structure of nuclear glasses, noble metals are not soluble in the glassy matrix (see note 14).

durable glassy or (single phase or multiphase) crystalline matrices (**Figure 4b**). In these conditions, elements of the wastes are mainly immobilized at granular scale and the waste form appears as a composite material. If the particles containing the wastes exhibit good immobilization properties, the matrix can be considered as a second barrier against dissolution by water. The number of examples in literature of such composite matrices is less important than that in which wastes are immobilized at atomic scale [7]. They can be prepared by sintering a mixture of powders of wastes (calcine powder, crystalline or glass powders in which wastes were previously dissolved) and ceramic or glass powders that will act as encapsulating highly durable matrix after sintering. For instance, composite materials prepared by sintering and made of pyrochlore particles encapsulated in borosilicate or lead silicate glasses have been recently proposed as Pu waste forms [34]. Moreover, glass composite materials prepared from glasses by controlled crystallization (glass-ceramics) or by uncontrolled crystallization during cooling of the melt can also be considered as composite waste forms even if they were not prepared by sintering of powders. Nevertheless, in this case a high proportion of wastes may remain dissolved in the continuous glassy phase. For instance, this is the case of the glass composite waste forms that have been developed for the immobilization of UMo wastes containing high concentrations of Mo and P. They consist of crystalline molybdate and phosphate particles formed during melt cooling and dispersed in a glassy borosilicate matrix [13,35] (**Figure 5**).

When looking for an efficient waste form for HLW solutions or separated wastes, several important points must be kept in mind concerning both the properties of the matrix and the difficulties that can be encountered for its synthesis in radioactive environment.

Concerning the properties of the potential waste form, the following points must be considered:

- The matrix must incorporate all the elements (radioactive or not) of the wastes with a high loading. Moreover, for radioactive elements, the matrix must also incorporate the daughter products. If high concentrations of thermal radionuclides occur in the wastes, loading is limited by the strong heating of waste forms. For instance, the high concentrations of ^{137}Cs and ^{90}Sr in HLW solutions (**Table IV**) is one of the points that limits the amount of wastes that can be incorporated in classical borosilicate nuclear glasses. Nevertheless, rare earth-rich borosilicate

glasses with higher glass transformation temperature are currently under development to increase waste loading [9].

- The incorporation capacity of the matrix must not be sensitive to small fluctuations of the wastes composition.
- The matrix must exhibit very good long term behavior concerning both its resistance against lixiviation by water and its resistance against self-irradiation. Indeed, radioactive wastes must be isolated from the biosphere at least until their radiotoxicity level will drop back to the radiotoxicity level of the initial uranium ore used to prepare the fuel. Even if structural evolutions occur under the effect of α -decays (amorphization of ceramics for instance), the chemical durability and the capacity of the matrix to retain radionuclides must remain very good. The existence of natural analogues for a given potential waste form is generally considered as a good indication of its good long term behavior. Natural analogues are durable minerals that have high natural radionuclide contents (U, Th) and that have been preserved in natural conditions for geological times (radionuclides were retained in their structure for millions of years). For nuclear borosilicate glasses, there are not true natural glass analogues that have contained boron and high concentration of natural radionuclides. Nevertheless, in spite of composition differences, natural basaltic glasses are often considered as good natural analogue of borosilicate nuclear glasses because of their similar chemical lixiviation properties [36,37]. Most of the ceramic waste forms proposed for the specific conditioning of long-lived radionuclides are based on natural analogues. In order to evaluate the long term behavior of glass or ceramic synthetic samples envisaged as potential waste forms, numerous accelerated tests of lixiviation and irradiation are performed. For instance, in order to simulate the long-term effects of self-radiation damages produced by α -decays, samples can be prepared by incorporating short-lived actinides such as ^{238}Pu (half-life 87.7 years) or ^{244}Cm (half-life 18.1 year) [38,39]. Nevertheless, external irradiation experiments with charged particles (heavy ions, α -particles) are more frequently used to simulate the effects of actinides self-irradiation (α -particles and α -recoils effects) because it is not easy to prepare and to study highly radioactive samples doped with ^{238}Pu or ^{244}Cm . The effects of γ -irradiation can be simulated using external ^{60}Co or ^{137}Cs sources. β -irradiation can be simulated by external irradiation with electrons generated by a Van de Graaff accelerator. Concerning the long-term chemical

durability of potential waste forms, dynamic and static lixiviation tests can be performed under different conditions (temperature, pH, composition of the leaching solution...). For instance, dynamic experiments with a high flow rate of renewed distilled water at 100°C (so-called Soxhlet experiment) are classically used to determine the initial dissolution rate r_0 of samples in pure water. The initial dissolution rate of the French nuclear glass R7T7 is $1.7 \text{ g.m}^{-2}.\text{day}^{-1}$ at 100°C [40]. During static lixiviation tests (i.e. without solution renewal), the samples alteration generally drops by several orders of magnitude below r_0 more or less rapidly. For glasses, this decrease of dissolution rate (by 4-5 orders of magnitude) is attributed to the formation of an amorphous gel layer with highly protective properties that acts as a diffusion barrier [41]. Concerning nuclear glasses, predictive modelling of long-term alteration rate is currently developed [42].

- The matrix must exhibit very good mechanical properties in order to avoid fracturation risks during manipulation and transport. Moreover, the matrix must have a low porosity for chemical durability reasons. Indeed, a high porosity would increase its specific area and would thus increase its reactivity with aqueous solutions.
- The matrix must be stable under the heating produced by the decay of radionuclides. For instance, nuclear glasses must exhibit transformation temperatures T_g about 100°C higher than the temperature in the bulk of the containers to avoid crystallization risks during disposal.
- The volume of the matrix must be several times smaller (5-6 for glasses) than that of HLW solutions.

Concerning the synthesis of the potential waste form:

- The process to incorporate the wastes into the matrix must be as simple as possible. The number of steps must be small in order to avoid the production of high amounts of secondary radioactive wastes and to reduce the cost of immobilization.
- The temperature of synthesis must not be too high. This is particularly the case for the wastes containing high quantities of volatile radionuclides such as Cs, I and Ru. This is one of the points that limits the melting temperature of nuclear glasses.

III.B. Glasses, ceramics and glass-ceramics waste forms.

In order to illustrate the previous paragraph, several examples of waste forms belonging to the glass, ceramic or glass-ceramic categories will be presented. Today, glass and ceramic matrices are generally retained to immobilize respectively non separated and separated wastes. Nevertheless, multiphase ceramics were also proposed as waste forms for HLW solutions. Glass-ceramic matrices constituted of crystals dispersed in a glassy matrix were mainly envisaged for the immobilization of non separated wastes. But recently, glass-ceramics were also studied as potential waste forms for the specific immobilization of separated MA [20,43,44].

III.B.1. Glassy waste forms

Even if several studies have been performed on glass compositions in order to immobilize separated long-lived radionuclides such as Cs, MA or Pu (see §IV.A.2.a and §IV.B.2), more durable single phase ceramic matrices (such as zirconolite for MA and hollandite for Cs) appear today as better candidates for this application. Nevertheless, for reasons that will be developed below, glasses remain the best waste forms for the immobilization of non separated radionuclides. Indeed, glasses are still today the only kind of waste form produced industrially in nuclear plants for the immobilization of HLW solutions originating from civil or military spent fuel reprocessing.

The first potential use of glass as nuclear waste form was proposed in Canada in the 1950s [7], but the first industrial plant to produce borosilicate nuclear glasses was developed by the CEA and started in France in 1978 with the AVM¹⁰ process using metallic melter for the immobilization of HLW originating from the reprocessing of gas cooled reactors spent fuel. Since this date, others industrial vitrification plants have been developed over the world using either metallic or ceramic melters [7,16,45]. In 1989 and 1992 at La Hague (France), two other vitrification plants called respectively R7 and T7 started to produce a nuclear borosilicate glass (so-called R7T7 glass) for the immobilization of HLW originating from the reprocessing of PWR reactors spent fuel. This process (so-

¹⁰ AVM: Atelier de Vitrification de Marcoule

called AVH¹¹) is also used in UK by BNFL to vitrify HLW solutions in the Sellafield Vitrification Plant. The AVH process is very similar to the AVM process and vitrification of HLW solutions is carried out in two steps (**Figure 6**) [15,16]. In the first step, the concentrated radioactive solutions are evaporated and calcined in a rotating kiln (500°C). The calcine (made essentially of oxides and nitrates) is then introduced simultaneously with a glass frit into an induction-heated metallic melter at about 1150°C for melting (**Figure 7**). After melt homogenization and fining, the glass is poured into canisters (containing 400 kg of glass). As there is no glass former (SiO₂, B₂O₃, Al₂O₃) in the composition of the wastes¹², it is necessary to introduce simultaneously a glass frit containing SiO₂, B₂O₃, Al₂O₃, Na₂O, CaO, Na₂O, ZnO and Li₂O. This glass frit contains alkali and alkaline earth elements which are well known in glass chemistry and technology for their role as fluxing agents during melting and for their structural role as modifiers near non-bridging oxygen anions (NBO) or charge compensators near [AlO₄]⁻ and [BO₄]⁻ entities in the glassy network¹³ [46,47] (**Figure 8**). To illustrate the chemical complexity of nuclear glasses used to immobilize non separated radioactive wastes, the composition of the R7T7 glass is given in **Table VII** [48]. It is the flexibility of the glass structure and the availability of charge compensators (such as alkali and alkaline earth ions) that enables the dissolution of such a variety of chemical elements in the waste form. This glass composition was optimized according to the points developed in previous paragraph. The amount of wastes incorporated in this glass ranges from 12 to 18 wt% [14]. Since 1989, using this vitrification process, more than 10 000 glass containers (which represents less than 2000 m³ of glass) have been produced at La Hague [8]. The world production of all nuclear vitrification plants by the end of 2000 was about 10 000 tons of radioactive glass in 20 000 canisters [16]. As indicated in the introduction of this Chapter, a new kind of metallic melter so-called cold crucible melter (CCM) will be soon installed in the vitrification plant of La Hague [13]. It enables to melt glass compositions at higher temperature than the AVH and AVM processes and suppresses the problems of corrosion of the metallic pot by the melt. In CCM, the glass melt is heated directly by induction currents and is

¹¹ AVH: Atelier de Vitrification de La Hague

¹² There is only a small amount of phosphorus (P₂O₅ is a glass former) in the HLW solutions recovered after the Purex process (**Table IV**).

preserved inside a cooled volume of glass-batch material isolating the melt from the water cooled cold metallic crucible transparent to electromagnetic field [14,16,27]. As the crucible is not corroded by the molten glass, glass compositions with higher refractory character than classical nuclear glasses can be melted with this melter.

There are three main reasons that can explain the success of glasses for HLW solutions immobilization:

- The first point is the relative simplicity of vitrification processes: melting (waste + glass frit) and casting [27,49]. The preparation of ceramic waste forms is generally more complex and may need grinding and (cold or hot) pressing steps. For instance, even if an inactive demonstration plant was developed for the Synroc multiphase ceramic fabrication [50], processes to prepare ceramic waste forms have never been used in nuclear industry. Moreover, as nuclear glasses fabrication is industrialized since almost 30 years, the nuclear industry has a very good knowledge of this technology. This technique also enables to prepare glass composite materials by controlled or natural cooling of the melt (**Figure 5**).

- The second advantage of glasses concerns their amorphous nature which enables to incorporate a very large range of elements (the majority of the elements occurring in HLW solutions except noble metals¹⁴ for instance [51]) by dissolution at atomic scale (**Figure 4a**) because of the flexibility of the glassy structure. Moreover, glass waste forms are able to accept larger waste composition fluctuations than ceramics. Due to the lack of long range order, alkali aluminoborosilicate nuclear glasses can be considered as a 3-dimensional random network of tetrahedra (SiO_4 , $[\text{AlO}_4]^-$, $[\text{BO}_4]^-$) and triangles (BO_3) linked by their corners by bridging oxygen (BO) anions (**Figure 8**). The other elements of the glass and particularly the ones coming from wastes, generally play the role of modifiers (i.e. they form non bridging oxygen (NBO) anions, this the case for instance of Na^+ , Cs^+ , Sr^{2+} , Ba^{2+} , Nd^{3+} , La^{3+} ...) or charge compensators near negatively charged polyhedra. A schematic picture showing the insertion of several of these cations in a rare-earth rich glass [52] envisaged to immobilize highly concentrated HLW solutions is shown in **Figure 8**. For this rare earth-rich

¹³ For more details concerning glass structure and the role of the different oxides, see for instance [46,47,112]

glass, it was shown that Nd^{3+} ions play a modifier role (creation of NBO) rather than a role of charge compensator [11,52]. In order to illustrate the effect that may induce wastes (such as rare earths which are the most abundant FP) on glass structure, we will give another interesting result obtained for this rare-earth rich-glass. It concerns the effect of rare earth concentration (La_2O_3) on the relative proportion of BO_3 and $[\text{BO}_4]^-$ units in the glass and was obtained using ^{11}B MAS-NMR spectroscopy¹⁵ (**Figure 9**). Study of this figure clearly shows that the fraction of BO_3 units strongly increases at the expenses of $[\text{BO}_4]^-$ units as La_2O_3 concentration increases. This effect can be explained by the existence of a competition between the rare earth and boron for their association with both Na^+ and Ca^{2+} ions for local charge compensation in the structure of the glass (**Figure 8**). Such a competition induces a decrease of the fraction of $[\text{BO}_4]^-$ units (initially compensated for instance by Na^+ or Ca^{2+} ions) when La_2O_3 increases.

- The third reason concerns the good long term behavior of nuclear glasses due to their resistance to irradiation and their high chemical durability. As very numerous studies have been performed and published on chemical durability of nuclear glasses [40,41,53,54,55], this point will be not developed in this Chapter. Concerning resistance to irradiation of glasses, internal and external irradiation experiments simulating α -decays showed only very small evolution of their density [38]. For instance, the density of ^{244}Cm doped R7T7 glass only decreases by 0.6 % after more than $4 \cdot 10^8$ disintegrations/g (this simulates the effect of about 10 000 years of α -decays in the R7T7 nuclear glass) [56]. This results can be explained by the fact that the structure of glasses is already disordered (amorphous) before irradiation and by the ease of reconstruction of the broken bonds very rapidly after α -recoils as shown by molecular dynamics simulations [56]. Only small effects were observed under external electron irradiation used to simulate β -decays: migration of alkali ions accompanied by a small decrease of the number of NBO and formation of molecular O_2 in the glass network [57]. Nevertheless, no significant effect on the chemical durability of nuclear glasses was observed after α - or β -irradiation experiments [56].

¹⁴ Nevertheless, a small amount of elements such as Ru, Pd, Rh and Te, that are not soluble in the melt occurred as crystalline phases such as RuO_2 and polymetallic (Pd,Rh,Te) inclusions in borosilicate nuclear glasses (less than 3 vol%) [51].

¹⁵ MAS-NMR: Magic Angle Spinning-Nuclear Magnetic Resonance

One of the main drawbacks that is frequently given about glasses concerns their thermodynamic instability in comparison with the crystalline state. Indeed, they can be considered as frozen undercooled melts and are thus in non-equilibrium state [58]. In spite of intrinsic instability of the glassy state, numerous examples of very old natural glass samples exist on the Earth and on the Moon that have not crystallized [59]. For instance, most of the volcanic glasses found on Earth are more than 65 million years old. The apparent thermodynamic stability of these glasses even for geological periods could be explained by both a high kinetic barrier to crystallize and a low crystallization driving force¹⁶ [60]. The risk of instability of these glasses is mainly chemical (lixiviation by water for instance). Concerning the French nuclear R7T7 glass, an interesting study concerning the risks of crystallization for very long periods at fixed temperature was performed by Orhac [61]. An important point of this work (using experimental results and modelling), was that even for heating periods higher than several thousands years at a temperature 180°C higher than the glass transformation temperature ($T_g \sim 510^\circ\text{C}$), the amount of crystals formed in the glass will remain small. The formation of crystals may also occur during cooling of the melt after casting (as shown in **Figure 5** for a glass composite waste form). Indeed, just after cooling, the temperature in the bulk of the canisters decreases slowly at about 1°C/min. It is important to underline that nuclear glass (such as R7T7 glass) compositions used for the immobilization of classical HLW solutions were optimized in order to avoid significant crystallization during cooling. Indeed, the formation of high amounts of crystals in nuclear glasses may affect their capacity to retain radionuclides and their long term behavior. Nevertheless, if the tendency of particular melt compositions to crystallize can be controlled, the preparation of glass-ceramics waste forms can be envisaged (see §III.B.3).

III.B.2. Ceramic waste forms.

Ceramics are multiphase or single phase polycrystalline materials generally obtained after pressing and sintering of precursor powders at relatively high temperature. Numerous examples of multiphase and single phase ceramics have been reported in literature for the conditioning of HLW solutions or to immobilize separated long-lived radionuclides [62,63,64,65,7,7]. Nevertheless, as shown in

¹⁶ Concerning the crystallization of glasses see for instance [60].

previous paragraph, only glass waste forms are currently produced industrially. However, ceramics may exhibit several important advantages in comparison with glasses:

- Ceramics may exhibit superior mechanical properties.
- Ceramics are more stable thermally (glasses may partially crystallize under heating and for $T > T_g$ their viscosity rapidly decreases) and their thermal conductivity is generally higher than that of glasses.
- Ceramics may be more durable by several orders of magnitude than borosilicate glasses because of the occurrence in their composition of high amounts of oxides with very low solubility in water such as ZrO_2 . Moreover, the existence of very old natural analogue samples for several of these ceramics shows that in spite of metamictization phenomena (i.e. amorphization of their structure as a result of the self-radiation damages associated with the α -decay of U and Th), these samples still exhibit very good durability.
- Ceramics can accommodate in their structure higher concentrations of particular kinds of wastes such as MA and Pu which generally exhibit limited solubility in borosilicate glasses.

For an efficient immobilization, it is expected that all the elements of the wastes are incorporated in the crystalline structure of the durable phases of the ceramics and not in minor phases segregated along grain boundaries. Consequently, all the constituent crystalline phases must provide sites in solid solution for the variety of ion sizes of all radionuclides and non radioactive elements of wastes. Ionic substitution may be generally possible if the ionic radii difference between cations does not exceed 15 % [63]. Moreover, the overall charge balance must be maintained in the crystals. In order to maintain local electroneutrality multiple substitutional schemes can be envisaged. For instance in zirconolite ($CaZrTi_2O_7$), the partial substitution of Ca^{2+} ions by trivalent actinides or rare earths can be achieved by substituting partially Ti^{4+} by Al^{3+} ions in order to compensate the positive charge excess in calcium sites (see §IV.B). Thus, in this example, it appears that in order to incorporate preferentially trivalent actinide or rare earth ions in calcium site it is necessary to add Al_2O_3 to the precursors mixture. All these crystal chemical considerations clearly show that ceramics structure is less flexible than that of glasses to accommodate ions of various size and charge and waste composition fluctuations.

III.B.2.a. Ceramic waste forms for the immobilization of non separated radioactive wastes

To immobilize the wide spectrum of elements occurring in HLW solutions, ideal ceramic waste forms must have relatively complex structure with a high number of different coordination polyhedra of various size and shape. Moreover, for charge balance, multiple substitutional schemes must exist. Several single-phase ceramic formulations with high structural flexibility were proposed for conditioning HLW solutions such as solid solutions based on sodium zirconium phosphate $\text{NaZr}_2(\text{PO}_4)_3$ (NZP) [7,65]. However, the main examples of ceramics envisaged to immobilize the complex HLW solutions were generally multiphase assemblages (tailored ceramics) with unequal partitioning of radionuclides and non radioactive elements between the phases [66,65]. In Supercalcine ceramics, the complex mixture of elements of HLW was modified by minimum chemical additions of Ca, Sr, Al and Si salts to encourage the formation of an assemblage of crystalline phases able to incorporate all the wastes. About eight phases were reported in literature [65,67] such as silicate apatite (for MA and rare earths immobilization) and pollucite (for Cs immobilization). However, because of the presence of SiO_2 , a liquid phase may exist at high temperature during sintering that may persists after cooling as an undesirable Cs-rich glassy phase with lower leach resistance than the crystalline phases. Alumina-rich multiphase ceramics containing for instance magnetoplumbite, spinel and uraninite phases were also envisaged to immobilize HLW defence wastes in United States [63,66]. For both Supercalcine and alumina-rich ceramics the principle was to take the greatest possible advantage of HLW in order to minimize the amounts of constituent added in the mixture before sintering. This was not the case for the thermodynamically stable Synroc titanate-based ceramics for which the additives introduced with wastes were employed to produce the constituent phases in which all the radionuclides and non radioactive elements were dissolved in dilute solid solution.

Different kinds of Synroc (Synthetic Rock) waste form formulations were developed in Australia in the 1970s to immobilize civil or military HLW solutions [7]. The reference form of Synroc (Synroc-C) largely developed by Ringwood and co-workers [50,68,69] consisted of an assemblage of four main titanate

crystalline phases: zirconolite, hollandite, perovskite and titanium oxide (**Table VIII**). These phases have the capacity to incorporate almost all the radioactive or not elements present in HLW. Examples of the main elements incorporated in zirconolite, perovskite and hollandite are given in **Table VIII**. Detailed crystal chemical information on these phases and on the incorporation schemes of the main radionuclides were given by Fielding and White [70]. The work of Ringwood and co-workers [50,69] was based on a geochemical approach of waste immobilization. Indeed, very old and stable natural analogues of zirconolite and perovskite phases exist in nature [50]. After synthesis under reducing conditions with some added Ti metal, minor amounts of metal alloys are also present in the multiphase Synroc-C ceramic. This metal alloys incorporating elements such as noble metals, molybdenum and also probably technetium are microencapsulated by the primary titanate phases. Literature reports that because of the large number of incorporation schemes, the mineralogy of Synroc was able to adjust within certain limits to the fluctuations of the composition of the wastes [7]. In the early stages of the research program on Synroc, ceramics were prepared by oxide route (i.e. a conventional ceramic method using oxide, carbonate and hydroxide powders as precursor materials). In order to increase both the homogeneity of the mixture of precursors and the densification of the ceramic, wet chemistry processes were then developed mixing alkoxide and hydroxide precursors with simulated HLW solutions [50]. The slurry thus obtained was then dry, calcined under reducing conditions and hot pressed in graphite dies. Such a preparation method is thus more complex than glass melting. However, because of the occurrence of high amounts of TiO_2 and ZrO_2 , Synroc ceramics have better chemical durabilities than nuclear glasses [50]. Nevertheless, the presence of impurities may lead to the formation -near grain boundaries- of water soluble phases containing radioactive species. Although, Synroc ceramics were never used in nuclear industry to immobilize HLW solutions, two of the titanate phases (zirconolite and hollandite) are currently envisaged as single-phase for the specific conditioning of separated long-lived radionuclides. Moreover, a zirconolite-rich Synroc formulation was proposed for excess weapons Pu immobilization [71].

III.B.2.b. Ceramic waste forms for the specific immobilization separated long-lived radionuclides

It was mainly in 1990s that begun intensive research on ceramic matrices for the immobilization of separated long-lived radionuclides under both the impulsion of the disposal option of excess weapons Pu in United States and Russia and the French law concerning the reduction of the potential long-term impact on biosphere of HLW recovered after nuclear spent fuel reprocessing.

Concerning Pu conditioning, mainly single-phase ceramics were proposed to incorporate high amounts of plutonium. In this case, it is very important that the crystalline phase can also incorporate high amounts of neutron poisons (Gd, Hf) to avoid criticality risks. Different matrices (mainly zirconate and phosphate phases) were proposed as potential waste forms. For instance, zircon ($ZrSiO_4$), in spite of its high tendency to swelling under α -radiation [39], is an extremely durable phase that can incorporate Pu^{4+} and Hf^{4+} ions in zirconium site was proposed as an interesting candidate for this application [72,73]. Zirconia (ZrO_2) was also proposed for Pu conditioning because of its excellent resistance to both chemical alteration and α -radiation (lack of amorphization), the existence of a total solid solution between ZrO_2 and both PuO_2 and HfO_2 , and the possibility to incorporate Gd^{3+} in zirconium site [74,75,76]. A more considerable number of studies were performed on zirconolite (as single-phase or in zirconolite-rich multiphase Synroc) and pyrochlore ceramics. For instance, it was shown that Pu, Hf and Gd could be incorporated in the zirconolite phase of zirconolite-rich Synroc ceramics containing up to 80 wt% zirconolite [71]. Vance et al. justify the choice of a multiphase ceramic rather than single-phase zirconolite for Pu immobilization by the that zirconolite-rich Synroc could accommodate more easily variations in the ratio Pu/precursors and the occurrence of other crystalline phases than zirconolite would reduce grain size. This small grain size would reduce the risks of microcracking under Pu α -radiation in the zirconolite phase and would increase the mechanical properties of the ceramic. Another advantage was that it could be envisaged to incorporate simultaneously highly radioactive ^{137}Cs in the hollandite phase of zirconolite-rich Synroc in order to reduce diversion risks. Nevertheless, the titanate pyrochlore phase $(U, Pu, Hf, Gd)_2Ti_2O_7$ was finally retained by the Americans as the best candidate for Pu conditioning [6,77]. It must be underline that these pyrochlore waste forms were not single-

phase. Even if pyrochlore was the major phase, minor phases such as zirconolite, brannerite, and rutile were also present [78]. Other phases such as apatite and monazite were also proposed to immobilize Pu [72]. However, the program concerning the immobilization of Pu excess was abandoned in 2002 in United States in favor of conversion of PuO_2 into MOX fuel [77].

Concerning the conditioning of the long-lived radionuclides (MA, ^{135}Cs , ^{129}I) that can be separated from HLW solutions, several ceramic compositions were proposed. These studies were mainly performed in France (CEA) and in Australia (ANSTO). Examples of highly durable ceramics candidates for I, Cs or MA immobilization are presented in **Table IX** [19,23,18,79,80,81]. Waste incorporation amounts of 7 wt% (I), 5 wt% (Cs) and 10 wt% (MA) can be reached respectively for the iodoapatite, the hollandite and the three matrices developed for MA conditioning given **Table IX** [82]. The case of ^{129}I specific conditioning was already presented in §II. Detailed results concerning the synthesis and the properties of hollandite for radioactive cesium conditioning are presented in §IV.A. Zirconolite is able to incorporate both trivalent and tetravalent minor actinides mainly in the calcium site of its structure (see §IV.B). Britholite is a fluorophosphosilicate apatite also able to incorporate trivalent and tetravalent MA. The studies performed on this apatite ceramic were based on natural analogues such as the mineral phases crystallized during the natural nuclear reactions at Oklo (Gabon) [83]. Moreover, the phosphosilicate apatite structure seems capable of annealing the defects created by self-irradiation, even at low temperatures. Moreover, external irradiation experiments (simulating α -particles and recoils nuclei) clearly demonstrated that this capacity of annealing of britholite increased with the P/Si ratio [84]. Another highly durable phosphate ceramic (TDP), but without natural analogue, was envisaged for MA immobilization [81]. However, this matrix is only suitable for tetravalent MA immobilization by substitution at thorium site [23]. In this case, TPD/monazite composite ceramic waste forms are envisaged to immobilize simultaneously tetra- and trivalent MA [23,85]. Indeed, monazite (LnPO_4) is a highly durable matrix able to incorporate trivalent MA following the scheme $\text{Ln}_{1-x}\text{MA}_x\text{PO}_4$ [86] (Ln: lanthanides).

III.B.3. Glass-ceramic waste forms.

III.B.3.a. Definition and principles of preparation of glass-ceramics

Glass-ceramics are composite materials generally obtained by controlled crystallization (nucleation + crystal growth steps) of a glass (so-called parent glass) between its glass transformation temperature T_g and its liquidus temperature T_{liq} (i.e. in the region of undercooled melt)¹⁷. A schematic illustration showing the relative position of nucleation I (number of nuclei/time.volume unit) and crystal growth u (average crystals size/time) rate curves are shown in **Figure 10a,c**. In this figure, two cases are envisaged, either I and u curves are well separated (**Figure 10a**) or there exists a temperature field in which crystals can both nucleate and grow (grey zone in **Figure 10b**). A scheme showing an example of nucleation and crystal growth thermal treatment to prepare a glass-ceramic from a glass is shown in **Figure 10b**. More rarely, the preparation of glass-ceramics can also be envisaged by controlled cooling of the melt (i.e. without decrease the melt temperature below T_g before nucleation and crystals growth steps, **Figure 10d,e**). Such a method of glass-ceramic preparation is only possible if I and u curves are not well separated (**Figure 10c**).

In glass-ceramic literature [87,88], glass composites samples that contain either relatively big crystals (with size > several tens μm) heterogeneously dispersed in the bulk of a glass (so-called residual glass) or crystals nucleating only from the glass surface and growing towards the bulk, are not considered as true glass-ceramics. Generally glass-ceramists called true glass-ceramic, samples obtained by controlled crystallization of a parent glass and containing several tens vol% of micrometric crystals homogeneously dispersed in a residual glass. For these reasons, the samples shown in **Figures 5 and 12a** cannot be considered as true glass ceramics. Very often, it is necessary to adapt the parent glass composition by adding nucleating agents to the batch before melting in order to favor the nucleation of a very high amount of nuclei homogeneously dispersed in the bulk of the glass [87,88,89]. The nucleating agents are generally high field strength¹⁸ elements soluble in glass melt at high temperature but which tend to separate from the glassy network in the undercooled melt by glass-in-glass phase separation or

¹⁷ Below T_g , the undercooled melt transforms to a glass and its viscosity η becomes very high ($\eta > 10^{13}$ - 10^{14} dPa.s). In these conditions, I and u rates are generally considered as negligible.

¹⁸ The field strength F of a cation in an oxide material can be defined as $F=Z/d^2$ with Z the cation charge and d the mean cation-oxygen distance.

by formation of small crystals in the bulk that will then serve as nucleation sites (heterogeneous nucleation) for partial crystallization of parent glass. Glass-ceramics can contain either only kind of crystalline phase or several different crystalline phases. The development of detailed thermodynamic and kinetics theories of nucleation and crystals growth in undercooled melts is behind the scope of this Chapter. For more explanations concerning these points, the reader can consult for instance [60, 89,90].

Even if the formation of crystals by thermal treatment of glasses is known for a very long time by glass makers, the first tentative to use this phenomenon for practical application was published in literature by Réaumur in 1739 [91]. Nevertheless, this tentative was unsuccessful because in the glass compositions studied by Réaumur, nucleation occurred essentially from glass surface. True glass-ceramics were discovered only in 1957 accidentally by Stookey [92] from the Corning Company. Since this date, glass-ceramic materials have found numerous applications particularly for their excellent thermo-mechanical properties [87]. In nuclear waste management, glass-ceramic waste forms were initially envisaged in 1976 [93] in Germany, to improve the thermal stability and mechanical properties of borosilicate nuclear glasses by partial crystallization. Since this date, different examples glass-ceramic waste forms have been envisaged mainly for the immobilization of non separated radionuclides of HLW solutions recovered after civil or military nuclear spent fuel reprocessing. The amount of works reported about the immobilization of long-lived separated radionuclides is very limited. Several examples of glass-ceramics will be briefly presented in the next paragraph whereas an example of glass-ceramic studied in our laboratories and containing zirconolite crystals will be largely developed in §IV.C.

III.B.3.b. Glass-ceramics as nuclear waste forms for non separated HLW

As indicated in previous paragraph, for nuclear wastes immobilization, glass-ceramics were initially envisaged only to improve the thermal stability and mechanical properties of nuclear glasses. In this case, modified borosilicate nuclear glass compositions containing simulated non separated wastes were selected to lead to the crystallization of different phases by nucleation and crystal growth thermal treatments. Among the different compositions that were studied,

we can give the examples of barium aluminoborosilicate glass-ceramics and barium titanium silicate based glass-ceramics leading respectively to the crystallization of celsian ($\text{BaAl}_2\text{Si}_2\text{O}_8$) and fresnoite ($\text{BaTiSi}_2\text{O}_8$) as major phases. However, if we consider the ability of these major phases to incorporate elements of the wastes, celsian crystals were only able to incorporate Ba whereas fresnoite crystals were able to incorporate Ba and Sr [93]. Nevertheless, additional minor phases able to incorporate several elements of the wastes were also observed such as pyrochlore, scheelite (BaMoO_4) and pollucite ($\text{CsAlSi}_2\text{O}_6$) for the celsian-based glass-ceramics. Detailed results concerning these two kinds of glass-ceramic waste forms were summarized in the papers of Hayward [94,95]. In comparison with nuclear borosilicate glasses, the mechanical properties of these glass-ceramics were improved. However, their chemical durability was not enhanced. Thus, the development of these glass-ceramics as potential waste forms was abandoned. One of the most important work performed on glass-ceramics for the immobilization of non separated HLW wastes was performed in Canada by Hayward and his colleagues [94,95,96,97,98,99,100] in the 1980s. Their objective was to develop titanite¹⁹ (CaTiSiO_5)-based glass-ceramics (i.e. with titanite as major crystalline phase) for the immobilization of HLW solutions originating from the eventual reprocessing of Canadian nuclear spent fuel (CANDU²⁰ fuel). In these glass-ceramics, the aim was to incorporate wastes in the Ca and Ti site of titanite crystals and in the residual glass. Titanite as major crystalline phase in these glass-ceramics was selected for different reasons:

- The capacity of its structure to incorporate a wide range of the elements occurring in wastes (An, Ln, Sr, Ba....)
- Its good chemical durability and its thermodynamic stability in the saline environment that was envisaged for waste forms disposal in Canada
- The existence of metamict natural analogue samples.

In their work, the parent glass compositions chosen by Canadians belong to the SiO_2 - Al_2O_3 - CaO - TiO_2 - Na_2O system. It was envisaged to immobilize between 10 and 15 wt% wastes in the glass-ceramics. Parent glasses were melted in the temperature range 1250-1450°C. They were then nucleated between 650 and 1050°C and crystal growth was performed between 950 and 1050°C. In these

¹⁹ Titanite is also called sphene.

²⁰ CANDU: CANada Deuterium Uranium

glass-ceramics, titanite was the only or the major crystalline phase that can occupy 40 vol% of the samples and residual aluminosilicate glass was highly durable. However, it appeared that crystallization of these glass-ceramics was not easy to control and all parent glasses undergo rapid glass-in-glass phase separation during cooling from the melt. In compositions containing no wastes, the crystallization of titanite takes place either by surface nucleation or sporadically by heterogeneous nucleation in the bulk. The effect of individual elements occurring in wastes and of the simulated mixture of HLW wastes on crystallization was also studied. Some of the individual elements such as rare earths and uranium exhibit major influence on nucleation and crystallization processes. Concerning partitioning of wastes between titanite and residual glass, it appeared that lanthanides and Y strongly partitioned in the titanite crystals, where they replace calcium ions. Two charge compensation schemes were envisaged for trivalent lanthanides in order to compensate the positive charge excess in Ca site of titanite, either $(\text{Ca}^{2+}, \text{Ln}^{3+} + \text{Na}^+)\text{TiSiO}_5$ or $(\text{Ca}^{2+}, \text{Ln}^{3+})(\text{Ti}^{4+}, \text{Al}^{3+})\text{SiO}_5$. This could indicate that trivalent MA would preferentially partition in titanite crystals. Similarly, Zr^{4+} ions from wastes preferentially partitioned into titanite. However, U^{6+} , Ba^{2+} and Cs^+ ions from wastes remained into the residual glass. In spite of its relatively good properties as waste forms for HLW solutions immobilization, titanite-based glass-ceramics were never used industrially. The reason was that Canada finally decided (as United States) not to reprocess its nuclear spent fuel. Nevertheless, the results that were obtained on titanite-base glass-ceramics were very interesting and helpful for our own studies on zirconolite-based glass-ceramics.

III.B.3.c. Glass-ceramics as nuclear waste forms for separated long-lived radionuclides

Most of the work performed on glass-ceramics for nuclear waste management concerns non separated wastes (HLW solutions). Nevertheless, several studies were realized in France and in United States to immobilize respectively MA and Pu in glass-ceramics. As these wastes are α -emitters, they may induce amorphization and swelling of the crystals in which they are incorporated. In this situation, the swelling of crystals in residual glass can result in microfracturing of the waste form, which can greatly increase the surface area for radionuclide

release. Such microfracturations were observed for instance in glass-ceramics containing ^{244}Cm doped apatite and pyrochlore big crystals [39]. In order to reduce local constraints around crystals and the risks of microfracturation during disposal, their size must not exceed several μm .

Examples of specific and highly durable single phase ceramic waste forms for conditioning relatively high amounts of separated MA or Pu were presented in §III.B.2. However, one of the main drawbacks of radioactive single-phase ceramic waste forms is that they remain more difficult to prepare (grinding + sintering) than radioactive glasses (melting + casting) in nuclear facilities. To benefit at the same time from the ease of glass preparation and from the very good long term behavior and high incorporation capacity of ceramics, the preparation of glass-ceramic waste forms consisting of small highly durable crystals (which would preferentially incorporate MA or Pu) homogeneously dispersed in a durable glassy matrix - acting as a second barrier of containment (double containment principle) - appears as an interesting alternative to ceramics for MA and Pu conditioning (**Figure 2**). The principle of immobilization of MA in glass-ceramics is illustrated in **Figure 11**. Nevertheless, for such an application, MA or Pu must be incorporated preferentially in the crystalline phase (i.e. the partitioning ratio of MA or Pu between crystals and residual glass must be high). Moreover, due to the existence of a residual glassy phase embedding the crystals, such waste forms could accommodate more easily waste composition fluctuations and impurities than single phase ceramics. Indeed, because of the crystalline structure of ceramics, impurities and waste composition fluctuations could generate low durability parasitic phases containing radioactive elements in ceramic waste forms. Two examples of glass-ceramics for MA immobilization containing either zirconolite or rare-earth silicate apatite as only crystalline phase in their bulk will be firstly presented.

By controlled crystallization of a parent glass belonging to the $\text{SiO}_2\text{-Al}_2\text{O}_3\text{-CaO-TiO}_2\text{-ZrO}_2\text{-Ln}_2\text{O}_3$ system (where Ln such as Nd simulates trivalent MA), it has been shown that it was possible to prepare glass-ceramics with zirconolite as only crystalline phase in their bulk [101,102]. In these zirconolite-based glass-ceramics, the highly durable zirconolite crystals were shown to incorporate MA surrogates (Ln) [103,104]. For instance, the composition of the zirconolite crystals was $\text{Ca}_{0.82}\text{Nd}_{0.19}\text{Zr}_{1.05}\text{Ti}_{1.77}\text{Al}_{0.17}\text{O}_7$ for a parent glass containing 6 wt%

Nd₂O₃. Such waste forms were envisaged as potential candidates for the specific immobilization of MA. The effects of parent glass composition, of surrogate's nature and of preparation method on the microstructure of the glass-ceramics and on the structure and the composition of the crystals formed either in their bulk or near their surface were studied in our laboratories and the main results of these studies are presented in §IV.C of this Chapter. Nevertheless, in these glass-ceramics a significant amount of Ln remains in the residual glass after zirconolite crystallization.

During the optimization of a rare earth-rich glass composition for the immobilization of highly concentrated HLW solutions [9], a glass composition was found that could be melted at 1300°C and that lead easily to a glass-ceramic constituted of a high density of small crystals of rare earth-rich silicate apatite homogeneously dispersed in the bulk of the samples after controlled nucleation + crystal growth heat treatments [20] (**Figure 12b**). The composition of parent glass is given in the legend of **Figure 12** and the composition of crystals was approximately Ca₂Nd₈(SiO₄)₆O₂. As shown by X-rays diffraction (XRD), apatite was the only phase nucleating and growing in the bulk and near the surface of this glass-ceramic (**Figure 13**). As Nd is generally considered as a good trivalent MA surrogate, such glass-ceramics could also be envisaged for MA conditioning. By slow cooling of the glass melt, a smaller number of big crystals with typical shape were formed (**Figure 12a**). These crystals were also identified by XRD as neodymium silicate apatite (**Figure 13**). The strong decrease of the number of nuclei between the two methods of crystallization shown in **Figure 12** can be easily understood considering the relative positions of u and I curves in **Figure 10**. These apatite-based glass-ceramics were more efficient to concentrate lanthanides in the crystalline phase than the zirconolite-based glass-ceramics. This is not really surprising because neodymium ions occupied a smaller fraction of the cation sites in zirconolite crystals. Indeed, Nd³⁺ ions occupied about 20% of the Ca²⁺ sites in zirconolite whereas Nd³⁺ ions occupied 80% of the cation sites available in the apatite crystals according to the composition of the crystals given above. Nevertheless, according to literature, rare earth silicate apatite crystals do not exhibit as good long term behavior as zirconolite [105].

Among, the different options that were initially envisaged for immobilizing excess Pu in United States, it was envisaged to dissolve plutonium in a glassy

matrix along with enough fission products (β -emitters) for non-proliferation reasons. Considering the solubility of Pu in silicate glasses as problematic, it was also proposed to immobilize Pu at the same time as neutron absorbers (for criticality control) in highly durable crystals dispersed in a glass-ceramic waste form. A glass-ceramic composition containing numerous crystalline phases and able to immobilized 17 wt% PuO₂ incorporated mainly in zirconia and zirconolite phases was proposed [106]. It was also envisaged to incorporate simultaneously highly radioactive HLW wastes in this glass-ceramic to discourage recovery of the Pu.

IV. Studies on specific matrices for the immobilization of long-lived radionuclides

As shown in §II of this chapter, after 2-3 hundreds years disposal, minor actinides (Np, Am, Cm) will have the main contribution to potential radiotoxicity of HLW (**Figure 1**). If the transmutation of these long-lived radionuclides (after selective separation) into short-lived or non-radioactive elements appears as the best solution to minimize the potential long-term impact of HLW on living environment, their immobilization in specific host matrices– such as ceramics or glass-ceramics- with greater chemical durability than nuclear borosilicate glasses can also be envisaged as an alternative method to reach this objective. Moreover, even if long-lived fission products such as ¹³⁵Cs and ¹²⁹I have a lower contribution to long term radiotoxicity of spent fuel than MA, these radionuclides are more mobile in geological media than MA because of their physicochemical properties (**Table II**). These FP may thus reach the biosphere before significant decrease of their radioactivity if they are incorporated in low durability phases. As transmutation of ¹³⁵Cs and ¹²⁹I does not appear feasible for technical reasons [22], the specific conditioning of these long-lived radionuclides in very durable waste forms will minimize their potential impact on biosphere. The case of radioactive iodine (which does not occur in HLW solutions) specific immobilization was presented in §III.

In this part are presented the main results we obtained concerning synthesis, microstructural and structural characterizations and several properties (effect of external irradiations to simulate α or β self-irradiation during waste forms storage

and disposal, thermodynamic stability of glass-ceramics...) of three different matrices that have been envisaged to specifically immobilize either cesium (hollandite) or minor actinides (zirconolite ceramic, zirconolite-based silicate glass-ceramic). Examples of other matrices proposed in literature to immobilize these long-lived radionuclides will be also presented.

IV.A. The specific immobilization of radioactive cesium

Cesium is one of the most abundant fission products in HLW (**Table IV**) in which it occurs both as non radioactive (^{133}Cs) and radioactive isotopes with short half-life (^{134}Cs , ^{136}Cs , ^{137}Cs) or long half-life (^{135}Cs) (**Table I**). Because of the short half-life isotopes, cesium is also one the main responsible (with ^{90}Sr and ^{241}Am) for the heating power of HLW. The high thermal power of cesium thus limits the amount of cesium that can be incorporated in specific matrices. Cesium will have also one of the highest contributions (with Pu) to potential radiotoxicity of spent fuel during the first centuries after discharge. Another important problem with cesium is the high mobility of Cs^+ ions in geological environment (**Table II**) due to its big size, low charge and low electronegativity [25,107]. Currently, cesium is conditioned simultaneously with all FP of HLW in glassy matrices but glass and wastes compositions must be adapted in order to avoid the formation during melt cooling of poorly durable parasitic crystalline phases (called “yellow phases”) that can concentrate cesium [108,109]. All these considerations clearly point out that dispersion of radioactive cesium in biosphere must be absolutely avoided even after long periods of waste form disposal because of the occurrence of ^{135}Cs . All Cs isotopes can be selectively extracted (simultaneously with Rb) from HLW solutions using enhanced separation process with calixarenes crown molecules [110] complementary to the Purex process²¹ (**Figure 14**). As transmutation of ^{135}Cs is not achievable reasonably without isotopic separation [111], the conditioning of radioactive cesium (mixture of all isotopes) in specific ceramic waste forms with greater leach resistance than borosilicate glasses, appears as an interesting alternative to transmutation. The selective immobilization of cesium in a specific highly durable matrix would reduce the risks of ^{135}Cs migration towards biosphere. However, it must be kept in mind that because cesium is a big alkali

²¹ Extraction of Cs can be done either immediately before or after extracting MA from HLW solutions.

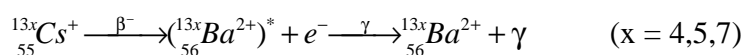
cation with low electronegativity, it has a high volatility at high temperatures [27,112] during waste form fabrication (because of the small strength of Cs-O bonding) and tends easily to form water-soluble compounds.

In the following paragraphs we will give more precise information about radioactive cesium and we will briefly review the different kinds of matrices that have been envisaged as potential candidates for its immobilization. We will then present the main results (microstructural and structural study, stability under β -irradiation) we obtained concerning a $\text{Ba}_x\text{Cs}_y(\text{M},\text{Ti})_8\text{O}_{16}$ hollandite type matrix (with $x + y < 2$, M being a trivalent cation) which appears today as one of the best matrix for Cs conditioning [79,113,114,115,116,117,118]. Indeed, ferriferous hollandite ceramics (with $\text{M}^{3+} = \text{Fe}^{3+}$ or $\text{M}^{3+} = \text{Fe}^{3+} + \text{Al}^{3+}$) have been retained as the potential candidate for specific immobilization of radioactive cesium in the framework of the French law passed in 1991 concerning the research on long-lived radioactive waste management [18,79].

IV.A.1. Radioactive cesium in HLW

In France, a flux of about 2.8 tons of cesium is generated every year after reprocessing of 800 tons of nuclear spent fuel [32]. In the world, 46 kg of cesium are produced every day in nuclear reactors [119]. Whereas naturally occurring cesium is entirely non-radioactive (^{133}Cs), five main Cs isotopes are present in nuclear spent fuel (**Table X**) [120]. The relative proportions of these isotopes in HLW solutions depend on the nature of the fuel, on its burn up and on the time before reprocessing. Examples of proportions of Cs isotopes in different UOX spent fuels 4-5 years after discharge are given in **Table XI** [121]. It appears that ^{135}Cs represents approximately 14% of all the cesium isotopes in UO_2 spent fuel which corresponds to an amount of about 390 kg generated every year in France after reprocessing. Because of their short half-lives, ^{136}Cs rapidly disappears and ^{134}Cs concentration strongly decreases before conditioning. During the first three centuries after spent fuel discharge, the cesium radioactivity will be dominated by ^{137}Cs which then will become negligible in comparison with that of ^{135}Cs . Consequently, the radioactivity of cesium will be firstly controlled by ^{137}Cs during storage and the beginning of disposal and then only by ^{135}Cs . ^{137}Cs will be thus the main responsible of heating in waste forms among all cesium isotopes. In order to limit the temperature in the bulk of waste forms ($T \leq 300^\circ\text{C}$), no more

than 5 wt% Cs₂O must be incorporated in specific matrices. In the French nuclear glass R7T7, the amount of Cs₂O is about 1.29 wt%. The decay of radioactive cesium isotopes (¹³⁴Cs, ¹³⁵Cs, ¹³⁷Cs) involves the emission of β-particles (electrons) with energy E ranging from 0.089 to 1.454 MeV, γ rays (0.475 ≤ E ≤ 1.168 MeV) and the transmutation of Cs to stable Ba [122,123]:

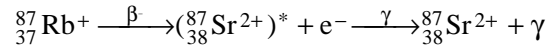


In **Figure 15** are shown the disintegration schemes of the main radioactive isotopes (¹³⁵Cs, ¹³⁷Cs) that will be present in waste forms during disposal. The energy of β-particles will not exceed 1.176 MeV and 95% of them will have energy of 0.514 MeV. γ-particles are only emitted by ¹³⁷Cs with energy of 0.662 MeV. ¹³⁴Cs emitted β-particles with energy ranging from 0.089 to 1.454 MeV but its concentration will become negligible 10 years after spent fuel discharge in comparison with others radioactive Cs isotopes [124].

Therefore, Cs-host forms must be stable under (β,γ)-irradiation (i.e. its capacity to retain cesium in its structure must not be significantly affected by irradiation) and must accommodate the valence and ionic radius changes resulting from cesium decay to barium. As the energy of the recoiling Ba nuclei resulting from Cs β-decay is very low (2-4.6 eV [125]) in comparison with that of actinides (α-recoil, 70-100 keV), it cannot involve atomic displacements and will be no more considered in this Chapter.

Rubidium is also an alkali element (fission product) occurring in HLW solution but its concentration represents only about 10 wt.% of that of cesium (**Table IV**). However, Cs⁺ and Rb⁺ ions are co-extracted during the enhanced separation process by calixarene molecules [126] and if a conditioning matrix is selected for cesium this one must also accept rubidium in its structure. It must be underlined that, except for ⁸⁷Rb (half-life 4.88.10¹⁰ years), all rubidium radioactive isotopes are (β,γ) emitters with very short half-life and will rapidly disappear before separation and conditioning. In HLW solutions, ⁸⁷Rb and ⁸⁵Rb (stable isotope) represent respectively 70.2 and 29.8 %.

As radioactive ^{87}Rb will be co-extracted with cesium during enhanced separation process, it is interesting to consider its decays into non radioactive ^{87}Sr during disposal:



Due to both the very long half-life and small concentration of ^{87}Rb in HLW, only a very small quantity of strontium will be formed before all radioactive cesium will decay to barium. Nevertheless, when dealing with specific waste forms for Cs conditioning, it is also interesting to consider their capacity to accept both Rb^+ and Sr^{2+} ions in their structure.

IV.A.2. Specific waste forms for cesium conditioning

Literature indicates that different kinds of solid matrices were studied for radioactive cesium conditioning: silicate and phosphate glasses, single or multiphase ceramics. In this paragraph, we will review several examples of these potential cesium waste forms and different methods to prepare them. The possibility to immobilize cesium in glass-ceramics will be also envisaged. For all these matrices, the criteria used to select the more suitable waste form for cesium immobilization were generally: synthesis possible in air without hot pressing, very low Cs vaporization during heat treatments, lack of Cs-rich parasitic phases of low durability and very low leach rates.

IV.A.2.a Glass and glass-ceramic matrices for cesium conditioning

Currently, after nuclear spent fuel reprocessing, radioactive cesium is incorporated in the structure of borosilicate glasses such as the R7T7 glass. In the glass structure, Cs^+ ions (as other alkali ions such as Li^+ , Na^+ and Rb^+) can act as network modifier in the borosilicate network or as charge compensator near tetrahedral BO_4^- or AlO_4^- units for instance (**Figure 8**). The R7T7 glass contains about 1.3 wt% Cs_2O and is melted in a metallic melter (AVH process, **Figure 6**) at 1150°C [28]. However, the possibility to prepare nuclear glasses at higher temperature in CCM enables to envisage glass compositions with higher refractory character than borosilicate nuclear glasses (and thus also more leach

resistant) to immobilize Cs. In this context, Bart et al. [127] synthesized different aluminosilicate glasses at temperatures between 1400 and 1600°C containing from 3 to 10 wt% Cs₂O. To increase chemical durability, neither Na₂O nor B₂O₃ were introduced in these glasses. This lack of fluxing agents was responsible for their high melting temperature. It appeared that the relative Cs₂O losses were always less than 5 wt%. Moreover, almost all glasses were homogeneous and a ten-fold improvement in leach rates over current borosilicate nuclear glasses was observed. In spite of these good results, the improvement of chemical durability of these glasses in comparison with that of current nuclear glasses was not considered high enough to retain them as potential specific waste forms for cesium. In another context, iron phosphate glasses that can be melted at lower temperature (950°C) than current nuclear borosilicate glasses were envisaged to incorporate radioactive cesium chloride in USA [128]. Even if very little cesium volatilized during melting of these phosphate glasses, the improvement of leach resistance was only about one tenth of that of borosilicate glasses.

Because of the capacity of pollucite (CsAlSi₂O₆) crystals to incorporate cesium and the good chemical resistance of this phase (see §IV.A.2.b), glass-ceramic waste forms containing pollucite crystals in their bulk formed by controlled crystallization of a parent glass may appear as good candidates for Cs conditioning (concept of double containment barrier, **Figure 11**). Indeed, it was shown that pollucite-based aluminosilicate glass-ceramics could be prepared after melting at very high temperature (1850-1900°C in a gas-fired furnace and rhodium crucibles) glasses belonging to the SiO₂-Al₂O₃-Cs₂O system [87,129]. Losses of cesium ranging from 5 to more than 20% were observed after melting. After quenching and controlled crystallization of glass, pollucite crystals were formed coexisting with mullite (Al₆Si₂O₁₃) crystals and residual glass. Such glass-ceramics that were initially envisaged for applications associated with their high refractoriness and their relatively low thermal expansion exhibit also good chemical durability [87,129]. Cesium ions incorporated into the pollucite crystals of the glass-ceramic benefit from a double containment barrier. Unfortunately, no information was given in literature about the amount of cesium remaining in the residual glassy phase. However, due to the very high melting temperature of parent glass and Cs vaporization occurring during melting, such glass-ceramic cannot be considered as good candidate for Cs immobilization.

IV.A.2.b Crystalline matrices for cesium conditioning

Different kinds of ceramic matrices (silicates, phosphates, titanates) were studied in literature as specific waste forms for Cs immobilization such as: pollucite ($\text{CsAlSi}_2\text{O}_6$) [130], CsZP ($\text{CsZr}_2(\text{PO}_4)_3$) [131], Synroc-type barium hollandite ($\text{Ba}_x\text{Cs}_y(\text{Ti},\text{Al})_{2x+y}\text{Ti}^{4+}_{8-2x-y}\text{O}_{16}$ ($x+y<2$)) [115] and iron-rich barium hollandite ($\text{Ba}_x\text{Cs}_y(\text{Fe},\text{Al})_{2x+y}\text{Ti}^{4+}_{8-2x-y}\text{O}_{16}$ ($x+y<2$)) [79]. Other matrices such as phosphate apatites or rhabdophane ($\text{CaCsNd}(\text{PO}_4)_2$) were also tested for their capacity to incorporate cesium but difficulties were encountered to obtain single phase samples [121]. Considering both the possibility to prepare well densified hollandite samples, the ability of this matrix to incorporate Cs^+ , Ba^{2+} and Rb^+ and Sr^{2+} ions [132,133,134] and the occurrence of Ti^{4+} ions in the structure that can act as electron traps during β -decay ($\text{Ti}^{4+} + e^-(\beta^-) \rightarrow \text{Ti}^{3+}$), hollandite-type matrices appear today as the best candidates for cesium immobilization in comparison with silicate and phosphate ceramic matrices. Indeed, even if pollucite is an aluminosilicate phase with high refractory character (melting point $> 1900^\circ\text{C}$) that can accommodate more than 40 wt% Cs into its structure and exhibits good chemical durability [135], it was difficult to obtain single phase pollucite ceramic samples with high density [136]. Moreover, other cesium aluminosilicate secondary phases such as CsAlSiO_4 which is poorly durable can formed during synthesis and coexist with pollucite in ceramics. Contrary to hollandite, none of the cations of pollucite (Al^{3+} , Si^{4+}) can act as efficient electron trap during β -decay. Concerning CZP, for which only a small number of studies were performed, a fraction of Zr^{4+} ions can probably be reduced to Zr^{3+} ions under β -decay but the ability of this matrix to incorporate Ba^{2+} ions was not demonstrated to the best of our knowledge.

IV.A.3. $\text{Ba}_x\text{Cs}_y(\text{M},\text{Ti})_8\text{O}_{16}$ hollandite ceramic as waste form for Cs immobilization

IV.A.3.a General characteristics of hollandite

Historically, (Ba,Al)-hollandite²² (nominally BaAl₂Ti₆O₁₆) was initially envisaged as one of the four main crystalline phases in the Synroc-C ceramic (**Table VIII**). To control the redox state of multivalent elements (Ti, Mo...) during Synroc synthesis, a small quantity of titanium metal was added to the mixture before hot pressing [116]. This induced the partial reduction of Ti⁴⁺ ions into Ti³⁺ ions which facilitates -by substituting partially Al³⁺ ions- the incorporation of Cs⁺ ions into the tunnels of the hollandite structure [137] (see §IV.A.3.b). Indeed, because of the small size of Al³⁺ ions, it is very difficult to incorporate significant amounts of cesium in the hollandite structure without partially reducing titanium. After partial reduction of titanium and cesium incorporation, the Synroc (Ba,Cs,Al)-hollandite has the following composition: Ba_xCs_y(Ti,Al)³⁺_{2x+y}Ti⁴⁺_{8-2x-y}O₁₆ (x+y<2) [138]. Chemical durability tests performed on single phase Synroc-hollandite showed its very good resistance to water attack over the pH range 2-13 [113].

Recently, in France, in the context of enhanced separation and specific immobilization of radioactive cesium, an iron-rich and single phase (Ba,Cs,Al+Fe)-hollandite Ba_xCs_y(Fe,Al)³⁺_{2x+y}Ti⁴⁺_{8-2x-y}O₁₆ ceramic with x = 1 and y = 0.28 that could be easily prepared under air (calcination at 1000°C and natural sintering at 1250°C) by an alkoxide route, was proposed by CEA as specific waste form for radioactive cesium immobilization [79]. No Cs vaporization was noticed during synthesis of this hollandite composition and the amount of Cs₂O incorporated (5 wt%) was chosen to limit the temperature in the bulk of the waste form during storage and disposal. By introducing iron in hollandite composition, it was not necessary to prepare the samples under reducing conditions contrary to Synroc-hollandite. After sintering under air, iron ions occurred mainly as Fe³⁺ ions in hollandite as shown by Mössbauer spectroscopy [120,139]. As ferric ions have ionic radius only slightly smaller than Ti³⁺ ions, they would also facilitate Cs⁺ ions incorporation in the tunnels of the structure (see §IV.A.3.b). Static alteration tests by water showed that the chemical durability of Ba_xCs_y(Fe,Al)³⁺_{2x+y}Ti⁴⁺_{8-2x-y}O₁₆ hollandite was as good as that of Synroc-hollandite [79] and was about two orders of magnitude higher than that of borosilicate nuclear glasses [140]. The alteration mechanism of hollandite begins with an initial release of cesium and barium followed by a severe drop of the

²² In this chapter, we will refer Ba_xCs_yM³⁺_{2x+y}Ti⁴⁺_{8-2x-y}O₁₆ hollandite samples as (Ba,Cs,M)-hollandite.

alteration rate ($8.10^{-5} \text{g.m}^{-2}.\text{day}^{-1}$ at 90°C under static conditions) [140]. Moreover, recent calorimetric measurements performed on $\text{Ba}_{1.00}\text{Cs}_{0.28}\text{Fe}_{0.82}\text{Al}_{1.46}\text{Ti}_{5.72}\text{O}_{16}$ hollandite ceramic showed that its thermodynamic stability was of the same order as that of rutile, which indicates the good stability of (Ba,Cs,Al+Fe)-hollandite [141]. Several studies were also performed recently by ANSTO on (Ba,Cs,M)-hollandites (with $\text{M}=\text{Fe}, \text{Mn}\dots$), prepared either by alkoxide route or by melting [142,143].

IV.A.3.b Structure of $\text{Ba}_x\text{Cs}_y(\text{M},\text{Ti})_8\text{O}_{16}$ hollandite

Natural hollandite has the formula $\text{BaMn}_8\text{O}_{16}$ where manganese can occur under various oxidation states ($\text{Mn}^{2+}, \text{Mn}^{3+}, \text{Mn}^{4+}$). However, there are a lot of structural isotypes, including titanate hollandites $\text{Ba}_x\text{Cs}_y(\text{M},\text{Ti})_8\text{O}_{16}$ ($x+y < 2$) in which Mn of natural hollandite is replaced by $\text{M} + \text{Ti}$. In our studies (§IV.A.3.c2.), M was a trivalent cation or a mixture of different cations ($\text{Al}^{3+} + \text{Fe}^{3+}$ for instance). The $\text{Ba}_x\text{Cs}_y(\text{M},\text{Ti})_8\text{O}_{16}$ type structure is shown in **Figure 16**. Approximately square tunnels running parallel to the short axis of the structure are enclosed by columns of two edge-sharing octahedra which then share corners. The Ti and M cations are located in these octahedral sites (site B). The big Ba^{2+} and Cs^+ cations (**Table XII** [144]) are set in the tunnels in box-shaped cavities of eight oxygen ions (site A). In spite of the relatively open-framework-type structure of (Ba,Cs,M)-hollandite, Ba^{2+} and Cs^+ ions have to overcome a large energy barrier associated with passing through the square planar arrangement of oxygen ions to migrate along the axis of the tunnels and these compounds appeared as very bad ionic conductors [120]. Thus, the large cations are well immobilized in hollandite tunnels. Hollandite cell symmetry may be tetragonal ($I4/m$ space group) or monoclinic ($I2/m$ space group). This mainly depends on the relative values of the radius of cations in sites A (r_A) and B (r_B) (r_A and r_B being respectively the average ionic radii of ($\text{Ba}^{2+}, \text{Cs}^+$) cations in site A and ($\text{M}^{3+}, \text{Ti}^{4+}$) cations in site B) [116,145]. Between these two symmetries, the cross-section of the tunnels changes from approximately square in shape (tetragonal cell) to a rhombus shape (monoclinic cell). The M^{3+} cations in site B insured the charge compensation of the positive charge excess in the tunnels due to Cs^+ and Ba^{2+} cations. In tetragonal hollandites, all octahedral sites B are identical whereas in monoclinic hollandites two different types of sites B can be distinguished [138]. Theoretically, a maximum of two ($\text{Ba}^{2+} + \text{Cs}^+$)

cations per formula unit (i.e. $x+y=2$) can be incorporated in the hollandite structure. However, it is only for small univalent cations (such as K^+) that the box-shaped cavities (site A) in the tunnels of hollandite can be all occupied ($K_2(Al_2Ti_6)O_{16}$) [133]. For hollandites containing only Ba^{2+} ions ($y = 0$) or a mixture of Ba^{2+} and Cs^+ ions, tunnels are only partially occupied ($x+y<2$) because vacant sites are necessary to accommodate both repulsion between Ba^{2+} ions and local distortions that occurred after incorporation of big Cs^+ ions. Moreover, studies performed on various compositions showed that stable hollandite existed only for $x+y>1$ [132]. Indeed, for each hollandite there is a lower limit of $(x + y)$ below which the intended composition cannot be obtained as a single phase. For instance, according to Zandbergen et al. [132], $Ba_x(Al,Ti)_8O_{16}$ hollandite can be obtained as a single phase only for $1.16<x<1.28$.

Concerning cations M in site B, it was shown that their size had a strong effect on the average (M,Ti)-O distance d , the cell volume V and the box-shaped cavities (site A) volume V_c as d , V and V_c increase with cation M radius [116]. The size of tunnel walls of hollandite is mainly controlled by cations in site B and not by cations in site A. This explains why partial reduction of titanium ions in Synroc-hollandite or partial substitution of Al^{3+} ions by bigger ions such as Fe^{3+} (**Table XII**) facilitates cesium incorporation into the tunnels and thus avoids the formation of parasitic phases with low chemical durability such as $CsAlTiO_4$ [137]. The occurrence of this phase can be detected directly by EDX²³ on SEM²⁴ images or by ¹³³Cs MAS-NMR for hollandite ceramics with low concentration of paramagnetic species (such as Fe^{3+} , Cr^{3+} , Ti^{3+} ions)²⁵ [146]. As ¹³³Cs MAS NMR (100% natural abundance, $I=7/2$) spectra are sensitive to Cs^+ ion environment in materials, they can give the number of different Cs environments in hollandite ceramics. By comparison with Cs-rich references (such as $CsAlTiO_4$), signals position (chemical shift) gives information about the nature of the phases in which Cs^+ ions are located (hollandite or parasitic phases) [146,118].

Depending on hollandite composition and more particularly on the nature of the M^{3+} cations in site B, the vacant sites and cations (Ba^{2+} , Cs^+) in the tunnels may take up an ordered arrangement (superlattice ordering) [116,147]. This ordering is

²³ Energy Dispersive X-ray analysis

²⁴ Scanning Electron Microscopy

at the origin of several broad and low intensity extra-lines (superlattice lines) observed at low angles on the XRD patterns (see **Figure 18** in §IV.A.3.c2.) of hollandite at angular positions incommensurate with hollandite cell [148,149]. A XRD study performed on $\text{Ba}_{1.16}\text{Al}_{2.32}\text{Ti}_{5.68}\text{O}_2$ and $\text{Ba}_{1.32}\text{Al}_{0.96}\text{Fe}_{1.28}\text{Ti}_{5.66}\text{O}_{16}$ single crystals prepared by a flux method in our laboratories²⁶, revealed diffraction patterns of a one-dimensional modulated incommensurate structure along the tunnels direction and confirmed that the XRD extra-lines were due to the ordering of barium ions and vacancies in the tunnels [120]. These lines can be indexed in the $I4/m(00\gamma)00$ super space group. This ordering may extend between adjacent tunnels (lateral correlation) and was shown to depend both on the size of cations M in site B and on the amount of barium cations in the tunnels (occupancy level) [116,150,151]. The size of ordered domains increases with the size of M. A tentative of explanation of the dependence of ordering in tunnels with the nature of cations M was proposed by Kesson et al.[134] using both structural and electrostatic screening considerations. Comparison of the diffuse superlattice spots on electron diffraction patterns of $\text{Ba}_{1.16}\text{Al}_{2.32}\text{Ti}_{5.68}\text{O}_{16}$ and $\text{Ba}_{1.16}\text{Fe}_{2.32}\text{Ti}_{5.68}\text{O}_{16}$ ceramics confirmed that substitution of aluminum by iron ions in site B of hollandite led to larger ordered domains [118,120].

IV.A.3.c Synthesis of $\text{Ba}_x\text{Cs}_y(\text{M},\text{Ti})_8\text{O}_{16}$ hollandite ceramics

IV.A.3.c.1. Synthesis of hollandite by alkoxide route and by melting

Most of papers reported the preparation of single phase $\text{Ba}_x\text{Cs}_y(\text{M},\text{Al})^{3+}_{2x+y}\text{Ti}^{4+}_{8-2x-y}\text{O}_{16}$ hollandites with $\text{M}^{3+} = \text{Ti}^{3+}$ [115,152] or $\text{M}^{3+} = \text{Fe}^{3+}$ [79] by alkoxide route using alkoxide, nitrate or acetate precursors in solution before drying, calcination and sintering as in the Synroc preparation method. This is the method generally

²⁵ High concentration of species with electronic spin $S \neq 0$ generally leads to a strong broadening and/or a displacement of NMR signals (see for example [146] in the case of high concentration of paramagnetic Ti^{3+} ions in hollandite).

²⁶ $\text{Ba}_{1.16}\text{Al}_{2.32}\text{Ti}_{5.68}\text{O}_2$ and $\text{Ba}_{1.32}\text{Al}_{0.96}\text{Fe}_{1.28}\text{Ti}_{5.66}\text{O}_{16}$ single crystals were prepared by melting at 1400°C and slow cooling (12°C/h from 1400 to 900°C and 240°C/h from 900°C to room temperature) of $0.47\text{BaF}_2 + 0.53\text{B}_2\text{O}_3$ flux containing 40 wt% of raw materials (oxides, carbonates) in the stoichiometric proportions of hollandite. Hollandite crystals were then extracted by dissolution of flux in hot acidified (HCl) water. Hollandite crystals have a needle shape (several mm length) with c axis along this direction. Attempts performed to prepared hollandite single crystals with cesium were unsuccessful probably because of cesium vaporization from the melt during melting and cooling, or because of an insignificant partitioning ratio of Cs^+ ions between the crystals and the borate melt during crystallization.

used by ANSTO and CEA to prepare single-phase hollandite or hollandite-rich ceramic samples for Cs immobilization. For instance, Bart et al.[79] mixed aluminum sec-butoxide and titanium isopropoxide in ethanol with barium, ferrous and cesium nitrates dissolved in water. After stirring, drying, calcination (1000°C), planetary ball milling and pressing, the samples were sintered at 1250°C in air and retained all the cesium (5 wt% Cs₂O) in hollandite structure. Difficulties were reported by Carter et al. [142] to prepare by melting both single phase hollandite and Synroc ceramics with Cs without the presence of the low durability parasitic phase CsAlTiO₄. However, they were able to synthesize hollandite-rich Synroc waste forms with about 7.5 wt% Cs₂O and different metals (Cr, Ni, Zn, Co, Fe...) in the site B of hollandite by melting in air (1450-1550°C in Pt crucibles) calcined precursors prepared by alkoxide route [143,143]. Their ceramics contained hollandite (sometimes more than 60 wt%) with zirconolite, perovskite and rutile. For several compositions, Cs entered only the hollandite with little loss during synthesis. For these compositions, chemical durability tests showed that Cs leachate concentration was two orders of magnitude lower than alkali leachate concentrations for a reference borosilicate glass.

IV.A.3.c2. Synthesis and characterization of hollandite by oxide route

In the study we performed on hollandite waste forms, we tried to prepare single phase (Ba,M)- and (Ba,Cs,M)-hollandite samples by oxide route using oxide, carbonate and nitrate powders without dissolving the reactants before heat treatments (natural sintering in air). We studied the effect of trivalent cation M (Al³⁺, Cr³⁺, Ga³⁺, Fe³⁺, Sc³⁺ of increasing size, **Table XII**) on the ease of preparation of single phase ceramics and on cesium retention during synthesis. Reagent-grade oxide, carbonate and nitrate powders (Al₂O₃, TiO₂, BaCO₃, Cr₂O₃, Fe₂O₃, Ga₂O₃, Sc₂O₃, CsNO₃) were used for preparation. By increasing the size of cation M in octahedral sites of hollandite, the aim was to increase the section of the tunnels in order to facilitate the entry of cesium into hollandite structure (**Figure 16**). In order to increase the reactivity of the powders, the mixture was ground by attrition milling after calcination and before natural sintering in air (**Figure 17**). Attrition enables to reduce the particle size of precursor to less than 1 µm. Indeed, after attrition, the mean particle size of our powders mixture was about 0.5 µm as determined with the help of a laser granulometer. To reduce the

risks of cesium vaporization during the sintering of pellets (pressed at 30 MPa), the temperature and duration were reduced to respectively 1200°C and 30h. Using these sintering conditions, dense samples were obtained only if the calcined precursors were previously finely ground by attrition (**Figure 17**). The main results we obtained concerning the effect of cation M on hollandite ceramics microstructure, structure and composition are given below, for more details see [117,118,120].

We first tried to prepare single phase $Ba_x(M,Ti)_8O_{16}$ hollandite ceramics without cesium for $x=1.16$ ²⁷ for all the cations M ($Ba_{1.16}^{2+}(M_{2.32}^{3+}Ti_{5.68}^{4+})O_{16}$). For each single phase (Ba,M)-hollandite sample, we then tried to prepare single phase (Ba,Cs,M)-hollandite samples with cesium ($Ba_{1.04}Cs_{0.24}(M_{2.32}Ti_{5.68})O_{16}$), keeping the same amount of cations M as in (Ba,M)-hollandites (i.e. 2.32 per formula unit). For charge compensation reasons, it was necessary to increase the total amount of cations in the tunnels. Mixed hollandite ceramics with $M^{3+} = Al^{3+} + Ga^{3+}$ and $M^{3+} = Al^{3+} + Fe^{3+}$ were also prepared.

For $M^{3+}=Al^{3+}$, Cr^{3+} , Ga^{3+} and Fe^{3+} , single phase $Ba_{1.16}M_{2.32}Ti_{5.68}O_{16}$ hollandite ceramics with tetragonal structure were obtained by oxide route. Mixed hollandite ceramics $Ba_{1.28}Al_{1.64}Ga_{0.92}Ti_{5.44}O_{16}$ and $Ba_{1.28}Al_{1.64}Fe_{0.92}Ti_{5.44}O_{16}$ were also single phase with tetragonal structure. XRD patterns of $Ba_{1.16}M_{2.32}Ti_{5.68}O_{16}$ ceramics are shown in **Figure 18**. The corresponding lattice parameters and cell volume are given in **Table XIII**. In agreement with literature on hollandite structures [153], the lattice parameters of $Ba_{1.16}M_{2.32}Ti_{5.68}O_{16}$ hollandites increased linearly with the average radius r_B of cations in site B (**Figure 19**). It is easy to understand that increase of lattice parameters leads to an increase of the size of the box-shaped cavities in tunnels (**Figure 16**) which is supposed to facilitate Cs incorporation in the structure. Only a small amount parasitic phase containing P, Ba, Si and O was detected by SEM in several samples (phase A, **Figure 20**). This phase was due to pollution and could be suppressed by changing raw materials and the nature of attrition balls (without Si). Contrary to $Ba_{1.16}Fe_{2.32}Ti_{5.68}O_{16}$ and $Ba_{1.16}Ga_{2.32}Ti_{5.68}O_{16}$ ceramics (**Figure 20c,d**), $Ba_{1.16}Al_{2.32}Ti_{5.68}O_{16}$ and $Ba_{1.16}Cr_{2.32}Ti_{5.68}O_{16}$ samples were badly densified after sintering at 1200°C (**Figure 20a,b**). This difference of densification can be explained by the high

²⁷ The choice of $x=1.16$ for all the (Ba,M)-hollandite samples was made according to the boundaries of the single phase domains of hollandite reported in literature [132].

melting point of hollandites ($\text{Ba}_{1.16}\text{Al}_{2.32}\text{Ti}_{5.68}\text{O}_{16}$ 1517°C, $\text{Ba}_{1.16}\text{Cr}_{2.32}\text{Ti}_{5.68}\text{O}_{16}$ 1650°C) and of the corresponding oxides (Al_2O_3 2054°C, Cr_2O_3 2330°C) [118]. Consequently, the occurrence of Al or Cr in hollandite composition slowed down densification processes. The strongest effect was observed for chromium (**Figure 20b**). For (Ba,Al+Fe)- and (Ba,Al+Ga)-hollandites, the introduction of Fe and Ga induced a decrease of ceramics porosity in comparison with $\text{Ba}_{1.16}\text{Al}_{2.32}\text{Ti}_{5.68}\text{O}_{16}$ (pictures not shown). This result confirmed the positive effect of Fe_2O_3 and Ga_2O_3 on densification. The ceramic sample prepared with Sc by oxide route at 1200°C was not single phase. This was probably due both to the high melting point of Sc_2O_3 (2485°C) and to the high radii difference between Ti^{4+} and Sc^{3+} ions in site B (**Table XII**) slowing down crystals organization during sintering [118]. For $\text{M}^{3+}=\text{Al}^{3+}$, Cr^{3+} and Ga^{3+} , (Ba,Cs,M)-hollandite ceramics retained only a fraction of Cs in their structure and were either multiphase and/or badly densified after sintering at 1200°C (**Figure 20e,f**). The composition of the hollandite samples determined by EPMA²⁸ are given in **Table XIII**. The high refractory character of both Cr_2O_3 and (Ba,Cr)-hollandite and the small size of Al^{3+} ions (**Table XII**) could explain the strong difficulties of Cs^+ ions to enter into the (Ba,Al)- and (Ba,Cr)-hollandite tunnels. In this case, a high fraction of cesium evaporated during synthesis and disturbed densification. For instance, more than 54% of cesium did not enter into the (Ba,Cs,Cr)-hollandite tunnels. For the (Ba,Cs,Ga)-hollandite sample, a Cs-rich parasitic phase ($\text{CsGaSi}_{0.4}\text{Ti}_{0.6}\text{O}_4$) was detected both by SEM and ¹³³Cs MAS NMR [118]. By analogy with CsAlTiO_4 , this phase exhibited probably low chemical durability against water. Consequently, the low densification of ceramics and/or the occurrence of low durability Cs-rich parasitic phases show that (Ba,Cs,M)-hollandite ceramics with $\text{M}^{3+} = \text{Al}^{3+}$, Cr^{3+} and Ga^{3+} , prepared by oxide route at 1200°C, are not suitable as waste forms for Cs.

(Ba,Cs,Fe)-hollandite was shown to be dense and to retain all cesium in its structure (**Table XIII**). Even if a significant amount of iron-rich secondary phase (Fe_2TiO_5) was detected (**Figure 20g**), the presence of this phase –that did not concentrate cesium– is not a problem for the use of (Ba,Cs,Fe)-hollandite ceramic as Cs waste form. Contrary to (Ba,Cs,M)-hollandite ceramics with Al, Cr or Ga, the introduction of cesium in (Ba,Cs,Fe)-hollandite had not strong effect on

²⁸ Electron Probe Microanalysis

ceramic porosity. Thus, introduction of Fe_2O_3 in powders mixture and of Fe^{3+} ions in site B had favourable effects on densification and Cs incorporation processes. This can be explained both by the relatively low melting point of Fe_2O_3 (1565°C) and by the high size of Fe^{3+} ions in comparison with Al^{3+} , Cr^{3+} and Ga^{3+} ions (**Table XII**). The mixed (Ba,Cs,Al+Fe)-hollandite ($\text{Ba}_{1.00}\text{Cs}_{0.28}\text{Al}_{1.46}\text{Fe}_{0.82}\text{Ti}_{5.72}\text{O}_{16}$) prepared by oxide route was also shown to retain almost all cesium ($\sim 90\%$) but its porosity was higher (**Figure 20h**) than that of the (Ba,Cs,Fe)-hollandite sample. According both to the high retention of cesium, to the lack of Cs-rich parasitic phase of low lixiviation resistance and to their low porosity, the (Ba,Cs,Fe)- and (Ba,Cs,Al+Fe)-hollandite ceramics prepared by oxide route can thus be envisaged as good candidates for radioactive cesium immobilization. The oxide route with sintering at relatively low temperature (1200°C) can be thus envisaged as an alternative method to prepare hollandite waste form suitable for Cs immobilization.

IV.A.3.d Local structure of $\text{Ba}_x\text{Cs}_y(\text{M},\text{Ti})_8\text{O}_{16}$ hollandite

The knowledge of the hollandite local structure before and after external electron irradiation (simulating β -decay of radioactive Cs) is an important element to evaluate its long term behavior as Cs waste form during storage and disposal. XRD studies performed on ceramics and single crystals gave only average local information on the interatomic distances and positions for sites A (occupied by Ba^{2+} and Cs^+) and B (occupied by M^{3+} and Ti^{4+}) in (Ba,Cs,M)-hollandite structure. According to XRD studies of the (Ba,Al)- and (Ba,Al+Fe)-hollandite single crystals prepared by flux method (see §IV.A.3.b), the modulated structure along tunnels direction (corresponding to a modulation of the barium ions occupancy and position in site A) induced a high distribution of Ba^{2+} ions arrangement near the cations ($\text{Al}^{3+}, \text{Fe}^{3+}$) located in site B [120]. Thus, different kinds of local environments of cations in site B are expected due to variations of next nearest neighbors (barium ions and vacancies). To detect different environments for a given cation M, selective spectroscopic methods sensitive only to M must be used. In our case, ^{27}Al MAS NMR and ^{57}Fe Mössbauer spectroscopies were used to study the local structure around respectively Al^{3+} and Fe^{3+} ions in the octahedral site of hollandite (**Figure 16**).

^{27}Al MAS-NMR was used to get information on the different kinds of environments of Al^{3+} ions in hollandite ceramics with or without Cs. For this study, performed in collaboration with T. Charpentier (CEA Saclay, France), $\text{Ba}_{1.16}\text{Al}_{2.32}\text{Ti}_{5.68}\text{O}_{16}$, $\text{Ba}_{1.28}\text{Al}_{1.64}\text{Ga}_{0.92}\text{Ti}_{5.44}\text{O}_{16}$ and $\text{Ba}_{1.00}\text{Cs}_{0.28}\text{Al}_{1.46}\text{Ga}_{0.82}\text{Ti}_{5.72}\text{O}_{16}$ prepared by oxide route were selected because of the lack of paramagnetic elements (such as Fe^{3+} ions) in their composition [120]. ^{27}Al ($I=5/2$, 100% natural abundance) is a quadrupolar nucleus widely studied by MAS-NMR in crystalline and glassy materials. In order to increase the resolution of MAS-NMR spectra to determine the number of nonequivalent sites occupied by Al^{3+} ions in hollandite, triple quantum MQ-MAS (Multiple Quantum MAS)-NMR spectroscopy [154] was used. The triple quantum MAS-NMR spectrum of $\text{Ba}_{1.16}\text{Al}_{2.32}\text{Ti}_{5.68}\text{O}_{16}$ ceramic is shown in **Figure 21a** (isotropic dimension). At least three components corresponding to three different Al environments (referred as X, Y and Z on **Figure 21a**) were required to correctly simulate the spectrum. Whittle et al. [152] also observed at least two different Al environments by ^{27}Al MQ-MAS-NMR for a (Ba,Cs,Al)-hollandite sample. In our case, the three components correspond to aluminum ions located in distorted octahedral sites (according to their isotropic chemical shifts and quadrupole coupling constants [155]) of hollandite structure but with three different kinds of local environment in spite the existence of only one kind of crystallographic octahedral site (site B) for tetragonal hollandite (**Figure 16**). These different environments are due to different numbers of barium and vacancies in the six next nearest positions of Al (**Figure 22**). Study of NMR spectra of hollandite samples with Ga and Cs (**Figure 21b**) enable to assign X, Y and Z Al environments as follows (**Figure 22**): one Ba and two vacancies as second neighbors (X), two Ba and one vacancy as second neighbors (Y), three Ba as second neighbors (Z). Moreover, Cs^+ ions appeared to be preferentially located near the biggest cations in site B (Ga^{3+}). This result is not surprising because tunnel section probably expands near big M cations and facilitates Cs^+ incorporation.

Hollandite samples with iron were studied by ^{57}Fe Mössbauer spectroscopy (^{57}Fe , $I=1/2$, natural abundance 2.119 %) in collaboration with F. Studer and N. Nguyen (CRISMAT, Caen, France). This technique [156] enables to extract information on the oxidation state and on the local structure around Fe in materials, after isotopic enrichment or acquisition for long times (several days for our samples).

An example of transmission spectrum for a Fe-rich hollandite ($\text{Ba}_{1.16}\text{Fe}_{2.32}\text{Ti}_{5.68}\text{O}_{16}$) showing a quadrupolar doublet with its simulation using two components corresponding to different iron environments (sites 1 and 2) is shown in **Figure 23a**. The corresponding hyperfine parameters are indicated in **Table XIV**. For the different hollandite samples studied (with or without Cs and Al), all isomer shifts were typical of Fe^{3+} ions (no Fe^{2+} ions were detected) and sites 1 and 2 were attributed to different arrangements of barium ions in tunnels in the close environment of iron [139]. According to the evolution of Mössbauer hyperfine parameters with hollandite composition [120], Fe^{3+} ions in site 2 would have three Ba^{2+} ions as nearest neighbors whereas Fe^{3+} in site 1 would have one or two Ba^{2+} ions in its neighborhood.

IV.A.3.e Irradiation of $\text{Ba}_x\text{Cs}_y(\text{M},\text{Ti})_8\text{O}_{16}$ hollandite

We saw in §IV.A.1 that the immobilization of radioactive Cs isotopes (mainly ^{137}Cs and ^{135}Cs) involved the emission of β -particles and γ rays (**Figure 15**). Therefore, hollandite matrix envisaged as Cs-host form must be β - et γ -irradiation resistant (i.e. its good immobilization performances of radioactive Cs existing at the beginning of storage must not significantly decrease during storage and disposal). (Ba,Cs,M)-hollandite compositions with $\text{M} = \text{Fe}$ or $\text{Fe} + \text{Al}$ can be prepared easily (oxide route) and incorporate all cesium in hollandite structure. Moreover, these waste forms are able to accommodate the changes in chemistry resulting from Cs decay to Ba because of their high capacity to incorporate Ba^{2+} ions into their structure and because of the possibility of reduction of Ti^{4+} ions to insure charge balance. Nevertheless, β and γ resistance of hollandite was not yet proved. In the next paragraph, we will briefly review works than were published on hollandite irradiation. We will then present the main results we obtained concerning the effects of external electron irradiation on hollandite structure. The modification of local structure and the formation of paramagnetic defects (mechanism of formation, thermal stability) will be mainly presented.

IV.A.3.e.1 Stability of hollandite under irradiation

Most of the crystalline matrices that can be envisaged for MA or Pu immobilization (zirconolite, zircon, apatite...) have very old natural analogues containing actinides (U, Th) indicating the very good ability of these matrices to retain α , γ radioactive elements for very long periods. For such waste forms, actinides decay is known to induce a high number of atomic displacements that may lead to total or partial amorphization of their structure. Moreover, an important number of studies concerning the effect of external irradiations by heavy ions (simulating α -decay) on their structure and chemical durability have been performed. However, due to the lack of natural analogues containing radioactive cesium, (Ba,Cs,M)-hollandite radiation resistance was not proved as yet. Indeed, natural analogues with hollandite structure such as priderite $((K,Ba)_x(Ti,Fe)_8O_{16})$ [157] and henrymeyerite $(Ba(Fe,Ti_7)O_{16})$ [158] were not known to contain radioactive cesium. Moreover, to the best of our knowledge, the incorporation and the study of the effects of radioactive cesium in synthetic single-phase hollandite has not been already performed²⁹. Finally, literature reports only external irradiation experiments that are not relevant to simulate the effects of cesium decay on hollandite long-term behavior [70,159]. Indeed, the stability under irradiation of hollandite ceramics was initially studied within the framework of the multiphase Synroc ceramics. These works mainly concerned the effects on hollandite of α -radiation due to actinides decay in zirconolite and perovskite adjacent phases [160]. For instance, fast neutron irradiation experiments were performed on single-phase Ba-hollandite [161] in order to simulate the irradiation effects occurring in Synroc and generated structural changes. The effect of ion-beam (Ar^+ ions) irradiation was also studied [162]. The few works dealing with the stability of single-phase (Ba,Cs,M)-hollandite under external electron irradiation, used to simulate the β -irradiation of cesium, were performed with intense electron irradiation in transmission electron microscopes. In this case, strong structural evolutions were observed such as the hollandite \rightarrow rutile transformation [134] by loss of tunnel cations, and microtwinning followed by amorphization [159].

²⁹ For pollucite ($CsAlSi_2O_6$, see §IV.A.2a), different experiments were reported in literature by incorporating radioactive cesium in its structure. Only small structural and chemical durability variations were observed after several years of storage [130,135].

However it must be underlined that the electron dose rate caused by β self-irradiation in the radioactive Cs waste forms will be low in comparison with the electron dose rate received in electron microscopes. Thus, the latter overestimates the real effects of Cs decay. To the best of our knowledge, no results concerning the nature and the concentration of point defects formed either by β or γ external-irradiation of hollandite have been reported in literature. Such studies were neglected in the case of HLW immobilization compare to α -irradiation which produces a high number of atomic displacements and the effect of β -irradiation due to radioactive Cs was often considered as negligible in hollandite but this was not studied carefully.

In the next paragraph, our main results concerning the effects of external electron and γ -irradiations simulating Cs β -decay on single phase hollandite samples (ceramic and single crystal) will be presented.

IV.A.3.e2 External irradiation of (Ba,Al)-hollandite

Our study mainly focused on a simple (Ba,Al)-hollandite composition ($\text{Ba}_{1.16}\text{Al}_{2.32}\text{Ti}_{5.68}\text{O}_{16}$) for external electron irradiation experiments in order to easily allow the observation of irradiation-induced paramagnetic defects by EPR without be disturbed by high amounts of preexisting paramagnetic species. Nevertheless, few results concerning hollandite compositions with high amounts of paramagnetic ions ($\text{M}^{3+} = \text{Fe}^{3+}, \text{Cr}^{3+}$) will be briefly given at the end of this paragraph. As Cs entered with difficulties into (Ba,Al)-hollandite it was decided to mainly study composition without cesium, only few remarks concerning the effect of Cs^+ ions on the paramagnetic defects induced by irradiation will be given in §IV.A.6.c.

IV.A.3.e.2.a. External irradiation conditions and characterization of irradiated hollandite

External electron irradiations (1.0, 1.5 and 2.5 MeV)³⁰ with a Van de Graaff accelerator were used to simulate the β -particles and Compton electrons generated by γ rays emitted by radioactive cesium. Indeed, considerations about γ -particles interaction with hollandite showed that it was dominated by Compton effect [163] and that the 0.662 MeV γ rays emitted by ^{137}Cs (**Figure 15**) produced Compton electrons with energies $E \leq 0.477$ MeV [120]. Consequently, these Compton electrons have energies of the same order as that of β -particles (0.2-0.5 MeV, **Figure 15**.) emitted by radioactive cesium and will generate the same defects as β -particles in hollandite. Nevertheless, several external γ -irradiation tests were performed with the help of a ^{137}Cs source (0.662 MeV, **Figure 15**). (Ba,Al)-hollandite ceramic and single crystals³¹ samples 0.5-1 mm thick samples were irradiated at almost room temperature ($T < 50^\circ\text{C}$). The sample thickness was chosen so that electrons go through the sample. The samples were subjected to different electron fluences (quantity of incident electrons per cm^2) between $3.4 \times 10^{17} \text{ cm}^{-2}$ to $1.2 \times 10^{19} \text{ cm}^{-2}$ with 1.0 to 2.5 MeV electron energies, giving absorbed doses in the 1.4×10^8 - 7.5×10^9 Gy range. The maximal fluence (7.5×10^9 Gy) corresponds approximately to 30 years of storage when 5 wt% Cs_2O (recovered from the reprocessing of spent fuel) are incorporated in hollandite (**Figure 24**). At the beginning of Cs waste form disposal, the energy of β -particles will be mainly around 0.5 MeV (^{137}Cs) during several tens years (**Figure 15**). The energy of β -particles will be then of 0.2 MeV (^{135}Cs). It must be underlined that during external electron irradiation experiments, the dose rate ranged between 26.10^6 and $75.10^6 \text{ Gy.h}^{-1}$ whereas during disposal of Cs waste form, it will be at the beginning of 10^5 Gy.h^{-1} and then 3.10^3 Gy.h^{-1} after one century. These dose rate differences may induce defects accumulation in our samples that will not occur during disposal but this phenomenon is difficult to evaluate.

It is important to note that two other important differences exist between our irradiation experimental conditions and the actual conditions in hollandite waste forms containing radioactive cesium. First, electrons fly through the sample to avoid charge accumulation in hollandite for external irradiation conditions, and

³⁰ Electrons with energy lower than 1 MeV were not available with the Van de Graaff accelerator used for this study. Thus, the energy of electrons used in our work was higher than the one of the majority of β particles emitted by ^{137}Cs and ^{135}Cs (**Figure 15**).

thus electrons are not finally trapped by the hollandite host. Consequently, these experiments reproduce only the effect of β -particles and of Compton electrons (produced by γ -rays) emitted by Cs along their path in the hollandite structure, and do not simulate the effect of electron capture nor Cs transmutation to Ba. Secondly, all our experiments were performed at room temperature. However, because of the high thermal power of ^{137}Cs and ^{134}Cs isotopes (**Table X**), the temperature in the bulk of hollandite ceramics could reach 300 °C during the first years of storage for a 5 wt% loading of Cs_2O .

The influence of irradiation conditions on the nature and on the concentration of point defects (electron and hole centers) in hollandite was estimated by EPR (X band (9.5 GHz), temperature range 9-300 K). For more details concerning EPR techniques and theory see for instance [164]. Moreover, XRD, electron diffraction, ^{27}Al MAS NMR and ^{57}Fe Mössbauer (for hollandite samples containing iron which cannot be studied by EPR) experiments were performed before and after irradiation in order to monitor structural evolution.

IV.A.3.e.2.b. Effects expected on hollandite of electron external irradiations

β -particles with energy in the MeV range can impart energy to hollandite matrix through elastic and inelastic interactions. Along their path through hollandite samples, electrons will generate ionisations and electronic excitations but few atomic displacements. Indeed, due to the small mass of the electron, the energy transferred by ballistic collisions is quite small but could be even sufficient to cause subsequent atomic displacements, notably of light elements. Nevertheless, it is possible to induce displacements of the heavy ions in a two-steps process involving collisions with these displaced light elements. Damage depends on the mass and the threshold displacement energy E_d of each ion, currently unknown for hollandite. For instance, **Figure 25** shows that the value of energy of electron (1.0-2.5 MeV in this study) has a strong effect on the probability of Ba displacement in hollandite (whatever may be $E_d(\text{Ba})$ the threshold displacement energy of Ba) whereas the probability of oxygen displacement is not so much affected by the variation of electron energy. It is interesting to notice from **Figure**

³¹ (Ba,Al)-hollandite single crystals prepared by flux method (composition $\text{Ba}_{1.23}\text{Al}_{2.04}\text{Ti}_{5.85}\text{O}_{16}$ as determined by EPMA) were irradiated in order to help the identification of the paramagnetic

25 that for electron with energy $E=0.5$ MeV (which corresponds to β -particles emitted by ^{137}Cs), Ba will be not displaced whereas oxygen can be displaced (look the vertical lines in **Figure 25**). On the other hand, as electron irradiations imply mainly electronic excitations, the creation of electron and hole centers, resulting from the trapping of the produced electron-hole pairs, is expected (**Figure 26**). These created defects have respectively the same nature as the bottom of the conduction band (CB) formed by titanium orbitals (3d) or as the top of the valence band (VB), comprised of oxygen orbitals (2p) with antibonding O-O character [120]. The character of these bands (CB and VB) was determined from the hollandite electronic band structure calculated by the Hückel tight-binding method (**Figure 27**) [120]. Therefore, it is expected that electron centers would be Ti^{3+} ions (after electron trapping by Ti^{4+} ions) and hole centers would be of O^- or O_2^{n-} ($n < 4$) type (after hole(s) trapping by oxygen ions).

IV.A.3.e.2.c. Effect of external electron irradiation on hollandite

Comparison of XRD patterns of $\text{Ba}_{1.16}\text{Al}_{2.32}\text{Ti}_{5.68}\text{O}_{16}$ hollandite before and after electron irradiation is shown in **Figure 28**. It appeared that XRD line width only slightly increased after irradiation which indicates only a small increase of disorder in hollandite structure. Moreover, no significant evolution of Raman spectra (not shown) was observed after irradiation which shows that bonding was not affected by irradiation. Nevertheless, an increase of disorder in tunnels was put in evidence by electron diffraction and high resolution transmission electron microscopy (decrease of barium ions-vacancies ordering) showing that Ba^{2+} ions were displaced under electron irradiation [120]. Comparison of MAS NMR spectra of $\text{Ba}_{1.16}\text{Al}_{2.32}\text{Ti}_{5.68}\text{O}_{16}$ hollandite before and after electron irradiation (spectra not shown) indicated that no significant evolution was observed concerning the relative proportions of sites X, Y and Z (**Figure 21a**) [155]. This indicated that the arrangement of Ba^{2+} ions around Al^{3+} ions was not significantly modified after irradiation in spite of Ba^{2+} ions displacement in tunnels. However, **Figure 29** shows the appearance of a weak signal around + 45 ppm after irradiation corresponding to the chemical shift of Al in 5-fold coordination. Consequently, oxygen vacancies have been produced by electron irradiation because of all Al was 6-fold coordinated before irradiation. ^{17}O MAS NMR

defects induced after electron irradiation of ceramics.

($I=5/2$, natural abundance 0.037 %) of a $\text{Ba}_{1.16}\text{Al}_{2.32}\text{Ti}_{5.68}\text{O}_{16}$ sample³² confirmed that the oxygen lattice of hollandite was affected by electron irradiation [120]. For the iron-rich hollandite $\text{Ba}_{1.16}\text{Fe}_{2.32}\text{Ti}_{5.68}\text{O}_{16}$, the evolution of Mössbauer spectra after electron irradiation is shown in **Figure 23b** and **Table XIV**. After irradiation a new Fe site (site 3) was observed and the relative proportions of sites 1 and 2 changed. However, partial reduction of Fe^{3+} in Fe^{2+} under electron irradiation did not occur within the Mössbauer sensitivity scale. Site 3 was identified as Fe in 5-fold coordination because of its hyperfine parameters [120,139]. This indicated oxygen displacement around Fe (initially all Fe^{3+} ions were in octahedral sites). The evolution of relative proportions of sites 1 and 2 was attributed to atomic displacement of Ba^{2+} ions in tunnels [120].

Figure 30 shows the EPR spectra of pristine and electron irradiated $\text{Ba}_{1.16}\text{Al}_{2.32}\text{Ti}_{5.68}\text{O}_{16}$ hollandite samples for different fluences (electron energy of 1 MeV)³³. Three signals (T_r , E_1 , E_2) corresponding to three kinds of paramagnetic point defects are induced by irradiation. Other defects (diamagnetic) may also be induced by irradiation but cannot be detected by EPR. Such diamagnetic centers are probably formed because the sum of electron centers concentrations was higher than the hole centers concentrations. The same paramagnetic defects (T_r , E_1 , E_2) were generated in hollandite after γ -irradiation but with significantly smaller concentrations. According to their magnetic field position on EPR spectra (**Figure 30**) and corresponding g factor, E_1 and E_2 signals were attributed to electron centers ($g < g_e$) and T_r signal to hole centers ($g > g_e$)³⁴. Intensities of all these signals increase with increasing fluence without saturation at least up to 1.4

³² This sample was prepared by oxide route with ^{17}O enriched TiO_2 as raw material and sintered under nitrogen to avoid ^{16}O - ^{17}O exchange with air oxygen.

³³ EPR concerns transitions between spin sublevels of paramagnetic centers, arising from the superposition of an external high magnetic field B . The resonance which gives rise to EPR signals occurs when $h\nu = g\beta B$, where h is the Planck's constant, ν the microwave frequency, g the g-factor (for a free electron, $g = g_e = 2.0023$), β the electron Bohr Magneton. The signal position for a given magnetic field B defines the g factor (without unit) characteristic of the paramagnetic center. However, because of the local structural anisotropy of paramagnetic centers in crystalline structure, the EPR signal position also depends on the orientation of the crystals of the ceramic with respect to B direction. For a low symmetry center, instead of an isotropic g-factor, the spectrum will be described by a (g_x, g_y, g_z) tensor (x , y and z corresponding to its eigen directions that are not necessary correlated with crystallographic axis). The spectrum of ceramic samples results from the sum of the signals of all the crystallites oriented in every direction. Due to the short spin-lattice relaxation time of several of the paramagnetic centers induced in hollandite, EPR spectra were recorded at low temperature to enable their detection. For instance, E_1 signal was detectable up to room temperature whereas E_2 signal vanished above 170 K.

10^{19} cm^{-2} but their relative intensities depend on fluence (relative intensity of signal E_2 grows notably with fluence) and electron energy [120]. An increase of the intensity of E_2 signal with electron energy was observed in comparison with that of E_1 and T_r centers. This indicated that the formation of E_2 center was related to Ba displacements upon electron irradiation according to the evolution of the calculated probability of atomic displacement with electron energy (**Figure 25**). In order to assign all these signals, experimental spectra were simulated to extract their corresponding (g_x, g_y, g_z) tensors and their lineshape and intensity evolution was monitored upon variations of experimental parameters (temperature, incident microwave power...). Centers concentrations were also quantified. The simulation of E_1 and E_2 signals is shown in **Figure 31** and simulation parameters of E_1, E_2 and T_r centers are given in **Table XV**. T_r signal can be simulated by the superposition of at least three individual spectra representing three hole centers of the same type. According to the calculated hollandite electronic band structure (**Figure 27**), it is expected that electron centers are Ti^{3+} ions (after electron trapping by Ti^{4+} ions) and hole centers are of O^- or O_2^{n-} ($n < 4$) type (after hole(s) trapping by oxygen ions). The details of identification of the different paramagnetic centers are given in [155,120] and will be only briefly summarized below.

According to the value of their g tensors, hole centers (T_r signal) cannot be assigned to O^- type centers but rather to superoxide O_2^- centers in at least three different type of environments. These different environments were tentatively attributed to O_2^- centers close to cations of different charges (Ba^{2+} , Al^{3+} or Ti^{4+}) in hollandite. Electron centers E_1 and E_2 were attributed to Ti^{3+} formed in the bulk of hollandite but with different local environments. E_2 center has an axial symmetry with the axial component of crystal field parallel to the crystallographic c axis of hollandite as shown by EPR study of an irradiated single crystal. On the contrary, E_1 center is located in a more distorted environment and probably originates from oxygen displacement during irradiation (the occurrence of oxygen displacement in hollandite was shown by ^{27}Al MAS NMR and ^{57}Fe Mössbauer spectroscopy, see §IV.A.3.e.2.c). E_1 center was attributed to an electron trapped by a Ti^{4+} ion adjacent to an oxygen vacancy (Ti^{3+} in five-fold coordination). E_2 center probably

³⁴ Electron centers are formed by electron trapping (for instance, $\text{Ti}^{4+} (3d^0) \rightarrow \text{Ti}^{3+} (3d^1)$). Hole centers result from hole trapping (for instance, $\text{O}^{2-} (2p^6) \rightarrow \text{O}^- (2p^5)$). Depending on the number of

originates from Ba displacements by elastic collisions with electrons (the occurrence of such displacements was shown by electron diffraction). According to identification results, the position of the energy levels of E_1 , E_2 and T_r centres with respect to CB and VB extrema are schematically represented in **Figure 32**.

A mechanism of formation of E_1 , E_2 and T_r centers was proposed in [155] based on electron-hole creation and displacement of Ba and O ions. The proposed global mechanism implies that the defects induced by barium and oxygen displacements followed by electron and hole trapping are of two types; (i) oxygen centers which can be paramagnetic (O_2^- , T_r center) or diamagnetic (O_2^{2-} or T_r^- center), and (ii) Ti^{3+} centers which can be paramagnetic (E_2 and E_1 centers) or diamagnetic (E_1^- center). A maximum defect concentration of the order of 10^{18} cm^{-3} was obtained with our irradiation conditions (simulating the first 30 years of hollandite waste form storage and corresponding to about 40% of the dose that will receive hollandite during disposal, **Figure 24**) which is relatively low. However, the total concentration of defects can be higher if diamagnetic defects are also produced.

In order to study the impact on the nature of paramagnetic defects created by electron irradiation of the nature of M^{3+} cations in site B and of the nature and occupancy level of cations (Ba^{2+} , Cs^+) in site A, an EPR study of electron irradiated $Ba_{1,16}Ga_{2,32}Ti_{5,68}O_{16}$, $Ba_{1,21}Al_{2,42}Ti_{5,68}O_{16}$ and $Ba_1Cs_{0,28}Al_{1,46}Ga_{0,82}Ti_{5,72}O_{16}$ hollandite samples was performed. For all these samples, paramagnetic defects of same nature as that induced in $Ba_{1,16}Al_{2,32}Ti_{5,68}O_{16}$ hollandite were formed: O_2^- type hole centers were detected in the three samples whereas E_2 and E_1 centers were clearly detected only for $Ba_{1,21}Al_{2,42}Ti_{5,68}O_{16}$ and $Ba_1Cs_{0,28}Al_{1,46}Ga_{0,82}Ti_{5,72}O_{16}$ samples. E_1 signal was not detected for $Ba_{1,16}Ga_{2,32}Ti_{5,68}O_{16}$ sample. These results showed that Cs incorporation and occupancy level of tunnels of hollandite have no effect on the nature of the paramagnetic defects induced by electron irradiation.

Chemical durability tests were conducted at 100°C with continuously flowing water in a Soxhlet device before and after irradiation (electron energy 1.5 MeV, fluence $1.2 \cdot 10^{19} \text{ cm}^{-2}$) on a $BaCs_{0,28}Fe_{0,82}Al_{1,46}Ti_{5,72}O_{16}$ ceramic sample prepared by alkoxide route. Leaching rates indicated that electron irradiation did not significantly affect the capacity of the ceramic to retain cesium [120].

electrons or holes trapped, these centers can be paramagnetic or not.

IV.A.3.e.2.d. Thermal evolution of irradiation-induced paramagnetic defects in hollandite

At room temperature the electron and hole centers discussed in previous paragraph were stable at least during more than 2 years (no concentrations change). As at the beginning of storage, the temperature in the bulk of radioactive Cs waste form will reach 300°C (5 wt% Cs₂O), the stability with temperature of electron (E₁, E₂) and hole (T_r) centers was studied. **Figure 33** shows the evolution of the EPR spectra of an irradiated Ba_{1,16}Al_{2,32}Ti_{5,68}O₁₆ hollandite sample at each step after 15 min annealing at temperature in the range 50-800°C. E₂, E₁ and T_r signals vanished at 150, 300 and 350°C respectively (**Figure 34**). Thus, hole centers are more stable than electron centers and these defects do not recombine together. Annealing lead also to the formation of new signals G₂ and E₃, shown in **Figure 33**, in the temperature range 450-750°C and 350-700°C respectively. These defects were not observed after annealing of a pristine hollandite sample, which shows that they result from irradiation. Signal E₃ is an electron center (g < g_e) that was assigned to titanyl Ti³⁺ ions located at the surface of the crystals of hollandite ceramic [120]. A mechanism was proposed to explain formation of these centers by migration of E₁ center towards surface of the crystals of hollandite ceramic [120]. E₂ center probably vanished by liberation of the trapped electron in the conduction band of hollandite. It was suggested that the defects responsible for the G₂ signal were light paramagnetic element (probably oxygen) segregated as aggregates [120]. These aggregates were probably clusters of O₂⁻ centers formed by migration in the bulk of the crystals (**Figure 35b**). A diffusion mechanism was proposed for the migration of O₂⁻ centers (**Figure 35a**) [120]. Nevertheless, contrary to what was observed by Raman spectroscopy for electron irradiated silicate glasses [165], the presence of a peak at 1550 cm⁻¹ characteristic of molecular O₂ was not detected on Raman spectra of the irradiated and heat treated hollandite samples studied in this work.

The scheme presented **Figure 35b** summarized paramagnetic centers formation after electron irradiation and their evolution after annealing. It was necessary to heat the sample to 800°C to get a spectrum similar to the pristine one (**Figure 33**). Therefore at 300°C all the defects discussed previously would not be annealed and the formation of secondary defects (E₃ and G₂) clearly indicated that a part of the electrons and holes generated during irradiation were separated after

annealing. However, because of their small concentrations, these defects will have probably no negative effect on the long term behavior of hollandite during disposal. However, as discussed above, all these external irradiation experiments were performed with electron energy higher than 0.5 MeV which probably conducts to an overestimation of elastic collisions (Ba displacements). Moreover, to compare our results (with irradiation at room temperature + annealing) with real conditions at the beginning of disposal, it would be interesting to perform directly electron irradiation of hollandite at 300°C.

IV.B. The specific immobilization of MA

As indicated in the Introduction of this chapter, after spent fuel reprocessing, the contribution of MA ((α,γ)-emitters) will dominate the radiotoxic inventory of HLW after 2-3 centuries because of their long half-lives in comparison with the majority of FP (**Figure 1**). After a brief overview on the MA occurring in HLW and on several kinds of matrices (glasses, ceramics and glass-ceramics) that could be envisaged for their specific immobilization (or for Pu immobilization) after selective separation, results will be develop concerning more particularly single phase zirconolite ceramics and zirconolite-based glass-ceramics that have been studied in our laboratories.

IV.B.1. MA in HLW

MA (^{237}Np , $^{241,243}\text{Am}$, $^{243,244,245}\text{Cm}$) are mainly produced in nuclear reactors during fuel burn-up by neutron capture by ^{235}U and ^{238}U nuclei. Both the concentrations of MA and the MA/FP concentrations ratio in HLW depend on spent fuel burn-up [1,11] (**Table VI**). However, MA-rich wastes can also have different origins. For instance, the decision to stop military Pu production (for use in nuclear weapons) lead to a necessary periodic recycling of the existing military Pu stocks in order to extract $^{241}\text{Am}^{35}$ formed from ^{241}Pu by α -decay [166]. This leads to Am-rich wastes that must also be immobilized.

In commercial nuclear reactors, MA represent only a small weight fraction in nuclear spent fuel (approximately 0.1 wt% for UOX1 spent fuel, **Figure 3**) and of

³⁵ ^{241}Am is a neutron poison that must be periodically extracted from military Pu after melting and treatment with alkaline chlorides.

HLW as compared to fission products (only 2-3 wt% of all FP after Pu and U extraction for UOX1 spent fuel, **Table IV**). Nevertheless, about 1100 kg of MA are produced in France every year in HLW solutions after spent fuel reprocessing [32]. The main properties of MA and their individual fluxes are given in **Table XVI**. In power reactors using natural uranium (0.7 % ^{235}U) and in military reactors³⁶ used to produce Pu for nuclear weapons fabrication, the MA weight fraction in spent fuels is still lower [7]. Nevertheless, because of the expected increase of nuclear fuel burn-up in commercial reactors (**Table VI**), the weight fraction of MA in spent fuel and in HLW after reprocessing will increase in the future (**Table V**). In comparison with Np and Am, the amount of Cm is small in spent fuel (3.8 wt% of all MA in UOX1, **Figure 3**). Moreover, because of the highest half-life of ^{237}Np ($2.14 \cdot 10^6$ years) in comparison with Am isotopes (432-7370 years), the radiotoxicity of MA will be dominated by Am during about nearly 100 000 years [167]. After this long period, the radiotoxicity of neptunium will dominate and will be lower than that of initial nuclear fuel.

Because the high structural flexibility of glasses, all MA are currently incorporated by dissolution in glassy matrices with all FP and (U,Pu) traces not extracted by the Purex process, additional elements and corrosion products occurring in HLW solutions (**Table IV**). As MA are mainly responsible for the long-term radiotoxic inventory (**Figure 1**), we saw above that studies on advanced partitioning and specific immobilization (or transmutation to short-lived or non-radioactive elements) of MA in more durable matrices than current nuclear glasses are in progress in France. In nuclear borosilicate glasses, MA represent currently less than 0.4 wt% (**Table VII**) whereas concentrations of about 10 wt% are aimed to be immobilized in new specific matrices. The relatively high proportion of Am (46.6 wt% of all MA in UOX1 spent fuel, **Figure 3**), which has a significant thermal power (**Table XVI**), partly explains the limit of MA concentration in waste forms in order to avoid strong heating in their bulk³⁷. This problem is still more crucial for Cs waste forms because of the high proportion of the short-lived ^{137}Cs isotope (**Table XI**). Concerning, the selective separation of

³⁶ In order to produce Pu with an isotopic quality adapted to weapons fabrication, the burn-up of military spent fuel must be low.

³⁷ After 2-3 centuries, the thermal power of radioactive nuclear glasses will also be controlled by Am isotopes.

MA from HLW solutions (for transmutation or selective immobilization) it has been demonstrated that it was successively possible [24,168,169]:

- To separate Np in combination with U and Pu using a modified version of the Purex process.
- To co-extract (Am + Cm + lanthanides) from all other FP of HLW (Diamex process).
- To separate (Am + Cm) from the high amount of lanthanides (all lanthanides represent more than 30 wt% of the wastes produced in power reactors, **Tables III and IV**) (Sanex process).
- To finally separate Am from Cm.

Because of the close chemical properties (stable oxidation state and cations size) of (Am, Cm) and the main lanthanides occurring in HLW solutions (La, Ce, Pr, Nd, see **Table IV**), the separation of MA and lanthanides is not easy³⁸. Nevertheless, for transmutation of MA it is necessary to separate MA from lanthanides. However, for MA immobilization in specific waste forms the simultaneous occurrence of lanthanides and MA is not a serious problem. Indeed, as it will be discussed below, in numerous matrices it can be envisaged to incorporate simultaneously lanthanides and MA. This is also the case for the waste forms developed for military Pu immobilization for which addition of Gd was envisaged as neutron poison to avoid criticality risks during disposal.

Concerning the studies on MA or Pu waste forms in laboratories that are not able to work with radioactive materials containing (α , γ)-emitters, it is important to point out that trivalent lanthanide ions (4f elements) are generally considered as good surrogates for the heaviest transuranic elements (5f elements) occurring in HLW such as Am and Cm. For instance, as the majority of lanthanides, these two actinide elements occur as trivalent ions in glasses [170,171] and have cation radii r similar to that of Nd^{3+} ion (for instance in six-fold coordination: $r(\text{Am}^{3+})=0.0975$ nm and $r(\text{Nd}^{3+})=0.0983$ nm [144]). In comparison, other actinide elements of HLW (U, Np, Pu, **Table IV**) generally occur under oxidation state higher than +III in glasses and are not well simulated by trivalent lanthanides. For instance, plutonium mainly occurs as Pu^{4+} ions in nuclear glasses prepared under neutral or oxidizing conditions [172]. Thus, trivalent lanthanides are not good Pu surrogates

except if the Pu containing glasses are prepared under strongly reducing conditions (using for instance strong reducing agent such as Si_3N_4 in the melt, almost all Pu^{4+} ions can be reduced to Pu^{3+} ions [173]). The differences of behavior between the heaviest and the lightest actinides of HLW are due to the increase of nuclear charge for the heaviest actinide elements which affects the energy and the spatial extension of 5f orbitals. Because of the possibility to prepare materials with both Ce^{3+} and Ce^{4+} ions, cerium is sometimes considered as a good plutonium surrogate. Nevertheless, it must be underlined that cerium is easier to reduce into its trivalent state than plutonium when the temperature is raised during the synthesis of waste forms. Moreover, in glasses prepared under air, plutonium is essentially in tetravalent state whereas both Ce^{3+} and Ce^{4+} ions exist in these conditions [174,175,176]. Moreover, as neptunium exists mainly in +IV oxidation state in glasses melted under air [177,178] and in zirconolite ceramics for instance [179], it is sometimes simulated by Ce^{4+} or Th^{4+} ions [180]. Because of its very long half-life ($>1.4 \cdot 10^{10}$ years), natural ^{232}Th is an actinide that can be manipulated in all laboratories but with some precautions. Moreover, thorium – which exists only in +IV oxidation state – is often considered as a good Pu^{4+} surrogate in spite of strong differences of solubility between Pu^{4+} and Th^{4+} in several ceramic matrices such as ZrO_2 [74].

IV.B.2. Specific waste forms for MA and Pu conditioning

In France, after numerous studies performed conjointly by CEA and CNRS, different kinds of highly durable single phase or multiphase ceramic matrices have been retained as potential candidates for MA conditioning [32:82] (zirconolite [18,19], britholite [23], monazite/brabantite [23], thorium phosphate-diphosphate [23]) (**Table IX**). These ceramics are more durable than current nuclear borosilicate glasses used for the conditioning of non separated HLW solutions. The case of zirconolite ceramic is developed below (§IV.B.3). Zirconolite-based glass ceramics have also been proposed for MA immobilization [101,103]. The potential advantages of glass-ceramics as specific waste forms in comparison with ceramics were already given in §III. The effect of parent glass composition and crystallization thermal treatment conditions on the structure and

³⁸ Indeed, as discussed below, trivalent lanthanide ions such as Nd^{3+} (neodymium is the most abundant lanthanide in FP, **Table IV**) are classically used as americium and curium surrogates for inactive waste forms preparation.

the composition of zirconolite crystals have been widely studied in our laboratories and the main results obtained are presented in §IV.B.4.

Other countries have also studied the possibility to immobilize selectively MA (Japan, Australia, Russia) or weapons Pu excess (United States, Russia, Australia) in highly durable matrices. For instance, in United States, an important amount of work has been performed on titanate and zirconate ceramics for Pu immobilization. In this case, the pyrochlore-type phase ($\text{Ln}_2(\text{Ti,Zr})_2\text{O}_7$ with Ln: lanthanide that can be replaced by actinides) was identified as one of the best waste form candidate [181,182]. However, the American Pu disposition programme was abandoned in 2002 [78]. Nevertheless, several studies seem to indicate that zirconolite is more long term resistant than pyrochlore [183,184]. Moreover, zircon ($(\text{Zr,Pu})\text{SiO}_4$) [185] and zirconia ($(\text{Zr,Gd,Pu})\text{O}_2$) [186] ceramics are other examples of matrices that have been envisaged in Russia for the immobilization of Pu excess. It must be underlined that, zircon [72] and zirconia [74] were also proposed in the United States for Pu immobilization. The comparison of these different crystalline waste forms (titanates, zirconates and phosphates) will be not developed in this chapter.

We saw in part III that, because of their very high structural flexibility (due to the lack of long range order), glassy waste forms remained the best candidates for non separated HLW immobilization. Nevertheless, recent studies were performed on glassy waste forms for actinides-rich wastes conditioning. For instance, studies were undertaken to get information on the solubility limits of actinides or of their surrogates (lanthanides) in a simplified version of the French nuclear glass R7T7 prepared in different conditions. It appeared that it was possible to raise actinides and lanthanides concentrations in the glass by increasing the melting temperature and/or by using strong reducing agent during melting to reduce tetravalent actinides or lanthanides³⁹ [174,173]. Other studies concerning the solubility of military Pu-rich wastes and Pu surrogates in sodium borosilicate glasses were also performed in United States [187,188]. Even if high concentrations of Pu or MA surrogates can be incorporated in these glasses at laboratory scale, the risks of uncontrolled crystallization of Pu- or MA-rich phases could be important during natural cooling of the melt in the metallic containers after casting. This could modify the long term behavior of the waste form in comparison with

³⁹ Indeed, trivalent actinides and lanthanides are more soluble in glasses than tetravalent ones.

homogeneous glasses. However, if this crystallization can be controlled in the bulk, interesting glass-ceramic waste forms may be prepared. Glass compositions containing lower fluxing agent (i. e. alkaline oxides, boron oxide) concentrations ($T_{\text{melting}} > 1450^{\circ}\text{C}$) and more durable than sodium borosilicate glasses ($T_{\text{melting}} \sim 1100\text{-}1150^{\circ}\text{C}$) were also proposed for actinide-rich wastes immobilization: lanthanide aluminoborosilicate glasses (LaBS) [189,190] and lanthanide aluminosilicate (LnSiAlO) [191] glasses.

The fact that glasses are generally considered as less durable than the titanate, zirconate and phosphate ceramics seen above and the existence of very old natural analogues for the majority of these ceramics explains why a considerable amount of experimental works (synthesis, characterization, study of properties) have been performed on ceramics for the specific immobilization of actinides (MA, Pu) in comparison with glasses.

IV.B.3. Zirconolite ceramic as specific waste form for MA or Pu

IV.B.3.a General characteristics of zirconolite

Zirconolite ($\text{CaZrTi}_2\text{O}_7$) is the most durable phase designed for the incorporation of actinides and lanthanides in Synroc phase assemblages (**Table VIII**). For instance, zirconolite is more durable than perovskite (CaTiO_3) [192], the other phase of Synroc able to incorporate actinides and lanthanides and that can form as parasitic phase during zirconolite preparation.

In the next paragraph, different incorporation schemes of trivalent or tetravalent An or Ln (considered here as An surrogates or neutron poisons) in the Ca and Zr sites of the zirconolite structure will be described. In order to avoid criticality risks during disposal (particularly for Pu immobilization), it is interesting to notice that high amounts of neutron absorbers (Gd, Hf) can also be introduced in zirconolite structure at the same time as actinides. Indeed, Gd and Hf are very good neutron absorbers with thermal neutron capture cross-sections of 49000 and 104 barns respectively.

The existence in nature of very old zirconolite minerals (of sometimes more than several hundred million years) that have successfully retained U and Th (up to 25 wt% UO_2 and 18 wt% ThO_2) [193] even though they have been rendered

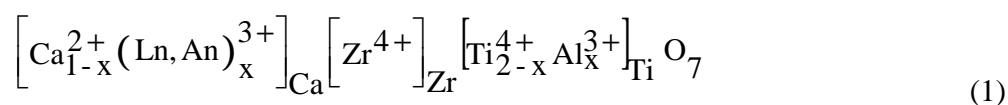
metamict (i.e. amorphous under α -self irradiation) [192,194,195] by alpha decay, is generally considered as a good indication of their excellent long-term behavior (i. e. the effects of radiation-induced damage on their chemical durability were minimal) and explains why such phases are envisaged to securely immobilize Pu and MA for several thousands of years. For example, Lumpkin et al. [195] indicated that 550 million years old metamict zirconolite samples⁴⁰ from Sri Lanka showed only minor signs of geochemical alteration. These samples were known to survive even after the complete destruction of their host rocks during weathering. Moreover, recent laboratory experimental results showed that amorphization produced by external irradiation (by Au²⁺ ions, simulating α -recoils of actinides) did not significantly affect the dissolution rate of zirconolite [183]. This very good resistance of zirconolite was confirmed both by leaching tests performed on ²³⁹Pu-doped zirconolite (self-irradiation tests) [196] and by leaching tests performed on inactive zirconolite pellets irradiated externally above the critical amorphization dose by 510 keV Pb³⁺ ions [18] (simulating also α -recoils of actinides). The study of self-radiation effects on the structure of zirconolite can be investigated by examination of natural samples containing ThO₂ and UO₂ that have experienced high α -doses using XRD, HRTEM and X-rays absorption spectroscopies (EXAFS, XANES) [195,197,198]. Molecular dynamics simulation has also been used to study irradiation damage in zirconolite [199]. Various leaching tests performed at different temperatures on non irradiated zirconolite ceramics showed that the initial alteration rate was at least two orders of magnitude lower than that measured for the most resistant borosilicate and aluminosilicate glasses [19,200]. After a few hours to a few days, this alteration rate quickly decreased by several orders of magnitude (\approx absence of alteration) [19,200]. This excellent chemical durability properties was explained by Leturcq et al. considering the existence of a decalcified zirconolite phase on the surface of altered zirconolite samples which could act as a passivation layer with protective properties [201]. All these results published in literature confirmed the very good long term performances of zirconolite as MA or Pu waste form.

IV.B.3.b Structure and incorporation capacity of zirconolite

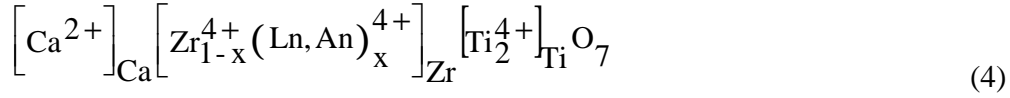
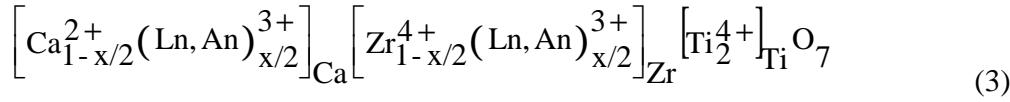
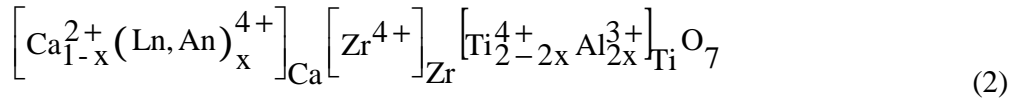
⁴⁰ These samples contained about 18 wt% ThO₂ and 2 wt% UO₂ (EPMA study) [195]

Pure zirconolite (nominally $\text{CaZr}_x\text{Ti}_{3-x}\text{O}_7$ with $0.83 \leq x \leq 1.36$ [202,203] or more simply written as $\text{CaZrTi}_2\text{O}_7$ ($x=1$)⁴¹ has a monoclinic layered structure ($C_{2/c}$ space group) referred as to zirconolite-2M polytype consisting of alternate planes containing either Ti^{4+} ions or both Ca^{2+} and Zr^{4+} ions [70,204,205] (**Figure 36**). Nevertheless, the structure of zirconolite can change according to its composition and the kind of foreign elements that are incorporated. These structural transformations lead very often to the formation of polytypes that can be roughly described from zirconolite-2M by a modification of the stacking sequence: the main ones are zirconolite-3T, zirconolite-3O and zirconolite-4M [205]. In zirconolite-2M, calcium and zirconium ions are ordered within the planes in eight and seven-fold coordinated sites respectively. There is only one kind of site for Ca (called Ca(1)) and Zr (called Zr(1)) (**Figure 36**). However, titanium ions occupy three distinct sites, two of which (called Ti(1) and Ti(3) sites) are six-fold coordinated whereas the third (called Ti(2) site), half-occupied, is five-fold coordinated (**Figure 36**). Oxygen anions occupy seven distinct sites referred as O(i) with $i=1$ to 7. For $x < 1$, titanium excess is accommodated in Zr(1) site. Whereas for $x > 1$, zirconium excess is accommodated mainly in sites Ti(1) and Ti(2). It is interesting to notice that even for stoichiometric zirconolite (i.e., $x = 0$), there exists a slight distribution of Ti and Zr between Zr(1), Ti(1) and Ti(2) sites.

Zirconolite is also well known for its excellent capacity to incorporate An and Ln ions into the Ca and Zr sites of its structure. The preferential incorporation in Ca and Zr sites can be easily understood from ionic radius arguments: because of the small size of the Zr site, incorporation of Ln and An (in natural or artificial zirconolite samples) in this site is very limited in comparison with the amount of Ln and An that can be incorporated in the Ca site without structural changes (**Table XVII**). Four different incorporation schemes (1-4) can be envisaged – if we exclude any vacancies in the structure - for trivalent (Ln^{3+} , An^{3+}) and tetravalent (Ln^{4+} , An^{4+}) lanthanides and actinides into the Ca and Zr sites of zirconolite-2M:



⁴¹ This solid solution range was shown to depend on the synthesis temperature.



The subscripts Ca, Ti and Zr correspond respectively to the Ca, Ti and Zr sites of zirconolite-2M structure (**Figure 36**). Trivalent and tetravalent (Ln,An) cations incorporation in the divalent calcium site needs charge compensation with cations such as Al³⁺ in titanium sites (incorporation schemes (1) and (2)). More precisely, we showed [206,207] from XRD Rietveld structural refinement of Ca_{0.7}Nd_{0.3}ZrTi_{1.7}Al_{0.7}O₇ (ceramic sample) that Al³⁺ ions mainly entered the Ti(2) site of the structure. The preferential incorporation of aluminum ions in the five-fold coordinated Ti site of zirconolite was also confirmed recently by Vance et al. [208].

The amount of (An, Ln) that can be incorporated in zirconolite-2M without structural changes (which means without new zirconolite-polytype, pyrochlore or perovskite formation for instance) strongly depends on its nature and more particularly on cation radius. Incorporation scheme (1) is the most efficient one. For instance, following this scheme, approximately 65% and 70% of the Ca²⁺ cations can be replaced respectively by Nd³⁺ and Gd³⁺ ions keeping the zirconolite-2M structure [209,71]. Using a different preparation method (oxide route) than that used by Vance et al. (alkoxide route) we confirmed that Ca_{1-x}Nd_xZrTi_{2-x}Al_xO₇ remained zirconolite-2M for x ≤ 0.6 [206]. To the best of our knowledge, the limit of incorporation of actinides in zirconolite is not well known and may strongly depend on the processing atmosphere. For instance, Pu valence state in zirconolite may change from completely tetravalent (when firing in air) to trivalent (when firing in reducing atmosphere) [210]. Vance et al. [71] indicated that it was possible to incorporate 0.4 Pu³⁺ ions by formula unit in the Ca site and 0.15 Pu⁴⁺ ions by formula unit in the Zr site of zirconolite-2M. This last result was confirmed by Begg et al. [211]. According to Begg et al. [179], neptunium occurred predominantly as Np⁴⁺ in zirconolite for oxidizing or reducing conditions. Concerning americium and curium, by analogy with the behavior of these actinides in glasses [212], we may expect that they occurred as Am³⁺ and

Cm^{3+} ions in zirconolite. Indeed, concerning curium, a 3 wt% ^{244}Cm doped (apparently single phase) zirconolite-2M sample was prepared by firing in air for self-radiation study following the charge compensation scheme (3) in which 2Cm^{3+} ions replace $1\text{Ca}^{2+} + 1\text{Zr}^{4+}$ ions [213].

As Zr^{4+} and Hf^{4+} ions have nearly identical radii (respectively 0.78Å and 0.76Å in seven-fold coordination [144] corresponding to the one of the Zr site in zirconolite) and belong to the same column of the periodic table, these two elements have very similar chemical properties and are expected to be incorporated in similar crystalline structures. Indeed, this was demonstrated for natural or synthetic Zr-rich crystalline phases such as zircon [214,72], baddeleyite [74] and zirconolite. For instance, natural zirconolite samples were shown to incorporate 2.4 wt% HfO_2 [194]. Moreover, the possibility to prepare (Zr,Hf)-zirconolite⁴² $\text{CaZr}_{1-x}\text{Hf}_x\text{Ti}_2\text{O}_7$ ($0 < x \leq 1$) ceramic samples was reported in literature [71,215,216,217]. As hafnium has a high thermal neutron capture cross-section in comparison with zirconium (respectively 104 and 0.184 barns [218]), it is considered as a neutron poison for fission reactions. This is why it would be interesting to substitute either totally or partially Zr by Hf in the zirconolite crystals of the ceramics (and in zirconolite-based glass-ceramics, see §IV.C) to prevent criticality events in waste forms heavily loaded with fissile actinide isotopes such as ^{239}Pu . The possibility to incorporate both trivalent and tetravalent plutonium in Hf-zirconolite was also demonstrated [210]. Concerning the chemical durability of zirconolite containing hafnium, several results reported in literature indicated that there is only little difference between the leaching behavior of Hf and Zr [219,220].

In the following paragraphs we will present structural and microstructural results we obtained in our laboratories concerning mainly the incorporation of Nd^{3+} ions in zirconolite (following essentially scheme (1) with aluminum as charge compensator). In this case, Nd^{3+} ion will be considered as a simulant of trivalent MA. Indeed, Nd^{3+} has a ionic radius similar to those of trivalent MA in eight-fold coordination (corresponding to the coordination of Ln in the Ca site of zirconolite): $r(\text{Nd}^{3+})=1.109\text{Å}$ and $r(\text{Am}^{3+})=1.09\text{Å}$ [144]. Several results will be also given concerning the incorporation in zirconolite-2M of lanthanides of

various size (Ce, Eu, Gd, Yb) to investigate the influence of the ionic radius of the lanthanide on the zirconolite cell parameters. An actinide (Th^{4+}) was also incorporated in zirconolite following incorporation scheme (1). It must be noticed that ytterbium cannot be considered as a good actinide surrogate because of its too small ionic radius, but it was chosen in order to bring out the effect of lanthanide ionic radius on zirconolite structure. Structural results concerning the incorporation of Nd^{3+} ions in $\text{CaHfTi}_2\text{O}_7$ following the charge compensation scheme (1) will be also presented. The choice of the compensation scheme (1) for the majority of our samples partly relied on results concerning natural samples. Indeed, from the compositions of natural zirconolite samples, it was inferred that the incorporation of lanthanides and actinides mainly occurred in the calcium site of zirconolite structure [221]. In this case, lanthanide and actinide ions being 3+ or 4+, a charge compensation is always needed: it is often ensured by the substitution of Ti^{4+} ions of zirconolite by $\text{Fe}^{2,3+}$, Al^{3+} or Mg^{2+} ions [222].

IV.B.3.c Synthesis of zirconolite ceramics

Because of the non-congruent melting of zirconolite [223], single-phase samples cannot be obtained by melting + casting (using a cold crucible melter for instance). Indeed, after melting at 1700°C and cooling a stoichiometric mixture to prepare zirconolite, different authors showed that the material obtained was multiphase. Zirconolite was the major phase (>50 vol%) but important amounts of other phases such as perovskite and zirconia were also formed during cooling of the melt [102, 200, 224].

So, the preparation methods reported in literature to synthesize single phase zirconolite ceramics were sintering methods. Among these different methods we can distinguished – as for hollandite ceramics preparation (§VA)- the conventional ceramic method with powders (oxide route) and the wet chemistry method using alkoxide, hydroxide or nitrate precursors in solution (alkoxide route). The alkoxide route was largely used by the ANSTO to prepare Synroc [50], zirconolite-rich Synroc [225] and single phase zirconolite [226] samples. This wet chemistry method was initially developed in order to obtain a high degree of homogeneity amongst the various chemical components of Synroc

⁴² In this chapter, when we write zirconolite without more indication, it means zirconolite with only zirconium in the 7-fold site of the structure (i.e. without hafnium). In the text, Hf-zirconolite means zirconolite with only hafnium and (Zr,Hf)-zirconolite means samples with both Zr and Hf.

before heat treatments. The CEA has also adopted this method to prepare single phase zirconolite samples [19] hydrolyzing a mixture of Al, Zr and Ti alkoxides with Ca and Ln nitrates. The powder obtained was then dried, calcined, pressed uniaxially and sintered (1400°C 96h for instance for an inactive $\text{Ca}_{0.8}\text{Nd}_{0.2}\text{ZrTi}_{1.8}\text{Al}_{0.2}\text{O}_7$ sample). In order to prevent the formation of perovskite as parasitic phase (that could incorporate Ln and An) a small excess of Zr and Ti was added in the precursors mixture but this lead to the formation of ZrTiO_4 as minor phase in their ceramics [19]. An almost similar wet chemistry method was used by Advocat et al. [227] to prepare zirconolite ceramic samples containing 10 wt% PuO_2 with Al^{3+} ions as charge compensators ($\text{Ca}_{0.87}\text{Pu}_{0.13}\text{ZrTi}_{1.74}\text{Al}_{0.26}\text{O}_7$). XANES spectroscopy showed that plutonium occurred mainly as Pu^{4+} in this ceramic [196].

As in §IV.A of this chapter, concerning the preparation of hollandite ceramics, for practical reasons we decided to use a conventional preparation method by oxide route to synthesize zirconolite ceramic samples. The following samples were synthesized:

- $\text{Ca}_{1-x}\text{Nd}_x\text{ZrTi}_{2-x}\text{Al}_x\text{O}_7$, with $x = 0$ to 0.8
- $\text{Ca}_{0.75}\text{Ln}_{0.25}\text{ZrTi}_{1.75}\text{Al}_{0.25}\text{O}_7$ for $\text{Ln} = \text{La}, \text{Ce}, \text{Nd}, \text{Eu}, \text{Gd}, \text{Yb}$
- $\text{Ca}_{0.9}\text{Th}_{0.1}\text{ZrTi}_{1.8}\text{Al}_{0.2}\text{O}_7$
- $\text{Ca}_{1-x}\text{Nd}_x\text{HfTi}_{2-x}\text{Al}_x\text{O}_7$, for $x = 0$ and 0.2

10-20 g ceramic of each sample were prepared by solid-state reaction from reagent grade powders. The starting materials were: CaCO_3 , ZrO_2 , HfO_2 , TiO_2 , Al_2O_3 , CeO_2 , Nd_2O_3 , Eu_2O_3 , Gd_2O_3 , Yb_2O_3 , ThO_2 . After drying at 400°C (1000°C for rare earth oxides), powders were weighed, thorough mixed in an agate mortar and uniaxially pressed at 20 MPa. The pellets (diameter: 2 cm) were fired in air at 1400°C for 100 h (**Figure 37**). They were then ground, re-pressed at 20 MPa into pellets and fired again in air at 1460°C for 100 h (**Figure 37**). Theses conditions of preparation enable to reduce the amount of parasitic phases and to increase the density of the pellets. Contrary, to hollandite (**Figure 17**), the heat treatment temperature and duration selected for zirconolite were higher for two reasons: there was no volatile element in the mixtures and oxides such as ZrO_2 and HfO_2 have high refractory character.

IV.B.3.d Structural characterizations of $\text{Ca}_{1-x}\text{Nd}_x\text{ZrTi}_{2-x}\text{Al}_x\text{O}_7$ zirconolite ceramics

IV.B.3.d.1 XRD study

Comparison of experimental XRD patterns (**Figure 38**) with database indicated that, for $x \leq 0.6$, $\text{Ca}_{1-x}\text{Nd}_x\text{ZrTi}_{2-x}\text{Al}_x\text{O}_7$ samples are almost single phase and corresponded to zirconolite-2M. Only very weak peaks near $2\theta = 38.6^\circ$ and $2\theta = 56^\circ$ (not seen on **Figure 38**), attributed to a perovskite phase, could be discerned on XRD diagrams⁴³. This parasitic phase is often mentioned in literature for preparation of zirconolite by solid state reaction. Perovskite is one of the main phases of Synroc ceramics (**Table VIII**), able to incorporate Ln and An. Probably for kinetics reasons [228], this phase could form easily during heating of the mixture of powders to prepare zirconolite, and was then difficult to destroy by reaction with ZrO_2 that had not reacted to form zirconolite. To limit the amount of perovskite in our ceramics, we selected high heating rates (**Figure 37**).

Nevertheless, back-scattered electron images confirmed that $\text{Ca}_{1-x}\text{Nd}_x\text{ZrTi}_{2-x}\text{Al}_x\text{O}_7$ materials with $x \leq 0.6$ were almost single phase (**Figure 39**) and EDX measurements showed that they had homogeneous compositions close to nominal ones. The occurrence of perovskite traces was difficult to detect by SEM probably due to a lack of contrast with zirconolite, but back-scattered electron images clearly shows the formation of a low amount of small zirconia crystals containing Ti of composition close to $\text{Zr}_{0.9}\text{Ti}_{0.1}\text{O}_2$ as determined by EDX, for all x values (**Figure 39**). The occurrence of $\text{Zr}_{0.9}\text{Ti}_{0.1}\text{O}_2$ crystals probably arises from the low reactivity of ZrO_2 powder. In spite of the existence of small amounts of parasitic phases it thus appears that almost all neodymium was incorporated in the structure of zirconolite-2M crystals. We will discuss below more precisely the location of Nd^{3+} ions in the zirconolite structure using spectroscopic techniques.

Qualitative analysis of the $\text{Ca}_{1-x}\text{Nd}_x\text{ZrTi}_{2-x}\text{Al}_x\text{O}_7$ XRD patterns indicates a clear evolution of line positions versus x . Notably, the structure of the doublet at $2\theta \approx 35.5^\circ$ progressively disappears with increasing x and becomes unresolved for $x = 0.6$ (**Figure 38**). This indicates a strong evolution for several lattice parameters as shown in **Table XVIII** and **Figure 40**. A (nearly) linear evolution of a , c and β

⁴³ A zirconolite ceramic sample of composition $\text{Ca}_{0.95}\text{Nd}_{0.1}\text{Zr}_{0.95}\text{Ti}_2\text{O}_7$ (i.e. following the charge compensation scheme (3) without aluminium charge compensator) was also prepared using the same method. The amount of perovskite was higher for this sample than for the samples prepared following scheme (1).

(**Table XVIII**) cell parameters is observed with increasing x : a and β increase whereas c decreases (**Figure 40**). However x has no strong effects on b . A rough interpretation of c and β evolutions can be proposed on the basis of simple considerations. From the comparison of ionic radii, Nd^{3+} ions incorporate into Ca/Zr planes while Al^{3+} ions incorporate into Ti planes. As c decreases with increasing x in $\text{Ca}_{1-x}\text{Nd}_x\text{ZrTi}_{2-x}\text{Al}_x\text{O}_7$, it means that the distance between the successive (001) layers decreases at the same time (**Figure 36**). This can simply be explained by the fact that Al^{3+} ions are smaller than Ti^{4+} ions ($r(\text{Al}^{3+})= 0.48 \text{ \AA}$ and $r(\text{Ti}^{4+})= 0.51 \text{ \AA}$ in five-fold coordination, $r(\text{Al}^{3+})= 0.535 \text{ \AA}$ and $r(\text{Ti}^{4+})= 0.605 \text{ \AA}$ in octahedral coordination [144]) whereas Nd^{3+} and Ca^{2+} ions have approximately the same ionic radii (**Table XVII**). Evolutions of the other cell parameters (a and b) are more difficult to understand because of the complex interactions occurring between the linked polyhedrons of zirconolite in (001) planes. It is interesting to notice that for the same amount of neodymium by formula unit ($x=0.1$), the lattice parameters of $\text{Ca}_{0.95}\text{Nd}_{0.1}\text{Zr}_{0.95}\text{Ti}_2\text{O}_7$ are larger than that of $\text{Ca}_{0.9}\text{Nd}_{0.1}\text{ZrTi}_{1.9}\text{Al}_{0.1}\text{O}_7$ (**Table XVIII**). This difference can be explained by the incorporation of Nd^{3+} ions in the small Zr site which induces an expansion of the lattice. Nevertheless, because of the difficulty of Nd^{3+} ions to enter into the Zr site following scheme (3), a higher amount of perovskite was detected by XRD in the $\text{Ca}_{0.95}\text{Nd}_{0.1}\text{Zr}_{0.95}\text{Ti}_2\text{O}_7$ ceramic. It will be seen below by Rietveld refinement, that for $\text{Ca}_{1-x}\text{Nd}_x\text{ZrTi}_{2-x}\text{Al}_x\text{O}_7$ ($x=0.3$) almost all Nd^{3+} ions are located in the Ca site.

To identify which kinds of crystallographic sites are occupied by Nd^{3+} and Al^{3+} ions, a Rietveld refinement was carried out on the $\text{Ca}_{0.7}\text{Nd}_{0.3}\text{ZrTi}_{1.7}\text{Al}_{0.3}\text{O}_7$ ceramic from its XRD pattern. The refinement was based on the $\text{CaZr}_{0.92}\text{Ti}_{2.08}\text{O}_7$ structure determination of Cheary [229]. Results of this refinement are presented in **Figure 41** and **Tables XIX** and **XX**. For more details concerning our refinement procedure, see [207,206]. Site occupancy results clearly demonstrate that:

- Nd^{3+} ions mainly enter into Ca(1) site (about 98.5 %). This result is in agreement with the assumptions that can be made from the comparison of ionic radii (Ca^{2+} and Nd^{3+} ions have very similar ionic radii whereas Zr^{4+} ions are significantly smaller, **Table XVII**). The fact that only a very small amount of

neodymium enter into the Zr site was confirmed by optical spectroscopy (§IV.B.3.d.2).

- Al^{3+} ions occupy only the split five-fold coordinated Ti(2) site. As already indicated above, this result is in agreement with the one of Vance et al. [208] for $\text{Ca}_{1-x}\text{Y}_x\text{ZrTi}_{2-x}\text{Al}_x\text{O}_7$ zirconolite ($0.1 \leq x \leq 0.3$) samples. This result is consistent with the solid solution limit $x = 0.6$ corresponding to $\text{Ca}_{1-x}\text{Nd}_x\text{ZrTi}_{2-x}\text{Al}_x\text{O}_7$ zirconolite-2M. Indeed, as Ti(2) can only be half-occupied, if Al^{3+} ions exclusively enter into Ti(2) site, the solid solution limit should be $x = 0.5$, which is in fairly good agreement with the experimental value ($x = 0.6$, **Figure 38**). Ti(2) sites constitute the closest cationic sites to Ca ones. So, Ti(2) occupation by Al^{3+} ions could be energetically favored, because it would ensure more efficiently the compensation charge necessary to the incorporation of Nd^{3+} ions into Ca sites. For $x = 0.65$, new XRD lines, whose the most characteristic are at $2\theta \approx 36.5^\circ$ (**Figure 38**) and $2\theta \approx 60.5^\circ$. They cannot be indexed in the space group of zirconolite-2M. From $x = 0.7$ to $x = 0.8$, the distinctive XRD lines of zirconolite-2M disappear (notably the peak at $2\theta \approx 37.5^\circ$) whereas all the new lines appeared for $x = 0.65$ remain. Most of the greatest XRD lines of this new phase remain in common with the ones of zirconolite-2M so that this new phase is probably a polytype of zirconolite-2M. In fact, the XRD diffraction patterns of $\text{Ca}_{1-x}\text{Nd}_x\text{ZrTi}_{2-x}\text{Al}_x\text{O}_7$ for $0.7 \leq x \leq 0.8$ can be fully indexed on the basis of the zirconolite-3O structure (space group $Acam$), an orthorhombic polytype of zirconolite [230]. Therefore, this range of composition seems to lead to the formation of almost single-phase zirconolite-3O. Rietveld refinement of $\text{Ca}_{0.3}\text{Nd}_{0.7}\text{ZrTi}_{1.3}\text{Al}_{0.7}\text{O}_7$ confirms that this composition leads to the crystallization of almost single phase zirconolite-3O [207,206].

IV.B.3.d.2 Study of local environment of Nd^{3+} ions in zirconolite-2M

The local environment of Nd^{3+} ions in zirconolite ceramic samples ($0 < x \leq 0.6$) was studied by EPR and optical absorption spectroscopy. Several results about the evolution of the neodymium environment in $\text{Ca}_{0.8}\text{Nd}_{0.2}\text{ZrTi}_{1.8}\text{Al}_{0.2}\text{O}_7$ samples irradiated by heavy ions (Pb^{3+}) in order to simulate α -recoils are presented in the next paragraph.

EPR was shown to be a very efficient and sensitive technique to detect and to identify the paramagnetic point defects formed by electron irradiation in

hollandite (§IVA). This technique is also very powerful to study paramagnetic rare earths such as Nd^{3+} ions and paramagnetic impurities in zirconolite and in parasitic phases. Nevertheless, because of the short spin-lattice relaxation time T_1 of neodymium due to its strong spin-orbit coupling, EPR signals can be only detected at very low temperature (near 10K, because the signal cannot be detected for $T \geq 60$ K). **Figure 42a** (middle) shows the EPR spectrum of $\text{Ca}_{0.97}\text{Nd}_{0.03}\text{ZrTi}_{1.97}\text{Al}_{0.03}\text{O}_7$ sample recorded at $T = 12$ K. For this composition, many paramagnetic elements can be detected, neodymium (in both the zirconolite and the parasitic perovskite phases) as well as other paramagnetic transition metals impurities (V^{4+} , Fe^{3+}) coming from the raw materials or the steel press. For $\text{Ca}_{0.97}\text{Nd}_{0.03}\text{ZrTi}_{1.97}\text{Al}_{0.03}\text{O}_7$, the very wide signal due to Nd^{3+} ions in zirconolite-2M is hardly visible. This signal dominates all the other contributions for heavily Nd-doped ceramics ($x \geq 0.1$, **Figure 42a**, top). A relatively narrow signal characteristic of Nd^{3+} ions in orthorhombic symmetry site between 2250 G and 3650 G was detected for $\text{Ca}_{0.97}\text{Nd}_{0.03}\text{ZrTi}_{1.97}\text{Al}_{0.03}\text{O}_7$ (**Figure 42a**, middle). This signal was attributed to Nd^{3+} ions in the perovskite parasitic phase by comparison with the EPR spectrum recorded in the same conditions for a pure $\text{Ca}_{0.9}\text{Nd}_{0.1}\text{Ti}_{0.9}\text{Al}_{0.1}\text{O}_3$ perovskite sample prepared by solid-state reaction at 1100°C (**Figure 42a**, bottom). Thus for low Nd_2O_3 concentration, a significant part of Nd^{3+} ions is incorporated in the Ca site of perovskite (probably with compensation charge insured by Al^{3+} ions in Ti site) which is in agreement with the results reported by Lumpkin et al.[231] about rare earth distribution between zirconolite and perovskite phases in Synroc samples. Indeed, these authors showed that for the biggest rare earths, the partitioning ratio of Ln^{3+} ions between perovskite and zirconolite was higher than 1. This was due to the fact that the size of the Ca site in perovskite is larger than in zirconolite. Nevertheless, for higher neodymium amounts ($x \geq 0.15$), the proportion of neodymium incorporated in the parasitic perovskite phase becomes negligible in our zirconolite ceramics.

An example of EPR spectrum for $x \geq 0.15$ is shown in **Figure 42b** ($\text{Ca}_{0.8}\text{Nd}_{0.2}\text{ZrTi}_{1.8}\text{Al}_{0.2}\text{O}_7$). This spectrum must be simulated with at least two components C1 and C2 (i.e. two g-tensors)⁴⁴ corresponding to two different environments for Nd^{3+} ions. Indeed, it is impossible to simulate this spectrum

⁴⁴ Concerning EPR signals simulation and g-tensor, see §IV.A.3.e.2.c. concerning the study of paramagnetic point defects in irradiated hollandite.

considering only one component. Moreover, the relative contributions of components C1 and C2 depend on the recording temperature (between 12 and 50K) which shows that they are associated with Nd^{3+} ions in two different sites having slightly different spin-lattice relaxation times T_1 . By double integration of the EPR signals it is possible to estimate the relative proportions of the two components: C1 (87%) and C2 (13%). As there is only one Ca site in zirconolite (**Table XIX**), the two components correspond to Nd^{3+} ions located in two slightly different calcium sites probably due to differences concerning their second neighbors. Moreover, we will see below that neither of the two components can correspond to Nd^{3+} ions in the Zr site.

Optical absorption spectra of Nd^{3+} ions were recorded at low temperature ($T=15\text{--}20\text{ K}$). In this temperature range, only the optical transitions from the lowest Stark doublet ($^4\text{I}_{9/2}$ ground state) to the excited states are observed. In this work, the $^4\text{I}_{9/2} \rightarrow ^2\text{P}_{1/2}$ transition - occurring in the 431-434 nm ($23050\text{-}23200\text{ cm}^{-1}$) range - is particularly interesting to study because the degeneracy of the $^2\text{P}_{1/2}$ state is not removed by the crystal field occurring around Nd^{3+} ions (**Figure 43a**). Thus, in these conditions, each kind of neodymium environment is characterized by only one absorption band. For more details concerning the spectroscopy of lanthanides and more particularly of neodymium see for instance references [232,233,234]. Optical absorption was very helpful to demonstrate that the very low amount of Nd^{3+} ions that are located in the zirconium site of zirconolite (**Table XIX**) do not give detectable absorption band on optical spectra. In **Figure 43b** are shown the optical absorption spectra of Nd^{3+} ions ($^4\text{I}_{9/2} \rightarrow ^2\text{P}_{1/2}$ transition) in $\text{Ca}_{0.95}\text{Nd}_{0.1}\text{Zr}_{0.95}\text{Ti}_2\text{O}_7$ and $\text{Ca}_{0.9}\text{Nd}_{0.1}\text{ZrTi}_{1.9}\text{Al}_{0.1}\text{O}_7$ (zirconolite-2M) and in perovskite $\text{Ca}_{0.9}\text{Nd}_{0.1}\text{Ti}_{0.9}\text{Al}_{0.1}\text{O}_3$ ceramics. The spectrum of $\text{Ca}_{0.95}\text{Nd}_{0.1}\text{Zr}_{0.95}\text{Ti}_2\text{O}_7$ shows two distinctive features in comparison with that of $\text{Ca}_{0.9}\text{Nd}_{0.1}\text{ZrTi}_{1.9}\text{Al}_{0.1}\text{O}_7$. Firstly, for the ceramic $\text{Ca}_{0.95}\text{Nd}_{0.1}\text{Zr}_{0.95}\text{Ti}_2\text{O}_7$ prepared following charge compensation scheme (3), a shoulder near 23130 cm^{-1} is observed on the high energy side of the main band centered near 23120 cm^{-1} . In comparison with the ceramic $\text{Ca}_{0.9}\text{Nd}_{0.1}\text{ZrTi}_{1.9}\text{Al}_{0.1}\text{O}_7$ prepared following charge compensation scheme (1), this shoulder can be attributed to Nd^{3+} ions in the Ca site of perovskite occurring as parasitic phase in the zirconolite ceramic (**Table XVIII**). Indeed, the maximum of the $^4\text{I}_{9/2} \rightarrow ^2\text{P}_{1/2}$ absorption band of neodymium in pure perovskite occurs at this energy (**Figure 43b**, top). Secondly, a broad and weak absorption

band centered near 22945 cm^{-1} is detected for $\text{Ca}_{0.95}\text{Nd}_{0.1}\text{Zr}_{0.95}\text{Ti}_2\text{O}_7$ and is not detected for $\text{Ca}_{0.9}\text{Nd}_{0.1}\text{ZrTi}_{1.9}\text{Al}_{0.1}\text{O}_7$ (**Figure 43b**, middle). This new band can be attributed to Nd^{3+} ions in the zirconium site of zirconolite. Thus no Nd^{3+} ions are detected in the in the zirconium site of zirconolite $\text{Ca}_{0.9}\text{Nd}_{0.1}\text{ZrTi}_{1.9}\text{Al}_{0.1}\text{O}_7$ ceramic (**Figure 43b**, bottom). The fact that the ${}^4\text{I}_{9/2} \rightarrow {}^2\text{P}_{1/2}$ transition of Nd^{3+} ions in Zr site is displaced towards lower energy in comparison with that of Nd^{3+} ions in Ca site can be explained by an increase of the covalent character of the bonding between the 4f orbitals of neodymium and the 2p orbitals of the surrounding oxygen anions. Indeed, as Zr site is smaller than Ca site, Nd-O distance is shorter for neodymium in Zr site (**Table XX**) and the covalent character of the Nd-O bonding increases. However, it is known that an increase of the covalency of the bonding between Nd^{3+} ion and its ligands induces a decrease of the gap between their energy levels (nephelauxetic effect) [233]. Consequently, this explains the displacement towards lower energies of the ${}^4\text{I}_{9/2} \rightarrow {}^2\text{P}_{1/2}$ transition for Nd^{3+} ions in Zr site of zirconolite.

The optical absorption spectra (${}^4\text{I}_{9/2} \rightarrow {}^2\text{P}_{1/2}$ transition) of the $\text{Ca}_{0.7}\text{Nd}_{0.3}\text{ZrTi}_{1.7}\text{Al}_{0.3}\text{O}_7$ ceramic shown in **Figure 43c** can be simulated with at least three relatively broad (half-width at half-maximum $\Delta \approx 30\text{ cm}^{-1}$) Gaussian shape components G_1 , G_2 and G_3 . This result shows that three different neodymium environments in zirconolite are detected using this technique (one more than with EPR, **Figure 42b**) for all samples. This difference between the results obtained using EPR and optical absorption can be explained by the fact that Nd^{3+} EPR spectrum in zirconolite is very anisotropic (the main components of the g tensors range from 0.80 to 3.21 [207]) and broad in comparison with the optical absorption spectrum. If it is assumed that the oscillator strength (linked to the transition probability) of the individual ${}^4\text{I}_{9/2} \rightarrow {}^2\text{P}_{1/2}$ transitions does not significantly vary from one Nd environment to another (due to the occupancy of the same basic Ca site in all cases), the area ratio of the absorption bands G_1 , G_2 and G_3 can be used to estimate the relative amounts of Nd^{3+} ions located in the three different environments. The G_1 and G_3 components which are the close (**Figure 43c**) are probably unresolved by EPR and would correspond to the strong C_1 component detected by EPR. The comparison of the relative surface area of the C_1 component in one hand (87%) with the relative surface area of the $G_1 + G_3$ components in the other hand (83%) seems to confirm this hypothesis. Moreover,

it must be underline that the Nd^{3+} ions optical absorption line width in zirconolite ($\Delta \approx 30 \text{ cm}^{-1}$) is relatively large in comparison with other crystalline materials such as Nd-doped $\text{Y}_3\text{Al}_5\text{O}_{12}$ (YAG) for which Δ does not exceed several cm^{-1} at low temperature [235]. This indicates that in zirconolite the neodymium absorption line width is strongly inhomogeneously broadened which can be explained by a disorder in the Nd^{3+} ions environment. The origin of this disorder which would explain both the occurrence of more than one environment for neodymium in the zirconolite calcium site and the large line width can be given as follows. The structural data obtained by Rietveld refinement of the $\text{Ca}_{0.7}\text{Nd}_{0.3}\text{ZrTi}_{1.7}\text{Al}_{0.3}\text{O}_7$ zirconolite clearly shows that the Nd^{3+} ions located in the Ca site have two Ti(2) splitted sites in their next nearest neighborhood (**Figure 44**). These four Ti(2) positions are located at different distances from the Nd^{3+} ions and are statistically occupied by Ti^{4+} or Al^{3+} ions (50 %) and vacancies (50 %). Consequently, it appears that the environment of neodymium ions (and thus the crystal field around them) in the calcium site can vary from one site to another. In this case, 16 possible different environments for neodymium can be envisaged [207].

IV.B.3.d.3 Study of local environment of Nd^{3+} ions in irradiated zirconolite

The studies reported in literature on internal or external irradiation experiments of zirconolite mainly concerned the effect of irradiation on its physical and chemical properties and the evolution of its amorphization followed by XRD or SAD [183,213,236,237]. Nevertheless, several works were performed on natural metamict (or annealed) zirconolite samples containing U and Th to study the local environment of several cations (Zr^{4+} , Th^{4+} , U^{4+} , Ti^{4+} , Ca^{2+}) using EXAFS and XANES spectroscopies [195,197,198].

Actinides α -decay induces damages in zirconolite mainly due to α -recoil nuclei and emission of α -particles leading to a progressive amorphization of the structure. α -particles transfer their energy of 4.5-5.8 MeV mainly by ionizations and electronic excitations [39]. They also induce several hundred atomic displacements by ballistic processes along their path but mainly at the end of their tracks (10-20 μm). The heavy α -recoil nuclei have energies of 70-100 keV, move over shorter distances (30-40 nm) and lose nearly all their energy by ballistic processes producing a highly localized displacement cascade with a high number

of atoms (1000-2000 atoms) [39]. These ballistic damages can be simulated by external irradiation experiments with heavy ions such as Au^{2+} and Pb^{3+} . In our work, $\text{Ca}_{0.8}\text{Nd}_{0.2}\text{ZrTi}_{1.8}\text{Al}_{0.2}\text{O}_7$ zirconolite samples prepared by alkoxide route at the CEA (Marcoule, France) were externally irradiated by Pb^{3+} ions of 510 keV (energy close to the one of heavy recoil nuclei) at three different doses: 10^{14} , 2.10^{15} and 10^{16} Pb^{3+} ions/cm². These samples mimic several stages of zirconolite amorphization, since the critical amorphization dose is estimated around 2.10^{15} Pb^{3+} ions/cm² (nearly equivalent to 5.10^{18} α/g). First insights into the mechanisms of zirconolite amorphization were obtained by Grazing Incidence X-ray Absorption Fine Structure (GIXAFS) in fluorescence detection mode at room temperature for the study of Nd local environment (L_{III} edge, 6208 eV)⁴⁵. The principle of this technique is the same as EXAFS but GIXAFS enables to record the EXAFS spectrum of only a small thickness of sample near the surface. The depth of amorphization induced by Pb^{3+} ions external irradiation was estimated around 400 Å from numerical simulations, transmission electron microscopy observations and grazing x-ray diffraction experiments. Due to the thinness of the surface layer to be probed by X-rays, GIXAFS measurements enabled to selectively analyze the damaged zone of the samples by working with a 100 mdeg grazing angle. Because a large surface area is illuminated by the X-rays beam at glancing incidence, all experiments were performed on polished ceramic pellets of 25 mm in diameter (1 mm thick), in order to maximize the intensity collected during GIXAFS experiments. As only a very small fraction of the thickness of zirconolite samples was damaged in these experiments (about 0.004 %), other techniques such as classical EXAFS detected by transmission or fluorescence, optical absorption spectroscopy and EPR were not adapted to follow the modification of Nd^{3+} ions environment.

In §IV.B.3b we saw that zirconolite can be regarded as a layered structure in which (Ca-Nd)/Zr and Ti-Al planes are stacked (**Figure 36**). From Rietveld refinement results of $\text{Ca}_{0.7}\text{Nd}_{0.3}\text{ZrTi}_{1.7}\text{Al}_{0.3}\text{O}_7$, Nd (substituting Ca) is expected to be surrounded by 8 oxygen anions at distances ranging from ~ 2.28 to 2.48 Å (mean distance 2.43 Å, **Table XX**). The second nearest neighbors consist of Ti-Al cations from 3.2 Å. But the contribution of other cations of different kinds (Zr and

⁴⁵ These experiments were performed at the synchrotron of ANKA on the INE beamline (Karlsruhe, Germany) with the help of M. Denecke, J. Roethe and K. Dardenne.

Ca in addition to Ti-Al) from 3.55 Å brings EXAFS contributions which strongly interfere in the investigated EXAFS region (up to 9 Å⁻¹). So, whereas the first shell can be accurately analyzed, only pseudo-quantitative information can be obtained concerning the second shell. For more details concerning EXAFS spectroscopy see for instance [238]. The GIXAFS results (coordination number around Nd, mean distances between Nd and its first and second neighbors, Debye-Waller factors σ which include both vibrational and static disorder effects) are presented in **Figure 45** and **Table XXI**. **Figure 45** shows a decrease (indicated by arrows) of the Fourier transforms peaks corresponding to the first and second shells around Nd with increasing irradiation dose. Simulation of the first shell (**Table XXI**) shows that Nd is eight-fold coordinated by oxygen anions in all the samples, irrespective of their irradiation dose. Moreover these oxygen anions always occur at the same mean distance 2.45 Å, in good agreement with the structural results of non irradiated Ca_{0.7}Nd_{0.3}ZrTi_{1.7}Al_{0.3}O₇ zirconolite (**Table XX**). However, a significant increase of the Debye-Waller factors σ (from $\sigma^2 = 0.007$ to 0.018 Å²) is observed with increasing the irradiation dose (**Table XXI**). This evolution of σ indicates that the local order around Nd is kept despite the amorphization of zirconolite structure (this is the case at least for the sample irradiated with 10^{16} Pb³⁺ ions/cm²). Only a broadening of the distribution of Nd-O distances occurs with the irradiation dose. The medium range order around Nd is much more sensitive to the irradiation dose. Above the critical dose of amorphization (estimated to $2 \cdot 10^{15}$ Pb³⁺ ions/cm²), no second shell contribution is even detectable in **Figure 45**. This phenomenon could be attributed to an increase of the distribution of Nd-O-M (M=Ti,Al) angles between polyhedra caused by irradiation. The lack of strong modifications of the short-range order around Nd tends to confirm the amorphization model proposed by Farges et al. [197] for zirconolite. In their model, using EXAFS results, these authors proposed that the loss of the long range periodicity in metamict zirconolite was due to changes in angles between polyhedra without strong modifications of short-range environment. Moreover, the slight increase of the distance between Nd and its second neighbors (**Table XXI**) could contribute to the macroscopic swelling reported in literature [213].

IV.B.3.e Structural characterization of zirconolite ceramics with La, Ce, Eu, Gd, Yb or Th

Among the different lanthanides (Ln=La, Ce, Nd, Eu, Gd, Yb) used to prepare $\text{Ca}_{0.75}\text{Ln}_{0.25}\text{ZrTi}_{1.75}\text{Al}_{0.25}\text{O}_7$ samples (charge compensation scheme (1)), two of them can adopt several oxidation states in air: it is the case of cerium ($\text{Ce}^{3+}/\text{Ce}^{4+}$) and europium ($\text{Eu}^{2+}/\text{Eu}^{3+}$). According to EPR results, to the high sintering temperature (1460°C) and to the kind of charge compensation scheme, the major part of cerium ions in $\text{Ca}_{0.75}\text{Ce}_{0.25}\text{ZrTi}_{1.75}\text{Al}_{0.25}\text{O}_7$ sample is expected to be in their trivalent state [207]. Moreover, the fact that $\text{Ca}_{0.75}\text{Eu}_{0.25}\text{ZrTi}_{1.75}\text{Al}_{0.25}\text{O}_7$ sample gives no EPR signal attributable to Eu^{2+46} , means that europium occurs exclusively as Eu^{3+} in this sample [239]. For Ln=Ce, Nd, Eu, Gd and Yb, qualitative analysis of XRD patterns indicates that the samples were almost single-phase zirconolite-2M. Nevertheless, as for Ln = Nd, very weak XRD lines attributed to perovskite traces could be detected for each material. For lanthanum, XRD analysis of the $\text{Ca}_{0.8}\text{La}_{0.2}\text{ZrTi}_{1.8}\text{Al}_{0.2}\text{O}_7$ sample shows that it is composed of a mixture of zirconolite-2M and perovskite and cannot be considered as single-phase. The Ca site of zirconolite-2M is probably too small for an efficient incorporation of lanthanum ions (**Table XVII**) whereas the calcium site of perovskite is significantly larger and more appropriate. So zirconolite-2M is able to incorporate all trivalent rare earths smaller than lanthanum following the $\text{Ca}_{1-x}\text{Ln}_x\text{ZrTi}_{2-x}\text{Al}_x\text{O}_7$ charge compensation scheme.

The cell parameters (a, b, c, β) of $\text{Ca}_{0.75}\text{Ln}_{0.25}\text{ZrTi}_{1.75}\text{Al}_{0.25}\text{O}_7$ increase with the ionic radius r of Ln^{3+} ions [207]. As all the lanthanides (except La) are very likely to substitute the Ca site of the structure, it means that the average size of cations in Ca site affects all the cell parameters in a similar way. On the basis of an ionic model, a linear evolution of $\text{Ca}_{0.75}\text{Ln}_{0.25}\text{ZrTi}_{1.75}\text{Al}_{0.25}\text{O}_7$ zirconolite-2M cell volume V is expected versus r^3 (Vegard's law) which is in agreement with **Figure 46**. This linear evolution is extremely well verified for the following ions: Nd^{3+} , Eu^{3+} , Gd^{3+} and Yb^{3+} . However, it seems that the cell volume of $\text{Ca}_{0.75}\text{Ce}_{0.25}\text{ZrTi}_{1.75}\text{Al}_{0.25}\text{O}_7$ does not lie exactly on the same line as the ones of the other compounds. This difference could be due to the oxidation of a small part of Ce^{3+} into Ce^{4+} . Indeed, as Ce^{4+} ion is much smaller than Ce^{3+} ion (in eight-fold

⁴⁶ Contrary to Eu^{3+} ions (${}^7\text{F}_0$ electronic state) that cannot be detected by EPR, Eu^{2+} ions (${}^8\text{S}_{7/2}$ electronic ground state) are easily detected [239].

coordination, $r(\text{Ce}^{4+})=0.97 \text{ \AA} < r(\text{Ce}^{3+})=1.143 \text{ \AA}$, **Table XVII**), its occurrence into the Ca site should reduce V in comparison with 100 % of Ce^{3+} .

Following the charge compensation scheme (2), a $\text{Ca}_{0.9}\text{Th}_{0.1}\text{ZrTi}_{1.8}\text{Al}_{0.2}\text{O}_7$ sample was also prepared⁴⁷. As thorium is only tetravalent, the incorporation of one Th^{4+} ion in Ca site needs two Al^{3+} ions in Ti site. According to literature [240], charge compensation scheme (2) was more efficient than scheme (4) to incorporate thorium in zirconolite-2M probably because of the big size of Th^{4+} ions (**Table XVII**)⁴⁸. Kesson et al.²⁴¹ indicated that no more than 0.24 Th^{4+} ions could be incorporated in the Ca site following scheme (2). However, according to Fielding et al. [70] this limit was certainly lower. In our case, we showed that the XRD pattern of $\text{Ca}_{0.9}\text{Th}_{0.1}\text{ZrTi}_{1.8}\text{Al}_{0.2}\text{O}_7$ can only be indexed in the zirconolite-2M space group and this was confirmed by HRTEM [242].

IV.B.3.f Structural characterization of $\text{Ca}_{1-x}\text{Nd}_x\text{HfTi}_{2-x}\text{Al}_x\text{O}_7$ zirconolite ceramics

XRD and SEM show that Hf-zirconolite samples ($\text{Ca}_{1-x}\text{Nd}_x\text{HfTi}_{2-x}\text{Al}_x\text{O}_7$ for $x=0$ and 0.2) are almost single-phase. Except a small amount of perovskite, all XRD lines can be indexed in the monoclinic $\text{C}_{2/c}$ space group of zirconolite-2M (patterns not shown). The corresponding lattice parameters are given in **Table XXII**. It appears that the cell volume V of Hf-zirconolite ceramics is slightly lower than the one associated with the corresponding Zr-zirconolite ceramics. This result can be explained by the fact that Hf^{4+} cation radius is slightly smaller than Zr^{4+} one (**Table XVII**). Similarly to the evolution of the lattice parameters of $\text{Ca}_{1-x}\text{Nd}_x\text{ZrTi}_{2-x}\text{Al}_x\text{O}_7$ with x (**Table XVIII**), Nd induces an increase of *a* parameter and a decrease of *c* parameter whereas *b* does not significantly change. The composition of Hf-zirconolite samples was determined by EPMA: $\text{Ca}_{0.99}\text{Hf}_{0.98}\text{Ti}_{2.00}\text{O}_7$ and $\text{Ca}_{0.797}\text{Nd}_{0.198}\text{Hf}_{0.998}\text{Ti}_{1.80}\text{Al}_{0.194}\text{O}_7$ respectively for $x=0$ and $x=0.2$. The composition of Hf-zirconolite is thus very similar to nominal composition.

Using the same spectroscopic techniques as for Zr-zirconolite, the environment of Nd^{3+} ions in $\text{Ca}_{0.8}\text{Nd}_{0.2}\text{HfTi}_{1.8}\text{Al}_{0.8}\text{O}_7$ was studied and compared to that of neodymium in $\text{Ca}_{0.8}\text{Nd}_{0.2}\text{ZrTi}_{1.8}\text{Al}_{0.8}\text{O}_7$. It appeared that EPR and optical

⁴⁷ As discussed in §IVB.1, Th^{4+} ion is sometimes considered as Pu^{4+} ion surrogate.

⁴⁸ Th^{4+} ion is the biggest tetravalent ion of the periodic classification.

absorption spectra were very similar for the two ceramics. Simulations of EPR and optical absorption spectra by respectively two and three components, showed that both the g-tensors and the absorption bands position were not very sensitive to the nature of tetravalent cation (Zr^{4+} or Hf^{4+}) in Zr(1) site. Moreover, the effect of the crystal field on the splitting of the neodymium $^4I_{9/2}$ state (**Figure 43a**) was very similar in the two matrices [243]. As for Zr-zirconolite, the different neodymium environments can be attributed to Nd^{3+} ions in Ca sites with disorder in their neighborhood. The existence of this disorder around Nd^{3+} ions is also probably due to the statistical occupancy of the splitted Ti(2) site by Al^{3+} and Ti^{4+} ions (**Figure 44**). All these results confirm the absence of significant effect of the replacement of Zr by Hf in the zirconolite structure and more particularly on Nd^{3+} ions environment. Consequently, zirconium can be totally replaced by hafnium to prepare zirconolite ceramic waste forms.

IV.C. Zirconolite-based glass-ceramic as specific waste form for MA immobilization

In this part we present the main results concerning the studies performed in our laboratories on zirconolite-based glass-ceramics. The definition and the main principles of glass-ceramics preparation were given in §III (**Figure 10**). Examples of glass-ceramic waste forms for the immobilization of non separated or separated wastes were also given in §III.

IV.C.1 Previous works on glass-ceramics containing zirconolite crystals

Several studies reported in literature on glass composite waste forms shown that zirconolite could crystallize in the bulk of different glass compositions containing relatively high amounts of TiO_2 and ZrO_2 . However, in all these studies, zirconolite crystals generally occurred with numerous others crystalline phases. One of the first works published on such materials concerned iron-enriched basalt with TiO_2 and ZrO_2 envisaged for the conditioning of high-level defense wastes [244]. An optimum composition and cooling cycle from the melt enabled crystallization of zirconolite but also of pseudo-brookite and augite. Moreover, using results of lixiviation tests, the authors of this paper [244] indicated that Am, Pu and Cm were incorporated into the zirconolite phase whereas neptunium

probably remained in the residual glassy phase. More recently, Kong et al.[245,246] also published a study on the crystallization of zirconolite in iron-enriched basalt glasses by isothermal treatments between 1000 and 1200°C (without nucleation stage) or by controlled cooling of the melt in order to develop waste forms to immobilize transuranic elements (simulated by lanthanides in their work) occurring in low-level wastes. The aim of these authors was to incorporate actinides into the zirconolite phase. They shown that zirconolite was formed in the bulk of their samples but additional crystalline phases (spinel, pyroxene, and plagioclase for instance) were also observed in the residual glass. However, actinide surrogates were preferentially incorporated into zirconolite crystals. A complex borosilicate glass-ceramic waste form containing zirconolite crystals was also proposed for the immobilization of Pu [106]. In this work, about ten different crystalline phases were identified coexisting with zirconolite. Moreover, the authors indicated that Pu was mainly incorporated in zirconolite and zirconia crystals. Other complex glass-ceramic materials containing zirconolite were developed by Feng et al. [247]. The crystallization of zirconolite with others phases (such as ZrO_2 , $ZrTiO_4$, $ZrSiO_4$, TiO_2) was also observed by Lin et al. [248] in B_2O_3 - SiO_2 - Al_2O_3 - CaO - ZrO_2 - TiO_2 glasses.

Nevertheless, to the best of our knowledge, preparation of glass-ceramic samples with zirconolite as the only crystalline phase in their bulk was reported for the first time by Fillet et al. [101,102] in the context of the French research on enhanced separation and conditioning of long-lived radionuclides occurring in HLW solutions. These materials were developed in order to immobilize separated MA. In their study, neodymium was used as trivalent MA surrogate. Their parent glass composition belonged to the $SiO_2 - Al_2O_3 - CaO - TiO_2 - ZrO_2$ system and the glass-ceramics were obtained by controlled thermal treatment of the parent glass. Using starting glass compositions close to the ones developed by Fillet et al. [101,102], numerous studies were then performed in our laboratories in order to improve both the amount of zirconolite in the glass-ceramics and the partitioning ratio of MA surrogate between residual glass and zirconolite crystals. These works that concerned mainly the study of bulk and surface crystallization, the effect of parent glass composition and of the crystal growth temperature on the nature and the structure of the crystals, the effect of the concentration and

nature of MA surrogates on bulk and surface crystallizations are presented in the next paragraphs.

IV.C.2 Synthesis and characterization of zirconolite-based glass-ceramics

In the next paragraph, we present the compositions and the method used to prepare parent glasses and zirconolite-based glass-ceramics. Results concerning the effect of heat-treatment temperature and of parent glass composition changes on both the microstructure of glass-ceramics and on the structure and composition of the crystals formed, will be largely developed in the following paragraphs.

IV.C.2.a Synthesis of parent glasses and preparation of glass-ceramics

In this paragraph, two glass compositions (A and B) leading to only zirconolite crystals in their bulk after appropriate thermal treatments will be considered (**Table XXIII**). Glass A is a composition without neodymium whereas in glass B, 6 wt% Nd₂O₃ were added to simulate trivalent MA (see §IV.B.1.). Concentration ratios between the other oxides were kept constant for the two glasses. Composition B is very close to that reported by Fillet et al. [101]. It must be noticed that if we consider molar concentrations, 6 wt% Nd₂O₃ (1.27 mol%, **Table XXIII**) is equivalent to 9 w % Am₂O₃ which is approximately the amount of MA (≈ 10 wt%) aimed to immobilize in specific waste forms.

If we consider only the three oxides SiO₂, Al₂O₃ and CaO, the corresponding glass composition is located near the SiO₂ rich eutectic point of the ternary SiO₂-Al₂O₃-CaO phase diagram [249]. The glasses belonging to this ternary system are known to be easy to melt, to exhibit a good chemical durability and a low bulk crystallization tendency [189,250]. This last point was important in our case because we wished to avoid the nucleation and growth of silicate crystals in the bulk of the glass at the expense or at the same time as zirconolite crystals. **Table XXIII** shows that TiO₂ and ZrO₂ were added to the SiO₂-Al₂O₃-CaO basic ternary composition in a molar ratio [Ti]/[Zr] \approx 2.2. This ratio is only slightly higher than the molar ratio corresponding to stoichiometric zirconolite (CaZrTi₂O₇). The high TiO₂ and ZrO₂ concentrations in glasses A and B were introduced in order to promote zirconolite crystallization. The lack of boron, the very low concentration of sodium and the high concentrations of zirconium, titanium, calcium and aluminum in glass compositions suggest a high chemical durability both for the

parent glass and for the corresponding glass-ceramics obtained after partial crystallization. In parent glasses, silica is only expected to dissolve the main oxides (CaO, Al₂O₃, Na₂O, ZrO₂, TiO₂) and Nd₂O₃, but SiO₂ is expected to remain totally in the residual glass after partial crystallization of zirconolite in the bulk because Si⁴⁺ ions do not enter into the zirconolite structure⁴⁹. This kind of glass-ceramic is thus different from classical ones (belonging for instance to the SiO₂-Al₂O₃-MgO-Li₂O system) for which SiO₂ is one of the main components of the crystalline phases formed after thermal treatments. The occurrence of alumina in parent glass compositions is also very useful for the charge compensation of neodymium ions in zirconolite crystals (see charge compensation scheme (1) in §IV.B).

Powder mixtures (50 g) were prepared by thorough mixing of reagent grade oxides (SiO₂, Al₂O₃, TiO₂, ZrO₂, Nd₂O₃) and carbonates (CaCO₃, Na₂CO₃), melted and refined at 1550°C for 10 h in Pt crucibles (**Figure 47**). Melts were poured in water in order to obtain a glass frit, ground and melted again for 4 h at 1550°C to ensure glass homogeneity. The melts were then cast in cylindrical metallic molds and the glass samples were annealed at 775°C for 2 h (i.e. at a temperature slightly higher than T_g) and slowly cooled to room temperature in order to relieve internal stresses. The glass samples were fully transparent and x-ray amorphous (**Figure 48**). Chemical analysis of glasses did not reveal significant deviations from nominal compositions. This is not surprising because (except a small Na₂O amount) none of the oxides present in glass compositions were volatile. The glass transformation temperature for glasses A and B were similar: T_g≈760°C. This temperature is more than 250°C higher than that of borosilicate nuclear glasses. This strong difference can be explained by the lack of B₂O₃ and the very small amount of alkalis in parent glass compositions.

Concerning the structure of parent glasses, several experiments using spectroscopic techniques were performed in order to study the environment around four cations (Ti³⁺, Zr⁴⁺, Nd³⁺, Al³⁺) occurring in parent glass B. For instance, EPR study of the small amount of paramagnetic Ti³⁺ ions formed during glass melting at 1550°C, revealed that titanium ions environment could be described by a C_{4v} or D_{4h} symmetry [207]. This could correspond to a square

⁴⁹ Nevertheless, it will be show below that two crystalline silicate phases (titanite, anorthite) may form near glass surface by heterogeneous nucleation process.

pyramidal $O=TiO_4$ or to a six-fold coordinated octahedron axially compressed. The coordination numbers involved in such geometries are close to the ones encountered in zirconolite (6 and 5) which is aimed to crystallize by heat treatment of the glasses. Moreover, Zr-K edge EXAFS spectra showed that Zr^{4+} ions occupied well defined 6-7 coordinated sites by oxygen at $2.20 \pm 0.01 \text{ \AA}$, close to the ones of zirconolite (**Table XX**) [251]. These results concerning titanium and zirconium are in agreement with the nucleating role of TiO_2 and ZrO_2 reported in literature [88]. Indeed, in the case of zirconolite-based glass-ceramics, the similarities between the sites occupied by titanium and zirconium in parent glass and in zirconolite could predispose parent glass to zirconolite nucleation. Concerning Nd^{3+} ions, optical absorption spectroscopy and EXAFS results agree to describe Nd environment as being constrained by the glassy network with coordination number and Nd-O distance significantly greater than Ca-O and Zr-O distances in zirconolite (**Table XX**) [251]. Indeed, Nd occupied a highly distorted 8-9-fold coordinated site in the parent glass with oxygen atoms at $2.53 \pm 0.02 \text{ \AA}$. Therefore, Nd^{3+} ion cannot act as a nucleating agent for zirconolite crystallization. Moreover, no second neighbors could be clearly identified by EXAFS at distances lower than 4 \AA around Nd. However, the study of Nd optical fluorescence decays in glass B suggested a strong interaction between Nd^{3+} ions which is likely to originate from a mean Nd-Nd distance lower than the statistical one [207]. ^{27}Al MAS-NMR study of glass A (without paramagnetic Nd^{3+} ions) showed that aluminum seems to enter glass network predominantly in four fold coordination [252]. This result suggests that modifier cations such as Ca^{2+} and Na^+ ions are present in sufficient concentrations in glass A to compensate all $[AlO_4]^-$ units. Indeed, as the molar ratio $([CaO] + [Na_2O])/[Al_2O_3] = 3.11 > 1$ for glass A (**Table XXIII**), the calcium and sodium oxide contents in this glass are higher than that needed for ensuring a full compensation of $[AlO_4]^-$ units. Nevertheless, ^{27}Al MQ-MAS-NMR (Multi Quanta-Magic Angle Spinning-Nuclear Magnetic Resonance) experiments are in progress in order to study if small amount of 5- or 6-fold coordinated aluminum is present in glass A. Moreover, Ca^{2+} and Na^+ ions are also expected to act as charge compensators near the negatively charged titanium and zirconium polyhedra in glass structure [253,254].

IV.C.2.b Preparation and characterization of zirconolite-based glass-ceramics

The zirconolite-based glass-ceramics were prepared by a two step heat treatment (nucleation + crystal growth, see §III.B.3.a. and **Figure 10**) of parent glasses. After annealing, parent glasses were firstly nucleated at $T_N=810^\circ\text{C}$ for 2 h (**Figure 49**). This temperature was slightly higher than T_g (760°C) and T_{\max} (790°C). T_{\max} corresponds to the temperature at which the zirconolite nucleation rate is maximal (**Figure 50**). After nucleation, the samples were immediately transferred in a furnace preheated at $T_c = 1050$ or 1200°C for crystal growth during 2 h. All furnaces were preheated at the corresponding nucleation and crystal growth temperatures in order to avoid embarrassing crystallization phenomena that can occur during a slow heating or cooling of samples between T_g and T_{liq} . The opaque glass-ceramics obtained were then directly annealed at 775°C for 2h (**Figure 51**). After cooling, the samples were cut in order to isolate the bulk from the surface to study separately by XRD, SEM and EDX the nature and the structure of phases crystallizing in their bulk and near their surface.

After cutting, a difference was observed visually between bulk and surface. A crystallized surface layer with a thickness depending on T_c (**Figure 52**) grown inward from the surface (heterogeneous crystallization) and was clearly different from the bulk (internal crystallization). For instance at $T_c=1200^\circ\text{C}$, the thickness of the crystallized layer was about $900\ \mu\text{m}$ and decreased to $200\ \mu\text{m}$ at $T_c=1050^\circ\text{C}$. XRD and SEM studies confirmed that different crystalline phases nucleated and grown in the bulk and from glass samples surface. The XRD patterns recorded for the bulk and the surface layer separated after cutting are shown in **Figure 53**, for glass A heat treated at $T_c=1200^\circ\text{C}$. For the two parent glasses, zirconolite was the only crystalline phase nucleating and growing in the bulk for $T_c=1000$ and 1200°C . However, crystallization of titanite (CaTiSiO_5) and anorthite (nominally $\text{CaAl}_2\text{Si}_2\text{O}_8$) occurred near sample surface for these two temperatures. Small crystals of baddeleyite (nominally ZrO_2) were also observed near sample surface at $T_c=1200^\circ\text{C}$. The contribution of residual glass to the XRD pattern (presence of a broad diffusion at low angle on the pattern, as in **Figure 53a**) was still important for the bulk (**Figure 53c**) whereas crystallization was stronger for the surface layer (**Figure 53b**). These results are confirmed by SEM observations (**Figure 54**). For $T_c=1200^\circ\text{C}$, elongated zirconolite crystals grown in the bulk. However, for $T_c=1050^\circ\text{C}$ zirconolite crystals have a dendritic shape

(**Figure 53a**). Using EDX, it was possible to analyze the composition of the crystals formed in the bulk and near the surface at $T_c=1200^\circ\text{C}$ (the very fine microstructure of the zirconolite crystals formed at 1050°C prevented to perform accurate analysis of their composition by EDX):

- Glass A: zirconolite ($\text{Ca}_{0.97}\text{Zr}_{1.07}\text{Ti}_{1.90}\text{Al}_{0.06}\text{O}_7$) in the bulk; titanite ($\text{Ca}_{0.99}\text{Ti}_{0.78}\text{Zr}_{0.23}\text{Al}_{0.02}\text{Si}_{0.98}\text{O}_5$) and anorthite ($\text{Ca}_{0.78}\text{Na}_{0.17}\text{€}_{0.05}\text{Al}_{1.73}\text{Si}_{2.27}\text{O}_8$ where € represents calcium vacancies) in the crystallized layer.

- Glass B: zirconolite ($\text{Ca}_{0.82}\text{Nd}_{0.19}\text{Zr}_{1.05}\text{Ti}_{1.77}\text{Al}_{0.17}\text{O}_7$) in the bulk; titanite ($\text{Ca}_{0.89}\text{Nd}_{0.11}\text{Ti}_{0.69}\text{Zr}_{0.22}\text{Al}_{0.11}\text{Si}_{0.98}\text{O}_5$), anorthite ($\text{Ca}_{0.77}\text{Na}_{0.19}\text{€}_{0.04}\text{Al}_{1.73}\text{Si}_{2.27}\text{O}_8$) and baddeleyite ($\text{Zr}_{0.93}\text{Ti}_{0.07}\text{O}_2$) in the crystallized layer.

These results show that Nd^{3+} ions enter preferentially into the calcium site of zirconolite crystals (in the bulk of the glass-ceramics) and the calcium site of titanite crystals (in the surface crystallized layer). For these two crystalline phases, the charge compensation was ensured by the simultaneous incorporation of Al^{3+} ions in titanium sites. Consequently for glass B, the charge compensation scheme (1) is more efficient to enable incorporation of neodymium into zirconolite than scheme (3) by self-compensation. This preference was confirmed by spectroscopic studies. Thus for glass B heat treated at 1200°C , nearly 20% of the Ca site of zirconolite crystals are occupied by Nd, the charge compensation being insured by the partial substitution of Ti^{4+} ions by Al^{3+} ions as in ceramics (see §IVB.3.).

Moreover, EDX results indicate that titanite is the only crystalline phase of the crystallized layer that incorporates neodymium, but to a less extent than zirconolite. We can consider that the presence of titanite near the surface of the glass ceramic is not a serious problem for the application envisaged here. Indeed, we saw in §III.B.3.b that titanite-based glass-ceramics were envisaged by Canadians to incorporate HLW solutions and titanite is known to be a good actinide-host phase [94]. It appears that Ln^{3+} ions are only incorporated in the calcium site of the titanite structure (there is only one type of calcium site in this structure and this site is 7-fold coordinated with oxygen anions [255]) because the tetrahedral silicon and the octahedral titanium sites are too small. This result is in agreement with the results of Higgins et al. for natural titanite samples [256]. In our glass-ceramic samples, the positive charge excess due to Ln^{3+} ions

incorporation in the calcium site of titanite is compensated by the simultaneous incorporation of Al^{3+} ions probably both in the titanium and silicon sites.

EDX results also showed that neodymium did not enter into the anorthite crystals. Anorthite has a totally polymerized (tri-dimensional silicate) structure constituted of SiO_4 and AlO_4 tetrahedra without non-bridging oxygen atoms [257]. This compact structure could explain the difficulty to incorporate neodymium in anorthite. Moreover, the lack of heavy elements in anorthite crystals explains why they appear as black crystals on the back-scattered SEM images (**Figure 54d**). EDX also showed that for A and B compositions, nearly 20 % of the calcium sites of the anorthite crystals (nominal composition $\text{CaAl}_2\text{Si}_2\text{O}_8$) were occupied by sodium ions. Therefore, this silicate phase must be more rigorously called plagioclase rather than anorthite [257]. However, for practical reasons, we will continue to use the name anorthite for this phase in this chapter. It is interesting to notice that this phase was the only crystalline phase to incorporate Na^+ ions in our glass-ceramics.

Area integration of zirconolite crystals in SEM images (**Figure 54c**) indicated that no more than 13 vol% zirconolite formed in the bulk of glass B at $T_c=1200^\circ\text{C}$. This value is lower than the one calculated by assuming that all ZrO_2 of parent glass was used to form crystals (17 vol%) because a part of ZrO_2 remains in residual glass as shown by EDX (SiO_2 (46.59), Al_2O_3 (13.38), CaO (20.26), TiO_2 (8.53), ZrO_2 (4.22), Nd_2O_3 (5.84), Na_2O (1.14) in wt%). In order to increase the amount of zirconolite crystals formed in the bulk of the glass-ceramics and the concentration of neodymium in these crystals, both parent glass composition and crystallization conditions (temperature and duration of crystal growth) were modified (see § IV.C.2.d,e).

The crystallization of glass B was also followed by DTA. This technique is classically used to study glass crystallization processes (which occur in the bulk and from the surface during heating, exothermic effects) and crystals melting (endothermic effects). In order to investigate nucleation mechanisms (surface/bulk) occurring during heating of glass B, the as quenched glass was crushed and sieved to obtain four different particle size fractions (<20, 125-250, 400-800, 1600-2000 μm). A massive sample was also studied. In this last case, the number of surface crystallization sites was minimal. **Figure 55** indicates a strong evolution of the position and width of exothermal effects C1, C2 and C3

when the particle size increases. In order to attribute the main exothermic effects observed on the DTA curves, 200 to 400 mg of as quenched glass B with same particle size were heated (at the same heating rate) at the corresponding temperatures in a classical furnace and were then quenched to room temperature. The partially devitrified samples obtained were then characterized by XRD. Details results of this study are reported in [258]. The main conclusions of this DTA study are the following:

- The most intense exothermic peaks C2 and C3 are respectively due to titanite and anorthite crystallization from sample surface after heterogeneous nucleation. The crystallization sequence observed during heating (1st-titanite and 2nd-anorthite) seems to indicate that anorthite begins to grow in the residual glass remaining between the elongated titanite crystals. The activation energy E_c associated with crystal growth of titanite and anorthite (493 and 405 kJ.mol⁻¹ respectively) were determined using the Kissinger or Ozawa methods [258,259].
- The small and broad exothermic effect C1 is not due neither to titanite nor to anorthite crystallization. It is more probably associated with zirconolite crystallization from sample surface. The low crystal growth rate of zirconolite $u(Z)$ in comparison with titanite and anorthite phases, respectively $u(T)$ and $u(A)$ (see below), may explain the weak amount of zirconolite formed in the surface crystalline layer [258]. It is important to underline that no thermal effect associated with crystallization events in the bulk of the glass was detected by DTA for glass B even for the massive sample. This is due to the low zirconolite nucleation and crystal growth rates in glass bulk for this composition in comparison with the ones of silicate phases growing from surface [260]. Thus, during DTA runs, the energy evolved by zirconolite crystallization in the bulk was too weak to be detected. The endothermic effects observed near 1260°C are associated with the melting of titanite and anorthite crystals.

For glass B, two other methods (without nucleation step at 810°C) were used to study the crystallization tendency of undercooled melt. The results obtained are widely detailed in [20] and show that for $T \geq 1050^\circ\text{C}$, zirconolite can nucleate heterogeneously on samples surface (**Figure 56b**) or on sporadic sites probably preexisting in the melt (**Figure 56a**). Thus, for $T \geq 1050^\circ\text{C}$, $I_Z^{\text{hom}}(T) \approx 0$ and $I_Z^{\text{het}}(T) \gg I_Z^{\text{hom}}(T)$, $I_Z^{\text{hom}}(T)$ and $I_Z^{\text{het}}(T)$ being respectively the zirconolite homogeneous and heterogeneous nucleation rates at T in composition B. This

result is in agreement with the nucleation rate curve of zirconolite in the bulk (homogeneous nucleation) shown **Figure 50**. Consequently, in these conditions (i.e. without nucleation step), the number of zirconolite crystals in the bulk is low and crystals are big (**Figure 56a**). Such methods are thus not efficient to prepare zirconolite-based glass-ceramic waste forms. The small size of the zirconolite crystals obtained using nucleation and crystal growth steps from glass samples (**Figure 49**) is more adapted to MA immobilization because it will reduce the risks of microfracturation of the waste form under α self-irradiation. (see §III.B.3.c.). Another interesting result of this study, is that for $T \geq 1050^\circ\text{C}$: $I_Z^{\text{het}}(T) \gg I_S^{\text{het}}(T), I_A^{\text{het}}(T) \approx 0$ ($I_S^{\text{het}}(T)$ and $I_A^{\text{het}}(T)$ being respectively the heterogeneous nucleation rates of titanite and anorthite at T) [20]. Indeed, neither titanite nor anorthite crystals were detected in the surface crystallized layer for $T \geq 1050^\circ\text{C}$ if the melt is transferred directly from 1550°C to T in a preheated furnace (**Figure 56b**). It was also shown that $I_S^{\text{het}}_{\text{max}} \gg I_Z^{\text{het}}_{\text{max}}$ and $I_A^{\text{het}}_{\text{max}} \gg I_Z^{\text{het}}_{\text{max}}$ where the subscript max refers to the maximum nucleation rates [20]. This last result indicates that the heterogeneous nucleation of titanite and anorthite on surface may occur very quickly during melt quenching and/or during glass heating. It is likely to happen in a temperature range slightly higher than T_g , where nucleation rates are generally known to be the highest. This implies that even a short stay of the undercooled melt in the temperature range where $I_T^{\text{het}}(T)$ and $I_A^{\text{het}}(T)$ are very high would then induce a strong effect on the nature of the crystalline phases growing from the surface at T_c . This can be one of the reasons why zirconolite was not observed in the crystallized layer (**Figure 54b,d**) for the glass-ceramics samples prepared using the method shown **Figure 49**. Moreover, concerning the crystal growth rates of zirconolite (u_Z), titanite (u_S) and anorthite (u_A), it was also demonstrated that $u_S(T) > u_A(T) \gg u_Z(T)$ at least for $1050^\circ\text{C} \leq T_c \leq 1200^\circ\text{C}$ [20]. Consequently, in order to favor the crystallization of a high number of zirconolite crystals in the bulk of the samples it is absolutely necessary to perform a nucleation step. Then, during the crystal growth step, the growth of zirconolite crystals in the bulk will strongly limit the development of titanite and anorthite from the surface towards the bulk of the samples.

IV.C.2.c Stability of glass-ceramics after prolonged heating at 1050 or 1200°C

The evolution at high temperature (1050°C or 1200°C) of the nature of the crystalline phases formed in the bulk and near the surface of the glass-ceramics prepared following the method described in **Figure 49** are reported in **Table XXIV** for different thermal treatment durations (2-300h) at $T_c=1050^\circ\text{C}$ and 1200°C . At 1200°C , these results clearly showed that titanite crystals, occurring initially in a thin crystallized layer near sample surface after 2 h thermal treatment (**Figure 54d**), have grown towards the bulk at the expense of zirconolite which almost totally disappeared (**Figure 57a**). This indicated that the zirconolite crystals formed initially in the bulk (**Figure 54c**) were unstable with respect to titanite and anorthite in the presence of the silica excess of the residual glass at $T_c=1200^\circ\text{C}$. Thus, at high temperature and for long duration heat treatments, titanite crystals grown from the surface towards the bulk leading to progressive disappearance of zirconolite crystals. In this case, the excess of ZrO_2 (which is only partially incorporated in the titanite crystals, see EDX results above) precipitated as baddeleyite crystals in the residual glass (**Figure 57a**). The same phenomena could explain the origin of the baddeleyite crystals observed above in the surface crystallized layer ($T_c=1200^\circ\text{C}$, **Figure 54d**). The growth of titanite at the expense of zirconolite could be explained by the existence of a competition between these two phases to incorporate Ti, as it is one of the main elements constituting these two crystalline phases. At 1050°C , the progress of titanite crystals towards the bulk became very slow in comparison with anorthite (**Figure 57b**). This can be due to the increase of melt viscosity at 1050°C , slowing down diffusive processes in the undercooled melt. Even after 300 h at 1050°C , a high amount of zirconolite remained in the bulk [20].

Thus, the results obtained for glass B for different durations of heat treatment showed that the zirconolite crystals initially formed in the bulk were not stable. Indeed, titanite appears as the most stable phase incorporating Ti in this case. For kinetics reasons due to its relatively high homogeneous nucleation rate $I_Z^{\text{hom}}(T)$, zirconolite is the only crystalline phase which nucleates and grows in the bulk. However, studies performed by Vance et al. [261], mixing and firing (at 1280°C for 2 days) titanite and zirconolite phases (without other silica-rich phase), showed that these two phases were compatible. In our case (glass B), it is probably the occurrence of a silica-rich residual glass coexisting with zirconolite crystals which is at the origin of their instability in comparison with titanite

crystals that are able to incorporate silicon in their structure. In order to reduce the risks of progression of the titanite crystals from the surface of the glass at the expense of zirconolite crystals formed in the bulk, T_c must not be too high ($T_c < 1200^\circ\text{C}$) and the duration at this temperature must not exceed 20 h. It is very important to underline that if MA (≤ 10 wt. %) are incorporated in such glass-ceramics, the internal temperature of the waste form will never exceed 400°C during disposal. In this temperature range, zirconolite would remain kinetically stable and no long-term evolution of both the structure and microstructure of the glass-ceramics is expected ($T < T_g$).

IV.C.2.d Effect of crystal growth temperature on crystals structure and microstructure

For the glass-ceramics prepared from glass A using the method described **Figure 49**, a clear evolution of the zirconolite XRD patterns and lattice parameters was observed with T_c . **Figure 58a,b** shows that splitting of several XRD lines (35.5° , 42° and 59.5°) and intensity of low angle ($15\text{-}30^\circ 2\theta$) diffraction lines increase with T_c between 1000 and 1200°C . This evolution also exists for the glass-ceramics prepared from glass B but is less evident. The XRD pattern of a zirconolite ceramic sample prepared by solid state reaction is also shown in **Figure 58e** for comparison. It is very similar to the one recorded for the glass-ceramic prepared at $T_c = 1200^\circ\text{C}$ (**Figure 58a**). XRD patterns evolution with T_c can be explained by an ordering of Ca^{2+} and Zr^{4+} ions in (Ca,Zr) planes (**Figure 36**) along with a lattice parameters variation. A confirmation of this hypothesis is given in **Figure 58c,d** in which calculated XRD patterns assuming either an order or a disorder in Ca and Zr sites occupancy, for the sample prepared at $T_c = 1000^\circ\text{C}$, are plotted. Comparison of the experimental and calculated patterns clearly shows that Ca^{2+} and Zr^{4+} ions are not ordered for $T_c = 1000^\circ\text{C}$. Moreover, it can be shown that for $T_c = 1200^\circ\text{C}$, the cationic ordering (organization of Ca^{2+} and Zr^{4+} rows) and the cell parameters get closer to the ones of zirconolite ceramic. This evolution of zirconolite structure in glass-ceramics with crystal growth temperature T_c is similar to the one reported by Vance et al. [226] for zirconolite ceramic ($\text{CaZrTi}_2\text{O}_7$) prepared at increasing temperature (from 600 to 1400°C) from an amorphous alkoxide precursor. These structural evolutions with T are due to the increase of thermal energy available for diffusion processes in zirconolite

crystals. Thus, the order in zirconolite (Ca,Zr) planes increases with T_c . Moreover, SAD and HRTEM studies of the zirconolite crystals formed in the two glass-ceramic samples ($T_c = 1000$ and 1200°C) shows that the density of extended defects in crystals decreases with T_c [262].

For parent glasses A and B, the effect of the crystal growth temperature T_c between 950 and 1350°C on both the microstructure of the glass-ceramics and the structure of the crystals formed in the bulk was studied. The results obtained for the two glasses were very similar and are summarized in **Figure 59**. The evolution of XRD patterns and SEM images of the bulk of the samples are shown respectively in **Figures 60 and 61**. For $1050^\circ \leq T_c \leq 1200^\circ\text{C}$, the results were already described in § IV.C.2.b. For $T_c > 1200^\circ\text{C}$, globular baddeleyite crystals form in the bulk of the glass at the expense of zirconolite (**Figure 61e,f**). At $T_c = 1250^\circ\text{C}$, isolated zirconolite and baddeleyite crystals coexist whereas, above $T_c = 1300^\circ\text{C}$, only scarce zirconolite crystals nucleate on the surface of ZrO_2 crystals by heterogeneous nucleation (**Figure 61f**). This results show that thermal treatments at $T_c > 1200^\circ\text{C}$ must be avoided in order to obtain zirconolite as the only crystalline phase in the bulk. For $T_c = 950^\circ\text{C}$, dendritic crystals have grown in the bulk of the glass (**Figure 61a**). XRD shows that these crystals consist of a mixture of zirconolite and fluorite-type phases [44]. However only one kind of crystal morphology is observed by SEM. For $T_c = 1000^\circ\text{C}$, no more crystals having the fluorite structure are detected by XRD but there is no significant microstructural evolution in comparison with the sample prepared at $T_c = 950^\circ\text{C}$ (**Figure 61b**). Therefore, it can be deduced that fluorite transforms totally into zirconolite between 950 and 1000°C for a 2h crystal growth stage. The fluorite-type phase probably corresponds to a highly cationic disordered zirconolite. Indeed, a structural relationship can be established between fluorite and zirconolite because this last phase can be described as a fluorite superstructure [203]. It is interesting to notice that the same sequence of crystallization has been reported for the preparation of zirconolite ceramic from an alkoxide precursor [226].

In order to elucidate the nature of the nuclei formed in the bulk during the nucleation step, complementary studies were performed on a sample obtained after nucleation thermal treatment of glass B at $T_N = 810^\circ\text{C}$ for 240 h. The sample was slightly opalescent and no surface crystallization was observed. XRD pattern

did not reveal any crystallisation. Nevertheless, TEM observations show that scarce dendritic crystals have nucleated and grown with a very low crystal growth rate in the bulk of the glass. Their diameter was about 300-400 nm. SAD showed that these dendritic crystals were fluorite-type single crystals (lattice parameter $a = 5.03 \text{ \AA} \pm 0.2 \text{ \AA}$). This result is not surprising because the same kind of microstructure was observed at $T_c=950^\circ\text{C}$ (**Figure 61a**) for which it was shown that the crystalline phase had mainly a fluorite structure. It seems reasonable to assume that fluorite (corresponding to a highly disordered form of zirconolite) nucleates homogeneously in the bulk of the glass. The fact that ordered zirconolite does not nucleate directly is in agreement with a general trend observed for the crystalline phases formed in glass-ceramics indicating that the lower the crystallization temperature, the more disordered the crystalline phases that form (increase of T_c facilitates the displacement of cations in crystals and thus structural ordering) [263]. It is interesting to notice that careful observations of the nucleated glass does not reveal any glass-in-glass phase separation which shows that nucleation occurs in an homogeneous glass. All these results seem to indicate that fluorite nucleation in glass B is homogeneous (i.e. the nature of the nuclei is similar to that of the crystals).

IV.C.2.e Effect of composition changes of parent glass on glass-ceramics characteristics

IV.C.2.e.1 Increase of (CaO, ZrO₂, TiO₂) concentration in parent glass

In order to increase the amount of zirconolite crystals in the bulk of the glass-ceramics, two parent glass compositions (C, D) derived from glass B were prepared (**Table XXV**). The relative molar ratios of SiO₂, Al₂O₃ and Na₂O were the same as for glass B. However, in order to increase the amount of zirconolite crystals in the bulk of the glass-ceramics, the concentrations of CaO, ZrO₂ and TiO₂ (the three oxides constituting zirconolite) were increased in parent glass composition. Glass C was prepared as glass B. However, because of the high amount of ZrO₂ in composition D, this glass was melted at 1650°C. The glass transformation temperatures were similar for glasses B, C and D. Glass-ceramics were prepared using the method described **Figure 49** at $T_c=1050^\circ\text{C}$ and 1200°C .

The XRD patterns recorded for the bulk of glass-ceramics B, C and D (not shown) indicated that zirconolite was the unique crystalline phase to form, independently on the composition of parent glass. Moreover, the zirconolite lattice parameters and the compositions determined by EDX ($T_c=1200^\circ\text{C}$) were very similar for the three samples [103]. SEM micrographs shown in **Figure 62** clearly indicated a strong and progressive increase of the degree of crystallinity of the glass-ceramics when ZrO_2 , TiO_2 and CaO concentrations were raised. SEM images analysis indicated that the amount of crystalline phase was approximately 9, 14 and 19 vol% respectively for the glass-ceramics B, C and D prepared at $T_c=1200^\circ\text{C}$. This result was confirmed by the monotonous increase of the intensity of the zirconolite XRD lines (**Figure 63a**). The dendritic microstructure of the zirconolite particles formed at $T_c=1050^\circ\text{C}$ in glass B (**Figure 62a**) became hardly to observe for glasses C and D (**Figure 62b,c**). For these two samples, the size of the zirconolite particles strongly decreased (≈ 100 nm) and their number strongly increased. A similar evolution between the three compositions was observed for the glasses heat-treated at $T_c=1200^\circ\text{C}$. These results clearly indicated that when the parent glass composition changed from B to D, the number of nuclei formed during the nucleation stage at $T_n=810^\circ\text{C}$ strongly increased. Consequently, the corresponding zirconolite nucleation rates at 810°C in the bulk I_{bulk} for the three glasses can be ranked in the following order: $I_{\text{bulk}}(\text{A}) < I_{\text{bulk}}(\text{B}) < I_{\text{bulk}}(\text{C})$. This evolution can be explained by an increase of the zirconolite crystallization driving force (corresponding to the free energy difference $|\Delta G_c|$ between the partially crystallized glass-ceramic and the undercooled melt) due to ZrO_2 , TiO_2 and CaO enrichment in the parent glass. Such glass compositions changes towards the composition of the crystallizing phase (zirconolite) are well known to raise $|\Delta G_c|$ [60]. The nucleation rate evolution observed could be also explained by a decrease of the nuclei-liquid interfacial energy σ and/or of the nucleation kinetic barrier (decrease of the activation energy associated with small distance diffusion near the surface of nuclei) [264].

The DTA curves of parent glasses B, C and D are shown in **Figure 64**. For glass A, we observe only broad exothermic effects that were attributed to the crystallization of titanite (C2) and anorthite (C3) from surface (**Figure 55**). The narrower exothermic effects F and Z detected for glasses C and D (**Figure 64**) can

be attributed respectively due to the crystallization of a fluorite-type phase (probably similar to the one detected in glass A heat treated at $T_c=950^\circ\text{C}$ (**Figure 60b**)) and to its reorganization (cationic ordering) into zirconolite structure at higher temperature. It can be noticed that the DTA peak Z associated with the transformation of fluorite into zirconolite occurs at T_p ranging from 1022°C (glass D) to 1029°C (glass C). These values are very similar to that reported by Vance et al. [226] for the same phase transformation for a zirconolite alkoxide precursor ($T_p=1025^\circ\text{C}$). Moreover the peaks F and Z do not significantly change (shape and position) for the different glass particle sizes [258]. This indicates that contrarily to titanite and anorthite, these peaks are associated with a crystallization process in the bulk. The fact that peak F is not detected for glass A and shifts to lower temperatures when we compare glasses C and D (**Figure 64**) can be explained by a higher nucleation rate – and consequently a higher crystallization rate - when the amounts of ZrO_2 , TiO_2 and CaO are increased, due to a higher zirconolite crystallization driving force. Thus, DTA study of glasses C and D confirms the crystallization in the bulk of a fluorite-type phase at relatively low temperature and its irreversible transformation by cationic ordering into zirconolite for $T>1000^\circ\text{C}$. Consequently, the following nucleation and crystallization sequence can be proposed with increasing temperature: glass \rightarrow homogeneous nucleation of a fluorite-type phase ($760^\circ\leq T\leq 830^\circ\text{C}$) \rightarrow crystal growth of the fluorite-type phase ($T<1000^\circ\text{C}$) \rightarrow transformation of the fluorite-type phase into zirconolite ($T\geq 1000^\circ\text{C}$).

Using EPR, it is possible to determine the percentage R of Nd^{3+} ions incorporated in the zirconolite crystalline phase formed in the bulk of the glass-ceramics. Indeed, Nd^{3+} ion ($4f^3$) can be used as a paramagnetic local probe, sensitive to the structure of its host phase. For instance, **Figure 65** shows the EPR spectra of neodymium in parent glass B, in the bulk of the corresponding glass-ceramic prepared at $T_c=1050^\circ\text{C}$ and in $\text{Ca}_{0,8}\text{Nd}_{0,2}\text{ZrTi}_{1,8}\text{Al}_{0,2}\text{O}_7$ ceramic sample prepared by solid state reaction. All ESR spectra are very broad and asymmetrical, which is characteristic of neodymium powder spectra [265] but are quite different for the different matrices. This indicates that neodymium environment strongly differs between these materials and that neodymium is an excellent local probe. The asymmetry of all the spectra indicates that Nd^{3+} ions are located in low symmetry sites. Details and results concerning Nd^{3+} spectra simulation in parent glass B and

glass-ceramics are reported in [266]. Concerning the bulk of glass-ceramic B, EPR signal can be simulated as a linear combination of two neodymium signals (**Figure 65b**): the first one corresponding to Nd^{3+} ions remaining in the residual glass whose spectrum is close to the one of the corresponding parent glass (**Figure 65a**), and the second one corresponding to neodymium incorporated in the zirconolite crystalline phase (**Figure 65c**). This interpretation was justified by the fact that the resulting spectrum, obtained after removing the glassy component (**Figure 65a**) from the glass-ceramic bulk spectrum (**Figure 65b**), is analogous to the spectrum of the neodymium-doped zirconolite ceramic (**Figure 65c**). A quantitative analysis of the ESR spectra of the bulk was then performed in order to estimate the amount of neodymium incorporated in zirconolite crystals. A partitioning ratio R equal to the molar percentage of neodymium incorporated in zirconolite can be calculated. As the double integral of ESR spectra is proportional to the quantity of probed paramagnetic ions (Nd^{3+}), R was calculated by dividing the double integral I_Z of the signal associated with zirconolite (isolated from the residual glass contribution as shown in **Figure 65b**) by the double integral I_{GC} of the global spectrum including residual glass and zirconolite contributions: $R = I_Z / I_{GC}$. Using this method for glass-ceramics B and D (**Figure 66**), the R values obtained for $T_c=1050^\circ\text{C}$ and 1200°C are shown in **Figure 63b**. A strong increase of the contribution of Nd^{3+} ions in the zirconolite phase was observed between glasses B and D. It clearly appears that R increases with the amount of zirconolite in glass-ceramic as expected from SEM results (**Figure 62**). For glass B, the decrease of R for the highest T_c value (1200°C) could be partly attributed to a decrease of the amount of crystals between the corresponding glass-ceramics. This can be associated with a higher solubility of zirconolite constituents in the melt when T_c increased. The difference between the R values for the two T_c temperatures was smaller for glass C and disappeared for glass D (**Figure 63b**). This shows that R evolution is mainly due to changes in the total amount of zirconolite between the samples (changing either T_c or glass composition). It is interesting to underline that approximately 43% of Nd^{3+} ions of the glass-ceramic D were incorporated in the zirconolite crystals in the bulk. For these ions, the glass-ceramic matrix thus acts as a double containment barrier.

IV.C.2.e.2 Other composition changes performed in order to try to increase zirconolite crystallization

Other changes were performed on the composition of glass B in order to try to increase the quantity of crystals formed in the bulk of the glass-ceramics. In this paragraph, we will briefly present several results concerning the effect on zirconolite crystallization of total or partial replacement of ZrO₂ by HfO₂ and of Al₂O₃ concentration in parent glass composition.

In §IV.B.3.b, we saw that it was possible to prepare (Zr,Hf)-zirconolite (CaZr_{1-x}Hf_xTi₂O₇, 0 < x ≤ 1) and Nd-doped Hf-zirconolite (Ca_{1-x}Nd_xHfTi_{2-x}Al_xO₇, 0 < x ≤ 0.2) ceramics. Moreover, these studies showed that the crystalline structure of Hf- and Zr-zirconolite ceramics were the same and that the different environments of Nd³⁺ ions in these two ceramics were similar. Consequently, it was interesting to try to substitute either totally or partially Zr by Hf in the parent glass composition, in order to prepared (Zr,Hf)-zirconolite-based glass-ceramics. Parent glasses derived from glass B and belonging to the SiO₂-Al₂O₃-CaO-TiO₂-(1-x)HfO₂-xZrO₂-Nd₂O₃ (0 ≤ x ≤ 1) system were prepared with x=0.5 (glass B(Hf0.5)) and x=0 (glass B(Hf1)) (**Table XXVI**). Thermal treatments performed at T_c=1050°C and 1200°C indicated that zirconolite-2M was the only phase to crystallize in the bulk of glasses B(Hf0.5) and B(Hf0). Similar structural and micro-structural evolutions as that of glass B were observed for these glass-ceramics when T_c increased. Moreover, a mixture of (titanite + anorthite) also formed a crystallized layer on samples surface. The composition of zirconolite crystals (T_c=1200°C) was determined by EPMA: Ca_{0.85}Nd_{0.21}Hf_{1.08}Ti_{1.71}Al_{0.18}O₇ (B(Hf0)) and Ca_{0.85}Nd_{0.20}Zr_{0.59}Hf_{0.49}Ti_{1.71}Al_{0.16}O₇ (B(Hf0.5)). These compositions are equivalent to the one of zirconolite crystals formed in glass B at T_c=1200°C and show that nearly the same amount of neodymium was incorporated in the crystals (Al³⁺ ions ensuring mainly charge compensation). For x=0.5, it appeared that the Zr amount in crystals ([Zr]/[Hf])=1.2) was higher than in parent glass ([Zr]/[Hf])=1) which could be explained by the slightly higher solubility of Hf in the undercooled melt in comparison with Zr [267]. However, **Figure 67** shows that zirconolite nucleation rate in glass B(Hf0) was very low in comparison with glass B (**Figure 54**). This was also true for glass B(Hf0.5). Nucleation rate curve of Hf-zirconolite in glass B(Hf0) was determined and can be compared to that of Zr-zirconolite in glass B (**Figure 68**). It clearly appears that the maximum of the

nucleation rate was displaced towards lower temperature for B(Hf0) and decreases by approximately 3 orders of magnitude. These strong differences between glasses containing Hf and Zr could be partly explained by the higher solubility of Hf in undercooled melt (decrease of the zirconolite crystallization driving force). Moreover, the mass difference between Zr ($91.2 \text{ g}\cdot\text{mol}^{-1}$) and Hf ($178.5 \text{ g}\cdot\text{mol}^{-1}$) could also slow down the diffusion of Hf^{4+} ions in the nucleation temperature range (increase of kinetic barrier). Consequently, the total or partial replacement of zirconium by hafnium in parent glass composition does not enable to obtain a higher amount of zirconolite in the bulk of glass-ceramics. Nevertheless, this kind of materials could be interesting for Pu immobilization because Hf is a neutron poison able to limit criticality risks as in Hf-zirconolite ceramics.

In order to study the effect of Al_2O_3 concentration in parent glass composition on the crystallization of zirconolite, two glasses derived from glass B (B(A11), B(A12)) were prepared by increasing or decreasing alumina content (**Table XXVI**). For $T_c=1050^\circ\text{C}$ and 1200°C , zirconolite crystallization in the bulk was suppressed in glass B(A12) whereas a crystallized layer made of only titanite crystals was formed on samples surface. The lack of zirconolite crystallization during heating could be explained by the increase of ZrO_2 and TiO_2 solubility in the undercooled melt B(A12), inducing the decrease of zirconolite crystallization driving force and nucleation rate. The hypothesis of an increase of ZrO_2 and TiO_2 solubility when Al_2O_3 concentration decreases can be explained by the increase of the amount of non-bridging oxygen anions (NBO) and of the amount of Ca^{2+} ions able to act as charge compensators in the structure of the glass and of the undercooled melt. As Ca^{2+} ions are known for their role of charge compensator of the negative charge excess of ZrO_x ($x\sim 6-7$) and TiO_y ($y\sim 5$) polyhedra, increasing the concentration of charge compensators would help Ti^{4+} and Zr^{4+} ions accommodation in the glass and undercooled melt structure. Indeed, Al^{3+} ions in silicate glasses are known to reduce the amount of NBO by associating with modifier cations such as Ca^{2+} cations (charge compensation of $(\text{AlO}_4)^-$ tetrahedra in the silicate network). Consequently, the amount of Ca^{2+} cations available to compensate ZrO_x and TiO_y polyhedra would decrease when Al_2O_3 concentration increases in parent glass composition. For glass B(A11) heat treated at $T_c=1050^\circ\text{C}$, zirconolite remained the only crystalline phase in bulk but its

nucleation rate strongly increased in comparison with glass B (**Figure 69**). This strong evolution is in agreement with the previous considerations about the effect of Al_2O_3 on zirconolite crystallization. A similar effect of Al_2O_3 concentration on apatite crystallization was observed recently in rare-earth rich borosilicate glasses [11]. For glass B(A11) ($T_c=1050^\circ\text{C}$), the molar percentage R of neodymium incorporated in zirconolite reached approximately 40 % at 1050°C as shown by EPR. However for this glass, a mixture of zirconolite ($\text{Ca}_{0.82}\text{Nd}_{0.19}\text{Zr}_{1.04}\text{Ti}_{1.78}\text{Al}_{0.17}\text{O}_7$) and anorthite (growing from glass surface) crystallized in the bulk of the sample at $T_c=1200^\circ\text{C}$. The proportion of anorthite crystals in the bulk of the glass-ceramic at 1200°C can be reduced by increasing sample size and/or by decreasing crystal growth duration. The fact that Al_2O_3 is one of the main component of anorthite (nominally $\text{CaAl}_2\text{Si}_2\text{O}_8$) could explain the increase of its crystal growth rate between glasses B and B(A11). Similarly, the nucleation rate of Hf-zirconolite in the bulk was strongly increased when Al_2O_3 concentration was raised in parent glass B(Hf0).

Consequently, for the glass composition studied in this work (glass B), the amount of zirconolite crystals in the bulk, their nucleation rate and the percentage of neodymium incorporated in the zirconolite phase can be increased by increasing either Al_2O_3 or $(\text{CaO}+\text{ZrO}_2+\text{TiO}_2)$ concentrations in parent glass.

IV.C.2.f Effect of Nd_2O_3 concentration and of the nature of MA surrogate

Parent glasses with various Nd_2O_3 contents ranging from 0.5 to 10 wt% were prepared by adding Nd_2O_3 to glass A, keeping constant the relative proportions of all other oxides. All glasses were prepared as glass A and glass-ceramics were prepared as described in **Figure 49** with a crystal growth step at $T_c=1050^\circ\text{C}$ or 1200°C . As for glass A, different crystallization processes occurred near the surface and in the bulk of the samples, irrespective of their neodymium content. For $T_c=1050^\circ\text{C}$ or 1200°C only zirconolite crystals form in the bulk of glass-ceramics. Although Nd_2O_3 content has no effect on the nature of the crystalline phases, its addition to the parent glass affects the nucleation rate of zirconolite. For instance, **Figure 70** shows SEM micrographs of the glass-ceramics containing 0, 4, 8 and 10 wt% Nd_2O_3 prepared at 1050°C . This figure clearly indicates that the nucleation rate of zirconolite crystals decreases with increasing Nd_2O_3 concentration. This result confirms the fact that Nd^{3+} ion does not act as a

nucleating agent for zirconolite crystallization in our glasses (§IV.C.2.a).

The decrease of zirconolite nucleation rate could be due to the increase of the kinetic activation barrier (controlled by diffusion processes) of zirconolite nucleation. Indeed, as neodymium does not play a driving role in the crystallization processes of zirconolite, it could induce diffusion difficulties in undercooled melts during nucleation. However, this evolution could also be explained -for unclear reasons- by thermodynamic considerations leading to an increase of the thermodynamic activation barrier: the introduction of neodymium in the parent glass could increase the crystal-melt interfacial energy and/or decrease the crystallization driving force.

The composition of the zirconolite crystals formed in the bulk for $T_c=1200^\circ\text{C}$ was determined by EDX for all the glass-ceramics containing various Nd_2O_3 contents (**Table XXVII**). A monotonous increase of neodymium concentration is observed with increasing Nd_2O_3 total amount in the parent glass (**Figure 71**). The two charge compensation schemes (1) and (3) given in §IV.B.3.b for neodymium incorporation into zirconolite can operate: either in the calcium site of the structure with a charge compensation ensured by aluminum in titanium sites (scheme (1): $(\text{Nd}^{3+}, \text{Al}^{3+}) \Leftrightarrow (\text{Ca}^{2+}, \text{Ti}^{4+})$), or in both calcium and zirconium sites simultaneously (scheme (3): $(\text{Nd}^{3+}, \text{Nd}^{3+}) \Leftrightarrow (\text{Ca}^{2+}, \text{Zr}^{4+})$). From **Figure 71**, it can be inferred that below 4 wt% Nd_2O_3 in parent glass, scheme (1) is probably dominant. There are even more Al^{3+} ions than Nd^{3+} ions in the crystals. A part of Al^{3+} ions is likely to compensate the incorporation of a few Zr^{4+} ions in the calcium site (in **Table XXVII** it can be notice that there is more than one Zr^{4+} ion by zirconolite formula unit even for the composition without neodymium). For higher Nd_2O_3 content, aluminum cannot totally compensate the excess of positive charge due to neodymium in calcium site and a part of Nd^{3+} ions is probably incorporated following scheme (3).

The occurrence of Nd^{3+} ions in the zirconium site of zirconolite crystals (scheme (3)) was confirmed by optical absorption spectroscopy. **Figure 72** shows two examples of neodymium optical absorption spectra corresponding to the $^4\text{I}_{9/2} \rightarrow ^2\text{P}_{1/2}$ transition recorded at low temperature for the bulk of the glass-ceramics prepared at $T_c=1200^\circ\text{C}$ containing 4 and 10 wt% Nd_2O_3 . Glass-ceramic spectra can be simulated with the help of three Gaussian components centered at 22950 cm^{-1} , 23125 cm^{-1} and 23222 cm^{-1} . From the study of $\text{Ca}_{0.9}\text{Nd}_{0.1}\text{ZrTi}_{1.9}\text{Al}_{0.1}\text{O}_7$ and

$\text{Ca}_{0.95}\text{Nd}_{0.1}\text{Zr}_{0.95}\text{Ti}_2\text{O}_7$ zirconolite ceramics prepared by solid state reaction, the neodymium absorption lines at 22950 cm^{-1} and 23125 cm^{-1} were respectively attributed to the incorporation of neodymium in the calcium and zirconium site of zirconolite (see §IV.B.3.d.2). The broad absorption line at 23222 cm^{-1} corresponds to Nd^{3+} ions remaining in the residual glass embedding zirconolite crystals (contribution similar to the absorption spectrum of parent glass). If we consider $A(\text{Zr})$ and $A(\text{Ca})$, the respective areas of the optical absorption contributions due to the incorporation of Nd^{3+} ions in the zirconium and in the calcium site of zirconolite crystals, the $A(\text{Zr})/A(\text{Ca})$ ratio increases with Nd_2O_3 concentration (**Figure 73**). This figure shows that a small fraction of Nd^{3+} ions incorporates effectively in the zirconium site of zirconolite, likely following scheme (3), and shows that the relative amount of Nd^{3+} ions incorporated in the zirconium site increases with neodymium content in parent glass, in agreement with **Figure 71**.

Table XXVIII and **Figure 74** show that similarly to zirconolite in the bulk (**Figure 71**), the titanite crystals formed near sample surface in the crystallized layer incorporate increasing neodymium amounts with increasing Nd_2O_3 amount in parent glass. However, for titanite crystals the amount of aluminum was always sufficient to totally compensate the positive charge excess due to the Nd^{3+} ions incorporated in calcium site.

In order to extend the previous studies, other lanthanides (Ce, Nd, Eu, Gd, Yb) and a tetravalent actinide (Th) were introduced in parent glass A to prepare glass-ceramics. The results obtained are detailed in [242]. For Th and all the rare earths, zirconolite was the only crystalline phase nucleating and growing in the bulk of the glass after 2h thermal treatment at either 1050°C or 1200°C . However, the nature of the dopant has a strong effect on the nucleation rate I_Z of zirconolite crystals at 810°C : $I_Z(\text{Nd}) < I_Z(\text{Eu}) < I_Z(\text{Gd}) < I_Z(\text{Ce}) < I_Z(\text{Th}) < I_Z(\text{Yb})$. EDX analysis of the zirconolite crystals grown at 1200°C showed that the amount of lanthanide progressively increases with decreasing Ln^{3+} ion radius (**Figure 75**). Moreover, at least for the trivalent lanthanide cations smaller than Ce^{3+} ions, Ln^{3+} ions are incorporated both into the Ca and Zr sites (following respectively charge compensation schemes (1) and (3)). Indeed, comparison of the evolution of Ln^{3+} and Al^{3+} ions concentrations in **Figure 75** clearly shows that the difference between these two amounts increases from neodymium to ytterbium. Except for

the sample containing cerium, the concentration of Al^{3+} ions in zirconolite crystals was not sufficient to compensate the positive charge excess due to incorporation of Ln^{3+} ions following only scheme (1). A fraction of Ln^{3+} ions is thus incorporated following scheme (3). The smaller the lanthanide size, the higher the proportion of Ln^{3+} ions entering the Zr^{4+} sites following scheme (3). Concerning the thorium-doped glass-ceramic, it appeared that Th^{4+} ions were preferentially incorporated into the calcium site in agreement with Th-rich zirconolite natural samples [193,194] following the incorporation scheme (2) (see §IV.B.3.b), but its concentration in the crystals remained relatively low ($\text{Ca}_{0.90}\text{Th}_{0.09}\text{Zr}_{1.04}\text{Ti}_{1.77}\text{Al}_{0.20}\text{O}_7$).

IV.C.2.g. Zirconolite-based glass-ceramics and MA immobilization

In previous paragraphs it was shown that the basic glass-ceramic composition chosen for this study (glass A) was able to incorporate lanthanides (from Ce to Yb) and actinides (Th) with different cation radii without changing the nature of the crystals formed in the bulk. Moreover, it was possible to replace totally or partially Zr by Hf in the composition of the zirconolite crystals which could be interesting for the immobilization of Pu-rich wastes. In order to confirm the ability of zirconolite-based glass-ceramic matrices to incorporate Pu, ^{239}Pu -doped samples have been prepared and studied recently by Deschanel et al. [268,269]. However, for technical reasons, their glass-ceramic samples were prepared by controlled cooling from the melt. Nevertheless, a strong Pu enrichment was observed in the zirconolite crystals. All these results show that zirconolite-based glass-ceramic could accept wide waste composition variations.

Concerning the chemical durability of zirconolite-based glass-ceramics, leaching tests in aqueous solutions were conducted by CEA and ANSTO on glass-ceramic samples containing either neodymium or cerium as actinides surrogate [200,270]. It appeared that the initial dissolution rate r_0 of the glass-ceramics and of the corresponding parent glasses were similar but were an order of magnitude lower than that of borosilicate nuclear glasses and basaltic glasses. However, in static alteration conditions at 90°C (see §III), the glass-ceramic alteration rate $r(t)$ dropped by four orders of magnitude and $r(t) < 10^{-5} \text{g.m}^{-2}.\text{day}^{-1}$. This value is lower than that of borosilicate glasses ($r(t) < 10^{-4} \text{g.m}^{-2}.\text{day}^{-1}$) but higher than that of zirconolite ceramic ($r(t) < 10^{-6} \text{g.m}^{-2}.\text{day}^{-1}$) [200]. Moreover, the amount of altered

material for zirconolite-based glass-ceramics was two orders of magnitude lower than that of nuclear borosilicate glasses but only about one order of magnitude higher than that of zirconolite ceramic. Moreover, Martin et al. [271] showed that the long term release of actinide surrogates was governed mainly by the alteration of the residual glass remaining between zirconolite crystals in the bulk of glass-ceramics. In comparison with nuclear borosilicate glasses, the higher chemical durability of zirconolite-based glass-ceramics can be explained by the occurrence of ZrO_2 and TiO_2 , the lack of boron and the very small amount of sodium in residual glass (**Table XXIII**).

Concerning the stability of zirconolite in glass-ceramics, it appeared that zirconolite crystals were not thermodynamically stable in comparison with titanite crystals. However, for kinetics reasons due to its relatively high homogeneous nucleation rate, zirconolite was the only crystalline phase nucleating and growing in the bulk. It is important to underline that during disposal, the temperature in the bulk would never exceed $400^\circ C$ even with 10 wt% MA (Cm isotopes, that would be mainly responsible for the heating, represent less than 5 wt% of all MA, **Figure 3**). In this temperature range ($T < 400^\circ C$), zirconolite would remain kinetically stable and no long-term evolution of both the structure and microstructure of the glass-ceramics is expected ($T < T_g$).

Even if the zirconolite crystals of the glass-ceramics prepared from glass B at $T_c = 1200^\circ C$ can incorporate 0.19 Nd^{3+} ions by zirconolite formula unit ($Ca_{0.82}Nd_{0.19}Zr_{1.05}Ti_{1.77}Al_{0.17}O_7$), one of the main drawbacks of zirconolite-based glass-ceramics is the high quantity of MA surrogate remaining in residual glass. EPR results showed that only 24 and 36 % of all the neodymium of glass B was incorporated in the zirconolite phase for $T_c = 1200^\circ C$ and $1050^\circ C$ respectively. However, by increasing TiO_2 and ZrO_2 concentrations in glass B composition, we showed that it was possible to incorporate nearly 43% of all neodymium in the zirconolite phase (57 % of all Nd_2O_3 still remaining in the residual glass of glass-ceramics). Consequently, the main problem of the zirconolite-based glass-ceramics is that a great fraction of MA surrogate remains in the residual glass and will not benefit from a double containment barrier.

V. CONCLUSION

The rising demand for energy, the risks of losing oil and gas sources of procurement are among the main reasons of current and future nuclear energy development that will lead to increasing amounts of nuclear wastes. Even if countries such as United States and Canada envisage direct disposal of nuclear spent fuel in deep geological formations without reprocessing, other countries reprocess it to extract Pu and U for reuse in new fuel. Nevertheless, reprocessing generates highly radioactive liquid wastes (HLW) containing fission products and minor actinides that are immobilized today in borosilicate glassy matrices.

Minor actinides are long-lived α -emitting radionuclides that will be mainly responsible for the potential radiotoxicity of glass waste forms after 2-3 hundred years disposal. Moreover, several long-lived fission products such as ^{135}Cs may be very mobile in geological formation. To minimize the potential long-term impact on biosphere of these radionuclides, investigations are currently in progress in France on enhanced separation these long-lived radionuclides from HLW followed by their transmutation or their immobilization in specific host matrices more durable than current nuclear glasses.

Because of their amorphous structure, glass remains the best kind of conditioning for the broad spectrum of radioactive and non-radioactive elements occurring in non-separated wastes. Nevertheless, new specific single phase ceramic (zirconates, titanates, phosphates) and glass-ceramic waste forms more durable than nuclear glasses are under study to immobilize minor actinides and long-lived fission products. Ceramic waste form can be prepared by sintering using alkoxide or oxide routes whereas glass-ceramics can be prepared by controlled crystallization from the glassy state or from the melt.

The main conclusions that can be drawn from our studies on ceramic and glass-ceramic matrices developed for the conditioning of Cs (hollandite) and minor actinides (zirconolite, zirconolite-based glass-ceramic) are the following:

i. Among the different matrices envisaged to immobilize radioactive cesium, (Ba,Cs,M)-hollandites ($\text{Ba}_x\text{Cs}_y(\text{M},\text{Ti})_8\text{O}_{16}$; $x+y<2$; M: trivalent cation) appeared as the best candidates. Hollandite ceramics were prepared using oxide route for

different cations M of increasing size to evaluate the effect of composition on microstructure, structure and cesium incorporation. To reduce the risks of Cs vaporization during synthesis, calcined powders were sintered in air at moderate temperature (1200°C). This oxide route appeared as an alternative to the alkoxide route generally proposed to prepare hollandite waste form. For $y = 0$, single phase $Ba_x(M,Ti)_8O_{16}$ were obtained only for $M^{3+} = Al^{3+}, Cr^{3+}$ and Fe^{3+} . For Fe^{3+} and $y \neq 0$, all cesium was incorporated in hollandite and ceramic samples were well densified. The occurrence of Fe^{3+} ions in site B of hollandite structure facilitated Cs incorporation in tunnels. Mixed hollandite samples with $M^{3+}=Ga^{3+}+Al^{3+}$ and $M^{3+}=Fe^{3+}+Al^{3+}$ were also synthesized but the best results were obtained with iron. Indeed, the ceramic without aluminum was the best one in terms of density and cesium retention. ^{27}Al MQ-MAS-NMR of (Ba,Cs,Al)-hollandite showed that aluminum ions were located in distorted octahedral sites with at least three different kinds of local environment in spite the existence of only one kind of site B in the structure. These different environments are due to different numbers of barium and vacancies in the six next nearest positions of Al. Using Mössbauer spectroscopy, only two different Fe^{3+} environments were detected for hollandite samples with iron. The effect of external electron irradiation (simulating the β -irradiation of radioactive cesium) on hollandite samples followed by EPR showed that the same kinds of Ti^{3+} centers (E_1, E_2) and O_2^- (T_r) centers were always produced whatever hollandite composition, electron energy and fluence. The same paramagnetic defects (E_1, E_2, T_r) were generated in hollandite after γ -irradiation but with significantly smaller concentrations. Moreover, barium and oxygen displacements were detected by SAD, MAS-NMR and Mössbauer spectroscopy. A mechanism of formation of Ti^{3+} and O_2^- centers based on electron-hole creation and displacement of barium and oxygen ions was proposed. A maximum paramagnetic defect concentration of the order of 10^{18} cm^{-3} was obtained with our irradiation conditions (simulating the first 30 years of hollandite waste form storage and corresponding to about 40% of the dose that will receive hollandite during disposal) which is relatively low. However, the total concentration of defects can be higher if diamagnetic defects were also produced. As at the beginning of storage, the temperature in the bulk of radioactive Cs waste form will reach 300°C (5 wt% Cs_2O), the stability with temperature of paramagnetic centers was studied. It appeared that E_2, E_1 and T_r signals vanished

at 150, 300 and 350°C respectively and the formation of new signals E₃ and G₂ was observed. These two signals were assigned respectively to titanyl Ti³⁺ ions located at the surface of the crystals and probably clusters of O₂⁻ centers formed by migration in the bulk of the crystals. Therefore at 300°C all the defects would not be annealed and the formation of secondary defects (E₃ and G₂) clearly indicated that a part of the electrons and holes generated during irradiation were separated after annealing. However, because of their small concentrations, these defects will have probably no negative effect on the long term behavior of hollandite during disposal. However, it must be underlined that all these external irradiation experiments were performed with electron energy higher than 0.5 MeV which probably conducts to an overestimation of elastic collisions (Ba displacements). Moreover, to compare our results (with irradiation at room temperature + annealing) with real conditions at the beginning of disposal, it would be interesting to perform directly electron irradiation of hollandite at 300°C. Nevertheless, chemical durability tests indicated that electron irradiation did not significantly affect the capacity of hollandite to retain cesium.

ii. Among the different single phase ceramic matrices proposed for MA immobilization, zirconolite appeared as one of the best candidate because of its ability to accept both trivalent and tetravalent MA surrogates, its excellent chemical durability and self-radiation resistance (existence of very old natural analogues). Moreover, this phase can be prepared easily using either alkoxide or oxide routes. Using oxide route, we showed that Ca_{1-x}Nd_xZrTi_{2-x}Al_xO₇ zirconolite samples were almost single phase for x ≤ 0.6 (zirconolite-2M polytype). Nd was used to simulate trivalent MA. Rietveld refinement of XRD patterns indicated that Al³⁺ ions were preferentially incorporated in Ti(2) site (simultaneously with Nd³⁺ ions in Ca site). This result can be easily understood because Ti(2) sites constitute the closest cationic sites to Ca ones. So, Ti(2) occupation by Al³⁺ ions could be energetically favored, because it would ensure more efficiently the compensation charge necessary to the incorporation of Nd³⁺ ions into Ca sites. For x > 0.6, the formation of a new polytype (3O) of zirconolite was observed. In spite of the existence of only one Ca site in zirconolite-2M structure, the study of EPR and optical absorption spectra of Nd³⁺ ions in samples for x < 0.6 demonstrated that at least three slightly different environments of neodymium in Ca site were

observed. These different environments of neodymium were probably due to differences concerning their second neighbors. Indeed, structural data obtained by Rietveld refinement showed that the Nd^{3+} ions located in the Ca site had two Ti(2) splitted sites in their next nearest neighbourhood corresponding to four Ti(2) positions that are statistically occupied by Ti^{4+} or Al^{3+} ions (50 %) and vacancies (50 %). Consequently, it appeared that the environment of neodymium ions in the calcium site can vary from one site to another which could explain the different environments detected by EPR and optical absorption spectroscopy. Study by GIXAFS of $\text{Ca}_{0.8}\text{Nd}_{0.2}\text{ZrTi}_{1.8}\text{Al}_{0.2}\text{O}_7$ zirconolite samples externally irradiated at different doses by Pb^{3+} ions simulating heavy recoil nuclei showed that Nd was eight-fold coordinated by oxygen anions in all the samples, irrespective of their irradiation dose. Moreover these oxygen anions always occurred at the same mean distance as in non irradiated zirconolite. Thus, the local order around Nd was kept despite the amorphization of zirconolite structure. Only a broadening of the distribution of Nd-O distances occurred with the irradiation dose. The medium range order around Nd was much more sensitive to the irradiation dose. Above the critical dose of amorphization, no second shell contribution was detectable. This phenomenon could be attributed to an increase of the distribution of Nd-O-M (M=Ti,Al) angles between polyhedra caused by irradiation.

iii. Zirconolite-based glass-ceramics prepared by crystallization of parent glasses belonging to the $\text{SiO}_2\text{-Al}_2\text{O}_3\text{-CaO-TiO}_2\text{-ZrO}_2\text{-Nd}_2\text{O}_3$ system were studied as potential waste form for the specific immobilization of MA. Trivalent minor actinides were mainly simulated by neodymium. Structural study of parent glasses showed that contrary to Nd^{3+} ions, Zr^{4+} and Ti^{4+} ions occupied very similar sites in glass and in zirconolite which could predispose parent glass to zirconolite nucleation. Different methods were tested to prepare glass-ceramics but the most efficient one consisted in a two-step heat treatment of glass samples (nucleation at T_N + crystal growth at T_c) rather than controlled cooling of the melt. It appeared that different crystalline phases formed in the bulk and on the surface of glass samples. After internal nucleation and crystal growth, zirconolite was formed for $T_c \geq 1000^\circ\text{C}$ whereas a fluorite-type phase – corresponding to a highly cationic disordered zirconolite – grew for $T_c < 1000^\circ\text{C}$. At the same time, the crystallization of silicate phases (anorthite and titanite) after surface nucleation

and crystal growth towards the bulk was observed and formed a crystallized layer. For $1000 \leq T_c \leq 1200^\circ\text{C}$ zirconolite was the only crystalline phase formed in the bulk, whereas crystallization of ZrO_2 occurred for $T_c > 1200^\circ\text{C}$ at the expense of zirconolite. Consequently, the following nucleation and crystallization sequence was proposed with increasing temperature: glass \rightarrow homogeneous nucleation of a fluorite-type phase ($760^\circ \leq T \leq 830^\circ\text{C}$) \rightarrow crystal growth of the fluorite-type phase ($T < 1000^\circ\text{C}$) \rightarrow transformation of the fluorite-type phase into zirconolite ($T \geq 1000^\circ\text{C}$). Moreover, a decrease of disorder in the (Ca,Zr) planes of the zirconolite structure was observed with increasing T_c . Parent glass composition changes showed that when TiO_2 , ZrO_2 and CaO amounts increased, the zirconolite nucleation rate, the amount of zirconolite in the glass-ceramics and the percentage of Nd^{3+} ions incorporated in the zirconolite phase also increased. However, the composition of the zirconolite crystals remained almost constant ($\text{Ca}_{0.82}\text{Nd}_{0.19}\text{Zr}_{1.05}\text{Ti}_{1.77}\text{Al}_{0.17}\text{O}_7$, $T_c=1200^\circ\text{C}$). EDX results showed that Nd^{3+} ions entered preferentially into the calcium site of zirconolite crystals rather than in the zirconium site as confirmed by spectroscopic studies. The charge compensation was ensured by the simultaneous incorporation of Al^{3+} ions in titanium sites. Thus, for $T_c=1200^\circ\text{C}$, nearly 20% of the Ca site of zirconolite crystals were occupied by Nd. The study of the stability of zirconolite crystals in the undercooled melt showed that in the system studied in this work, zirconolite was not thermodynamically stable in comparison with titanite. However, for kinetics reasons zirconolite was the only crystalline phase that crystallized in the bulk. It is important to underline that during the disposal of waste forms envisaged for MA immobilization, the temperature in the bulk would never exceed 400°C even with 10 wt% MA. In these conditions zirconolite would remain kinetically stable and no long-term evolution of both the structure and microstructure of the glass-ceramics are expected ($T < T_g$). The study of crystallization of parent glasses with other rare earths or with thorium showed that zirconolite (2M-polytype) remained the only crystalline phase that formed in the bulk of glass-ceramics for $1000^\circ\text{C} \leq T_c \leq 1200^\circ\text{C}$. This result showed that the basic parent glass composition was very flexible against the fluctuations of waste composition without changing the nature of the crystals. Nevertheless, the charge and the ionic radius of the rare earth influenced the nucleation rate of zirconolite. However, the main problem of the zirconolite-based glass-ceramics studied in this work was that a great part of MA

surrogates remained in the residual glass. Indeed, for all the Nd-doped samples studied in our work, more than 50 % of Nd was not incorporated in zirconolite crystals even if TiO_2 and ZrO_2 contents were increased in parent glass. Consequently, the percentage of neodymium incorporated in zirconolite crystals remained too small to make realistic the use of such materials for the conditioning of actinides in comparison with more durable bulk zirconolite ceramic.

Acknowledgments

The studies presented in this chapter about hollandite, zirconolite and zirconolite-based glass-ceramics were performed with the financial support of CNRS, CEA and French Group NOMADE. We thank C. Fillet (CEA Marcoule, France) for fruitful discussions about zirconolite ceramics and zirconolite-based glass-ceramics. We are grateful to G. S. Esnouf (Ecole Polytechnique, France) for his help during irradiation of hollandite samples with the Van de Graaff accelerator and J. M. Costantini (CEA Saclay, France) for fruitful discussions on hollandite irradiation effects. L. Mazerolles is gratefully acknowledged for its collaboration for TEM and SAD studies. T. Charpentier (CEA Saclay, France) is particularly acknowledged for his collaboration on the study of hollandite by MAS-NMR. We thank C. Gervais (University Paris VI, France) for her collaboration on the study of glasses by MAS-NMR. F. Studer and N. Nguyen (CRISMAT, Caen, France) are particularly acknowledged for their collaboration on the study of iron in hollandite by Mössbauer spectroscopy. We thank O. Pinet (CEA Marcoule, France) for fruitful discussions on the immobilization of UMo wastes in glass composite waste forms.

REFERENCES

-
- [1] Guillaumont, R.; C. R. Chimie 2004 , 7, 1129-1134.
- [2] Pradel, P. L'énergie nucléaire du futur. Quelles recherches pour quels objectifs (CEA-DEN); Editions du Moniteur: Paris, France, 2005.
- [3] Patterson, J. P.; Parkes, P. In The nuclear fuel cycle, from ore to waste; Oxford Science Publications: Oxford, UK, 1996; pp138-160.
- [4] Bonin, B. Clefs CEA 2002, 46, 88-92.
- [5] Schapira, J. P. In Les déchets Nucléaires; Les Editions de Physique: Les Ulis, France, 1997; pp 3-24.
- [6] Lee, W. E.; Ojovan, M. I.; Stennett, M. C.; Hyatt, N. C. Adv. Appl. Ceram. 2006, 105, 3-12.
- [7] Donald, I. W.; Metcalfe, B. L.; Taylor, R. N. J. J. Mater. Science 1997, 32, 5851-5887.
- [8] Devezeaux de Lavergne, J-G.; Boullis, B. Clefs CEA 2006, 53, 36-42.
- [9] Bardez, I.; Caurant, D.; Dussossoy, J. L.; Loiseau, P.; Gervais, C.; Ribot, F.; Neuville, D. R.; Baffier, N.; Fillet, C. Nucl. Sci. Eng. 2006, 153, 272-284.
- [10] Bardez, I.; Caurant, D.; Dussossoy, J. L.; Loiseau, P.; Baffier, N.; Fillet, C. Mat. Res. Soc. Symp. Proc. 2004, 807, 157-162.
- [11] Bardez, I. PhD. thesis, University of Paris VI (France), 2004 [E-text].
pastel.paristech.org/bib/archive/00001075/01/th%C3%A8se_Isabelle_Bardez.pdf
- [12] Boullis, B.; Devezeaux de Lavergne, J-G. Clefs CEA 2006, 53, 19-25.
- [13] Do Quang, R.; Petitjean, V.; Hollebecque, F.; Pinet, O.; Flament, T.; Prod'homme, A. Conference: Waste Management 2003 Symposium, Tucson, AZ, [E-text]. *www.wmsym.org/abstracts/2003/pdfs/92.pdf*
- [14] Moncoyoux, J. P.; Nabot, J. P. Clefs CEA, 2002, 46, 56-60.
- [15] Jouan, A.; Jacquet-Francillon, N.; Moncoyoux, J. P. Verre. 1997, 4, 4-10.
- [16] Jouan, A. Proc. Int. Cong. Glass (Edinburgh, Scotland). 2001, vol.1, 286-291.
- [17] Madic, C.; Lecomte, M.; Baron, P.; Boullis, B. C. R. Physique 2002, 3, 797-811.
- [18] Fillet, C.; Advocat, T.; Bart, F.; Leturcq, G.; Rabiller, H. C. R. Chimie 2004, 7, 1165-1172.

-
- [19] Guy, C.; Audubert, F.; Lartigue, J-E.; Latrille, C.; Advocat, T.; Fillet, C. C. R. Physique 2002, 3, 827-837.
- [20] Caurant, D.; Majerus, O.; Loiseau, P.; Bardez, I.; Baffier, N.; Dussosoy, J. L. J. Nucl. Mater. 2006, (in press).
- [21] Loiseau, P.; Caurant, D.; Baffier, N.; Fillet, C. Verre 2001, 7, 8-16.
- [22] Nabot, J. P.; Sudreau, F. Clefs CEA 2006, 53, 89-95.
- [23] Dacheux, N.; Clavier, N.; Robisson, A-C.; Terra, O.; Audubert, F.; Lartigue, J-E.; Guy, C. C. R. Chimie 2004, 7, 1141-1152.
- [24] Boullis, B. Clefs CEA 2006, 53, 80-87.
- [25] Toulhoat, P.; Grambow, B.; Simoni, E. L'Act. Chim. 2005, 285-286, 41-53.
- [26] Direction de la Recherche (République Française). (2003). Stratégies et programmes des recherches sur la gestion des déchets radioactifs à haute activité et à vie longue [E-text]. www.recherche.gouv.fr/technologie/energie/conj2.pdf
- [27] Ojovan, M. I.; Lee, W. E. An introduction to nuclear waste immobilization; Elsevier B. V.: Amsterdam, The Netherlands, 2005.
- [28] Lefèvre, J. Les déchets nucléaires ; Eyrolles: Paris, France, 1986.
- [29] Maddrell, E. R.; Abratis, P. K. Mat. Res. Soc. Symp. Proc. 2004, 807, 261-266.
- [30] Hyatt, N. C.; Hriljac, J. A.; Choudhry, A.; Malpass, L.; Sheppard, G. P.; Maddrell, E. R. Mat. Res. Soc. Symp. Proc. 2004, 807, 359-364.
- [31] Vance, E. R.; Perera, D. S.; Moricca, S.; Aly, Z.; Begg, B. D. J. Nucl. Mater. 2005, 341, 93-96.
- [32] Coutures, J. P.; Fillet, C.; Blondiaux, G. L'Act. Chim. 2005, 285-286, 60-65.
- [33] Salvatores, M.; Zaetta, A. In Les déchets Nucléaires; Les Editions de Physique: Les Ulis, France, 1997; pp 93-121.
- [34] Boccaccini, A. R.; Bernardo, E.; Blain, L.; Boccaccini, D. N. J. Nucl. Mater. 2004, 327, 148-158.
- [35] Henry, N.; Deniard, P.; Jobic, S.; Brec, R.; Fillet, C.; Bart, F.; Grandjean, A.; Pinet, O. J. Non-Cryst. Solids 2004, 333, 199-205.
- [36] Crovisier, J-L.; Advocat, T.; Dussosoy, J-L. J. Nucl. Mater. 2003, 321, 91-109.
- [37] Techer, I.; Advocat, T.; Lancelot, J.; Liotard, J-M. J. Nucl. Mater. 2000, 282, 40-46.

-
- [38] Weber, W. J.; Ewing, R. C.; Angell, C. A.; Arnold, G. W.; Cormack, A. N.; Delaye, J. M.; Griscom, D. L.; Hobbs, L. W.; Navrotsky, A.; Price, D. L.; Marshall Stoneham, A.; Weinberg, M. C. *J. Mater. Res.* 1997, 12, 1946-1978.
- [39] Weber, W. J.; Ewing, R. C.; Catlow, C. R. A.; Diaz de la Rubia, T.; Hobbs, L. W.; Kinoshita, C.; Matzke, H.; Motta, A. T.; Nastasi, M.; Salje, E. K. H.; Vance, E. R.; Zinkle, S. J. *J. Mater. Res.* 1998, 13, 1434-1484.
- [40] Matzke, H.; Vernaz, E. *J. Nucl. Mater.* 1993, 201, 295-309.
- [41] Rebiscoul, D.; Frugier, P.; Gin, S.; Ayrat, A. *J. Nucl. Mater.* 2005, 342, 26-34.
- [42] Gin, S.; Godon, N.; Ribet, I.; Jollivet, P.; Minet, Y.; Frugier, P.; Vernaz, E.; Cavedon, J. M.; Bonin, B.; Do Quang, R. *Mat. Res. Soc. Symp. Proc.* 2004, 824, 327-332.
- [43] Loiseau, P.; Caurant, D.; Bardez, I.; Majerus, O.; Baffier, N.; Fillet, C. *Mat. Res. Soc. Symp. Proc.* 2003, 757, 281-287.
- [44] Loiseau P.; Caurant D.; Majerus O.; Baffier N.; Mazerolles L.; Fillet C. *Phys. Chem Glasses*, 2002, 43C, 195-200.
- [45] Lutze, W. In *Radioactive waste forms for the future*; North Holland: Amsterdam, The Netherlands, 1988; pp. 1-159.
- [46] Mysen, B. O.; Richet, P. *Silicate glasses and melts*; Elsevier: Amsterdam, The Netherlands, 2005.
- [47] Varshneya, A. K. *Fundamentals of Inorganic Glasses*; Academic Press: San Diego, CA, 1994.
- [48] Lopez, C. PhD. thesis, University of Paris XI (France), 2002.
- [49] Plodinec, M. *J. Non-Cryst. Solids.* 1986, 84, 206-214.
- [50] Ringwood, A. E.; Kesson, S. E.; Reeve, K. D.; Levins, D. M.; Ramm, E. J. In *Radioactive waste forms for the future*; North Holland: Amsterdam, The Netherlands, 1988; pp. 233-335.
- [51] Pacaud, F.; Fillet, C.; Jacquet-Francillon, N. *Mat. Res. Soc. Symp. Proc.* 1992, 257, 161-167.
- [52] Bardez, I.; Caurant, D.; Loiseau, P.; Baffier, N.; Dussossoy, J. L.; Gervais, C.; Ribot, F.; Neuville, D. R. *Phys. Chem. Glasses* 2005, 46, 320-329.
- [53] Vernaz, E. Y.; Dussossoy, J. L. *Appl. Geochem. Suppl.* 1992, 1, 13-22.

-
- [54] Ménard, O.; Advocat, T.; Ambrosi, J. P.; Michard, A. *Appl. Geochem.* 1998, 13, 105-126.
- [55] Jollivet, P.; Montanelli, T.; Vernaz, E. *Verre* 1997, 3, 11-21.
- [56] Vernaz, E. *Clefs CEA* 2002, 46, 81-84.
- [57] Ollier, N.; Boizot, B.; Reynard, B.; Ghaleb, D.; Petite, G. *J. Nucl. Mater.* 2005, 340, 209-213.
- [58] Perez, J. *Matériaux non cristallins et science du désordre*; Presses polytechniques et universitaires romandes: Lausanne, Switzerland, 2001.
- [59] Bouska, V.; Borovec, Z.; Cimbalnikova, A.; Kraus, I.; Lajcakova, A.; Pacesova, M. *Natural Glasses*; Ellis Horwood: Chichester, England, 1993.
- [60] James, P. F. In *Nucleation and Crystallization in Glasses*, *Advances in Ceramics* vol.4; The American Ceramic Society: Columbus, OH, 1982. pp 1-48.
- [61] Orlhac X., PhD thesis, University of Montpellier II (France), 1999.
- [62] Ewing R. C.; Lutze W. *Ceram. Int.* 1991, 17, 287-293.
- [63] Clarke D. R. *Ann. Rev. Mater. Sci.* 1983, 13, 191-218.
- [64] Reeve K. D. *J. Australian Ceram. Soc.* 1990, 26, 45-58.
- [65] Glasser F. P. *Br. Ceram. Trans. J.* 1985, 84, 1-8.
- [66] Harker. A. B. In *Radioactive waste forms for the future*; North Holland: Amsterdam, The Netherlands, 1988; pp 335-392.
- [67] McCarthy, G. J.; Pepin J. G.; Pfoertsch D. E.; Clarke D. R. *Ceramics in nuclear waste management*, *Proceedings of an international symposium*, Cincinnati, OH, 1979, pp 315-320.
- [68] Ringwood, A. E.; Kesson, S. E.; Ware, N. G.; Hibberson, W.O.; Major, A. *Nature* 1979, 278, 219-223.
- [69] Ringwood, A. E.; Kesson, S. E.; Ware, N. G.; Hibberson, W.O.; Major, A. *Geochem. J.* 1979, 13, 141-165.
- [70] Fielding, P. E., White, T. J. *J. Mater. Res.* 1987, 2, 387-414.
- [71] Vance, E. R.; Jostsons, A.; Day, R. A.; Ball, C. J.; Begg, B.D.; Angel, P. J. *Mat. Res. Soc. Symp. Proc.* 1996, 412, 41-47.
- [72] Ewing, R. C.; Weber, W. J.; Lutze, W. In *Disposal of Weapons Plutonium*, Kluwer Academic Publishers: Dordrecht, The Netherlands, 1996; pp 65-83.
- [73] Anderson, E. B.; Burakov, B. E. *Mat. Res. Soc. Symp. Proc.* 2004, 807, 207-212.
- [74] Gong, W. L.; Lutze, W.; Ewing, R. C. *J. Nucl. Mater.* 2000, 277, 239-249.

-
- [75] Burakov, B. E.; Yagovkina, M. A.; Zamoyanskaya, M. V.; Kitsay, A. A.; Garbuzov, V. M.; Anderson, E. B.; Pankov, A. S. *Mat. Res. Soc. Symp. Proc.* 2004, 807, 213-217.
- [76] Burakov, B.; Anderson, E.; Yagovkina, M.; Zamoryanskaya, M.; Nikolaeva, E. *J. Nucl. Science Technol.*, 2002, suppl. 3, 733-736.
- [77] Strachan, D. M.; Scheele, R. D.; Buck, E. C.; Icenhower, J. P.; Kozelisky, A. E.; Sell, R. L.; Elovich, R. J.; Buchmiller, W. C. *J. Nucl. Mater.* 2005, 345, 109-135.
- [78] Icenhower, J.P.; Strachan, D. M.; McGrail, B. P.; Scheele, R. D.; Rodriguez, E. A.; Steele, J. L.; Legore, V. L. *Amer. Mineral.* 2006, 91, 39-53.
- [79] Bart, F.; Leturcq, G.; Rabiller, H. *Environmental issues and waste management technologies in the ceramic and nuclear industry IX*, 2004, 155, 11-20.
- [80] McGlenn, P. J.; McLeod, T.; Leturcq, G.; Aly, Z.; Blackford, M. G.; Zhang, Z.; Li, H.; Lumpkin, G. R. *Mat. Res. Soc. Symp. Proc.* 807, 2004, 219-224.
- [81] Dacheux, N.; Thomas, A. C.; Brandel, V.; Genet, M. *J. Nucl. Mater.* 1998, 257, 108-117.
- [82] Blondiaux, G.; Fillet, C. *Clefs CEA* 2006, 53, 88.
- [83] Carpena, J.; Lacout, J-L. *L'Act. Chim.* 1997, 2, 3-9.
- [84] Soulet, S; Carpena, J.; Chaumont, J.; Kaitasov, O.; Ruault, M-O.; Krupa, J-C. *Nucl. Instrum. and Meth. Phys. Res. B*, 2001, 184, 383-390.
- [85] Clavier, N. ; Dacheux, N. ; Podor, R. ; Le Coustumer, P. *Mat. Res. Soc. Symp. Proc.* 2004, 802, 113-118.
- [86] Boatner, L. A.; Sales B. C. In *Radioactive waste forms for the future*. North Holland: Amsterdam, The Netherlands, 1988; pp 495-564.
- [87] Höland, W.; Beall, G. *Glass-ceramic technology*; The American Ceramic Society: Westerville, OH, 2002.
- [88] McMillan, P. W. *Glass-ceramics*; Academic Press: London, England, 1979.
- [89] Strnad, Z. *Glass-Ceramic Materials, Glass Science and Technology 8*; Elsevier: Amsterdam, The Netherlands, 1986.
- [90] Bergeron, C. G. In *Introduction to glass science*; Plenum Press: New York, NY, 1972; pp 173-197.
- [91] de Réaumur, M. *Mémoires de l'Académie Royale (France)*, 1739, 370-388.

-
- [92] Stookey, S. D. Explorations in Glass; The American Ceramic Society: Westerville, OH, 2000.
- [93] Dé, A. K.; Luckscheiter, B.; Lutze, W.; Malow, G.; Schiewer, E. Am. Ceram. Soc. Bull. 1976, 55, 500-503.
- [94] Hayward, P. J. In Radioactive waste forms for the future; North Holland: Amsterdam, The Netherlands, 1988; pp 427-493.
- [95] Hayward, P. J. Glass Technol. 1988, 29, 122-136.
- [96] Hayward, P. J. Mat. Res. Soc. Symp. Proc. 1985, 50, 355-362.
- [97] Hayward, P. J.; Vance, E. R.; Cann, C. D.; Mitchell, S. L. In Advances in Ceramics vol.8, The American Ceramic Society: Columbus, OH, 1984; pp 291-301.
- [98] Tait, J. C.; Hayward, P. J.; Rummens, H. E. C.; Wilkin, D. L. Phys. Chem. Glasses 1986, 27, 134-139.
- [99] DeLu Liu; Piercy, G. R.; Purdy, G. R.; Hayward, P. J. Phys. Chem. Glasses 1985, 26, 197-207.
- [100] Vance, E. R.; Hayward, P. J.; George, I. M. Phys. Chem. Glasses 1986, 27, 107-113.
- [101] Fillet, C.; Marillet, J.; Dussossoy, J. L.; Pacaud, F.; Jacquet-Francillon, N.; Phalippou, J. Ceram. Trans. 1997, 87, 531-539.
- [102] Advocat, T.; Fillet, C.; Marillet, J.; Leturcq, G.; Boubals, J. M.; Bonnetier, A. Mat. Res. Soc. Symp Proc. 1998, 506, 55-62.
- [103] Loiseau, P.; Caurant, D.; Majerus, O.; Baffier, N.; Fillet, C. J. Mater. Science 2003, 38, 843-852.
- [104] Loiseau, P.; Caurant, D.; Baffier, N.; Fillet, C. Phys. Chem. Glasses 2002, 43C, 201-206.
- [105] Wald, J. W.; Weber, W. J. In Advances in Ceramics Nuclear Waste Management vol. 8, The American Ceramic Society: Columbus, OH, 1984; pp 71-75.
- [106] O'Holleran, T. P.; Johnson, S. G.; Frank, S. M.; Meyer, M. K.; Noy, M.; Wood, E. L.; Knecht, D. A.; Vinjamuri, K.; Staples, B. A. Mat. Res. Soc. Symp. Proc. 1997, 465, 1251-1258.
- [107] Emsley, J. The elements; Clarendon Press: Oxford, England, 1991; pp 40-41.

-
- [108] LeGrand, M. PhD thesis, University of Paris VII (France), 1999.
- [109] Calas, G.; Le Grand, M.; Galoisy, L.; Ghaleb, D. J. Nucl. Mater. 2003, 322, 15-20.
- [110] Dozol, J. F.; Lamare, V. Clefs CEA 2002, 46, 28-31.
- [111] Carré, F.; Mathonnière, G. Clefs CEA 2002, 46, 40-47.
- [112] Shelby, J. E. Introduction to Glass Science and Technology; The Royal Society of Chemistry: Cambridge, UK, 2005; pp 38-39.
- [113] Carter, M. L.; Vance, E. R.; Mitchell, D. R. G.; Hanna, J. V.; Zhang, Z.; Loi, E. J. Mater. Res. 2002, 17, 2578-2589.
- [114] Whittle, K.R.; Lumpkin, G.R.; Ashbrook, S.E. Mat. Res. Soc. Symp. Proc. 2004, 824, 243-248.
- [115] Kesson, S. E.; White, T. J. Proc. R. Soc. Lond. A 1986, 405, 73-101.
- [116] Cheary, R. W. Materials Science Forum 1988, 27-28, 397-406.
- [117] Aubin, V.; Caurant, D.; Gourier, D.; Baffier, N.; Advocat, T.; Bart, F.; Leturcq, G.; Costantini, J-M. Mat. Res. Soc. Symp. Proc. 2004, 807, 315-320.
- [118] Aubin-Chevaldonnet, V.; Caurant, D.; Dannoux, A.; Gourier, D.; Charpentier, T.; Mazerolles, L.; Advocat, T. J. Nucl. Mater. (submitted)
- [119] Sala, S. PhD. thesis, University of Provence (France), 1995.
- [120] Aubin-Chevaldonnet, V. PhD. thesis, University of Paris VI (France), 2004 [E-text]. pastel.paristech.org/bib/archive/00001091/01/memoirethesefinal.pdf
- [121] Campayo, L. PhD. thesis, University of Limoges (France), 2003.
- [122] Browne, E.; Dairiki, J.M.; Doebler, R.E. Table of Isotopes; John Wiley: New York, NY, 1978.
- [123] Lide, D. R. Handbook of Chemistry and Physics, CRC Press: Boca Raton, FL, 1997.
- [124] Saito, M.; Apse, V.; Artisyuk, V.; Shmelev, A. J. Nucl. Sci. Technol. 2000, 37, 1024-1031.
- [125] Bursill, L. A. J. Solid State Chem. 1987, 69, 355-359.
- [126] Asfari, Z.; Bressot, C.; Vicens, J.; Hill, C.; Dozol, J. F.; Rouquette, H.; Eymard, S.; Lamare, V.; Tournois, B. Anal. Chem. 1995, 67, 3133-3139.
- [127] Bart, F.; Sunilhac, S.; Dussossoy, J. L.; Bonnetier, A.; Fillet, C. Ceram. Trans. 2001, 116 353-360.
- [128] Mesko, M. G.; Day, D. E.; Bunker, B. C. Waste Management 2000, 20, 271-278.

-
- [129] Beall, G. H.; Rittler, H. L. In *Nucleation and Crystallization in Glasses. Advances in Ceramics vol.4*; The American Ceramic Society: Columbus, OH, 1982; pp 301-312.
- [130] Hess, N. J.; Espinosa, F. J.; Conradson, S. D.; Weber, W. J. J. *Nucl. Mater.* 2000, 281, 22-33.
- [131] Roy, R.; Vance, E. R. *Mat. Res. Bull.* 1982, 1, 585-589.
- [132] Zandbergen, H. W.; Everstijn, P. L. A.; Mijlhoff, F. C.; Renes, G. H.; Ijdo, D. J. W. *Mat. Res. Bull.* 1987, 22, 431-438.
- [133] Cheary, R. W. *Acta Cryst. B* 1987, 43, 28-34.
- [134] Kesson, S. E.; White, T. J. *Proc. Roy. Soc. A* 1986, 408, 295-319.
- [135] Fortner, F.; Aase, S.; Reed, D. *Mat. Res. Soc. Symp. Proc.* 2002, 713, 527-533.
- [136] MacLaren, I.; Cirre, J.; Ponton, C. B. *J. Am. Ceram. Soc.* 1999, 82, 3242-3244.
- [137] Kesson, S. E. *Radioactive Waste Management and The Nuclear Fuel Cycle*, 1983, 4, 53-72.
- [138] Cheary, R. W. *Acta Cryst. B* 1986, 42, 229-236.
- [139] Aubin, V.; Studer, F.; Caurant, D.; Gourier, D.; Nguyen, N.; Ducouret, A.; Baffier, N. *Advocat, T. Conference Atalante 2004: Advances for future nuclear fuel cycles*, 21-24 June 2004, Nîmes (France).
- [140] Bart, F.; Rabiller, H.; Leturcq, G.; Rigaud, D. *Conference Atalante 2004: Advances for future nuclear fuel cycles*, 21-24 June 2004, Nîmes (France).
- [141] Leinekugel-Le-Cocq-Errien, A-Y. *PhD. thesis, University of Nantes (France)*, 2005.
- [142] Carter, M. L.; Vance, E. R.; Li, H. *Environmental issues and Waste management Technologies in the Ceramic and Nuclear Industry*, 2004, 9, 21-30.
- [143] Carter, M. L.; Vance, E. R.; Li, H. *Mat. Res. Soc. Symp. Proc.* 2004, 807, 249-254.
- [144] Shannon, R. D. *Acta Cryst. A* 1976, 32, 751-767.
- [145] Fanchon, E. *PhD thesis, University of Grenoble (France)*, 1987.

-
- [146] Hartman, J. S.; Vance, E. R.; Power, W. P.; Hanna, J. V. *J. Mater. Res.* 1998, 13, 22-27.
- [147] Cheary, R. W.; Thompson, R.; Watson, P. *Materials Science Forum* 1996, 228-231, 777-782.
- [148] Cheary, R. W.; Kwiatkowska, J. *J. Nucl. Mater.* 1984, 125, 236-243.
- [149] Cheary, R. W.; Squadrito, R. *Acta Cryst. A* 1992, 48, 15-27.
- [150] Cheary, R. W.; Squadrito, R. *Acta Cryst. B* 1989, 45, 205-212.
- [151] Fanchon, E.; Hodeau, J. L.; Vicat, J. *J. Solid State Chem.* 1991, 92, 88-100.
- [152] Whittle, K. R.; Ashbrook, S. E.; Redfern, S. A. T.; Lumpkin, G. R.; Atfield, J. P.; Dove, M.; Farnan, I. *Mat. Res. Soc. Symp. Proc.* 2004, 807, 339-344.
- [153] Zhang, J.; Burnham, C. W. *Amer. Mineral.* 1994, 79, 168-174.
- [154] Frydman, L.; Harwood, J. S. *J. Am. Chem. Soc.* 1995, 117, 5367-5368.
- [155] Aubin-Chevaldonnet, V.; Gourier, D.; Caurant, D.; Esnouf, S.; Charpentier, T.; Costantini, J. M. *J. Phys. Condens. Matter.* 2006, 18, 4007-4027 .
- [156] Gutlich, P.; Link, R.; Trautwein, A.; In *Mössbauer Spectroscopy and Transition Metal Chemistry*, Springer-Verlag: Berlin, Germany, 1978.
- [157] Platt, R. G. *Mineral. Mag.* 1994, 58, 49-57.
- [158] Mitchell, R.H.; Yakovenchuk, V. N.; Chakhmouradian, A. R.; Burns, P. C.; Pakhomovsky, Y. A. *Canadian Mineralogist* 2000, 38, 617-626.
- [159] Bursill, L.A.; Smith, D.J. *J. Solid State Chem.* 1987, 69, 343-354.
- [160] Weber, W. *J. Mat. Res. Soc. Symp. Proc.* 1985, 44, 671-678.
- [161] Ball, C.J.; Woolfrey, J.L. *J. Nucl. Mater.* 1983, 118, 159-164.
- [162] Barry, J.C.; Hutchinson, J.L.; Segall, R.L. *J. Mater. Science* 1983, 18, 1421-1425.
- [163] Knoll, G. F. *Radiation detection and measurement*; John Wiley: New York, NY, 2000.
- [164] Wertz, J. E.; Bolton, J. R. *Electron Spin Resonance. Elementary, Theory and Practical Applications*; Chapman and Hall: New York, NY, 1986.
- [165] Neuville, D. R.; Cormier, L.; Boizot, B.; Flank, A-M. *J. Non-Cryst. Solids* 2003, 323, 207-213.

-
- [166] Bataille, C. L'évaluation de la recherche sur la gestion des déchets nucléaires à haute activité-Tome II : Les déchets militaires; Rapport N° 179 de l'Assemblée Nationale (France), 1997-1998 [E-text]. www.senat.fr/rap/o97-179/o97-179.html
- [167] Boullis, B. In Les déchets Nucléaires; Les Editions de Physique: Les Ulis, France, 1997; pp 69-92.
- [168] Madic, C.; Hudson, M. J.; Liljenzin, J. O.; Glatz, J. P.; Nannicini, R.; Facchini, A.; Kolarik, Z.; Odoj R. New partitioning techniques for minor actinides. Nuclear science and technology. European Commission, report n°19149EN, 2000.
- [169] Dognon, J. P. Clefs CEA 1999, 42, 14-21.
- [170] Haire, R. G.; Stump, N. A. Mat. Res. Soc. Symp. 1997, 465, 39-46.
- [171] Liu, G. K.; Zhorin, V. V.; Antonio, M. R.; Li, S. T.; Williams, C. W.; Soderholm, L. J. Chem. Phys. 2000, 112, 1489-1496.
- [172] Lopez, C.; Deschanel, X.; Den Auwer, C.; Cachia, J-N.; Peugeot, S.; Bart, J-M. Physica Scripta 2005, 115, 342-346.
- [173] Cachia, J-N. PhD. thesis, University of Montpellier II (France), 2005.
- [174] Lopez, C.; Deschanel, X.; Bart, J- M.; Boubals, J. M.; Den Auwer, C.; Simoni, E. J. Nucl. Mater 2003, 312, 76-80.
- [175] Darab, J. G.; Li, H.; Schweiger, M. J.; Vienna, J. D.; Allen, P. G.; Bucher, J. J.; Edenstein, N. M.; Shuh, D. K. Plutonium Futures - The Science. Topical Conference on Plutonium and Actinides, Santa Fe (N M) August 25-27 (1997). Conference Transactions. pp 143-145.
- [176] Feng, X.; Li, H.; Li, L.; Darab, J. G.; Schweiger, M. J.; Vienna, J. D.; Bunker, B. C.; Allen, P. G.; Bucher, J. J.; Craig, I. M.; Edelstein, N. M.; Shuh, D. K.; Ewing, R. C.; Wang, L. M.; Vance, E. R. Ceram. Trans. 1999, 93, 409-419.
- [177] Petit-Maire, D. PhD thesis, University Paris VI (France), 1988.
- [178] Poirot, I. PhD thesis, University Paris VI (France), 1986.
- [179] Begg, B. D.; Vance, E. R.; Conradson, S. D. J. Alloys Compds 1998, 271-273, 221-226.
- [180] Krauskopf, K. B. Chem. Geol. 1986, 55, 323-336.
- [181] Strachan, D. M.; Scheele, R. D.; Kozelisky, A. K.; Sell, R. L.; Todd Schaefer, H.; O'Hara, M. J. C.; Brown, F.; Buchmiller, W. Mat. Res. Soc. Symp. Proc. 2002, 713, 461-468.

-
- [182] Sickafus, K. E.; Minervini, L.; Grimes, R. W.; Valdez, J. A.; Ishimau, M.; Li, F.; McClellan, K. J.; Hartmann, T. *Science*, 289, 748-751.
- [183] Smith, K. L.; Zhang, Z.; McGlenn, P.; Attard, D.; Li, H.; Lumpkin, G. R.; Colella, M.; McLeod, T.; Aly, Z.; Loi, E.; Leung, S.; Ridgway, M.; Weber, W. J.; Thevuthasan, S. *Mat. Res. Soc. Symp. Proc.* 2003, 757, 289-296.
- [184] Roberts, S. K., Bourcier, W. L., Shaw, H. F., *Radiochim. Acta*, 2000, 88, 539-543.
- [185] Burakov, B. E.; Anderson, E. B.; Zamoryanskaya, M. V.; Yagovkina, M. A.; Strykanova, E. E.; Nikolaeva, E. V. *Mat. Res. Soc. Symp. Proc.* 2001, 663, 307-313.
- [186] Burakov, B. E.; Anderson, E. B.; Zamoryanskaya, M. V.; Yagovkina, M. A.; Nikolaeva, E. V. *Mat. Res. Soc. Symp. Proc.* 2002, 713, 333-336.
- [187] Li, L.; Strachan, D. M.; Li, H.; Davis, L. L.; Qian, M. *Ceram. Trans.* 2000, 107, 131-138.
- [188] Li, L.; Li, H.; Qian, M.; Strachan, D. M. *J. Non-Cryst. Solids* 2001, 183, 237-245.
- [189] Meaker, T. F.; Peeler, D. K.; Marra, J. C.; Pareizs, J. M.; Ramsey, W. G. *Mat. Res. Soc. Symp. Proc.* 1997, 465, 1281-1286.
- [190] Meaker, T. F.; Ramsey, W. G.; Pareizs, J. M.; Karkaker, D. G. *Ceram. Trans.* 1996, 72, 409-417.
- [191] Gavarini, S.; Carrot, F.; Matzen, G.; Trocellier, P. *J. Non-Cryst. Solids* 2003, 332, 115-127.
- [192] Lumpkin, G. R. *J. Nucl. Mater.* 2001, 289, 136-166.
- [193] Hart, K. P.; Lumpkin, G. R.; Gieré, R.; Williams, C. T.; McGlenn, P. J.; Payne, T. E. *Radiochim. Acta* 1996, 74, 309-312.
- [194] Gieré, R.; Williams, C. T.; Lumpkin, G. R. *Schweiz. Mineral, Petrogr. Mitt.* 1998, 78, 433-459.
- [195] Lumpkin, G. R.; Ewing, R. C.; Chakoumakos, B.; Greegor, R. B. F.; Lytle, W.; Foltyn, E. M.; Clinard, F. W.; Boatner, L. A.; Abraham, M. M. *J. Mater. Res.* 1986, 1, 564-575.

-
- [196] Deschanel, X.; Broudic, V.; Jegou, C.; Peugeot, S.; Roudil, D.; Jorion, F.; Advocat, T. Conference Atalante 2004: Advances for future nuclear fuel cycles, 21-24 June 2004, Nîmes (France)
- [197] Farges, F.; Ewing, R. C.; Brown, G. E. *J. Mater. Res.* 1993, 8, 1983-1995.
- [198] Farges, F. *Amer. Mineral.* 1997, 82, 44-50.
- [199] Veiller, L.; Crocombette, J. P.; Ghaleb, D. J. *Nucl. Mater.* 2002, 306, 61-72.
- [200] Advocat, T.; McGlenn, P. J.; Fillet, C.; Leturcq, G.; Schuller, S.; Bonnetier, A.; Hart, K. *Mat. Res. Soc. Symp. Proc.* 2001, 663, 277-284.
- [201] Leturcq, G.; McGlenn, P. J.; Barbe, C.; Blackford, M. G.; Finnie, K. S. *Applied Geochem.* 2005, 20, 899-906.
- [202] Rossell, H. J. *J. Solid State Chem.* 1992, 99, 52-57.
- [203] Rossell, H. J. *Nature* 1980, 283, 282-283..
- [204] Gatehouse, B.; Gray, I. E.; Hill, R. J.; Rossell, H. J. *Acta Cryst. B* 1981, 37, 306-312.
- [205] Smith, K. L.; Lumpkin, G. R. In *Defect and Process in the Solid State: Geosciences Applications. The McLaren Volume.* Elsevier Science Publishers: Amsterdam, The Netherlands, 1993, pp 401-422.
- [206] Loiseau, P.; Caurant, D.; Baffier, N.; Fillet, C. *Mat. Res. Soc. Proc.* 2003, 757, 243-250.
- [207] Loiseau, P. PhD thesis, University of Paris VI (France), 2001.
- [208] Vance, E. R.; Hanna, J. V.; Hunter, B. A.; Begg, B. D.; Perera, D. S.; Li, H.; Zhang, Z-M. *Ceram. Trans.* 2003, 143, 313-320.
- [209] Vance, E. R.; Ball, C. J.; Day, R. A.; Smith, K. L.; Blackford, M. G.; Begg, B. D.; Angel, P. J. *J. Alloys Compds* 1994, 213-214, 406-409.
- [210] Begg, B. D.; Vance, E. R.; Day, R. A.; Hambley, M.; Conradson, S. D. *Mat. Res. Soc. Symp. Proc.* 1997, 465, 325-332.
- [211] Begg, B. D.; Day, R. A.; Brownscombe A. *Mat. Res. Soc. Symp. Proc.* 2001, 663, 259-266.
- [212] Haire, R. G.; Assefa, Z.; Stump, N.; *Mat. Res. Soc. Symp. Proc.* 1998, 506, 153-160.
- [213] Weber, W. J.; Wald, J. W.; Matzke, H. J. *Nucl. Mater.* 1986, 138, 196-209.
- [214] Balan, E.; Neuville, D. R.; Trocellier, P.; Fritsch, E.; Muller, J-P.; Calas, G. *American Mineralogist* 2001, 86, 1025-1033.

-
- [215] McCauley, R. A.; Hummel, F. A. *J. Solid State Chem.* 1980, 33, 99-105.
- [216] Swenson, D.; Nieh, T. G.; Fournelle, J. H. *Mat. Res. Soc. Symp. Proc.* 1996, 412, 337-344.
- [217] Putnam, R. L.; Navrotsky, A.; Woodfield, B. F.; Shapiro, J. L.; Stevens, R.; Boerio-Goates, J. *Mat. Res. Soc. Symp. Proc.* 1999, 556, 11-18.
- [218] Emsley, J. *The elements*; Clarendon Press: Oxford, 1991, pp 82-83, 220-221.
- [219] Hart, K. P.; Vance, E. R.; Stewart, M. W.; Weir, J.; Carter, M. L.; Hambley, M.; Brownscombe, A.; Day, R. A.; Leung, S.; Ball, C. J.; Ebbinghaus, B.; Gray, L.; Kan, T. *Mat. Res. Soc. Symp. Proc.* 1998, 506, 161-168.
- [220] Gieré, R.; Malmström, J.; Reusser, E.; Lumpkin, G. R.; Düggelin, M.; Mathys, D.; Guggenheim, R.; Günther, D. *Mat. Res. Soc. Symp. Proc.* 2001, 663, 267-275.
- [221] Lumpkin, G. R.; Smith, K. L.; Gieré, R. *Micron.* 1997, 28, 57-68.
- [222] Bellatreccia, F.; Della Ventura, G.; Caprilli, E.; Williams, C. T.; Parodi, G. *C. Mineral. Mag.* 1999, 63, 649-660.
- [223] Xu, H.; Wang, Y. *J. Nucl. Mater.* 2000, 279, 100-106.
- [224] Knyazev, O. A.; Stefanovsky, S. V.; Ioudinstev, S. V.; Nikonov, B. S.; Omelianenko, B. I.; Mokhov, A. V.; Yakushev, A. I. *Mat. Res. Soc. Symp. Proc.* 1997, 465, 401-408.
- [225] Vance, E. R.; Angel, P. J.; Begg, B. D.; Day, R. A. *Mat. Res. Soc. Symp. Proc.* 1994, 333, 293-298.
- [226] Vance, E. R.; Ball, C. J.; Blacford, M. G.; Cassidy, D. J.; Smith, K. L. *J. Nucl. Mater.* 1990, 175, 58-66.
- [227] Advocat, T.; Jorion, F.; Marcillat, T.; Leturcq, G.; Deschanel, X.; Boubals, J. M.; Bojat, L.; Nivet, P.; Peugeot, S. *Mat. Res. Soc. Symp. Proc.* 2004, 807, 267-272.
- [228] Laverov, N. P.; Yudin, S. V.; Lapina, M. I.; Stefanovsky, S. V.; Chae, S. C.; Ewing, R. C. *Mat. Res. Soc. Symp. Proc.* 2003, 757, 321-328.
- [229] Cheary, R. W. *J. Solid State Chem.* 1992, 98, 323-329.
- [230] Mazzi, F.; Munno, R. *Amer. Mineral.* 1983, 68, 262-276.
- [231] Lumpkin, G. R.; Smith, K. L.; Blackford, M. G. *J. Nucl. Mater.* 1995, 224, 31-42.

-
- [232] Blasse, G.; Grabmaier, B. C. *Luminescent Materials*; Springer-Verlag: Berlin, Germany, 1994.
- [233] Gatterer, K.; Pucker, G.; Jantscher, W.; Fritzer, H. P.; Arafa, S. J. *Non-Cryst. Solids* 1998, 231, 189-199.
- [234] Henderson, B.; Imbusch, G. F. *Optical Spectroscopy of Inorganic Solids*; Oxford Science Publications, Clarendon Press: Oxford, England, 1989.
- [235] Kushida, T. *Phys. Rev.* 1969, 185, 500-508.
- [236] Wang, S. X.; Lumpkin, G. R.; Wang, L. M.; Ewing, R. C. *Nucl. Instr. and Meth. B* 2000, 166-167, 293-298.
- [237] Laverov, N. P.; YudinsteV, S. V.; Yudinseva, T. S.; Stefanovsky, S. V.; Ewing, R. C.; Lian, J.; Utsunomiya, S. Wang, L. M. *Geology of Ore Deposits* 2003, 45, 423-451.
- [238] Brown, G. E.; Farges, F.; Calas, G. *Rev. Mineral.* 1995, 32, 317-410.
- [239] Caurant, D.; Gourier, D.; Demoncey, N.; Ronot, I.; Pham-Thi, M. *J. Appl. Phys.* 1995, 78, 876-892.
- [240] Rossell, H. J. *J. Solid State Chem.* 1992, 99, 38-51.
- [241] Kesson, S. E.; Sinclair, W. J.; Ringwood, A. E. *Nuclear and Chemical Waste Management*, 1983, 4, 259-265.
- [242] Loiseau, P.; Caurant, D.; Baffier, N.; Mazerolles, L.; Fillet, C. *J. Nucl. Mater.* 2004, 335, 14-32.
- [243] Caurant, D.; Bardez, I.; Loiseau, P.; Baffier, N. (to be published).
- [244] Conley, J. G.; Kelsey, P. V.; Miley, D. V. In *Advances in Ceramics* vol. 8, Nuclear waste management, The American Ceramic Society: Columbus, OH, 1984; pp 302-309.
- [245] Kong, P. C.; Reimann, G. A.; *J. Environn. Sci. Health*, 1997, A32, 1207-1223.
- [246] Reimann, G. A., Kong P. C., *Actinide Processing Methods and Materials*, Proceedings of an International Symposium of the 123rd Annual Meeting of Minerals, Metals and Materials Society, Minerals, Metals and Materials Society: Warrendale PA, 1994, pp 275-288.
- [247] Feng, X.; Hahn, W. K.; Gong, M.; Gong, W.; Wang, L. *Ceram. Trans.* 1996, 72, 123-134.
- [248] Lin, J-S. ; Shen, P. J. *Non-Cryst. Solids*, 1996, 204, 135-140.

-
- [249] Phase diagrams for ceramists; The American Ceramic Society: Columbus, OH, 1964; vol. 1, 219.
- [250] Duan, R-G.; Liang, K-M.; Gu, S-R. *J. Eur. Ceram. Soc.* 1998, 18, 1729-1735.
- [251] Loiseau, P.; Caurant, D.; Dardenne, K.; Mangold, S.; Denecke, M.; Rothe, J.; Baffier, N.; Fillet, Conference Atalante 2004: Advances for future nuclear fuel cycles, 21-24 June 2004, Nîmes (France).
- [252] Loiseau, P.; Caurant, D.; Bardez, I.; Baffier, N.; Gervais, C.; Fillet, C. (to be published)
- [253] Galois, L.; Pélegrin, E.; Arrio, M-A. ; Ildefonse, P.; Calas, G.; Ghaleb, D.; Fillet, C.; Pacaud, F. *J. Am. Ceram. Soc.* 1999, 82, 2219-2224.
- [254] Cormier, L.; Calas, G.; Gaskell, P. H. *J. Phys. Cond. Matter.* 1997, 9, 10129-10136.
- [255] Hughes, J. M.; Bloodaxe, E. S.; Hanchar, J. M.; Foord, E. E. *Am. Mineral.* 1997, 82, 512-516.
- [256] Higgins, J. H.; Ribbe, P. H. *Am. Mineral.* 1976, 61, 878-888.
- [257] Wells, A. F. *Structural Inorganic Chemistry*; Oxford University Press: London, England, 1962.
- [258] Loiseau, P. ; Caurant, D. ; Majerus, O. ; Baffier, N. ; Fillet, C. *J. Mater. Science*, 2003, 38, 853-864.
- [259] Matusita, K.; Sakka, S., *Bull. Inst. Chem. Res. Kyoto Univ.* 1981, 59, 159-171
- [260] Loiseau, P; Caurant, D; Majerus, O; Baffier, N; Fillet, C. *Mat. Res. Soc. Symp. Proc.* 2004, 807, 333-338.
- [261] Vance, E. R., Agrawa, D. K., *Nucl. Chem. Waste Manage.* 1982, 3, 229-234
- [262] Loiseau, P. ; Caurant, D.; Baffier, N.; Mazerolles, L.; Fillet, C. *Mat. Res. Soc. Symp. Proc.* 2001, 663, 179-187.
- [263] Stoch L. In *Glass-ceramic materials, fundamentals and applications*. Series of monographs on material science, engineering and technology; Mucchi Editore: Modena, Italy, 1997, pp 41-64.
- [264] Uhlmann D. R. In *Nucleation and Crystallization in Glasses*, *Advances in Ceramics vol.4*; The American Ceramic Society: Columbus, OH, 1982; pp 80-124.

-
- [265] Mehta, V.; Gourier, D.; Mansingh, A.; Dawar, A. L. *Solid State Comm.* 1999, 109, 513-517.
- [266] Loiseau, P.; Caurant, D.; Baffier, N.; Fillet, C. *Mat. Res. Soc. Symp. Proc.* 2001, 663, 169-177.
- [267] Ellison A. J., Hess P. C., *Contrib. Mineral. Petrol.* 1986, 94, 343-351.
- [268] Deschanel, X.; Advocat, T.; Marcillat, T.; Boubals, J-M.; Bojat, M. *Conference Materiaux 2002*, 21-25 October 2002, Tours (France).
- [269] Advocat, T.; Marcillat, T.; Deschanel, X.; Leturcq, G.; Jorion, F.; Rabiller, H.; Loiseau, P., Veiller, L., *CEA Atalante: Rapport Scientifique 2002*, Direction de l'énergie nucléaire, CEA-R-6800 (ISSN 0429-3460), 2002 ; pp 144-153.
- [270] McGlenn, P. J.; Advocat, T.; Loi, E. ; Leturcq, G.; Mestre, J. P. *Mat. Res. Soc. Symp. Proc.* 2001, 663, 249-258.
- [271] Martin, C.; Ribet, I.; Advocat, T. *Mat. Res. Soc. Symp. Proc.* 2002, 713, 405-410.
- [272] Cousi, C.; Bart, F.; Phalippou, J. J. *Phys IV France*, 2004, 118, 79-83.
- [273] Cousi, C. PhD thesis, University of Montpellier II (France), 2004.

Radionuclides	Half-life (years)
Short half-life FP (≤ 30 years)	
^{90}Sr	28
^{137}Cs	30
Long half-life FP (> 30 years)	
^{79}Se	70000
^{93}Zr	$1.5 \cdot 10^6$
^{99}Tc	$2.1 \cdot 10^5$
^{107}Pd	$6.5 \cdot 10^6$
^{126}Sn	10^5
^{129}I	$1.57 \cdot 10^7$
^{135}Cs	$2 \cdot 10^6$
^{151}Sm	93
MA	
^{237}Np	$2.14 \cdot 10^6$
^{241}Am	432.7
^{243}Am	7370
^{244}Cm	18.1
^{245}Cm	8500
^{246}Cm	4760

Table I. Half-life of several isotopes of minor actinides (MA) and fission products (FP) occurring in HLW solutions recovered after spent fuel reprocessing [5]. FP are β -emitters and MA are mainly α -emitters. Most of these radionuclides are also γ -emitters.

Radionuclide	Mobility in geological environment
⁹³ Zr	--
⁹⁹ Tc	+
¹²⁹ I	++
¹³⁵ Cs	++
U	-
Np	-
Pu	-
Am	--
Cm	--

Table II. Qualitative comparison of the mobility in geological environment of the main long-lived radionuclides occurring in HLW (+: high, ++: very high, -: low, --: very low) [26].

Chemical family	weight (kg/U)
Rare gas (Kr, Xe)	5.6
Alkalis (Cs, Rb)	3
Alkaline earths (Sr, Ba)	2.4
Rare earths	10.2
Transition metals (Mo, Zr, Tc)	7.7
Chalcogens (Se, Te)	0.5
Halogens (I, Br)	0.2
Noble metals (Ru, Rh, Pd)	3.9
Others (Ag, Cd, Sn, Sb...)	0.1

Table III. Main families of fission products occurring in nuclear spent fuels [12]. The values presented in this table correspond to that of UO_2 spent fuel enriched with 3.5% ^{235}U (burn-up 33 GWday.t^{-1} , 3 years after discharge) given in kg by ton of U before burning. It can be underline that rare earths (Y + lanthanides) constitute the most abundant family of fission products (in wt%).

Fission products (g.t⁻¹U)		Actinides (g.t⁻¹U)	
SeO ₂	77.04	UO ₂	192.90
Rb ₂ O	385.06	NpO ₂	473.30
SrO	988.24	PuO ₂	7.10
Y ₂ O ₃	587.15	AmO ₂	363.94
ZrO ₂	4870.98	CmO ₂	28.71
MoO ₃	5017.74	Additional elements and corrosion products (g.t⁻¹U)	
TcO ₂	1091.11	Na ₂ O	13499.56
RuO ₂	2846.43	Fe ₂ O ₃	8580.60
Rh	488.30	NiO	1221.70
Pd	1245.40	Cr ₂ O ₃	1490.73
Ag ₂ O	82.35	P ₂ O ₅	835.96
CdO	89.03	ZrO ₂	1350.90
In ₂ O ₃	1.80		
SnO ₂	64.99		
Sb ₂ O ₃	12.57		
TeO ₂	591.99		
Cs ₂ O	2804.76		
BaO	1750.69		
La ₂ O ₃	1417.92		
Ce ₂ O ₃	2747.58		
Pr ₂ O ₃	1300.20		
Nd ₂ O ₃	4672.37		
Pm ₂ O ₃	79.62		
Sm ₂ O ₃	923.30		
Eu ₂ O ₃	151.80		
Gd ₂ O ₃	87.74		
Tb ₂ O ₃	2.16		
Dy ₂ O ₃	1.04		

Table IV. Composition of the HLW solution recovered after the reprocessing of UOX1 spent fuel (UO₂ with 3.5% ²³⁵U, burn up 33 GWday.t⁻¹ in PWR, 4 years after discharge) by the Purex process [28]. Reprocessing was performed 3 years after spent fuel unloading. Concentrations are given in g/ton of U in fuel before burning. It can be notice that only very small fractions of U and Pu remain in HLW solution.

Fission products (g.t⁻¹U)		Actinides (g.t⁻¹U)	
SeO ₂	136	UO ₂	188.7
Rb ₂ O	672.3	NpO ₂	1038
SrO	1639	PuO ₂	14.41
Y ₂ O ₃	1015	AmO ₂	892.3
ZrO ₂	8645	CmO ₂	150.7
MoO ₃	8993	Additional elements and corrosion products (g.t⁻¹U)	
TcO ₂	1860	Na ₂ O	15116.9
RuO ₂	5323	Fe ₂ O ₃	8590.60
Rh	739.8	NiO	1221.70
Pd	2667	Cr ₂ O ₃	1490.73
Ag ₂ O	138.6	P ₂ O ₅	1519.93
CdO	215.9	ZrO ₂	1350.90
In ₂ O ₃	2.44		
SnO ₂	123.6		
Sb ₂ O ₃	20.51		
TeO ₂	1083		
Cs ₂ O	4837		
BaO	3543		
La ₂ O ₃	2523		
Ce ₂ O ₃	4921		
Pr ₂ O ₃	2309		
Nd ₂ O ₃	8429		
Pm ₂ O ₃	53.06		
Sm ₂ O ₃	1583		
Eu ₂ O ₃	318.5		
Gd ₂ O ₃	329.6		
Tb ₂ O ₃	4.17		
Dy ₂ O ₃	2.4		

Table V. Composition obtained by simulation of the HLW solution that would be recovered after the reprocessing of UOX3 spent fuel (UO₂ with 4.9% ²³⁵U, burn up 60 GWday.t⁻¹, 6 years after discharge) by the Purex process [11]. Concentrations are given in g/ton of U in fuel before burning.

Fuel	UOX1	UOX3
²³⁵ U	3.5 %	4.9 %
Burn-up	33 GWday/t	60 GWday/t
Time in reactor	3 years	~ 5 years
Reprocessing after	3 years	5 years
Vitrification after	4 years	6 years
Composition of spent fuel before reprocessing	U (955 Kg) Pu (10 Kg) MA (0.6 Kg) FP (34 Kg)	U (924 Kg) Pu (13 Kg) MA (1.8 Kg) FP (61 Kg)

Table VI. Comparison of UOX1 and UOX3 spent fuels. The composition of UOX3 spent fuel was obtained by simulation [11]. (MA: minor actinides, FP: fission products)

Oxides	wt%
Glass frit introduced with the calcine	
SiO ₂	45.12
Al ₂ O ₃	4.92
B ₂ O ₃	13.92
Na ₂ O	10.06
CaO	4.01
Li ₂ O	1.96
ZnO	2.49
ZrO ₂	1.01
Fission products	
ZrO ₂	1.70
SrO	0.34
Y ₂ O ₃	0.20
MoO ₃	1.75
TcO ₂	0.38
Ag ₂ O	0.03
CdO	0.03
SnO ₂	0.02
SeO ₂	0.03
TeO ₂	0.20
Rb ₂ O	0.13
Cs ₂ O	0.97
BaO	0.61
Ce ₂ O ₃	0.95
Pr ₂ O ₃	0.45
Nd ₂ O ₃	1.63
La ₂ O ₃	0.49
Pm ₂ O ₃	0.03
Sm ₂ O ₃	0.32
Eu ₂ O ₃	0.05
Gd ₂ O ₃	0.03
RuO ₂	0.99
Rh ₂ O ₃	0.17
Pd	0.43
Additional and corrosion products	
Fe ₂ O ₃	2.98
NiO	0.42
Cr ₂ O ₃	0.52
P ₂ O ₅	0.29
Actinides	
UO ₂	0.06
NpO ₂	0.17
PuO ₂	0.0025
AmO ₂	0.13
CmO ₂	0.01

Table VII. Composition of the R7T7 glass produced at La Hague (AVH process) for the immobilization of HLW solutions recovered after reprocessing of UOX1 spent fuel [48].

Name of the phase	Nominal composition	wt% in Synroc	Examples of waste incorporated
hollandite	$Ba_{1,2}(Al,Ti)_8O_{16}$	30	Cs, Rb, Ba
zirconolite	$CaZrTi_2O_7$	30	Ln, MA, U
perovskite	$CaTiO_3$	20	Ln, MA, U, Sr
titanium oxide	Ti_nO_{2n-1} ($n \geq 0$)	15	-
intermetallic alloys ^a	Ti + other alloys	5	Ru, Pd, Rh, Te, Mo, Tc

Table VIII. Nominal composition of the phases occurring in the Synroc-C ceramic waste form. The global composition of Synroc-C with HLW as proposed by Ringwood et al.[50] was (wt%): TiO_2 (57.0), ZrO_2 (5.4), Al_2O_3 (4.3), BaO (4.4), CaO (8.9), HLW (20). Examples of waste incorporated in the different phases are given. Several elements such as Ln and MA may enter into the structure of different phases (zirconolite, perovskite). (Ln: lanthanides, MA: minor actinides). ^a: because of the reducing conditions during Synroc preparation and adding of Ti metal to the precursor mixture before sintering, intermetallic alloys formed that may contain noble metals and chalcogens from waste [70].

Radionuclides	Ceramic	Composition
Iodine (^{129}I)	iodoapatite	$\text{Pb}_{10}(\text{VO}_4)_{4.8}(\text{PO}_4)_{1.2}\text{I}_2$
Cesium (^{135}Cs)	hollandite	$\text{BaCs}_{0.28}(\text{Fe}_{0.82}\text{Al}_{1.46})\text{Ti}_{5.72}\text{O}_{16}$
Minor actinides (Np, Am, Cm)	zirconolite	$(\text{Ca}_{1-x}\text{MA}_x^{3+})\text{Zr}(\text{Ti}_{2-x}\text{Al}_x)\text{O}_7$ $(\text{Ca}_{1-x}\text{MA}_x^{4+})\text{Zr}(\text{Ti}_{2-2x}\text{Al}_{2x})\text{O}_7$
	britholite (apatite)	$\text{Ca}_{10-x}\text{MA}_x^{3+}(\text{PO}_4)_{6-x}(\text{SiO}_4)_x\text{F}_2$ $\text{Ca}_{10-x}\text{MA}_x^{4+}(\text{PO}_4)_{6-2x}(\text{SiO}_4)_{2x}\text{F}_2$
	thorium phosphate-diphosphate (TDP)	$\text{Th}_{4-x}\text{MA}_x^{4+}(\text{PO}_4)_2\text{P}_2\text{O}_7$

Ceramic	Synthesis / Remarks	Ref.
iodoapatite	Composite material with $\text{Pb}_3(\text{VO}_4)_{1.6}(\text{PO}_4)_{0.4}$ Prepared by hot pressing (580°C, 25MPa)	[19]
hollandite	Prepared by natural sintering (1250°C)	[18,79]
zirconolite	Prepared by natural sintering (1450°C)	[19,18,80]
britholite (apatite)	Prepared by natural sintering (1475°C)	[19,23]
thorium phosphate-diphosphate (TDP)	Prepared by natural sintering (1250°C). For Np^{4+} immobilization. Can be associated with monazite for immobilization of both MA^{3+} and MA^{4+}	[23,81]

Table IX. Examples of ceramic waste forms developed for the immobilization of long-lived radionuclides (^{129}I , ^{135}Cs , MA). Possible incorporation schemes of tri- and tetravalent MA in ceramics and preparation methods are indicated.

Cesium isotope	Half-life (y:years, d:days)	Activity (Bq/g)	Thermal power (W/g of cesium)
¹³³ Cs	stable	-	0
¹³⁴ Cs	2.06 y	4.8 10 ¹³	13.18
¹³⁵ Cs	2.3.10 ⁶ y	4.3 10 ⁷	3.85.10 ⁻⁷
¹³⁶ Cs	13 d	2.8 10 ¹⁵	-
¹³⁷ Cs	30.03 y	3.2 10 ¹²	0.417

Table X. Radioactive and thermal characteristics of the main cesium isotopes occurring in nuclear spent fuel [120].



Isotopes	UOX2		UOX3	
	g/t	%	g/t	%
¹³³ Cs	1.490 10 ³	42.3	1.889 10 ³	41.5
¹³⁴ Cs	4.808 10 ¹	1.4	5.204 10 ¹	1.1
¹³⁵ Cs	4.916 10 ²	14.0	6.802 10 ²	14.9
¹³⁷ Cs	1.500 10 ³	42.6	1.933 10 ³	42.4
Totality	3.519 10 ³	100	4.554 10 ³	100

Table XI. Proportions of cesium isotopes in two different kinds of nuclear spent fuel: UOX2 (UO₂ with 3.7% ²³⁵U, burn up 45GWj/t, 4 years after discharge), UOX3 (UO₂ with 4.5% ²³⁵U, burn up 60GWj/t, 5 years after discharge) [121]. The period of 4-5 years after discharge corresponds to the time during which the nuclear spent fuel is cooled before reprocessing. (g/t: g of Cs per U ton in fuel before burning).

Cation	Al ³⁺	Cr ³⁺	Ga ³⁺	Fe ³⁺	Ti ³⁺	Sc ³⁺	Ti ⁴⁺	Ba ²⁺	Cs ⁺
r (Å)	0.535	0.615	0.620	0.645	0.670	0.745	0.605	1.42	1.74
r _B (Å)	0.585	0.608	0.609	0.616	0.624	0.645	-	-	-

Table XII. Ionic radius of trivalent cations M (Al³⁺, Cr³⁺, Ga³⁺, Fe³⁺, Ti³⁺, Sc³⁺) in six-fold coordination (octahedral site B in hollandite) and of cations Ba²⁺ and Cs⁺ in eight-fold coordination (site A in hollandite) [144]. r_B is the average radius of cations in site B of Ba_{1,16}(M³⁺_{2.32}Ti_{5.68})O₁₆ hollandite samples.

Nominal composition	EPMA composition	a(Å)	c(Å)	V
Ba_{1.16}Al_{2.32}Ti_{5.68}O₁₆	Ba _{1.18} Al _{2.32} Ti _{5.67} O ₁₆	9.968	2.923	290.4
Ba_{1.16}Cr_{2.32}Ti_{5.68}O₁₆	Ba _{1.16} Cr _{2.29} Ti _{5.70} O ₁₆	10.054	2.952	298.4
Ba_{1.16}Ga_{2.32}Ti_{5.68}O₁₆	Ba _{1.18} Ga _{2.30} Ti _{5.68} O ₁₆	10.051	2.957	298.8
Ba_{1.16}Fe_{2.32}Ti_{5.68}O₁₆	Ba _{1.13} Fe _{2.32} Ti _{5.70} O ₁₆	10.103	2.971	303.2
Ba_{1.11}Cs_{0.10}Al_{2.32}Ti_{5.68}O₁₆	Ba _{1.17} Cs _{0.05} Al _{2.30} Ti _{5.67} O ₁₆	9.972	2.923	290.7
Ba_{1.04}Cs_{0.24}Cr_{2.32}Ti_{5.68}O₁₆	Ba _{1.08} Cs _{0.11} Cr _{2.10} Ti _{5.86} O ₁₆	10.069	2.951	299.3
Ba_{1.04}Cs_{0.24}Ga_{2.32}Ti_{5.68}O₁₆	Ba _{1.15} Cs _{0.15} Ga _{2.45} Ti _{5.55} O ₁₆	10.065	2.963	300.1
Ba_{1.04}Cs_{0.24}Fe_{2.32}Ti_{5.68}O₁₆	Ba _{1.06} Cs _{0.26} Fe _{2.28} Ti _{5.70} O ₁₆	10.122	2.972	304.5

Table XIII. Cell parameters of (Ba,M)-hollandite ($M^{3+}=\text{Al}^{3+}, \text{Cr}^{3+}, \text{Ga}^{3+}, \text{Fe}^{3+}$) and (Ba,Cs,M)-hollandite ($M^{3+}=\text{Cr}^{3+}, \text{Ga}^{3+}, \text{Fe}^{3+}$) ceramics prepared by oxide route (Figure 17). *a* and *c* parameters were obtained after refinement of XRD patterns in the I4/m space group (tetragonal structure). V: cell volume in Å³. The composition of hollandite samples was determined by EPMA (Electron Probe Microanalysis).

Sample	sites	I.S. (mm/s)	Q.S. (mm/s)	Γ (mm/s)	R (%)
Before irradiation	1	0.493	0.884	0.25	63
	2	0.494	0.56	0.19	37
After irradiation	1	0.490	0.76	0.23	77
	2	0.492	0.55	0.12	19
	3	0.36	1.21	0.23	4

Table XIV. Hyperfine parameters extracted from the least-squares fits of the ^{57}Fe transmission Mössbauer spectra (Figure 23) of $\text{Ba}_{1.16}\text{Fe}_{2.32}\text{Ti}_{5.68}\text{O}_{16}$ hollandite before and after electron irradiation (1.5 MeV, $F=5.8 \cdot 10^{18} \text{ cm}^{-2}$). Isomer shift (I.S.), quadrupole splitting (Q.S.), full width at half maximum (Γ) and fraction (R) of the different sites (1, 2 and 3).

Signals	$g_x (\Delta B_z)$	$g_y (\Delta B_y)$	$g_z (\Delta B_x)$
T_r (3 components)	2.0038 (1.2)	2.009 (0.8)	2.035 (0.9)
	2.0038 (1.2)	2.009 (0.8)	2.026 (0.9)
	2.0038 (1.2)	2.009 (0.8)	2.018 (0.9)
E₁	1.953 (3)	1.972 (3)	1.981 (1.5)
E₂	1.885 (5.4)	1.912 (5.8)	1.966 (1.7)

Table XV. g -factors (g_x , g_y and g_z components) and corresponding half-width at half-maximum (ΔB , mT between parenthesis) determined by the simulation of the three signals T_r , E_1 and E_2 detected in $Ba_{1.16}Al_{2.32}Ti_{5.68}O_{16}$ hollandite after electron irradiation. For E_1 and E_2 centers, spectra simulations are shown in Figure 31.

MA	Half-life (years)	Quantity (kg/y)	%	Thermal power (W/g)
²³⁷ Np	2.14 10 ⁶	489	100	2 .08 10 ⁻⁵
²⁴¹ Am	432	540	63.2	0.074
²⁴³ Am	7370		36.6	
²⁴⁴ Cm	18	70	91.3	2.62
²⁴⁵ Cm	8500		6.2	
²⁴⁶ Cm	4760		1.4	
Total	-	1099	-	-

Table XVI. Physical characteristics (half-life, thermal power due to radioactive decay) and concentrations of MA in UOX2 spent fuel (UO₂ with 3.7% ²³⁵U, burn up 45 GWday.t⁻¹) after discharge [32].

Ionic radius (Å)	7-fold coordination	8-fold coordination
Ca ²⁺	1.06	1.12
Zr ⁴⁺	0.78	0.84
Hf ⁴⁺	0.76	0.83
La ³⁺	1.10	1.160
Ce ³⁺	1.07	1.143
Nd ³⁺	-	1.109
Eu ³⁺	1.01	1.066
Gd ³⁺	1.00	1.053
Y ³⁺	0.96	1.019
Yb ³⁺	0.925	0.985
Ce ⁴⁺	-	0.97
Th ⁴⁺	-	1.05
U ⁴⁺	0.95	1.00
Np ⁴⁺	-	0.98
Pu ⁴⁺	-	0.96
Am ³⁺	-	1.09

Table XVII. Comparison of the ionic radii of different lanthanide and actinide cations (in 7- and in 8-fold coordination) that can be incorporated into zirconolite-2M, with the ionic radii of Ca²⁺ (1.12 Å in 8-fold coordination), Zr⁴⁺ and Hf⁴⁺ (respectively 0.78 Å and 0.76 Å in 7-fold coordination) [144].

x	a (Å)	b (Å)	c (Å)	β (degrees)	V (Å³)	Phases^a
0	12.4436	7.2742	11.3813	100.554	1012.8	zirconolite-2M (main phase) + traces of perovskite and (Zr,Ti)O ₂
0.1	12.4529	7.2707	11.3709	100.609	1011.9	
0.2	12.4685	7.2697	11.3589	100.654	1011.9	
0.3	12.4876	7.2721	11.3495	100.723	1012.7	
0.4	12.5018	7.2712	11.3328	100.768	1012.0	
0.5	12.525	7.2746	11.3235	100.835	1013.4	
0.6	12.554	7.2777	11.318	100.874	1015.4	
0.1	12.465	7.280	11.387	100.554	1015.9	same phases ^b

Table XVIII. Lattice parameters (a,b,c,β) and cell volume V of zirconolite-2M obtained by XRD for Ca_{1-x}Nd_xZrTi_{2-x}Al_xO₇ ceramics (x ≤ 0.6). ^a: phases identified by XRD, SEM and EDX. The last line of the table corresponds to the Ca_{0.95}Nd_{0.10}Zr_{0.95}Ti₂O₇ ceramic without aluminum. ^b: the same phases were detected for this sample than for Ca_{1-x}Nd_xZrTi_{2-x}Al_xO₇ ceramics but the quantity of perovskite was higher for the sample without aluminum.

Site	Occupancy	x	y	z
Ca	0.7Ca + 0.296(7) Nd + 0.004(7)Zr	0.3742(3)	0.1239(7)	0.4952(3)
Zr	0.956(7)Zr + 0.004(7) Nd + 0.04(1)Ti	0.1217(3)	0.1209(4)	-0.0270(2)
Ti(1)	0.975(4)Ti + 0.025(4)Zr	0.2500(6)	0.117(1)	0.7472(5)
Ti(2)	0.2Ti + 0.3Al	0.468(1)	0.073(2)	0.255(2)
Ti(3)	0.970(8)Ti + 0.030(8)Zr	0	0.134(1)	0.25
O(1)	1	0.313(1)	0.112(2)	0.293(1)
O(2)	1	0.472(1)	0.158(2)	0.104(1)
O(3)	1	0.216(1)	0.085(2)	0.579(1)
O(4)	1	0.400(1)	0.169(2)	0.712(1)
O(5)	1	0.706(1)	0.168(2)	0.589(1)
O(6)	1	-0.000(1)	0.138(2)	0.416(1)
O(7)	1	0.121(1)	0.042(2)	0.801(1)

Table XIX. Results of the structural refinement of the XRD pattern of $\text{Ca}_{0.7}\text{Nd}_{0.3}\text{ZrTi}_{1.7}\text{Al}_{0.3}\text{O}_7$ (Figure 41) giving the position (x,y,z) and the occupancy of the different sites of the zirconolite-2M structure (Figure 36).

Ca		Zr		Ti(1)		Ti(2)		Ti(3)	
O(1)	2.278	O(7)	2.032	O(5)	1.870	O(2)	1.744	O(6)	1.889
O(3)	2.363	O(2)	2.086	O(1)	1.877	O(2)	1.823	O(6)	1.889
O(2)	2.415	O(3)	2.128	O(3)	1.897	O(4)	1.979	O(4)	1.898
O(6)	2.425	O(6)	2.151	O(7)	1.909	O(1)	2.079	O(4)	1.898
O(4)	2.446	O(5)	2.170	O(4)	2.016	O(4)	2.395	O(7)	1.984
O(5)	2.465	O(5)	2.406	O(1)	2.142			O(7)	1.984
O(3)	2.472	O(6)	2.426						
O(2)	2.482								
D	2.431		2.200		1.952		2.004		1.924

Table XX. Bond distances (in Å) determined from the Rietveld structural refinement of $\text{Ca}_{0.7}\text{Nd}_{0.3}\text{ZrTi}_{1.7}\text{Al}_{0.3}\text{O}_7$. For each site, the mean distance D cation-oxygen is indicated in the last line of the table.

Sample irradiation dose		Non irradiated	$10^{14} \text{ Pb}^{3+} \text{ ions/cm}^2$
First shell (oxygen)	Coordination number	8.0 ± 0.6	8.6 ± 1.3
	Mean distance	2.45 ± 0.01	2.45 ± 0.01
	$\sigma^2 (\text{\AA}^2)$	0.007 ± 0.001	0.012 ± 0.003
Second shell (titanium)	Coordination number	3.1 ± 1.1	3.3 ± 2.4
	Mean distance	3.47 ± 0.01	3.48 ± 0.02
	$\sigma^2 (\text{\AA}^2)$	0.004 ± 0.003	0.009 ± 0.008

Sample irradiation dose		$2 \cdot 10^{15} \text{ Pb}^{3+} \text{ ions/cm}^2$	$10^{16} \text{ Pb}^{3+} \text{ ions/cm}^2$
First shell (oxygen)	Coordination number	8.0 ± 0.7	8.3 ± 1.1
	Mean distance	2.45 ± 0.01	2.46 ± 0.01
	$\sigma^2 (\text{\AA}^2)$	0.011 ± 0.002	0.018 ± 0.003
Second shell (titanium)	Coordination number	4.9 ± 2.2	nd
	Mean distance	3.49 ± 0.02	nd
	$\sigma^2 (\text{\AA}^2)$	0.017 ± 0.007	nd

Table XXI. Results of GIXAFS study of neodymium in native and irradiated (by Pb^{3+} ions) $\text{Ca}_{0.8}\text{Nd}_{0.2}\text{ZrTi}_{1.8}\text{Al}_{0.2}\text{O}_7$ zirconolite samples giving the coordination numbers, mean distances and Debye-Waller factors σ for the two first shells around Nd. nd: no determined.

Ceramic samples	a (Å)	b (Å)	c (Å)	β (degrees)	V (Å³)
CaHfTi₂O₇	12.422	7.268	11.357	100.542	1008.1
CaZrTi₂O₇	12.443	7.274	11.381	100.554	1012.8
Ca_{0.8}Nd_{0.2}HfTi_{1.8}Al_{0.2}O₇	12.450	7.263	11.345	100.655	1008.3
Ca_{0.8}Nd_{0.2}ZrTi_{1.8}Al_{0.2}O₇	12.468	7.269	11.358	100.654	1011.9

Table XXII. Lattice parameters (a,b,c,β) and cell volume V obtained by XRD for Hf- and Zr-zirconolite ceramics.

		SiO₂	Al₂O₃	CaO	TiO₂	ZrO₂	Nd₂O₃	Na₂O
Glass A	wt %	43.16	12.71	20.88	13.25	9.00	0.00	1.00
	mol. %	48.84	8.48	25.33	11.28	4.97	0.00	1.10
Glass B	wt %	40.57	11.95	19.63	12.45	8.46	6.00	0.94
	mol %	48.23	8.37	25.01	11.14	4.90	1.27	1.08

Table XXIII. Composition in wt% and mol% of parent glasses A and B (respectively without and with Nd as MA surrogate) used for the preparation of zirconolite-based glass-ceramics.

Crystal growth thermal treatment	Surface	Bulk
2 h 1050°C	S + A	Z
20 h 1050°C	S + A + W	Z + A + W + I
300 h 1050°C	S + A + W + C	Z + A + W + S + C + I
2 h 1200°C	S + A + B	Z
20 h 1200°C	S + A + B	S + A + B + Z ^a

Table XXIV. Crystalline phases formed in the bulk and near the surface of glass B at $T_c=1050^\circ\text{C}$ and 1200°C using the method described Figure 49 for different durations. The samples were previously annealed and nucleated at 810°C for 2h. (Z: zirconolite, S: titanite, A: anorthite, W: wollastonite, C:cristobalite, B: baddeleyite, I: Nd-rich phase (probably $\text{Ca}_2\text{Nd}_8(\text{SiO}_4)_6\text{O}_2$ apatite). ^a: for this thermal treatment the amount of zirconolite in the bulk strongly decreased in comparison with the other treatments presented in the table.

	SiO₂	Al₂O₃	CaO	TiO₂	ZrO₂	Nd₂O₃	Na₂O
Glass C							
weight %	36.07	10.62	19.18	15.98	11.31	6.00	0.84
mol. %	43.83	7.61	24.97	14.61	6.70	1.30	0.98
Glass D							
weight %	32.47	9.56	18.82	18.81	13.59	6.00	0.75
mol. %	40.17	6.97	24.94	17.50	8.20	1.32	0.90

Table XXV. Composition of parent glasses C and D.

Glass	SiO₂	Al₂O₃	CaO	TiO₂	ZrO₂	HfO₂	Ln₂O₃	Na₂O
Glass B	48.22	8.37	25.01	11.14	4.90	0	1.27	1.08
Glass B(Hf0)	48.23	8.37	25.00	11.14	0	4.91	1.27	1.08
Glass B(Hf0.5)	48.23	8.37	25.00	11.14	2.45	2.45	1.27	1.08
Glass B(Al1)	46.81	11.00	24.27	10.81	4.76	0	1.29	1.05
Glass B(Al2)	49.73	5.57	25.78	11.48	5.06	0	1.25	1.11

Table XXVI. Composition of parent glasses B, B(Hf0), B(Hf0), B(Al1) and B(Al2) (mol%).

Nd₂O₃ (wt%)	zirconolite composition	V (10⁻²⁴cm³)
0 %	Ca _{0.97} Zr _{1.07} Ti _{1.90} Al _{0.06} O ₇	1010.6
0.5 %	Ca _{0.95} Nd _{0.025} Zr _{1.06} Ti _{1.89} Al _{0.075} O ₇	1011.5
1 %	Ca _{0.93} Nd _{0.05} Zr _{1.06} Ti _{1.87} Al _{0.09} O ₇	1011.7
2 %	Ca _{0.91} Nd _{0.08} Zr _{1.05} Ti _{1.86} Al _{0.10} O ₇	1013.0
4 %	Ca _{0.87} Nd _{0.13} Zr _{1.05} Ti _{1.82} Al _{0.13} O ₇	1015.0
6 %	Ca _{0.82} Nd _{0.19} Zr _{1.05} Ti _{1.77} Al _{0.17} O ₇	1016.5
8 %	Ca _{0.80} Nd _{0.23} Zr _{1.05} Ti _{1.75} Al _{0.17} O ₇	1016.3
10 %	Ca _{0.77} Nd _{0.26} Zr _{1.04} Ti _{1.73} Al _{0.20} O ₇	1018.9

Table XXVII. Composition (determined by EDX) of the zirconolite crystals formed in the bulk of glass-ceramics with increasing Nd₂O₃ content in parent glass. V: cell volume determined by XRD.

Nd₂O₃ (wt%)	Titanite composition
0 %	Ca _{0.99} Ti _{0.78} Zr _{0.23} Al _{0.02} Si _{0.98} O ₅
1 %	Ca _{0.97} Nd _{0.025} Ti _{0.77} Zr _{0.215} Al _{0.04} Si _{0.98} O ₅
2 %	Ca _{0.95} Nd _{0.045} Ti _{0.765} Zr _{0.22} Al _{0.06} Si _{0.97} O ₅
6 %	Ca _{0.89} Nd _{0.11} Ti _{0.69} Zr _{0.22} Al _{0.11} Si _{0.98} O ₅
10 %	Ca _{0.84} Nd _{0.16} Ti _{0.67} Zr _{0.21} Al _{0.16} Si _{0.96} O ₅

Table XXVIII. Composition (determined by EDX) of the titanite crystals formed near the surface of glass-ceramics with increasing Nd₂O₃ content in parent glass (T_c=1200°C, 2h).

Figure 1. Evolution of the potential radiotoxicity (expressed in Sv/ton of initial uranium metal) over time of: (a) UOX1 spent fuel (UO₂ enriched with 3.5 % of ²³⁵U, removed from the reactor at a burn up of 33 GW.day/ton (i.e. 3 years in reactor) and cooled for 3 years), (b) UOX3 spent fuel (UO₂ enriched with 4.9 % of ²³⁵U, removed from the reactor at a burn up of 60 GW.day/ton (i.e. 5 years in reactor) and cooled for 5 years). The composition of UOX3 spent fuel and radiotoxicity curves were obtained by simulation [11]. It can be noticed that after about 50 years, Pu is the largest contributor to the radiotoxic inventory in spent fuels. The contribution of MA is about 10 times less than that of Pu but 1000 times greater than that of FP after several centuries. The potential radiotoxicity of the initial ²³⁵U enriched uranium oxide fuels UOX1 and UOX3 is shown (horizontal lines) in (a) and (b) and the intersection point with the radiotoxicity curve of MA occurring in spent fuels is indicated. It appears that the time needed for MA to reach a radiotoxicity level equivalent to the one of the initial UO₂ fuel (vertical lines) increases from about 2000 years for UOX1 to more than 10 000 years for UOX3. For non reprocessed spent fuels, the radiotoxicity drops back to the one of initial fuels only after more than 200 000 years. (MA: minor actinides; FP: fission products).

Figure 2. Enhanced reprocessing of HLW and specific immobilization or transmutation of separated long-lived radionuclides.

Figure 3. Evolution of the composition of UO₂ fuel composition (wt%) after 3 years in PWR reactor [33]. The relative proportions of MA (Np, Am, Cm) are also given. (UOX1 fuel enriched with 3.5% ²³⁵U, discharged at 33 GW.day/tU).

Figure 4. Schematic illustration of immobilization of wastes by dissolution (a) or by encapsulation (b) in a glassy matrix. The principle is similar for single phase or multiphase ceramics.

Figure 5. Back-scattered electron image of an inactive version of the glass composite waste form for the immobilization of HLW solutions of reprocessed UMo spent fuel. The formation process of the white phases (either crystalline or glassy) during cooling of the melt is complex as shown by Cousi et al. [272,273] and consists in a glass-in-glass phase separation followed by crystallization of molybdate and phosphate phases. The black continuous phase in the image corresponds to residual glass depleted in Mo. (Picture by E. Fadel and D. Caurant (CNRS) on an inactive sample given by O. Pinet (CEA)).

Figure 6. Principle of the two-step AVH vitrification process (calcination-evaporation + melting) used to immobilize HLW solutions.

Figure 7. Samples of glass frit (F), inactive calcine (C) and inactive nuclear glass (G) occurring at different stages of the AVH process (**Figure 6**). The nuclear glass (G) is black because of the high amounts of elements absorbing in the visible range (transition metals, lanthanides) that occurred in its composition (**Table VII**). The glass frit is uncoloured (its composition is also given in **Table VII**).

Figure 8. Schematic representation of the structure of an aluminoborosilicate glass containing sodium, calcium and neodymium (neodymium is the most abundant lanthanide in HLW wastes (Table IV) and can also be considered as trivalent MA surrogate). In this figure are shown: SiO_4 tetrahedra, $[\text{AlO}_4]^-$ and $[\text{BO}_4]^-$ tetrahedral units that can be charge compensated by Na^+ or Ca^{2+} ions; BO_3 triangles; Nd^{3+} ions with only a part of its O (bridging and non-bridging) neighbors. Nd was shown to occur in 8-fold coordination by EXAFS [10,52] and Na^+ or Ca^{2+} ions act as charge compensators near non-bridging oxygen. Examples of both bridging oxygen (BO) and non bridging oxygen (NBO) are shown. From spectroscopic results [52], it was shown that if the amounts of sodium and calcium were sufficiently high, Nd^{3+} ions were preferentially located in NBO-rich regions of the aluminoborosilicate network (depolymerized regions, *DR* in the figure) separated by BO-rich regions (polymerized regions, *PR* in the figure). The dotted lines separate *DR* and *PR* regions. This scheme shows that this glass is not homogeneous at nanometric scale.

Figure 9. ^{11}B MAS-NMR (Magic Angle Spinning- Nuclear Magnetic Resonance) signals of glasses containing increasing amounts of lanthanide (La_2O_3): 0, 16 and 30 wt%. To facilitate comparison, intensities were normalized to the same arbitrary intensity. The approximate position of the contributions of $[\text{BO}_3]$ and $[\text{BO}_4]^-$ units are indicated on the spectra and the corresponding relative proportions are given in the table below spectra. These proportions were determined by simulation of the spectra and integration of the BO_3 and BO_4 contributions. In order to be not disturbed by paramagnetic Nd^{3+} ions, diamagnetic La^{3+} ions were used in this study. Chemical shifts were determined relative to liquid BF_3OEt_2 (spectrometer frequency 128.28 MHz). This study was performed in collaboration with C. Gervais (University Paris VI, France).

Figure 10. Schematic representations ((a), (c)) of the nucleation u and crystal growth I rate curves in the undercooled melt. u_{max} and I_{max} correspond respectively to the maxima of these curves. Above the liquidus temperature (T_{liq}), the melt is thermodynamically stable ($u = I = 0$). Below the glass transformation temperature (T_g), the undercooled melt is not stable but becomes very viscous ($\eta > 10^{13}$ - 10^{14} dPa.s) and transforms into glass. For $T < T_g$, I and u rates are generally considered as negligible ($u = I = 0$). Thus nucleation and crystals growth can only occur in undercooled melt (i.e. between T_g and T_{liq}). For thermodynamic reasons, the position of the maximum of the nucleation rate curve I_{max} is below that of the crystal growth curve u_{max} . In (a) and (c) are envisaged two possibilities, with either well separated I and u curves (a) or the existence of a temperature field in which crystals can simultaneously nucleate and grow (grey zone referred as Z in (c)). In case (a), glass-ceramic samples can only be prepared following the heat treatments shown in (b). In this case, nucleation and crystal growth heat treatments can be performed successively at temperatures corresponding respectively to I_{max} and u_{max} . However, in case (c), glass-ceramic samples can be prepared following the heat treatments shown in schemes (b, d or e). Even if different kinds of crystals can generally nucleate and grow in glasses, only one kind of crystal was considered in this figure.

Figure 11. Principle of specific immobilization of long-lived radionuclides (such as MA) in a highly durable glass-ceramic. In ideal case, the radionuclides initially homogeneously dispersed in the glass would be preferentially incorporated in numerous small and highly durable crystals formed in the bulk after partial crystallization. In such glass-ceramic waste forms, radionuclides incorporated in the crystals would benefit from a double barrier of containment by both crystals and residual glass.

Figure 12. Back-scattered SEM images of partially crystallized samples obtained after heat treatment ((a):slow cooling (6°C/min) of the melt; (b): nucleation at 640°C + crystal growth at 870°C) of glass (mol.%): SiO₂ (61.81), B₂O₃ (8.94), Al₂O₃ (5.95), Na₂O (12.40), CaO (5.44), ZrO₂ (1.89), Nd₂O₃ (3.56). In this sample, neodymium can be considered as trivalent MA surrogate. The corresponding XRD patterns shown in Figure 13 for the two samples indicate that the crystalline phase is a Nd-rich silicate apatite (Ca₂Nd₈(SiO₄)₆O₂). This was confirmed by energy dispersive X-rays analysis (EDX) and electron probe microanalysis (EPMA) studies. Apatite crystals appear as a white phase on the SEM images because of the heavy element enrichment (Nd) for these crystals in comparison with residual glass (continuous phase appearing in gray or black in the images). For more details concerning the preparation of these samples see [20].

Figure 13. XRD patterns of the apatite-based glass-ceramic samples of Figure 12 obtained after heat treatment of the glass by nucleation + crystal growth (a) or after slow cooling of the melt (b). XRD shows that apatite is the only crystalline phase in these samples (bulk + surface). In agreement with SEM images, the comparison of XRD lines intensity confirms that the proportion of crystalline phase is higher for the sample prepared by nucleation + crystal growth. For comparison, the XRD pattern of Ca₂Nd₈(SiO₄)₆O₂ apatite ceramic is shown (c). *: lines due to aluminum support. Patterns (a) and (b) can be indexed in the P63/m hexagonal system and are very similar to the pattern of ceramic (c). (λCoK_α: 1.78897Å).

Figure 14. Principle of enhanced separation of Cs from HLW with crown molecules (calixarenes [110]) and conditioning in specific highly durable matrices or transmutation (of long-lived ¹³⁵Cs).

Figure 15. Decay of ¹³⁷Cs and ¹³⁵Cs isotopes. The energies of β and γ particles are given in MeV. The percentages indicated in the figure correspond to the proportions of β particles emitted with the corresponding energy [122,123].

Figure 16. View of the Ba_xCs_y(M,Al)³⁺_{2x+y}Ti⁴⁺_{8-2x-y}O₁₆ hollandite structure (projection down the *c* axis) showing how large cations (Ba²⁺, Cs⁺) are incorporated in tunnels (site A) in the framework of (Al,M,Ti)O₆ octahedra (site B). M: trivalent cation. In this figure, the *c* axis is directed along the tunnels which corresponds to the tetragonal (*a=b*) structure of hollandite (for the monoclinic structure the tunnel direction corresponds to *b* axis). As (*x* + *y*) < 2, site A (box-shaped cavities of eight oxygen anions) is not totally occupied. The

effect of large cations in site B is to enlarge the tunnel cavities (site A), this facilitates inclusion of Cs^+ ions into the structure. The two kinds of oxygen sites (O1 and O2) occurring in hollandite tetragonal structure (I4/m space group) are also shown.

Figure 17. (a) Process used to prepare hollandite ceramics by oxide route showing the three stages: calcination (4h at 810°C in air) of cold pressed dried reagent powders (30 g) to decompose carbonates and nitrates, attrition milling and natural sintering (30h at 1200°C in air) of pellets (cold pressed at 30 MPa). Heating and cooling rates (°C/min) are indicated. A picture of a (Ba,Cs,Al+Fe)-hollandite ceramic pellet (2.5 cm diameter) prepared by oxide route is shown. (b) Scheme of the attrition milling apparatus used to grind the calcined powders mixture in water to particle size less than 1 μm .

Figure 18. XRD patterns of (Ba,M)-hollandite samples $\text{Ba}_{1.16}\text{M}_{2.32}\text{Ti}_{5.68}\text{O}_{16}$ prepared by oxide route (for $\text{M}^{3+}=\text{Al}^{3+},\text{Cr}^{3+},\text{Ga}^{3+},\text{Fe}^{3+}$). All the XRD lines of ceramics can be indexed in the I4/m space group. *: broad superlattice lines. S: aluminum support. ($\lambda\text{CoK}_{\alpha 1}=1.78897 \text{ \AA}$)

Figure 19. Evolution of a lattice parameter of single-phase $\text{Ba}_{1.16}\text{M}_{2.32}\text{Ti}_{5.68}\text{O}_{16}$ ($\text{M}^{3+} = \text{Al}^{3+},\text{Cr}^{3+},\text{Ga}^{3+},\text{Fe}^{3+}$) hollandite ceramics prepared by oxide route versus the average radius r_B of cations in site B (**Table XII**). A linear fit (least squares regression) of a versus r_B is shown in the figure.

Figure 20. SEM images of $\text{Ba}_{1.16}\text{M}_{2.32}\text{Ti}_{5.68}\text{O}_{16}$ with $\text{M} = \text{Al}$ (a), Cr (b), Ga (c) and Fe (d). A: parasitic phase containing P, Si, Ba and O. SEM images of (Ba,Cs,M)-hollandite ceramics: $\text{Ba}_{1.04}\text{Cs}_{0.24}\text{Cr}_{2.32}\text{Ti}_{5.68}\text{O}_{16}$ (e); $\text{Ba}_{1.04}\text{Cs}_{0.24}\text{Ga}_{2.32}\text{Ti}_{5.68}\text{O}_{16}$ (f), $\text{Ba}_{1.04}\text{Cs}_{0.24}\text{Fe}_{2.32}\text{Ti}_{5.68}\text{O}_{16}$ (g) and $\text{Ba}_{1.00}\text{Cs}_{0.28}\text{Al}_{1.46}\text{Fe}_{2.32}\text{Ti}_{5.72}\text{O}_{16}$ (h). C: $\text{CsGaSi}_{0.4}\text{Ti}_{0.6}\text{O}_4$. The dark regions in (a), (b), (c), (d), (e), (f) and (h) images correspond to pores. The gray continuous phase observed on all images corresponds to hollandite. (a-g): back-scattered electrons images. (h): secondary electrons image.

Figure 21. ^{27}Al Triple Quantum MQ-MAS-NMR spectra (projections along the isotropic dimension free of second order quadrupolar broadening) of: (a) $\text{Ba}_{1.16}\text{Al}_{2.32}\text{Ti}_{5.68}\text{O}_{16}$ ceramic, showing its simulation with three components (X, Y, Z) corresponding to three different Al environments in site B (see Figure 22) with similar proportions (37, 33 and 30 % respectively), (b) $\text{Ba}_{1.16}\text{Al}_{2.32}\text{Ti}_{5.68}\text{O}_{16}$, $\text{Ba}_{1.28}\text{Al}_{1.64}\text{Ga}_{0.92}\text{Ti}_{5.44}\text{O}_{16}$ and $\text{Ba}_{1.00}\text{Cs}_{0.28}\text{Al}_{1.46}\text{Ga}_{0.82}\text{Ti}_{5.72}\text{O}_{16}$ ceramics showing the evolution of X,Y and Z components. All samples were prepared by oxide route. (Magnetic field 11.75 T, Frequency 31500 Hz). This NMR study was performed in collaboration with T. Charpentier, CEA Saclay (France).

Figure 22. Local environment of Al^{3+} ions (black circle, site B) in $\text{Ba}_{1.16}\text{Al}_{2.32}\text{Ti}_{5.68}\text{O}_{16}$ hollandite showing the six possible positions of Ba^{2+} ions or vacancies (gray circles, site A) as second neighbors in the two tunnels near AlO_6 octahedron (Figure 16). For clarity, oxygen atoms are not shown in the figure.

The distances (in Å) between Al and Ba or vacancies shown in the figure were obtained by Rietveld refinement of $\text{Ba}_{1.16}\text{Al}_{2.32}\text{Ti}_{5.68}\text{O}_{16}$ XRD powder pattern [120]. Along tunnels, the two consecutive Ba positions (pairs of gray circles) separated by a mirror are distant from only 0.575 Å and cannot be occupied simultaneously by barium ions. From this figure and considerations about Ba^{2+} ions repulsion along tunnels (configuration with two consecutive cannot exist), only three different Al environments (X, Y and Z) can be envisaged in $\text{Ba}_{1.16}\text{Al}_{2.32}\text{Ti}_{5.68}\text{O}_{16}$: with one Ba and two vacancies as second neighbors (X), with two Ba and one vacancy as second neighbors (Y), with three Ba as second neighbors (Z).

Figure 23. ^{57}Fe transmission Mössbauer spectrum of $\text{Ba}_{1.16}\text{Fe}_{2.32}\text{Ti}_{5.68}\text{O}_{16}$ (300 K, $^{57}\text{CoRh}$ source) before (a) and after electron irradiation (b) (1.5 MeV, $F=5.8.10^{18}\text{ cm}^{-2}$) showing the contributions of respectively two or three Fe environments (sites 1, 2 and 3) needed to simulate the experimental spectra (global simulation: solid line, experiment: points). Simulation parameters are given Table XIV. The isomer shift (mm/s) was corrected using metallic iron as reference. The difference between experimental and simulated spectra is shown below each spectrum. Sample was prepared by oxide route without ^{57}Fe enrichment. This Mössbauer study was performed in collaboration with F. Studer and N. Nguyen, CRISMAT Caen (France).

Figure 24. Calculated evolution with time of cumulated β,γ radiation dose in radioactive Cs waste form containing 5 wt% Cs_2O extracted from HLW solutions recovered after UOX spent fuel reprocessing [120].

Figure 25. Evolution of the probability of Ba (a) and O (b) displacement (displacement cross section) in hollandite versus electrons energy, calculated for different values of the threshold displacement energy of Ba ($E_d(\text{Ba})$) and O ($E_d(\text{O})$) ranging from 20 to 55 eV [120]. Dotted vertical lines correspond to the different electron energies available during our study (1, 1.5 and 2.5 MeV). The full vertical line corresponds to 0.5 MeV which is the energy of the majority of the β -particles emitted during Cs decay (Figure 15).

Figure 26. Scheme showing electrons and holes trapping after the creation of (e^- , h^+) pairs by external electron irradiation (or β self-irradiation) respectively near the bottom of CB and near the top of VB of hollandite. CB: conduction band. VB: valence band. Electron irradiation induced mainly electronic excitations (inelastic interactions) along electrons path in the hollandite structure.

Figure 27. Electronic band structure around the gap of $\text{BaAl}_2\text{Ti}_6\text{O}_{16}$ hollandite: (a) projection of density of states on oxygen and titanium orbitals calculated using an extended Hückel tight-binding method, showing the top of the valence band (VB) and the bottom of the conduction band (CB). VB is mainly of O (2p) character, and represents bonding Ti-O interactions. (b) Overlap population. The top of the VB is of antibonding O-O character and of non-bonding Ti-O character. The CB is mainly Ti-O antibonding and of Ti(3d) character; it reflects the splitting of Ti (3d) orbitals in t_{2g} and e_g sets by the octahedral crystal field, t_{2g} set forming the bottom of the CB.

Figure 28. Partial view of the XRD pattern of $\text{Ba}_{1.16}\text{Al}_{2.32}\text{Ti}_{5.68}\text{O}_{16}$ hollandite before (solid line) and after electron irradiation (dotted line). Energy: 2.5 MeV. Fluence: $1.2 \cdot 10^{19} \text{ cm}^{-2}$. Indexation of XRD lines is given. ($\lambda_{\text{CoK}\alpha 1} = 1.78897 \text{ \AA}$)

Figure 29. ^{27}Al MAS-NMR spectra of $\text{Ba}_{1.16}\text{Al}_{2.32}\text{Ti}_{5.68}\text{O}_{16}$ hollandite before (black spectra) and after irradiation by 1.0 MeV electrons at a fluence of $8.7 \times 10^{18} \text{ cm}^{-2}$ (gray spectra). The figure is an extended and magnified view of Al spectra showing the presence of 5-fold coordinated aluminum. This NMR study was performed in collaboration with T. Charpentier, CEA Saclay (France).

Figure 30. Evolution of EPR spectra recorded at 70 K of $\text{Ba}_{1.16}\text{Al}_{2.32}\text{Ti}_{5.68}\text{O}_{16}$ hollandite before irradiation and after external electron irradiation (1 MeV) for different fluences F . Signals associated with hole center T_r and electron centers E_1 and E_2 are shown. The positions of the free electron g factor (g_e , vertical line) and of the g factor associated with electron centers EC (on the right of the vertical line, $g < g_e$) and holes centers HC (on the left of the vertical line, $g > g_e$) are indicated.

Figure 31. Simulations of the EPR signals of E_1 and E_2 centers formed after electron irradiation in $\text{Ba}_{1.16}\text{Al}_{2.32}\text{Ti}_{5.68}\text{O}_{16}$ hollandite. Solid lines: experimental spectra. Dotted lines: simulated spectra. The parameters deduced from these simulations are given in Table XV. To separate the contributions of E_1 and E_2 centers, EPR spectra were recorded at two different temperatures (10 K and 70 K).

Figure 32. Schematic energy levels of the irradiation-induced centers T_r , E_1 and E_2 with respect to the hollandite band structure (see Figure 27). The two Ti^{3+} centers E_1 and E_2 form two localized levels below the bottom of the CB (electron traps), while the T_r center (superoxide ion O_2^-) being of O(2p) character forms a level above the top of the VB (hole trap). The electronic configuration of O_2^- being $(1\pi_u)^4(1\pi_g^*)^3$, the T_r centre may be described as a hole trapped in an antibonding π_g orbital of a O-O pair. VB: valence band. CB: conduction band.

Figure 33. EPR spectra (recorded at 70 K) of an annealed sample of $\text{Ba}_{1.16}\text{Al}_{2.32}\text{Ti}_{5.68}\text{O}_{16}$ hollandite previously irradiated by 1 MeV electrons at a fluence of $1.4 \cdot 10^{19} \text{ cm}^{-2}$. The annealing (for 15 min) temperature is indicated near each spectrum. Electron and hole centers are indicated in the figure.

Figure 34. Evolution with annealing temperature of the concentrations of E_1 , E_2 and E_3 centers for a sample of $\text{Ba}_{1.16}\text{Al}_{2.32}\text{Ti}_{5.68}\text{O}_{16}$ hollandite previously irradiated by 1 MeV electrons at a fluence of $1.4 \cdot 10^{19} \text{ cm}^{-2}$.

Figure 35. (a): scheme showing the mechanism proposed for migration of O_2^- centers leading to G2 centers by clusterization during annealing (successive electrons and oxygen atoms jumps with intermediate O_2^{2-} and O^- species). (b): scheme summarizing the formation of paramagnetic centers during electron irradiation and their evolution after thermal treatment: migration of Ti^{3+} centers

(crosses) towards the surface of the grains in the hollandite ceramic and clusterization of O_2^- centers (circles) in their bulk. In (b), the rectangle represents a grain of hollandite ceramic.

Figure 36. Zirconolite-2M structure (monoclinic structure, space group $C_{2/c}$) showing the TiO_6 octahedra (Ti(1) and Ti(3) sites) layers and the (Ca^{2+} , Zr^{4+}) rows. The polyhedra corresponding to the Ti^{4+} ions in 5-fold coordination (Ti(2) site) are not drawn but this split site -which is statistically occupied- is shown (small balls in the Ti^{4+} layers). When Ln or An are incorporated in zirconolite structure they entered into the Ca or Zr sites and Al (used as charge compensator) entered preferentially into the Ti(2) site. The a, b and c cell parameters are shown in the figure.

Figure 37. Process used to prepare zirconolite ceramics by oxide route showing the three stages: first natural sintering (100h at 1400°C in air) of cold pressed reagent powders to decompose carbonates and nitrates and to form zirconolite, and second natural sintering (100h at 1460°C in air) after grinding + pressing (cold pressing at 20 MPa) of pellets to increase the homogeneity of the ceramics. Heating and cooling rates ($^{\circ}C/min$) are indicated. The choice of a high heating rate ($8^{\circ}C.min^{-1}$) was made to reduce the risks of formation of perovskite (parasitic phase). A picture of the $Ca_{0.85}Nd_{0.15}ZrTi_{1.85}Al_{0.15}O_7$ ceramic pellet prepared following this method is shown.

Figure 38. Portion of the XRD patterns of $Ca_{1-x}Nd_xZrTi_{2-x}Al_xO_7$ ceramic samples ($\lambda_{K\alpha_1}(Co)=1.78897 \text{ \AA}$). All the lines are attributed to zirconolite (small lines due to a parasitic phase (perovskite) appeared in another angular range not seen in this figure). For $x \leq 0.6$, all lines correspond to the zirconolite-2M polytype (monoclinic). For $x \geq 0.65$, new lines (\bullet) due to the zirconolite-3O polytype (orthorhombic) are detected. For $x = 0.65$, the two polytypes coexist.

Figure 39. Back-scattered electron image of $Ca_{0.9}Nd_{0.1}ZrTi_{1.9}Al_{0.1}O_7$ ceramic sample prepared by oxide route. The gray continuous phase Z (zirconolite) and the white parasitic phase $Zr_{0.9}Ti_{0.1}O_2$ (A) were identified and analyzed by EDX. P: porosities.

Figure 40. Evolution of a and c cell parameters of $Ca_{1-x}Nd_xZrTi_{2-x}Al_xO_7$ zirconolite-2M ceramics for $x \leq 0.6$ (monoclinic structure).

Figure 41. Rietveld refinement of $Ca_{0.7}Nd_{0.3}ZrTi_{1.7}Al_{0.3}O_7$ XRD pattern ($\lambda_{K\alpha_1}(Co)= 1.78897 \text{ \AA}$, $\lambda_{K\alpha_2}(Co)= 1.79285 \text{ \AA}$). Top: experimental (circles) and simulated patterns. Middle: line positions. Bottom: difference between experimental and simulated patterns showing the good quality of refinement.

Figure 42. (a) EPR spectra of $Ca_{0.97}Nd_{0.03}ZrTi_{1.97}Al_{0.03}O_7$, $Ca_{0.7}Nd_{0.3}ZrTi_{1.7}Al_{0.3}O_7$ zirconolite-2M ceramics and of $Ca_{0.9}Nd_{0.1}Ti_{1.9}Al_{0.1}O_7$ perovskite ceramic. The contribution of Nd^{3+} ions in zirconolite and perovskite to the EPR spectrum of $Ca_{0.97}Nd_{0.03}ZrTi_{1.97}Al_{0.03}O_7$ ceramic are indicated. (b)

Simulation of the EPR spectrum of $\text{Ca}_{0.8}\text{Nd}_{0.2}\text{ZrTi}_{1.8}\text{Al}_{0.2}\text{O}_7$ zirconolite-2M ceramic with two components C1 and C2.

Figure 43. (a) Schematic diagram of Nd^{3+} ion energy levels involved in the $^4\text{I}_{9/2}$ (ground state) \rightarrow $^2\text{P}_{1/2}$ optical transition. In low symmetry sites, as in glasses and in zirconolite, the five Stark levels of the fundamental state $^4\text{I}_{9/2}$ are splitted and can be all populated at room temperature. However, at low temperature ($T \sim 15$ K) only the lowest Stark level is populated and only one transition from this state to the $^2\text{P}_{1/2}$ excited state is observed for each kind of site occupied by neodymium (the energy position of this transition is known to depend on the degree of covalency of Nd-O bonds). (b) Optical absorption spectra ($T < 15$ K) of neodymium in $\text{Ca}_{0.95}\text{Nd}_{0.1}\text{Zr}_{0.95}\text{Ti}_2\text{O}_7$ et $\text{Ca}_{0.9}\text{Nd}_{0.1}\text{ZrTi}_{1.9}\text{Al}_{0.1}\text{O}_7$ zirconolite-2M ceramics and in $\text{Ca}_{0.9}\text{Nd}_{0.1}\text{Ti}_{1.9}\text{Al}_{0.1}\text{O}_7$ perovskite ceramic ($^4\text{I}_{9/2} \rightarrow ^2\text{P}_{1/2}$ transition). (c) Simulation of the optical absorption spectrum ($^4\text{I}_{9/2} \rightarrow ^2\text{P}_{1/2}$ transition) of $\text{Ca}_{0.7}\text{Nd}_{0.3}\text{ZrTi}_{1.7}\text{Al}_{0.3}\text{O}_7$ zirconolite-2M ceramic with three Gaussian components G1, G2 and G3.

Figure 44. Portion of the zirconolite $\text{Ca}_{0.7}\text{Nd}_{0.3}\text{ZrTi}_{1.7}\text{Al}_{0.3}\text{O}_7$ structure determined from Rietveld refinement showing the positions of the two next nearest Ti(2) splitted sites from the (Ca,Nd) site (8-fold coordinated by oxygen anions). The Zr site is not shown in the figure. The subscript a and b indicate that the corresponding Ti(2) sites belong to two different titanium planes (Figure 36). The $\text{Ti}(2)_a$ and $\text{Ti}(2)_b$ positions are statistically occupied (50 %) either by Ti^{4+} or Al^{3+} ions, the other positions (50%) being vacant.

Figure 45. Comparison of the GIXAFS Fourier transforms (FFT) of the $\text{Ca}_{0.8}\text{Nd}_{0.2}\text{ZrTi}_{1.8}\text{Al}_{0.2}\text{O}_7$ virgin and irradiated samples (doses: 1.10^{14} , $2 \cdot 10^{15}$ and 10^{16} Pb^{3+} ions/ cm^2) at Nd L_{III} edge in fluorescent mode (room temperature). R represents the distance between Nd and its neighbors.

Figure 46. Evolution of $\text{Ca}_{0.75}\text{Ln}_{0.25}\text{ZrTi}_{1.75}\text{Al}_{0.25}\text{O}_7$ cell volume V_m versus the lanthanide ionic radius cubed $r^3(\text{Ln}^{3+})$. $\text{Ca}_{0.75}\text{Ce}_{0.25}\text{ZrTi}_{1.75}\text{Al}_{0.25}\text{O}_7$ cell volume was not considered for the linear curve fit whose equation is given in the figure (R: linear regression coefficient).

Figure 47. Scheme $T = f(\text{time})$ showing the parent glasses preparation method.

Figure 48. Cylindrical samples of parent glasses containing different concentrations of Nd_2O_3 for the preparation of zirconolite-based glass-ceramics (diameter 1.4 cm).

Figure 49. Scheme $T = f(\text{time})$ showing the preparation method of zirconolite-base glass-ceramics from parent glasses A and B ($T_g = 760^\circ\text{C}$) with two steps (nucleation at $T_N = 810^\circ\text{C}$ and crystal growth at T_c ranging from 950 to 1350°C).

Figure 50. Nucleation ($I = f(T)$) and crystal growth rate ($u = f(T)$) curves of zirconolite in the bulk of glass B. These curves were obtained using the methods

described in [44]. The curve $u=f(T)$ was not plotted for $T>1200^{\circ}\text{C}$. This figure shows that I and u curves are well separated for zirconolite. This allows control of zirconolite crystallization in the undercooled melt which is very interesting for the preparation of glass-ceramics using two steps (nucleation + crystal growth). However, the lack of overlapping between u and I curves makes difficult the preparation of zirconolite-based glass-ceramics by cooling of the melt (see **Figure 10**).

Figure 51. Sample of glass B before (left) and after (right) nucleation at 810°C (2h) + crystal growth at 1050°C (2h). After nucleation, samples remain fully transparent. The opacity of glass-ceramic is due to diffusion of visible light by crystals.

Figure 52. Evolution of the thickness of the crystallized layer formed near the surface of glass B versus the temperature (T_c) of crystal growth (2 h). All the samples were annealed (775°C 2h) and nucleated (810°C 2h) before crystal growth.

Figure 53. XRD patterns of glass A before heat treatment (a) and after heat treatment for 2 h at 810°C (nucleation) and 1200°C (crystal growth): surface layer (b) and bulk (c). (*), (●), (○), (×) zirconolite, titanite, anorthite, aluminum support. The same crystalline phases were observed for glass B. ($\lambda_{\text{K}\alpha 1}(\text{Co})=1.78897 \text{ \AA}$)

Figure 54. Back-scattered SEM micrographs of glass B after nucleation for 2 h at 810°C and crystallization for 2 h at 1050°C (bulk (a) and surface layer (b)) or for 2 h at 1200°C (bulk (c) and surface layer (d)) showing zirconolite (Z), titanite (T), anorthite (A), baddeleyite (B) and residual glass (R) (the white scale bars correspond to $20\mu\text{m}$).

Figure 55. DTA curves for different particle size fractions and for a massive sample of glass B (heating rate: $10^{\circ}\text{C}\cdot\text{min}^{-1}$).

Figure 56. Back-scattered SEM images of the samples obtained after heat treatment of glass B by rapid cooling of the melt from 1550°C to $T_c=1200^{\circ}\text{C}$. Samples were kept at T_c for 2 h and then quenched to room temperature (bulk (a), surface (c)). Z: zirconolite. RG: residual glass.

Figure 57. Back-scattered SEM images of the bulk of the glass-ceramics obtained after prolonged heat treatment of glass B at: (a) $T_c=1200^{\circ}\text{C}$ (20h) or (b) $T_c=1050^{\circ}\text{C}$ (20h). Z: zirconolite. S: titanite. A: anorthite (appearing as dark phase). B: baddeleyite (appearing as a white phase in (a)). W: wollastonite. I: apatite. RG: residual glass. (see Table XXIV).

Figure 58. XRD patterns of zirconolite crystals formed in the bulk of glass A: nucleation at $T_N=810^{\circ}\text{C}$ (2h) and crystal growth for 2 h at $T_c=1200^{\circ}\text{C}$ (a) or $T_c=1000^{\circ}\text{C}$ (b). The pattern for a zirconolite ceramic (e) sample prepared by solid state reaction is also shown. Simulated patterns corresponding to the sample heat

treated at 1000°C using the zirconolite structural determinations of Gatehouse et al. [204]. are also shown assuming a complete disorder (c) or order (d) in Ca/Zr planes. Small angle XRD lines are the most sensitive to Ca/Zr ordering. ($\lambda_{K\alpha 1}(Co)=1.78897\text{\AA}$)

Figure 59. Evolution of the nature and/or structure of crystalline phases formed in the bulk and near the surface of the glass-ceramics prepared following the method described Figure 49, versus the crystal growth temperature T_c (horizontal axis). F: fluorite. Z: zirconolite. S: titanite. A: anorthite. B: baddeleyite.

Figure 60. XRD patterns of glass A before heat treatment (a) and after heat treatment (crystal growth) for 2h at 950°C (b), 2h at 1200°C (crystallized surface layer (c) and bulk (d)) and 2h at 1300°C (e). All the samples were annealed (775°C 2h) and nucleated (810°C 2h) before crystal growth. (*): zirconolite. (◆) fluorite-type phase. (●) titanite. (○) anorthite. (+) ZrO_2 . ($\lambda_{K\alpha 1}(Co) = 1.78897\text{\AA}$)

Figure 61. Back-scattered SEM image of the bulk of the glass-ceramic prepared from glass B at different T_c between 950 and 1350°C (2h) indicated in the figure. All the samples were annealed (775°C 2h) and nucleated (810°C 2h) before crystal growth. F :fluorite-type phase. Z : zirconolite. B : baddeleyite. T : titanite. A : anorthite.

Figure 62. Back-scattered SEM images of the bulk of the glass-ceramics prepared after nucleation for 2 h at $T_N=810^\circ\text{C}$ and crystallization for 2 h at $T_c=1050^\circ\text{C}$ (a, b, c respectively for annealed glasses B, C, D). Z: zirconolite. R: residual glass.

Figure 63. (a) Evolution of XRD pattern intensity of the bulk of the glass-ceramics B, C and D for $T_c=1050^\circ\text{C}$ and $T_c=1200^\circ\text{C}$. Intensity values (in arbitrary unit) were obtained by integration of the lines of XRD patterns. (b) Evolution of the percentage R of Nd^{3+} ions incorporated in the zirconolite crystalline phase formed in the bulk of glass-ceramics determined by EPR.

Figure 64. DTA curves of as-quenched glasses B, C and D (heating rate: $10^\circ\text{C}\cdot\text{min}^{-1}$, particle size 125-250 μm).

Figure 65. Neodymium X-band EPR spectra recorded at 12K. (a) parent glass B. (b) bulk of the glass-ceramic prepared at $T_c=1050^\circ\text{C}$ (individual contributions corresponding to Nd^{3+} ions located in zirconolite crystals and in the residual glass are shown). (c) $Ca_{0.8}Nd_{0.2}ZrTi_{1.8}Al_{0.2}O_7$ ceramic prepared by solid state reaction.

Figure 66. Neodymium X-band EPR spectra recorded at 12K for the bulk of glass-ceramic B(a) and D(b) prepared at $T_c= 1200^\circ\text{C}$ for 2 h (GC spectra). The individual contributions of Nd^{3+} ions located in the zirconolite phase (Z spectra) and in the residual glass (RG spectra) are also shown.

Figure 67. Back-scattered SEM images of the bulk of the glass-ceramic B(Hf0) ($T_N=810^\circ\text{C}$ for 2h): (a) bulk at $T_c=1050^\circ\text{C}$ (2h). (b) bulk at $T_c=1200^\circ\text{C}$ (2h). Z: zirconolite. RG: residual glass.

Figure 68. Zirconolite nucleation rate curves $I=f(T)$ in glass B and in glass B(Hf0). T_g is the same for the two glasses.

Figure 69. Back-scattered SEM images of the bulk of the glass-ceramics B (a) and B(Al1) (b) ($T_N=810^\circ\text{C}$ (2h), $T_c=1050^\circ\text{C}$ (2h)). Z: zirconolite. RG: residual glass.

Figure 70. Back-scattered SEM images of the bulk of the glass-ceramics containing: (a) 0, (b) 4, (c) 8 and (d) 10 wt% Nd_2O_3 . ($T_N=810^\circ\text{C}$ 2h, $T_c=1050^\circ\text{C}$ 2h). Z: zirconolite. RG: residual glass.

Figure 71. Evolution of Nd and Al amounts (determined by EDX) in zirconolite crystals formed in the bulk of the glass-ceramics as a function of Nd_2O_3 content in parent glass ($T_c = 1200^\circ\text{C}$).

Figure 72. Neodymium optical absorption spectra corresponding to the transition $^4I_{9/2} \rightarrow ^2P_{1/2}$ recorded at low temperature ($T \sim 15$ K) for the bulk of the glass-ceramics containing 4 (a) and 10 (b) wt% Nd_2O_3 ($T_c = 1200^\circ\text{C}$). The glass-ceramic spectra are simulated with three Gaussian contributions corresponding to three different local environments for Nd^{3+} ions indicated in the figure. This figure clearly shows that the covalency of Nd-O bonds is different in zirconolite and in residual glass (see legend of Figure 43). The broad band associated with Nd^{3+} ions in residual glass indicated a broader distribution of Nd sites in this phase in agreement with its amorphous structure.

Figure 73. Evolution of $A(\text{Zr})/A(\text{Ca})$ ratio calculated from the optical absorption spectra of the glass-ceramics prepared at $T_c=1200^\circ\text{C}$ versus Nd_2O_3 wt% in parent glass.

Figure 74. Evolution of Nd and Al amounts (determined by EDX) in titanite crystals formed near the surface of the glass-ceramics as a function of Nd_2O_3 content in parent glass ($T_c=1200^\circ\text{C}$, 2h).

Figure 75. Evolution of Ln and Al amounts in the zirconolite crystals formed in the bulk of the glass-ceramics ($T_c= 1200^\circ\text{C}$, 2h) containing Ln = Ce, Nd, Eu, Gd or Yb versus Ln^{3+} radius (in 8-fold coordination).

Figure 1

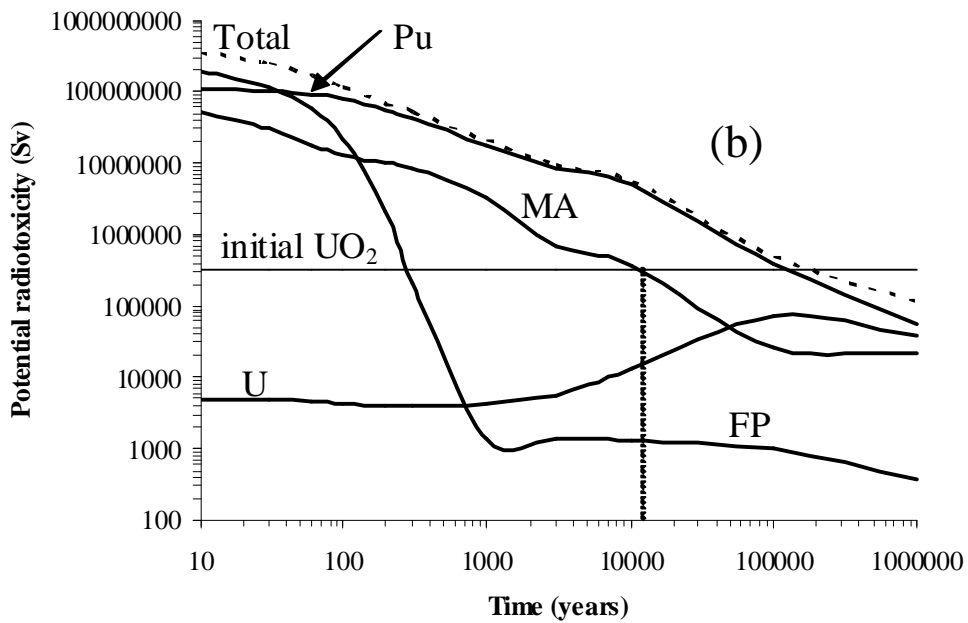
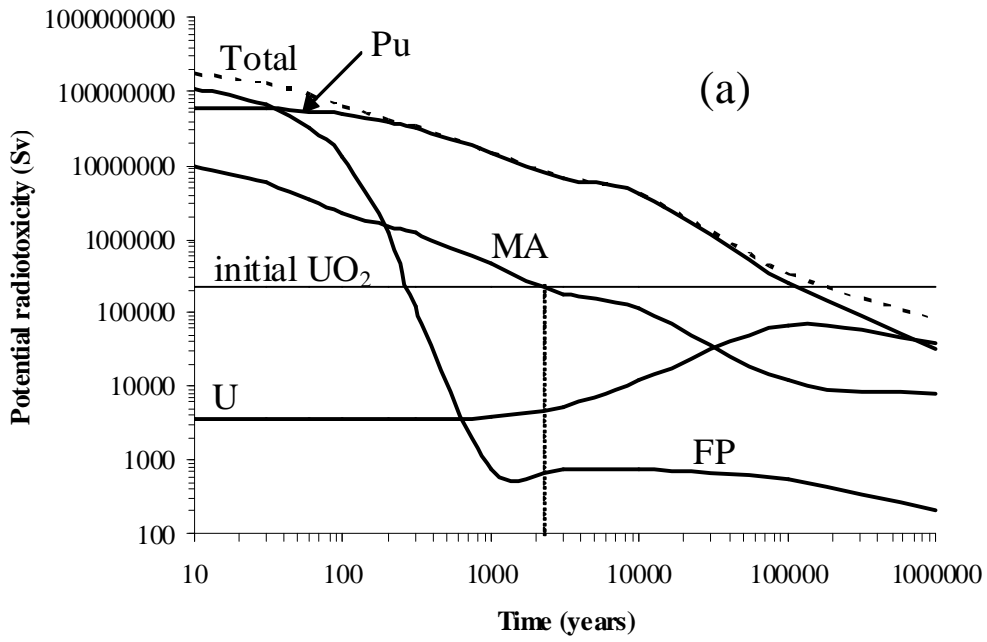


Figure 2

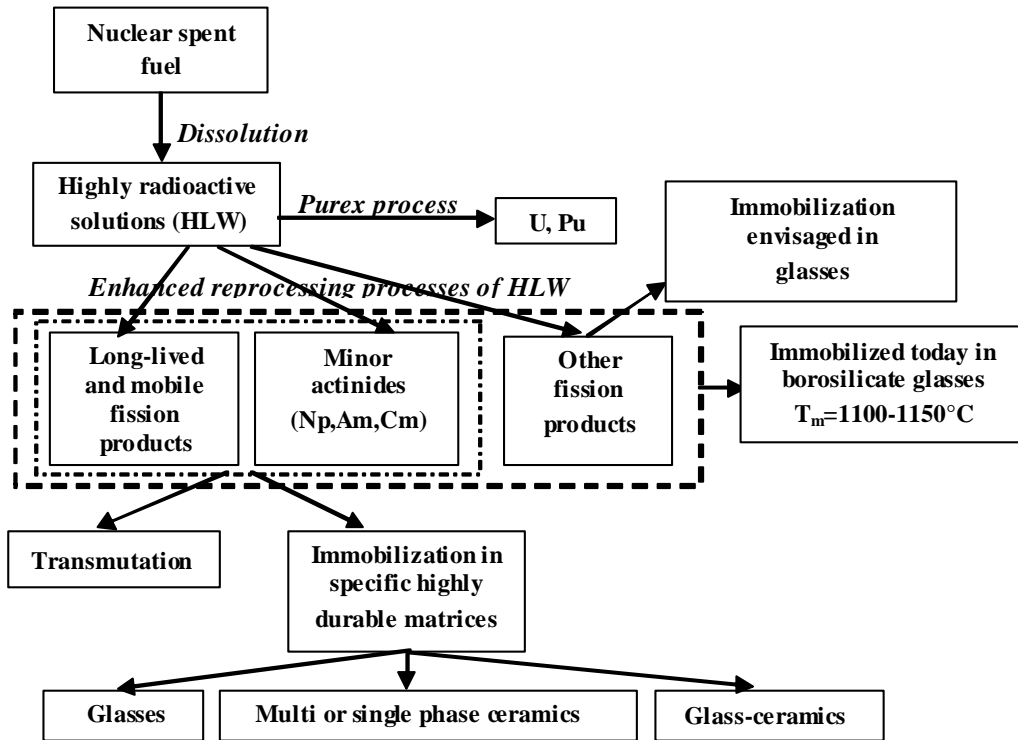


Figure 3

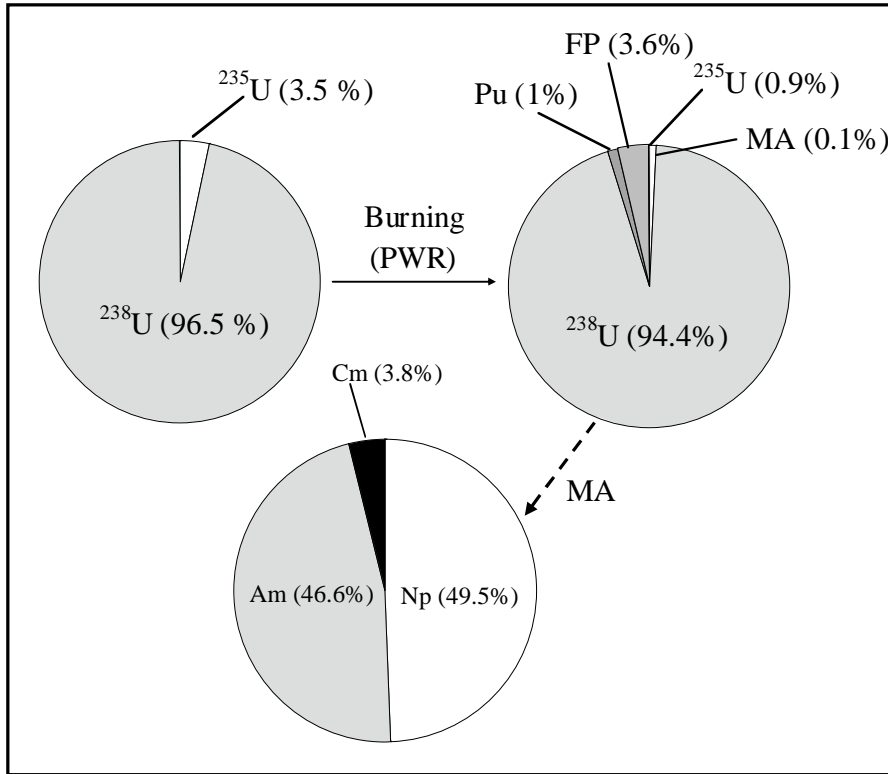


Figure 4

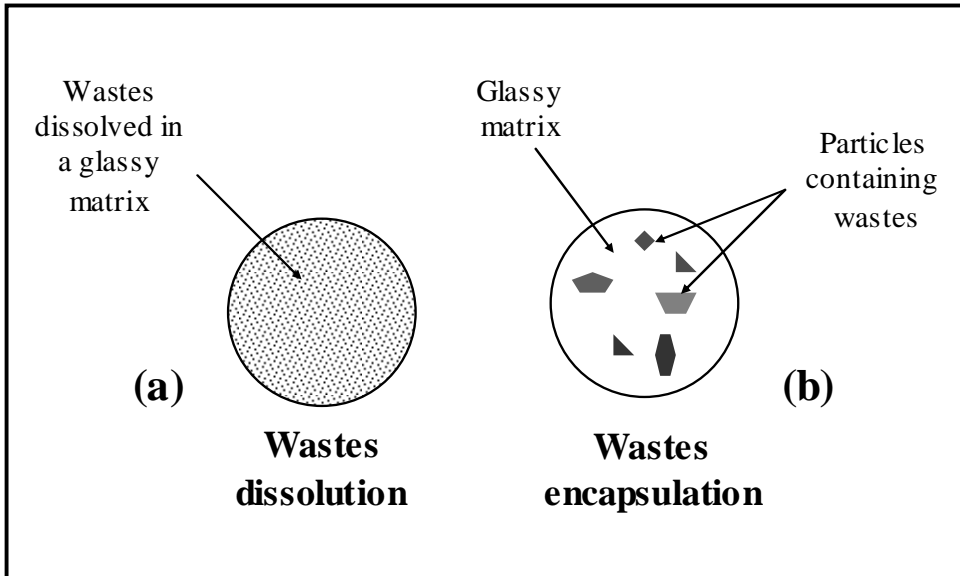


Figure 5

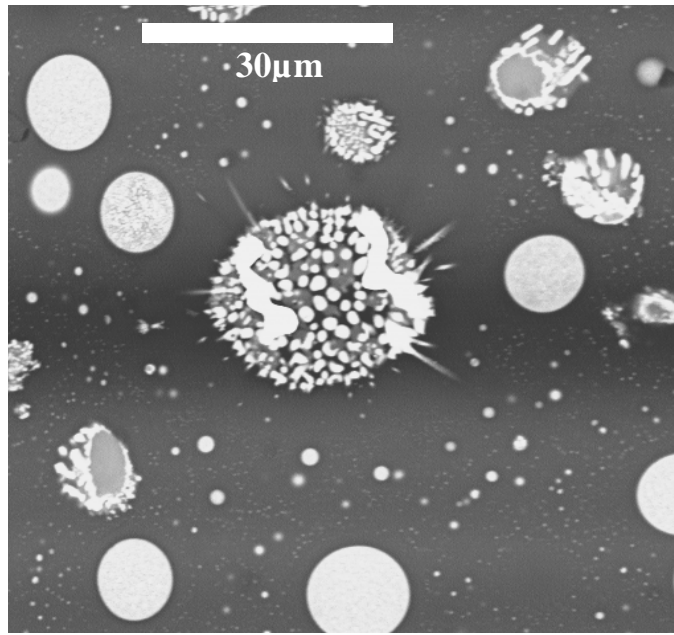


Figure 6

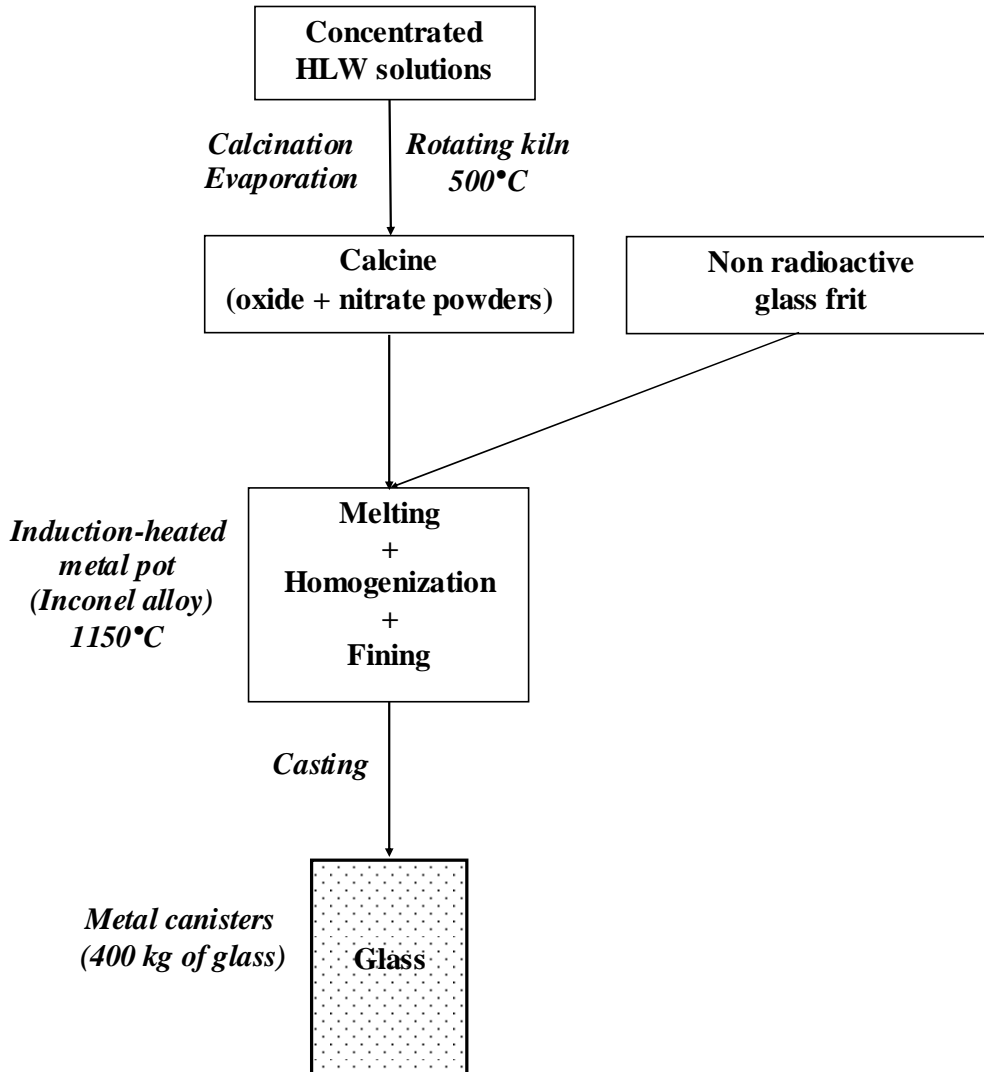


Figure 7



Figure 8

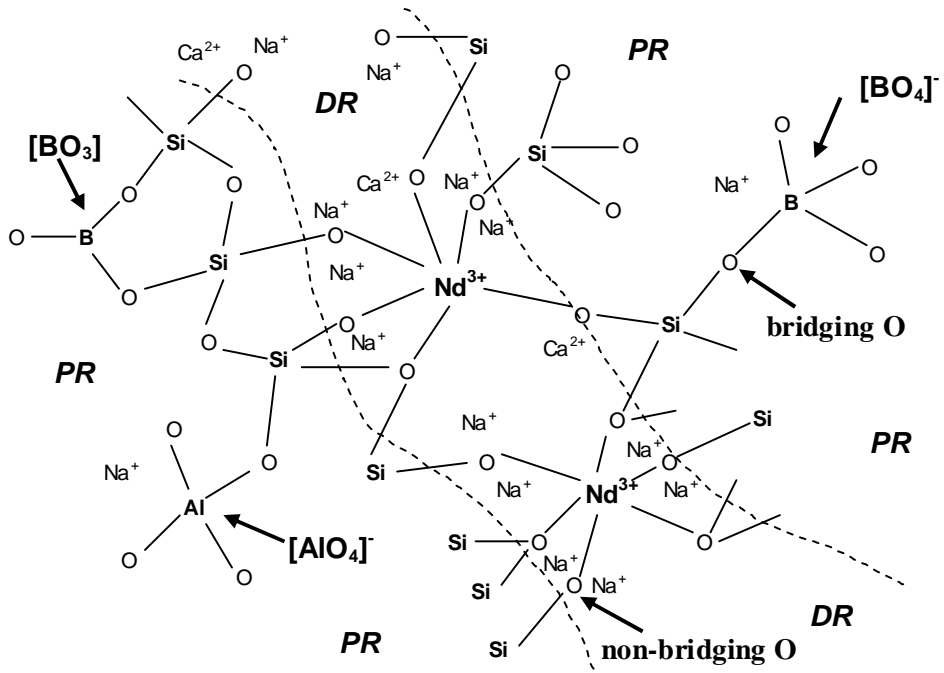
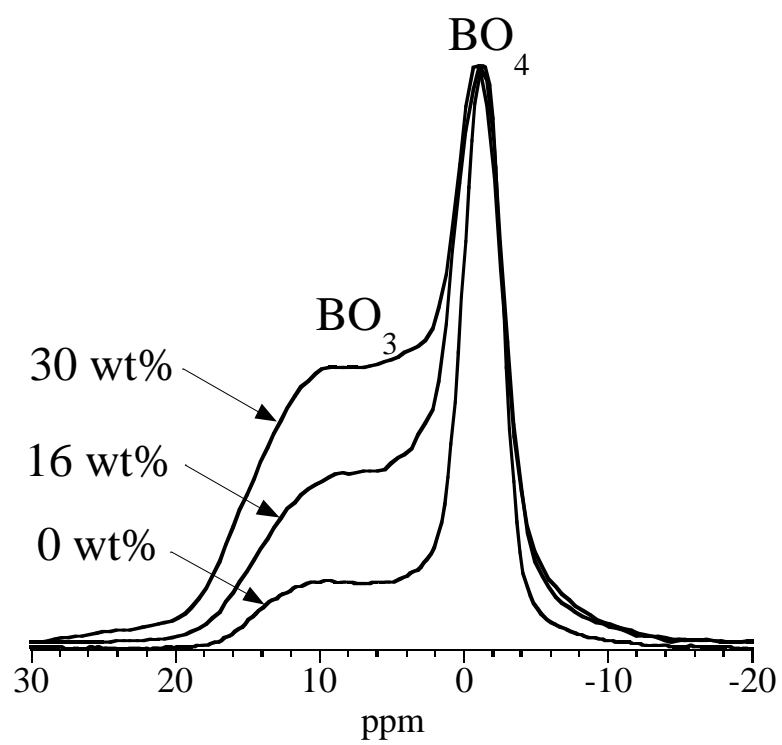


Figure 9



La_2O_3 wt%	% BO_3 units	% BO_4 units
0	42	58
16	62	38
30	80	20

Figure 10

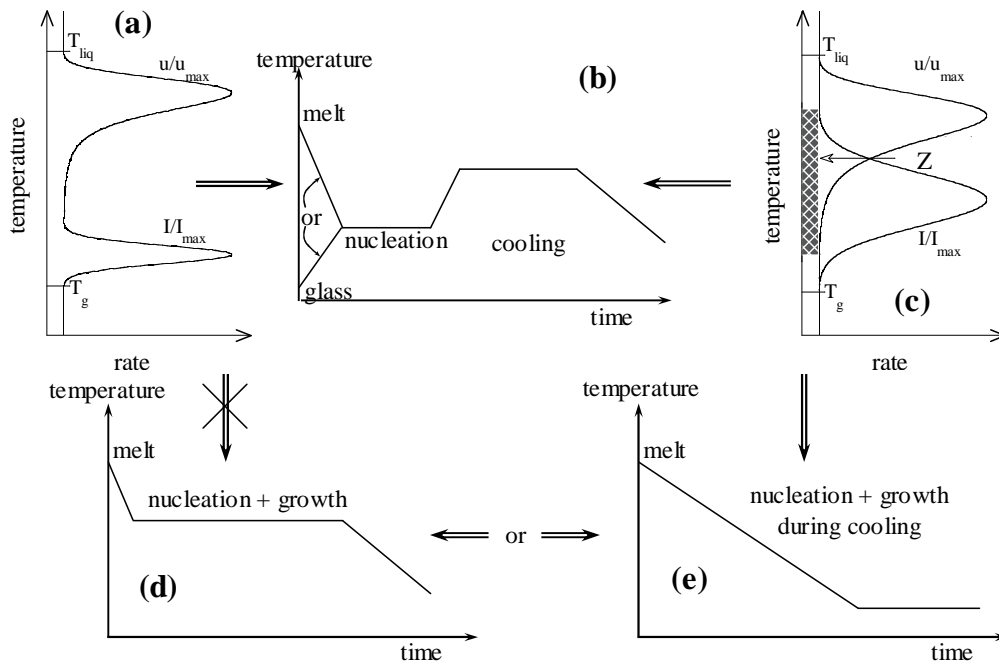


Figure 11

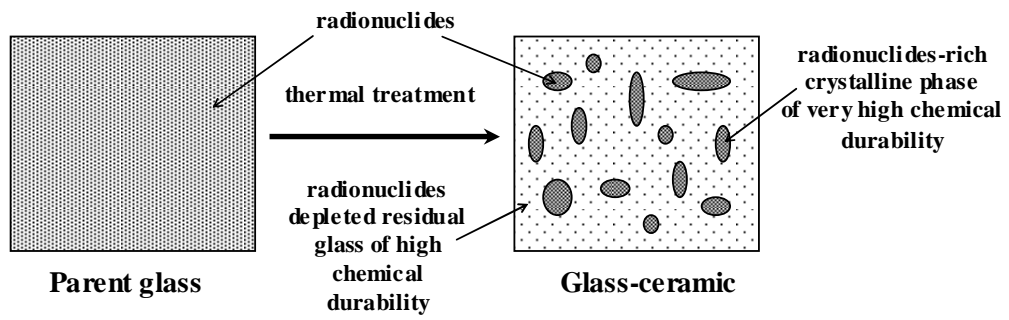


Figure 12

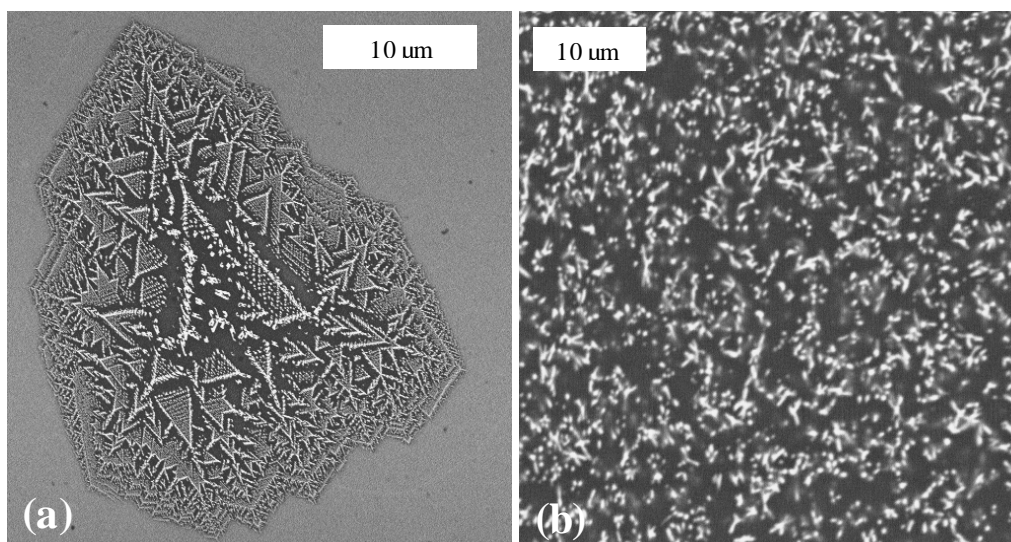


Figure 13

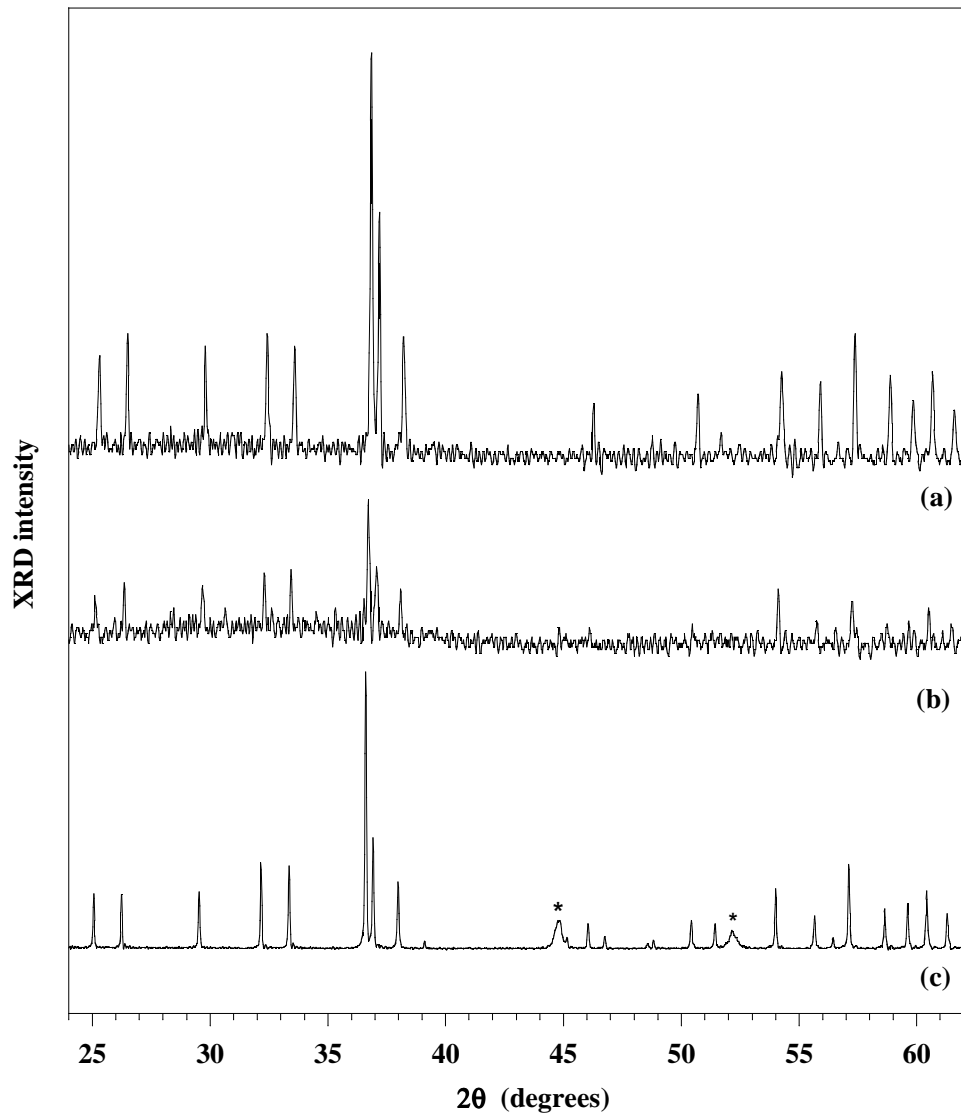


Figure 14

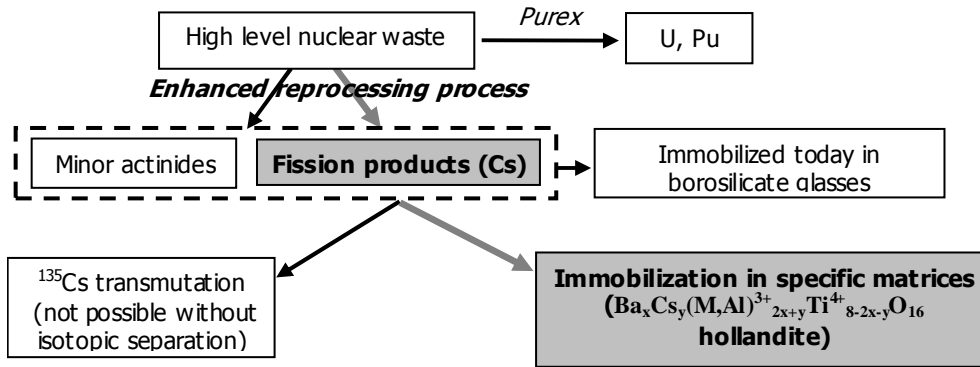


Figure 15

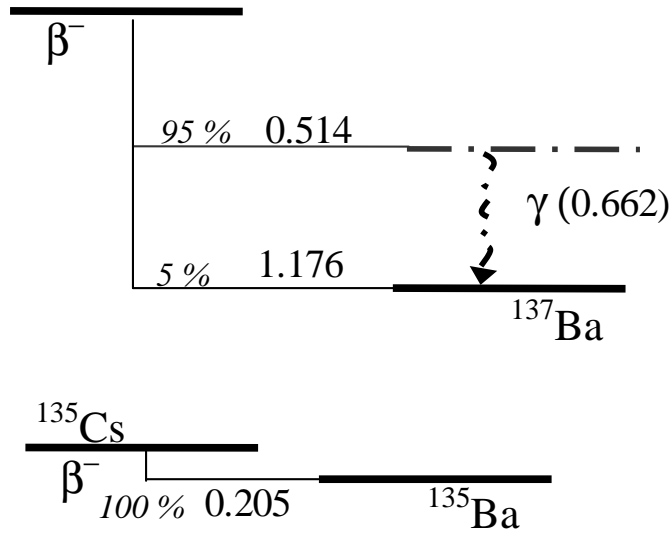


Figure 16

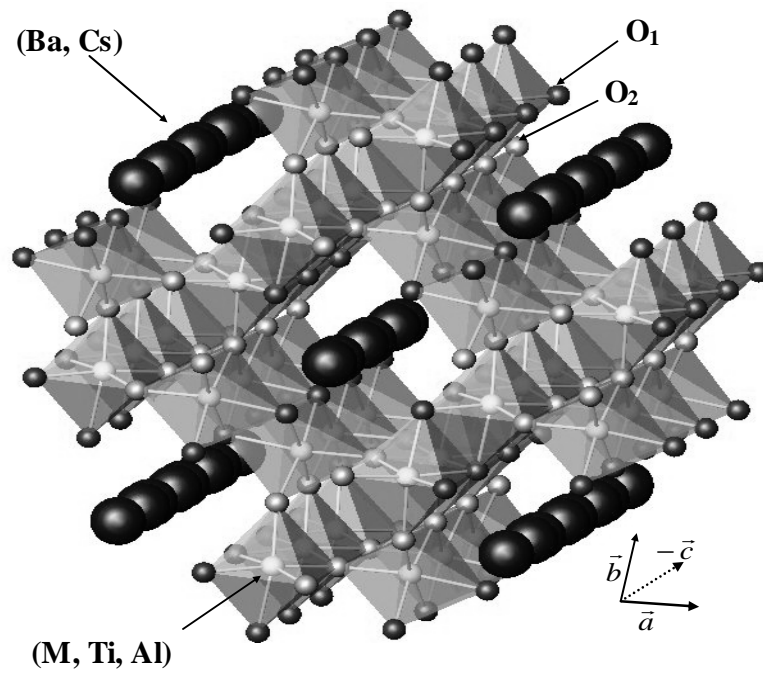


Figure 17

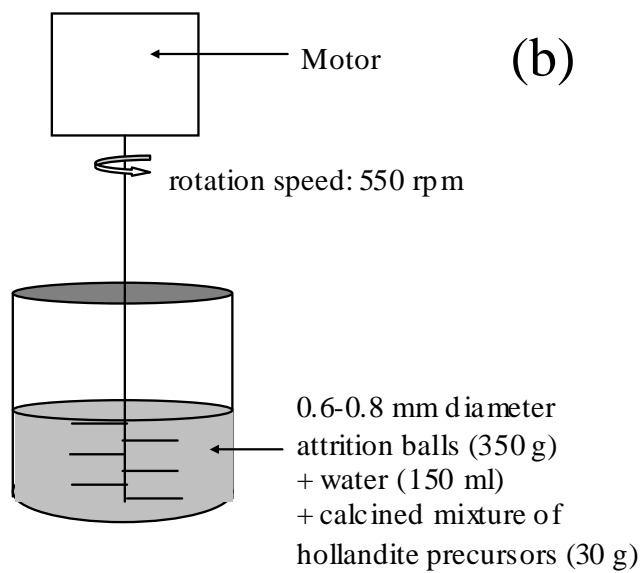
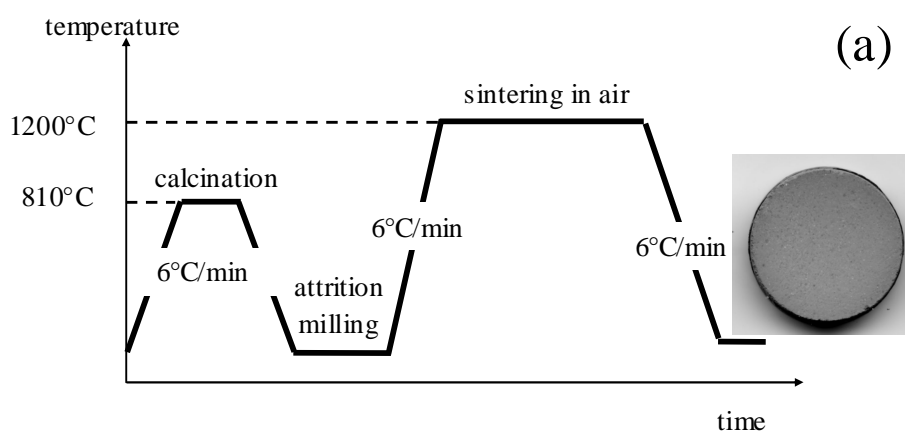


Figure 18

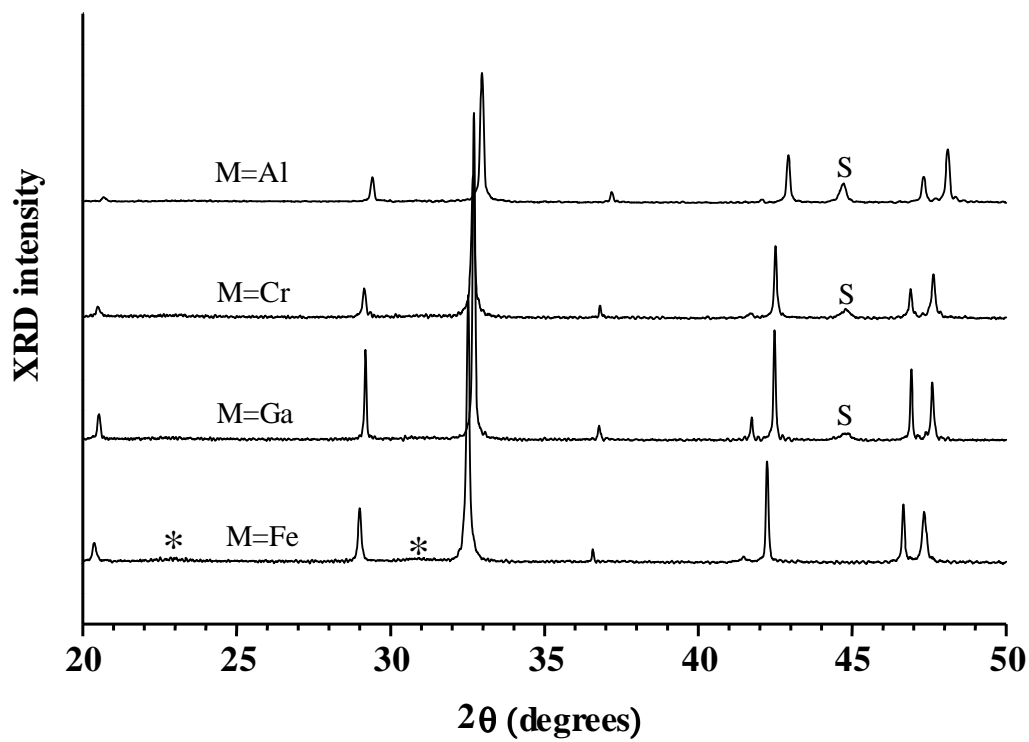


Figure 19

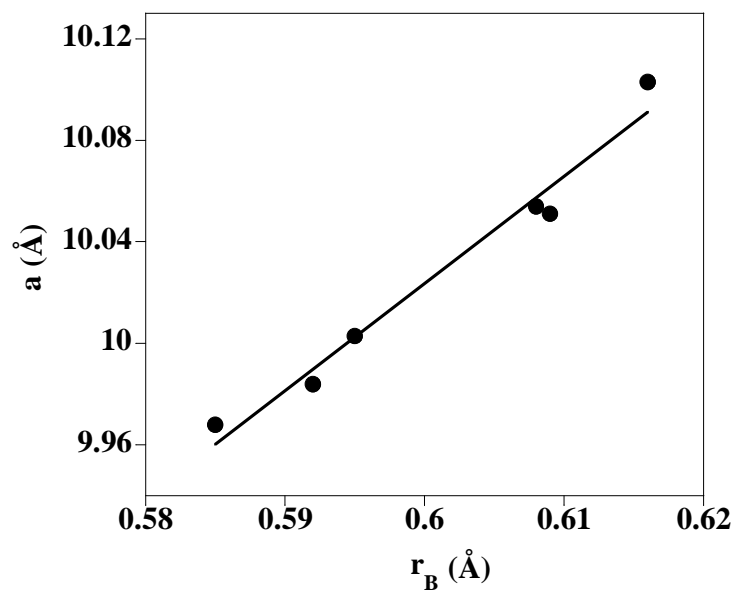


Figure 20

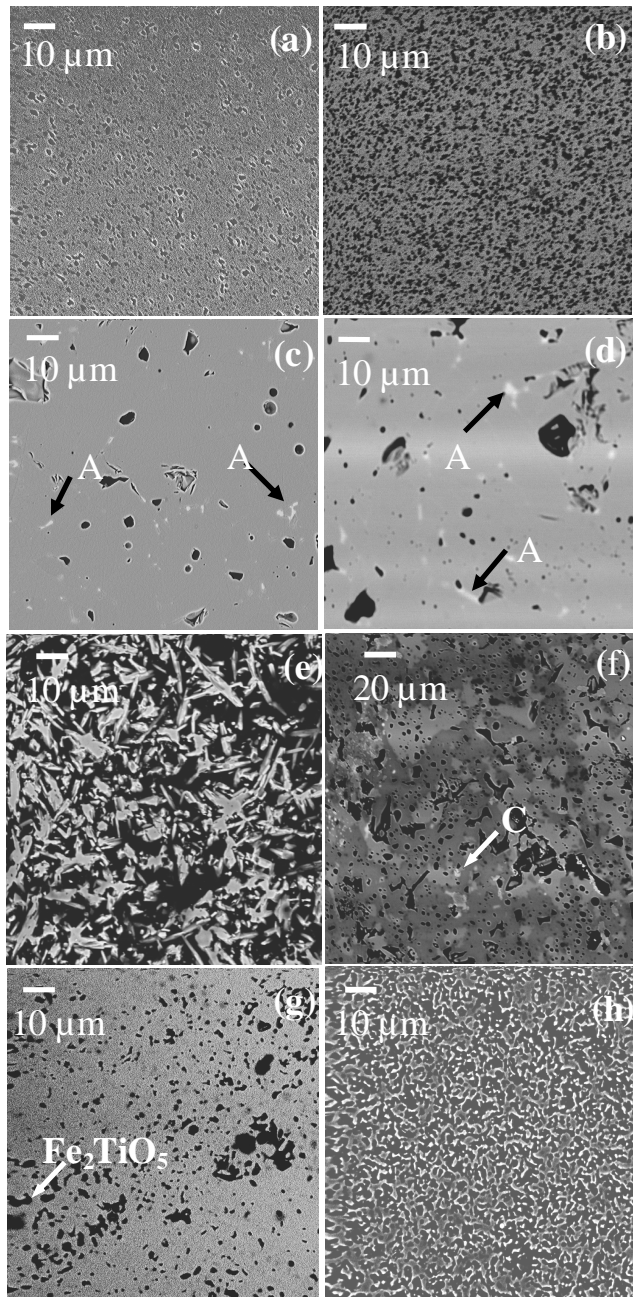


Figure 21

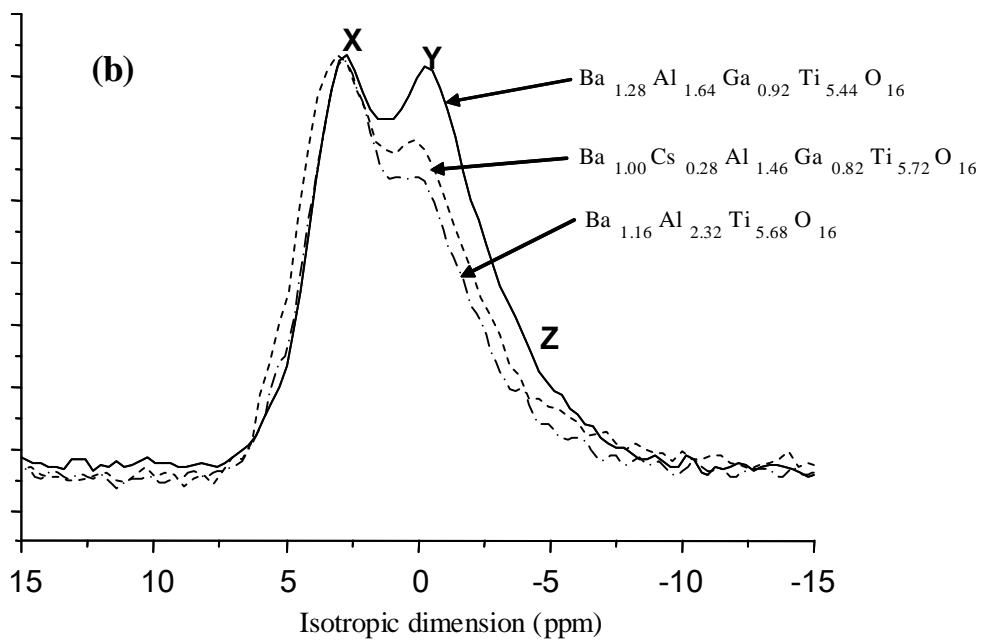
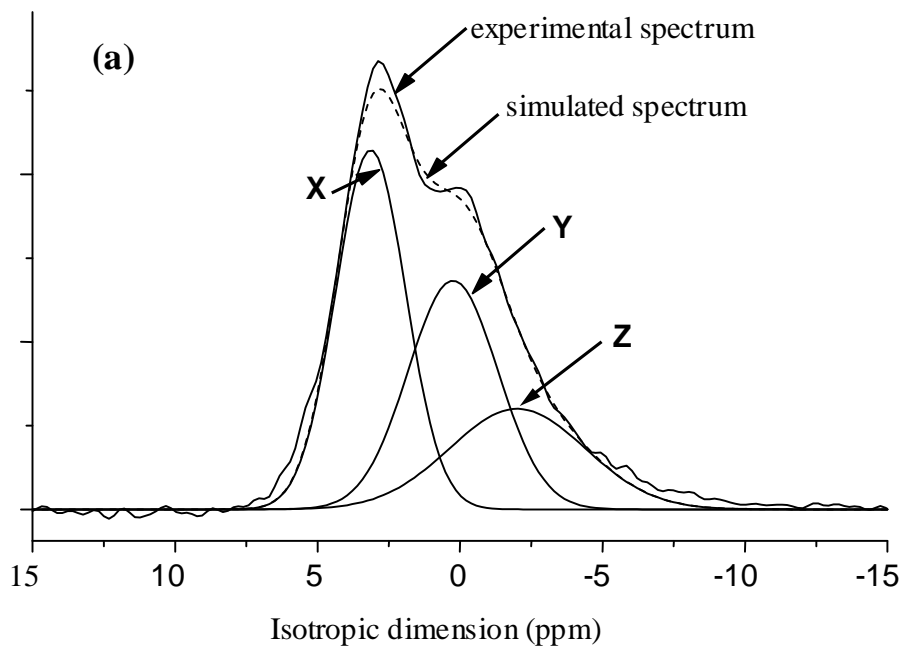


Figure 22

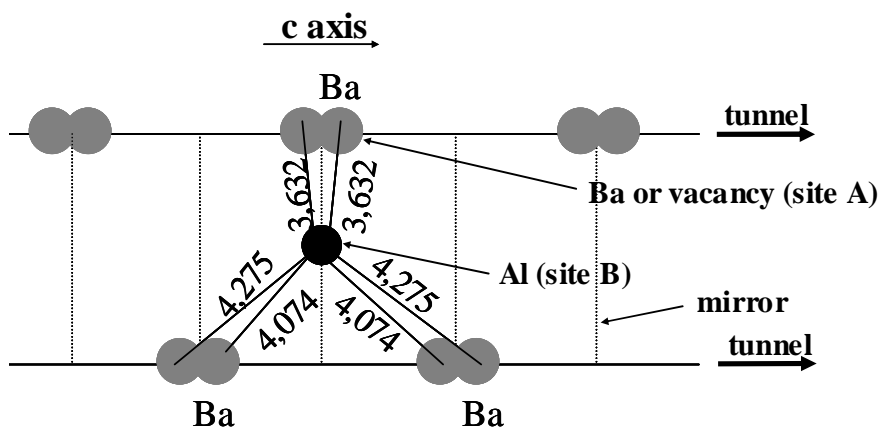


Figure 23

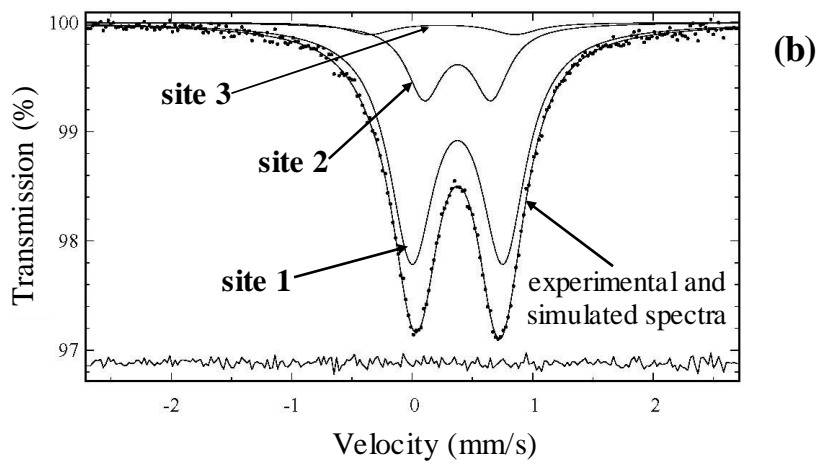
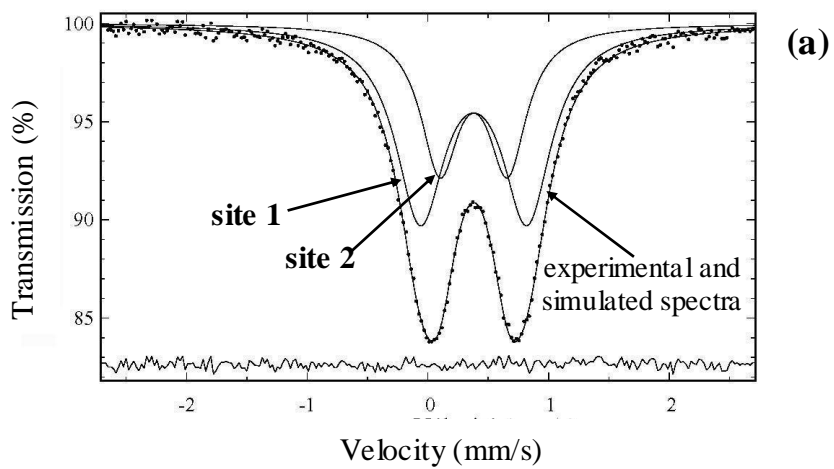


Figure 24

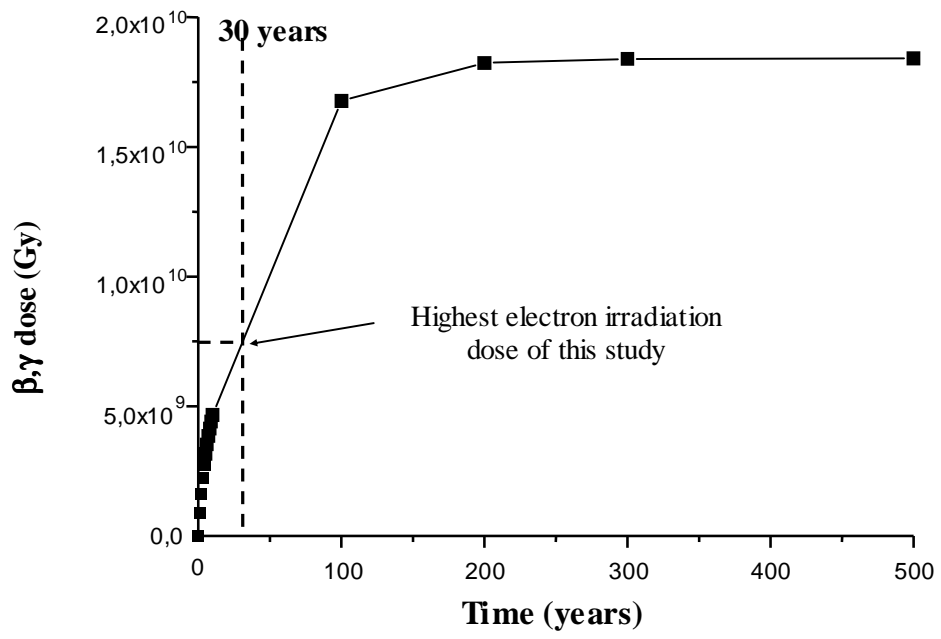


Figure 25

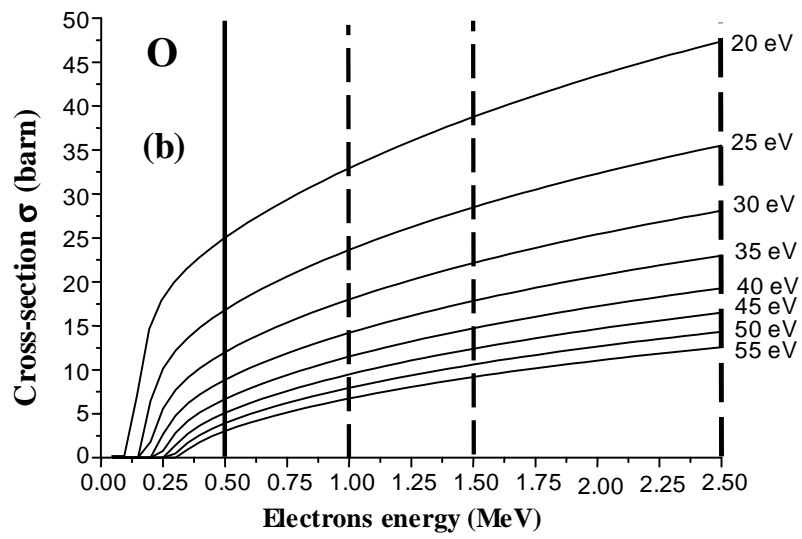
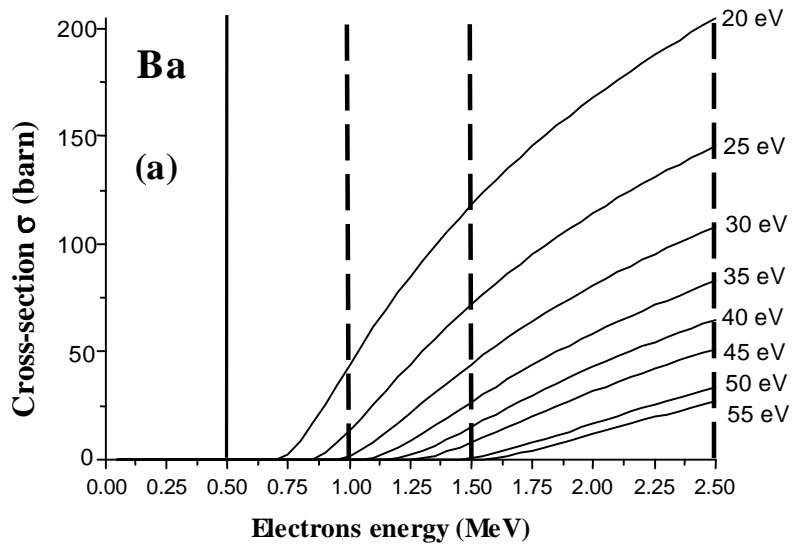


Figure 26

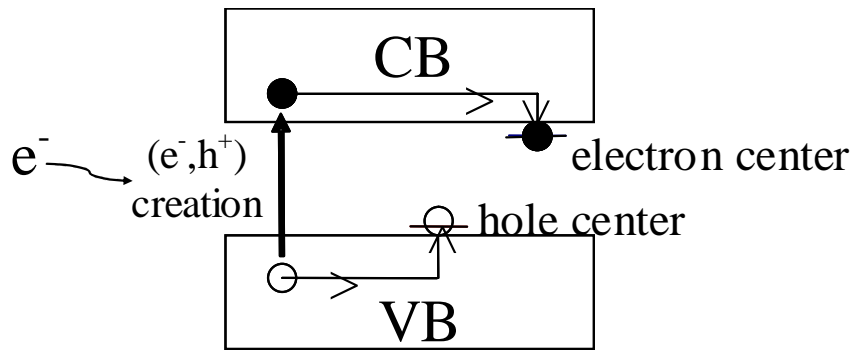


Figure 27

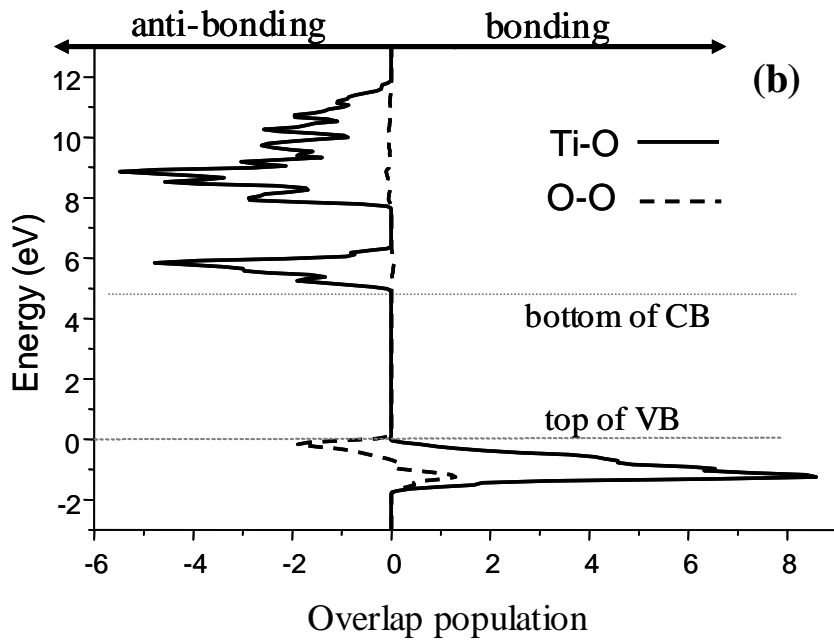
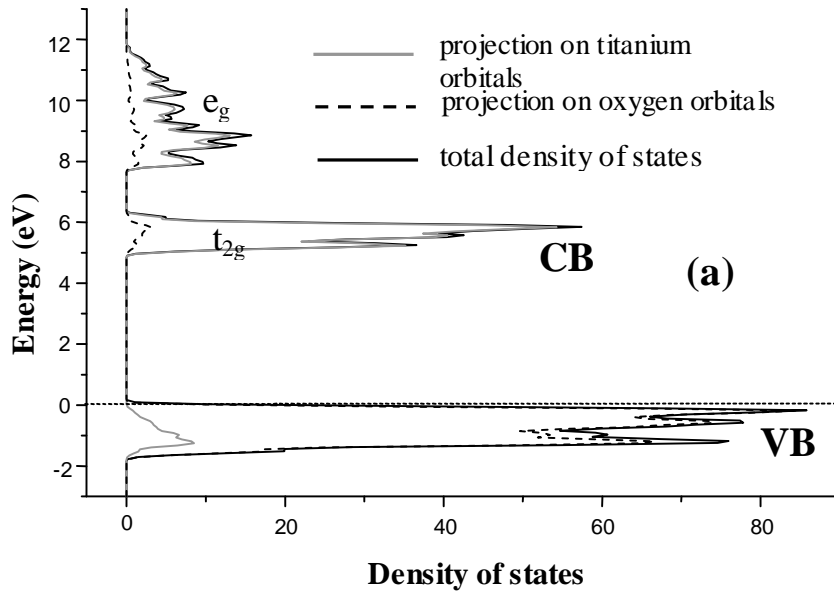


Figure 28

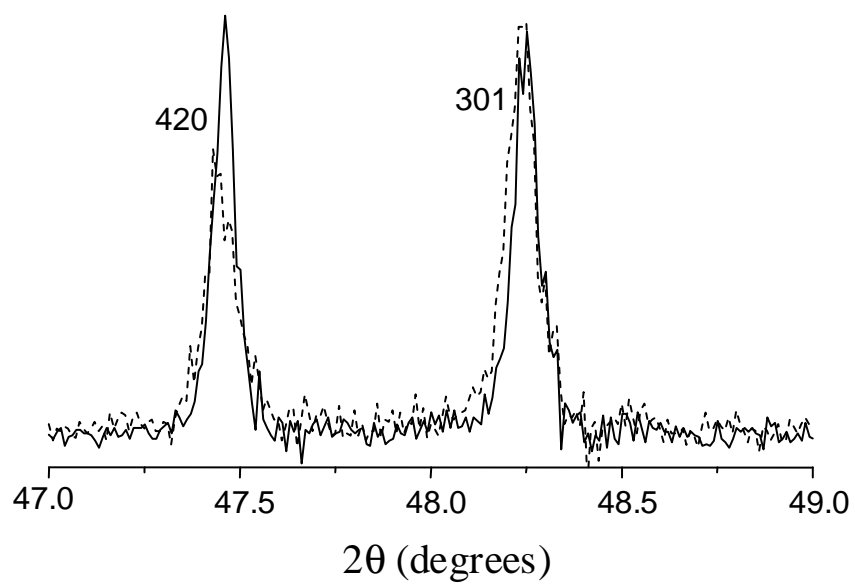


Figure 29

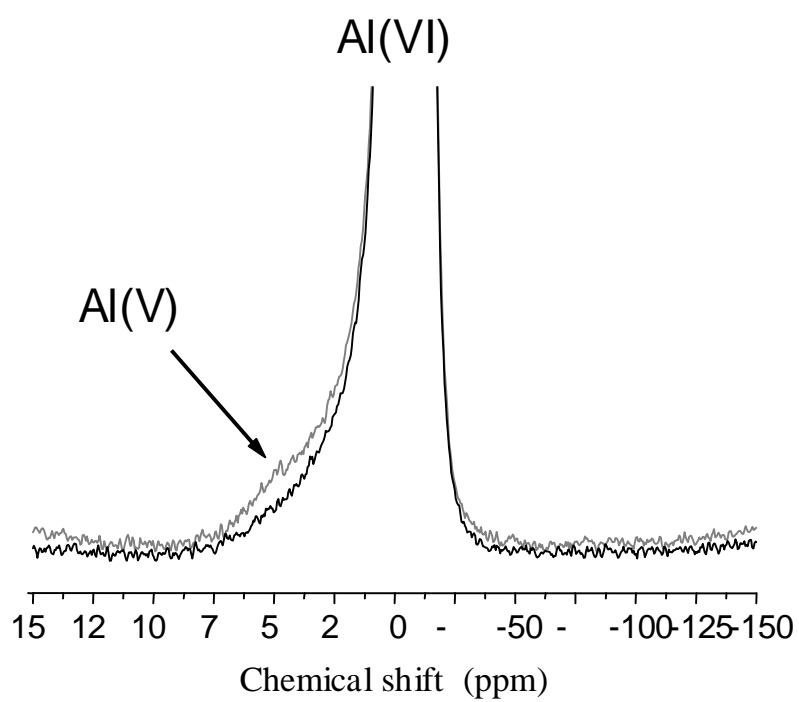


Figure 30

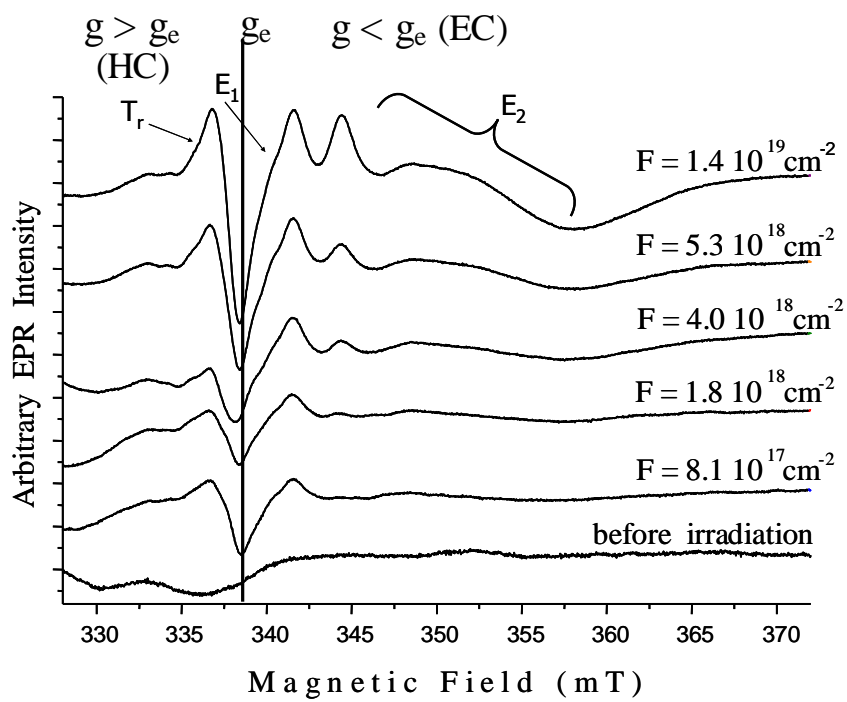


Figure 31

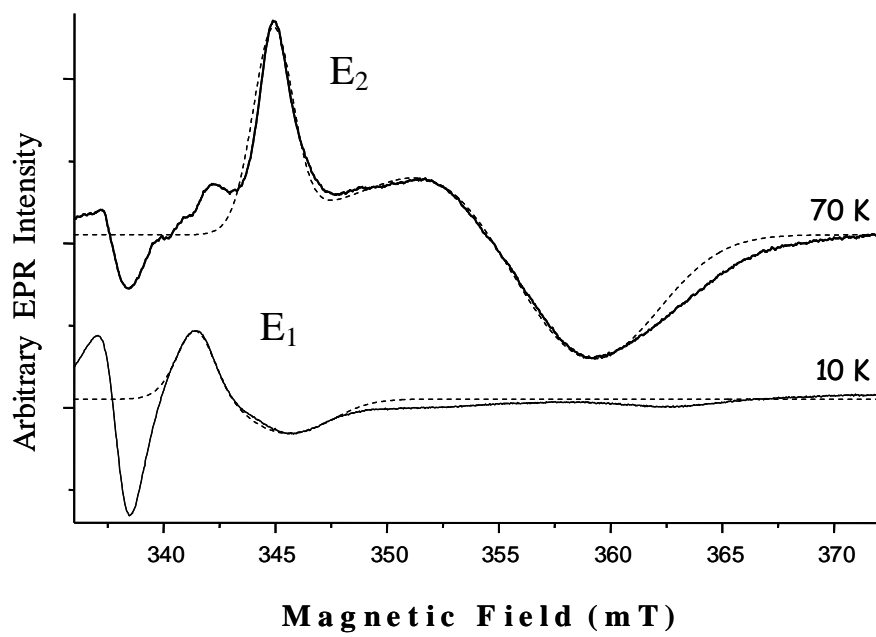


Figure 32

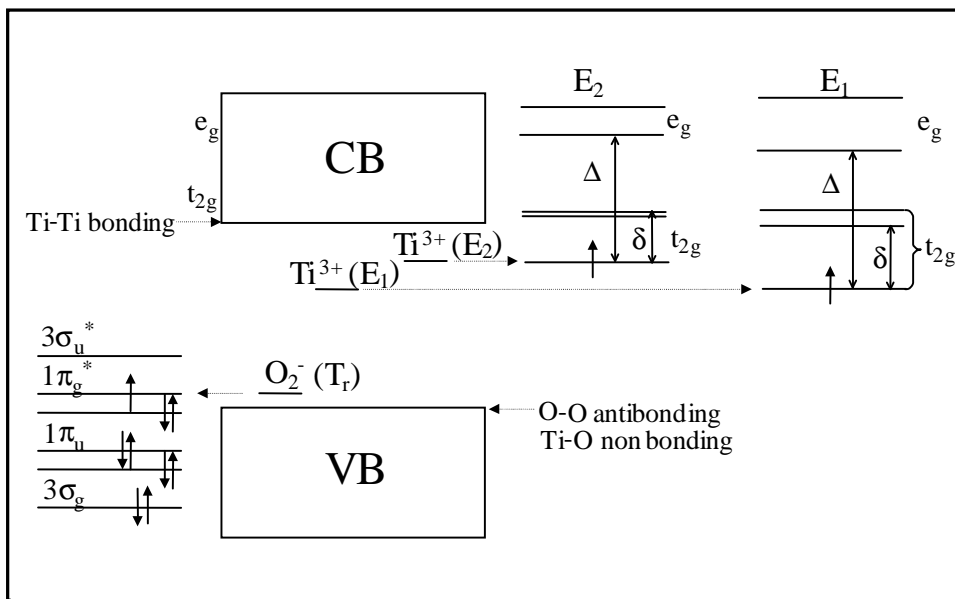


Figure 33

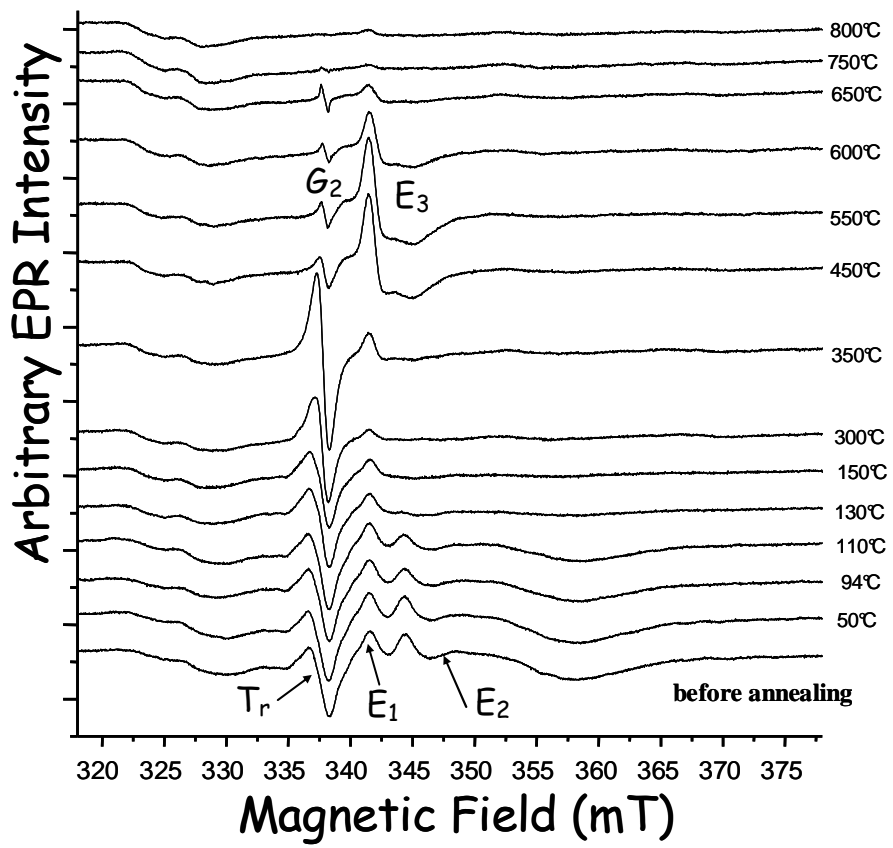


Figure 34

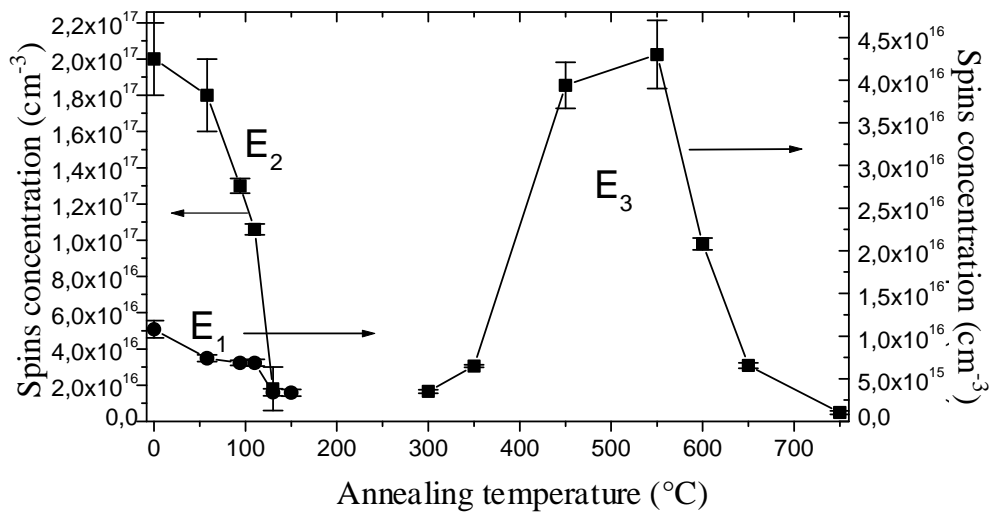
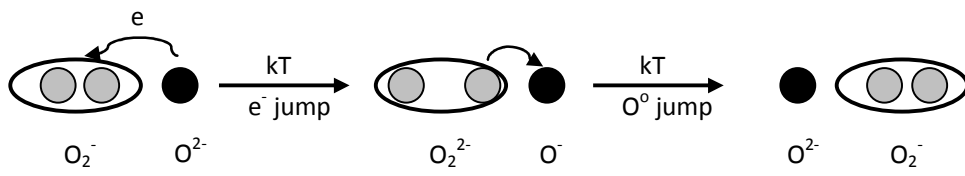


Figure 35



(b)

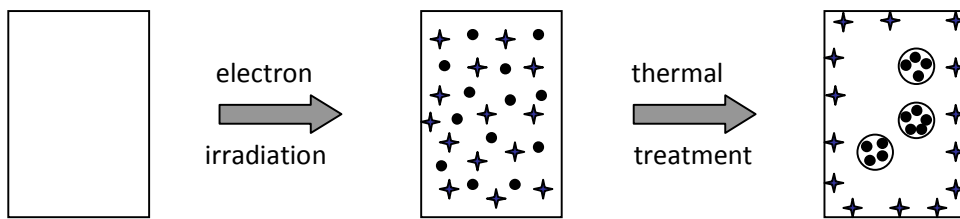


Figure 36

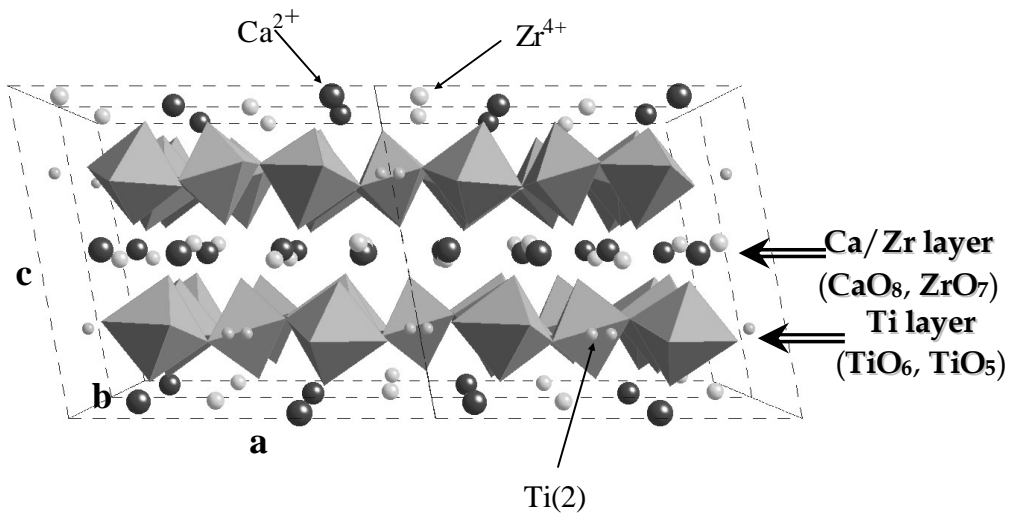


Figure 37

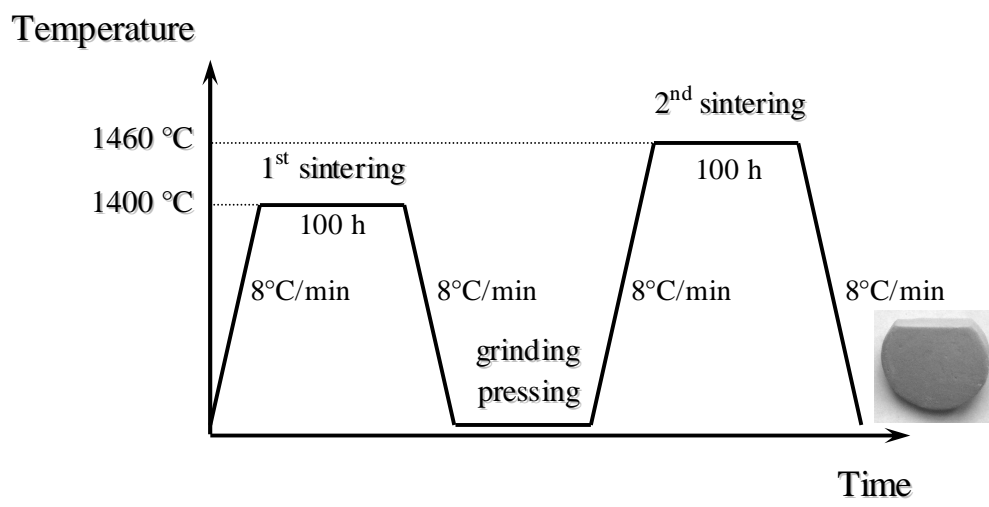


Figure 38

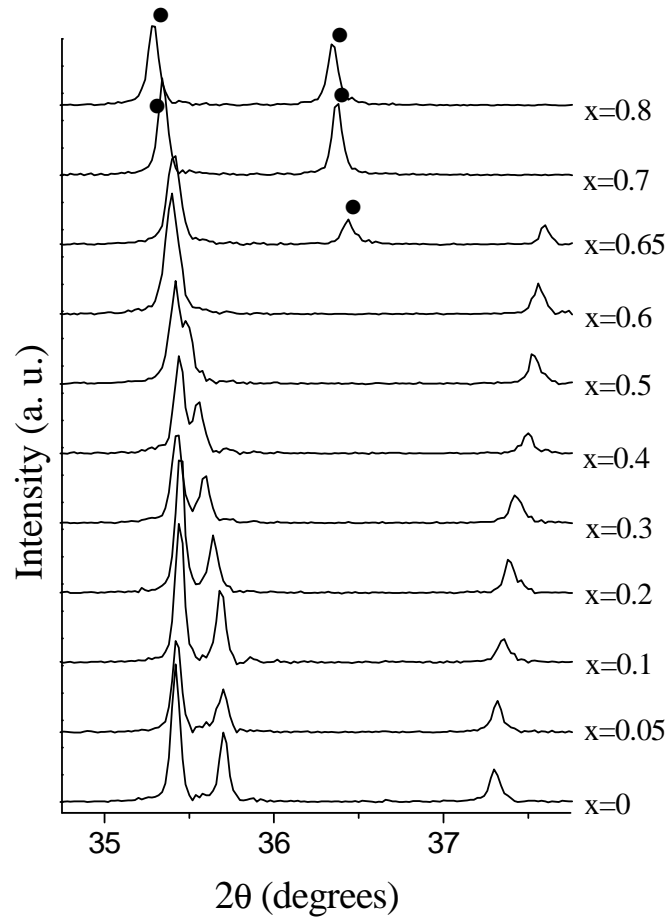


Figure 39

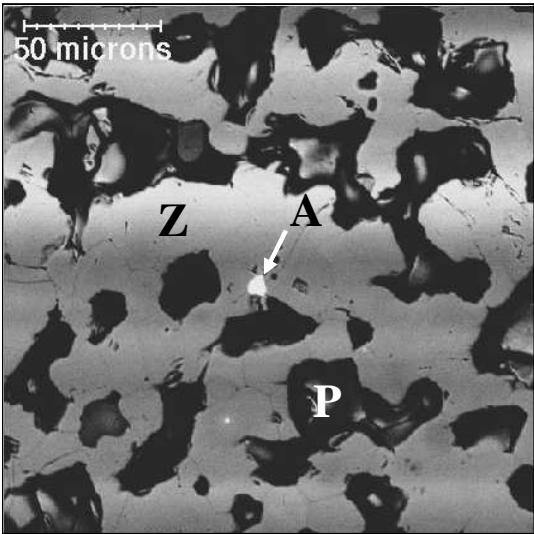


Figure 40

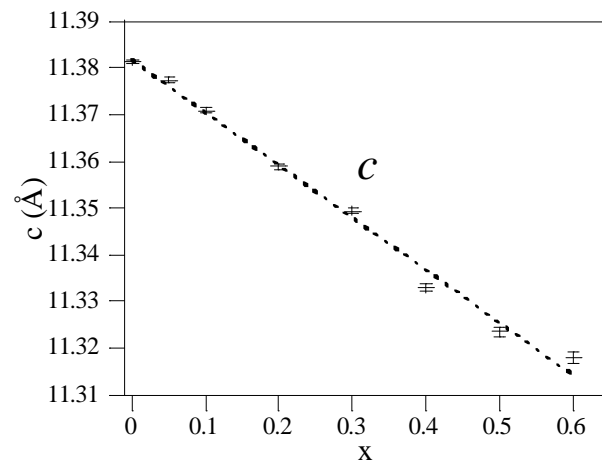
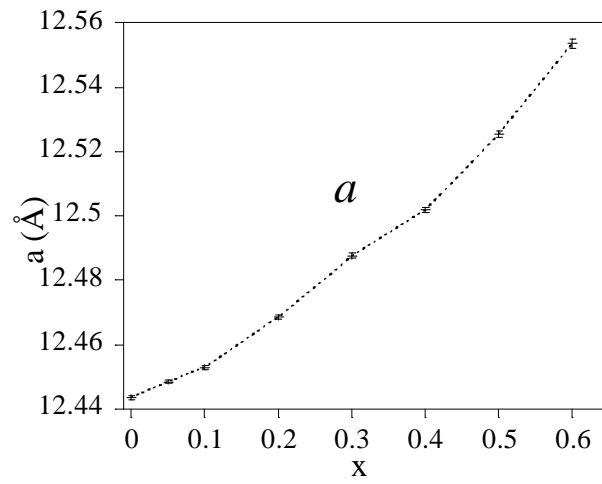


Figure 41

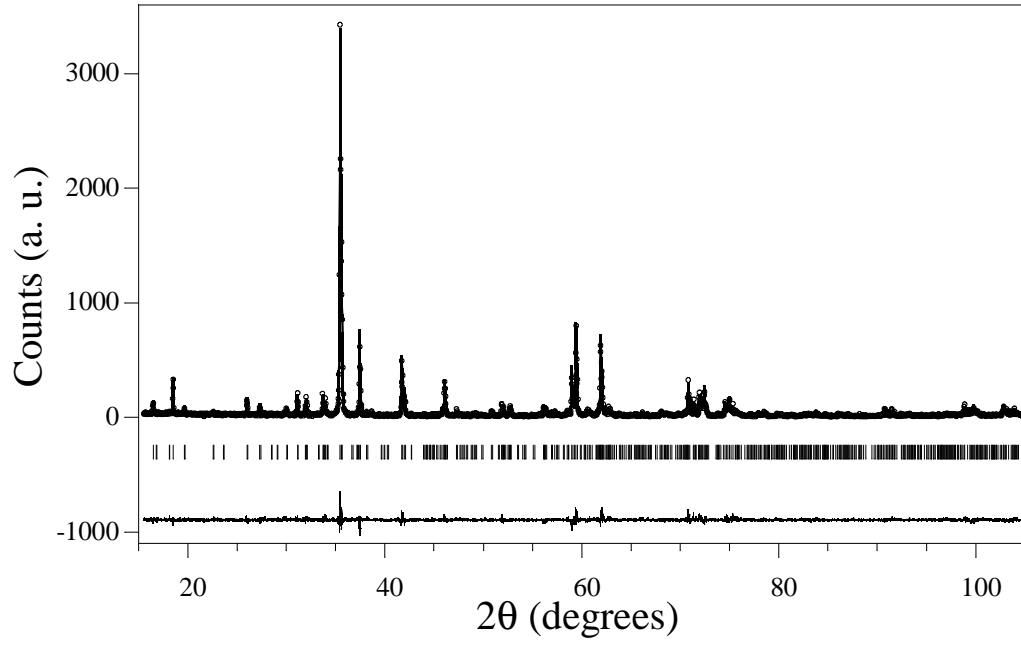


Figure 42

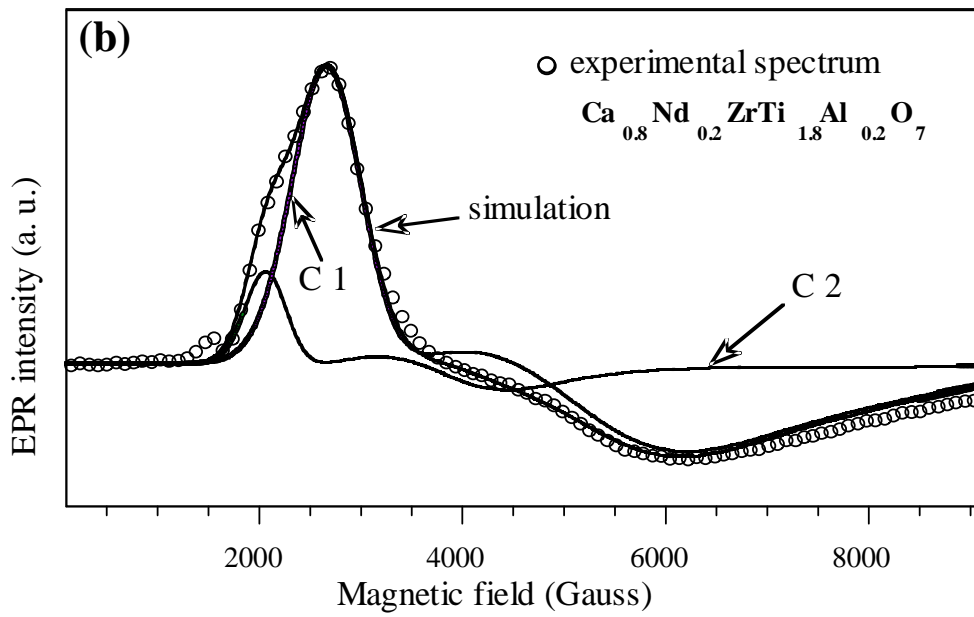
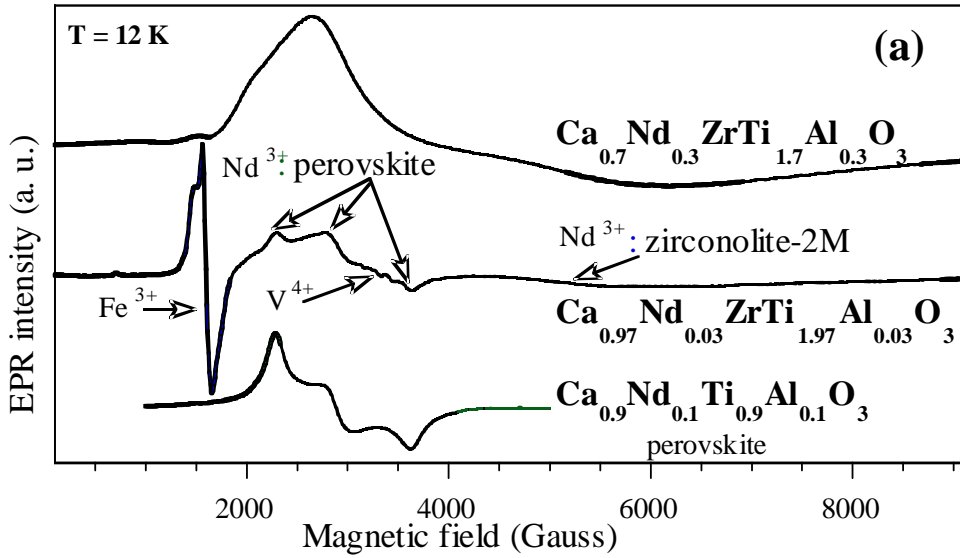


Figure 43

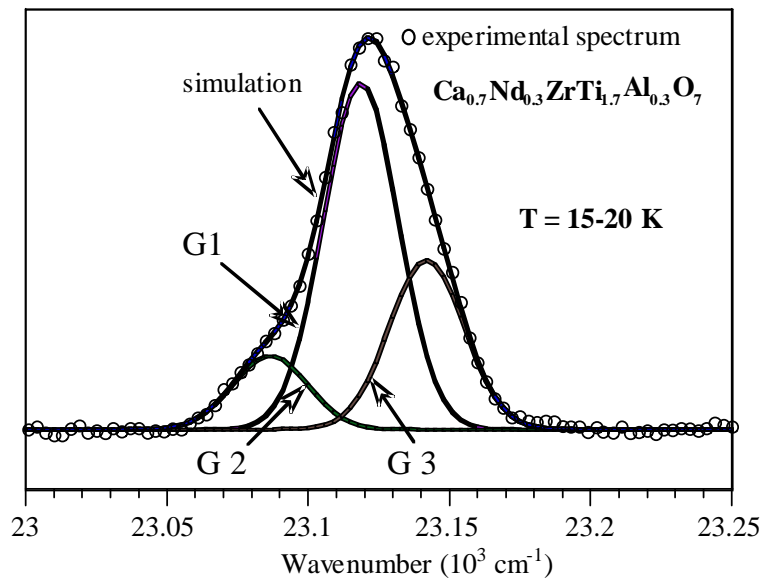
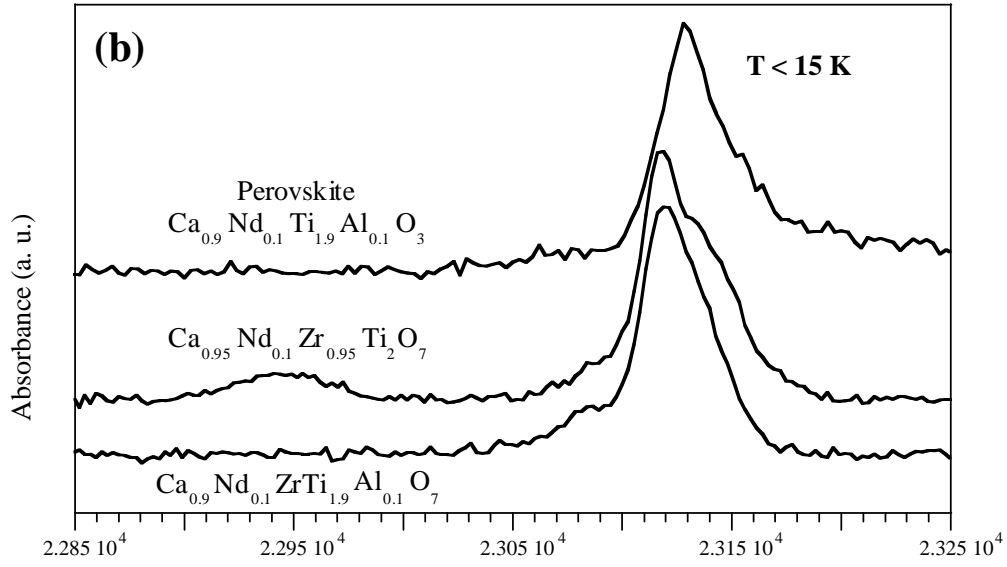


Figure 44

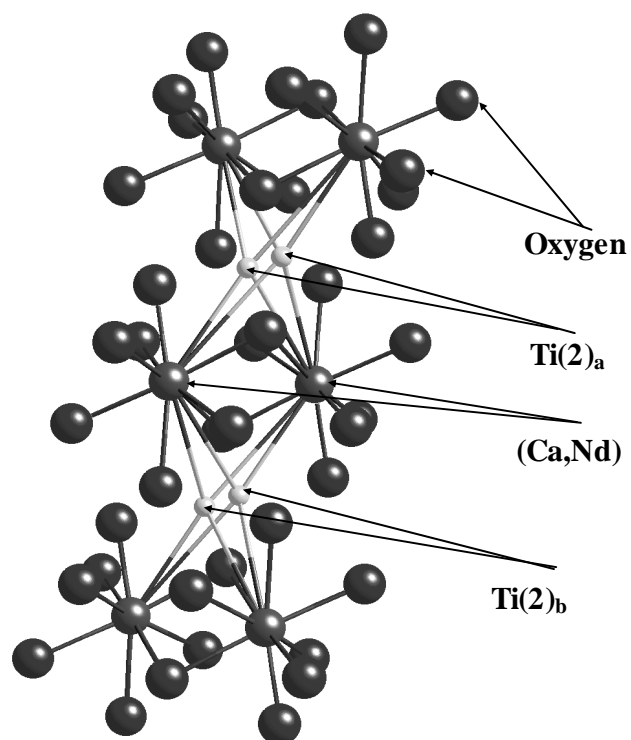


Figure 45

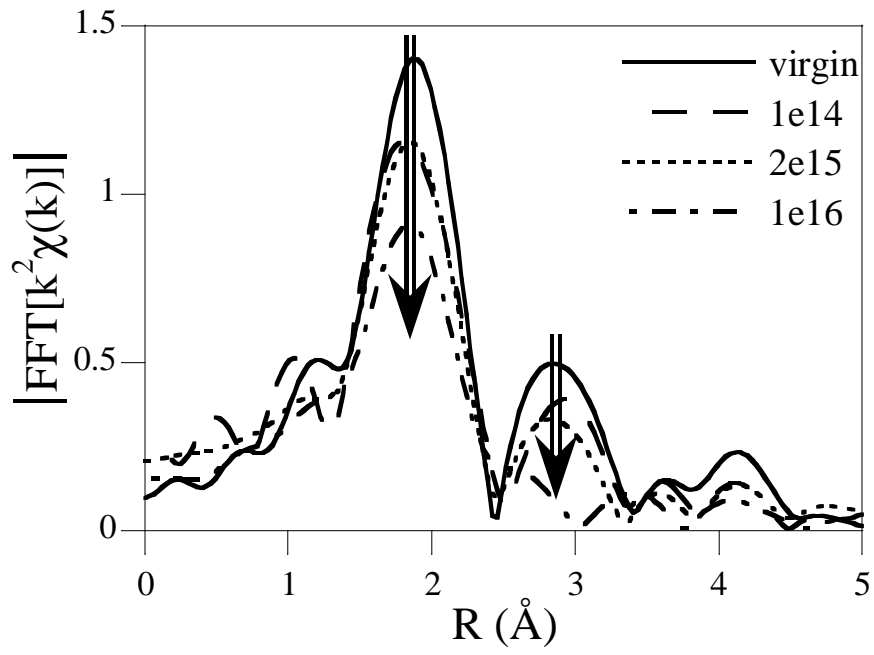


Figure 46

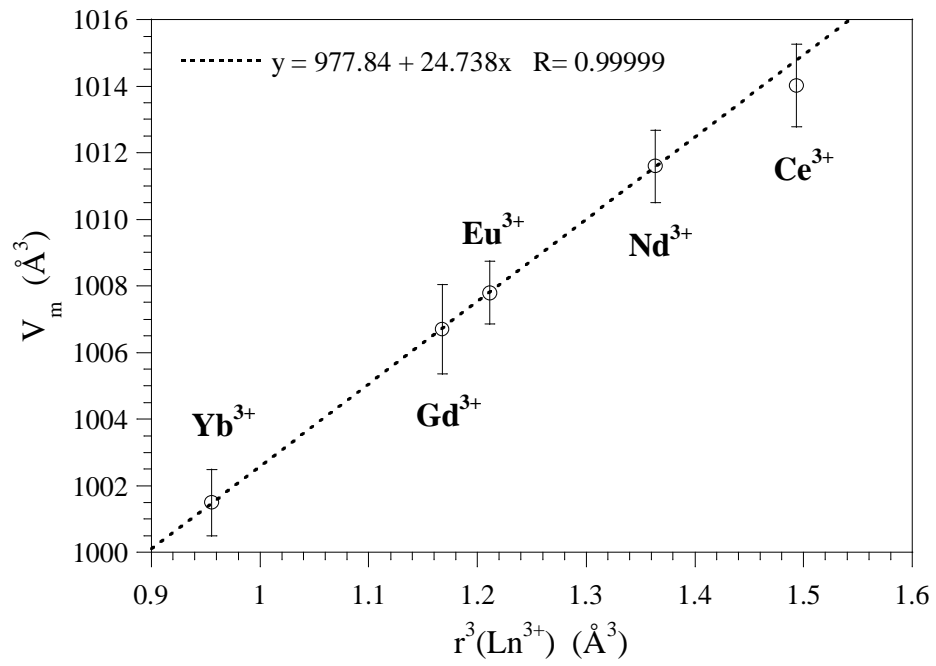


Figure 47

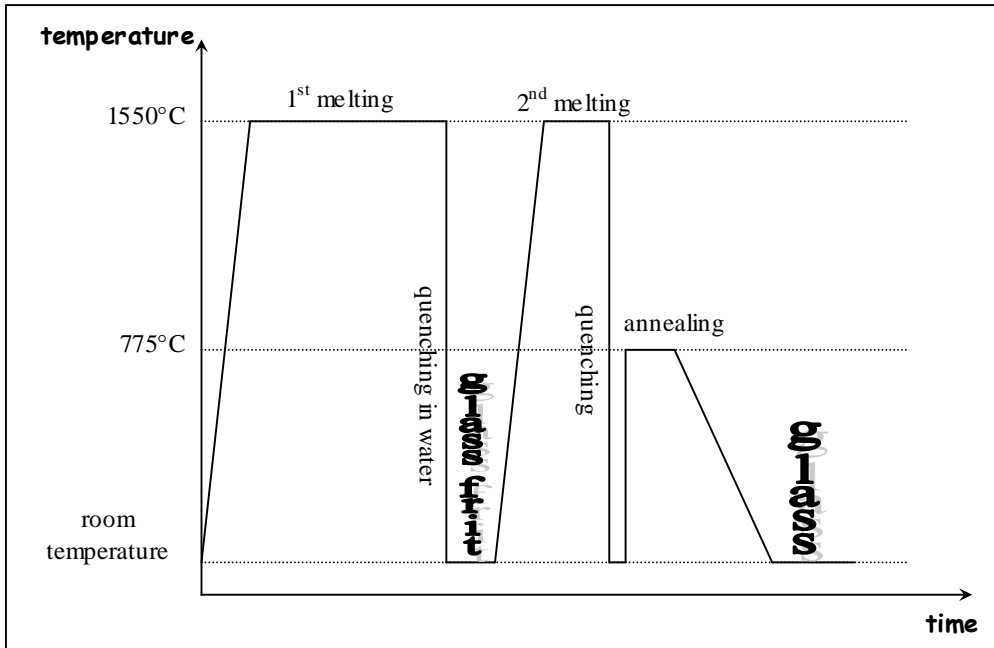


Figure 48

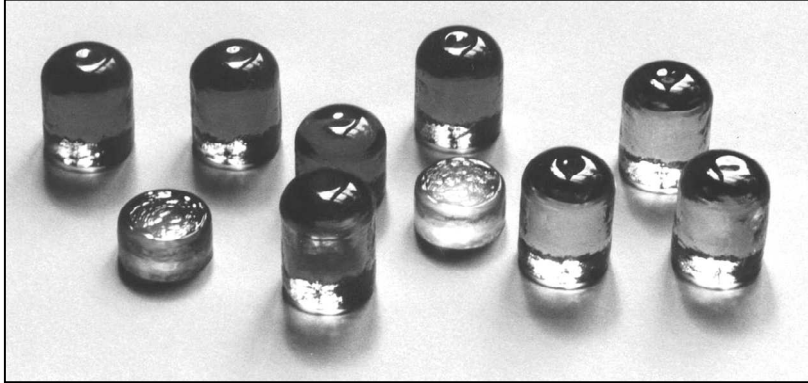


Figure 49

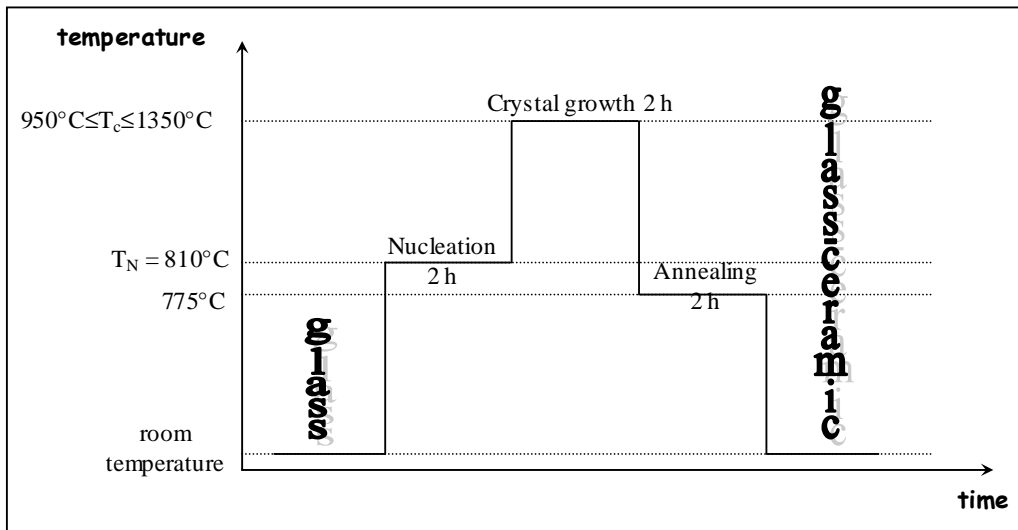


Figure 50

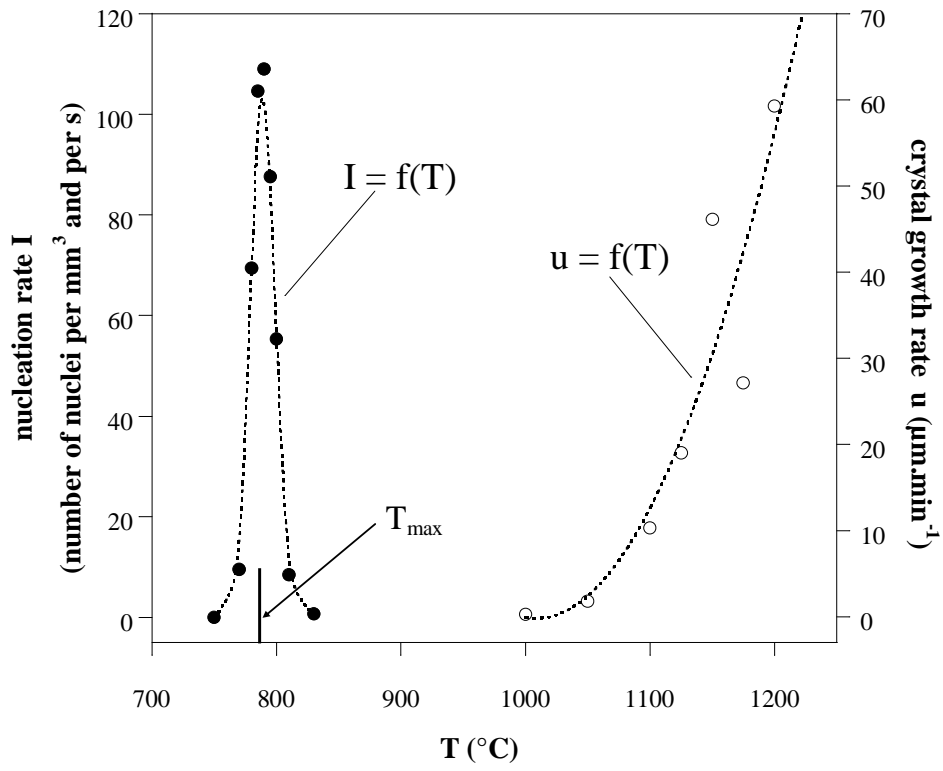


Figure 51

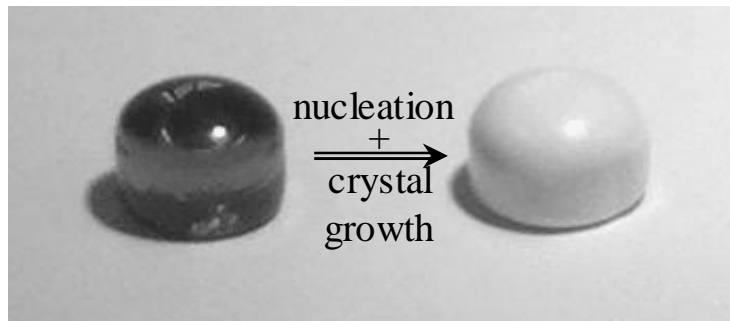


Figure 52

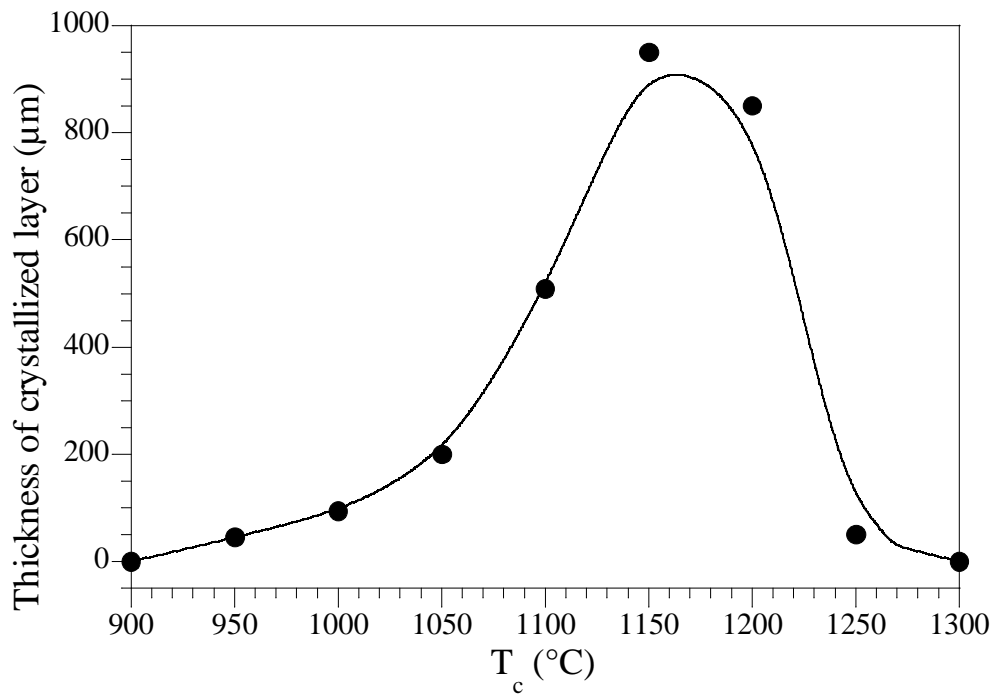


Figure 53

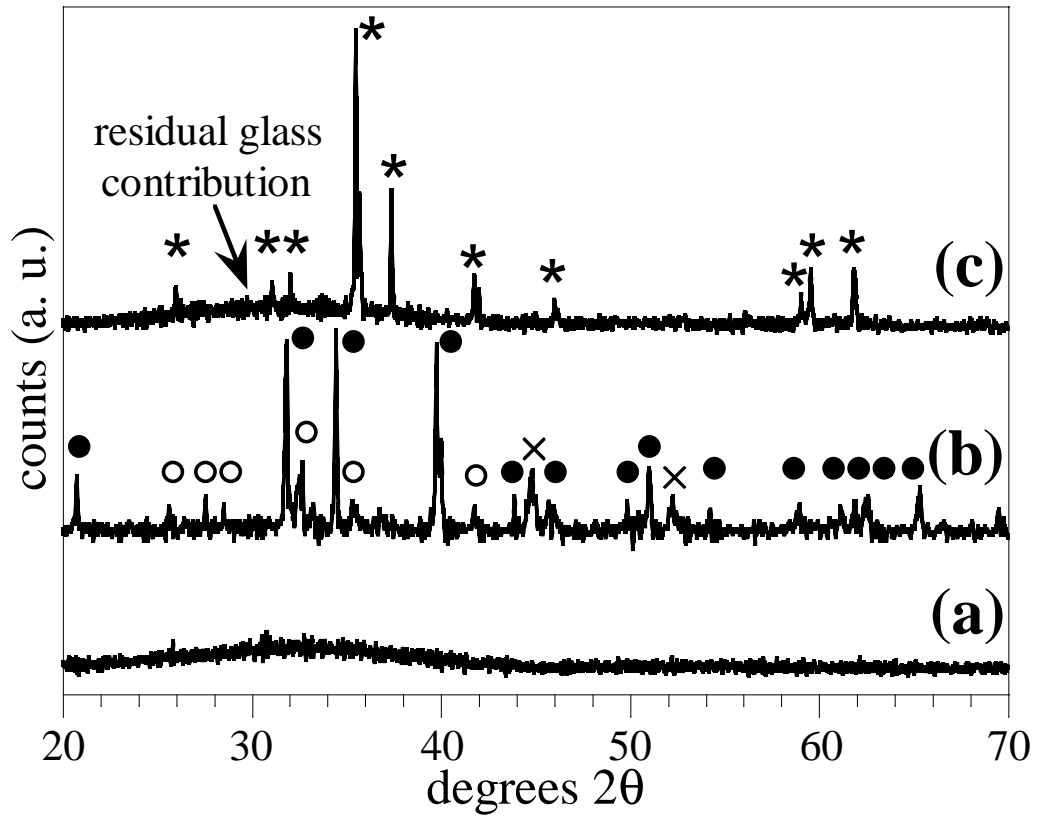


Figure 54

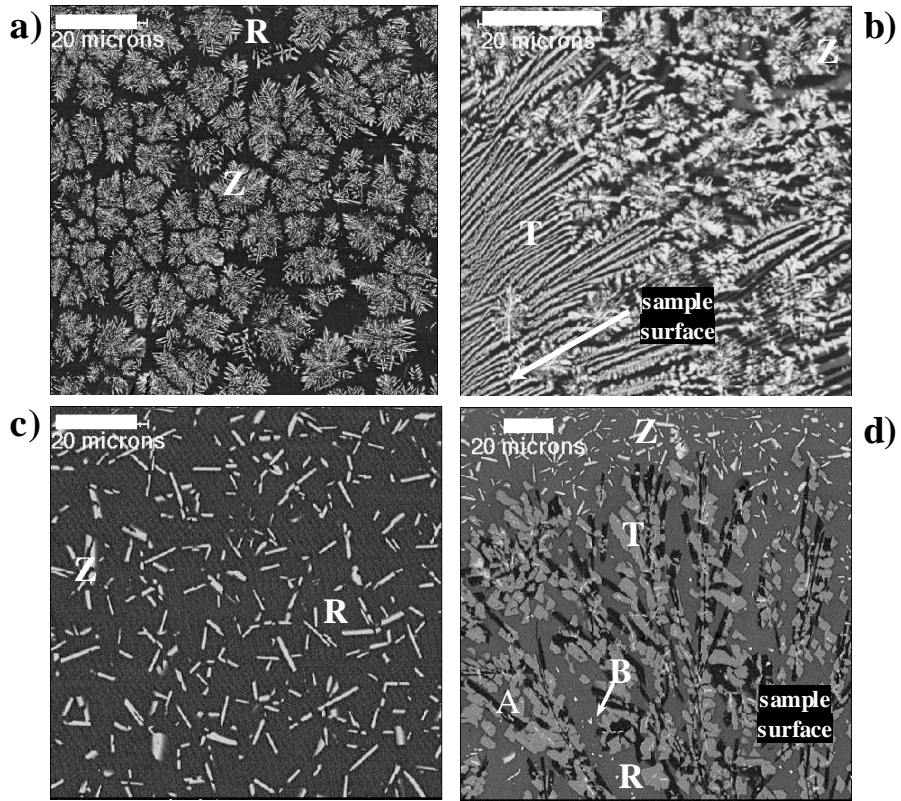


Figure 55

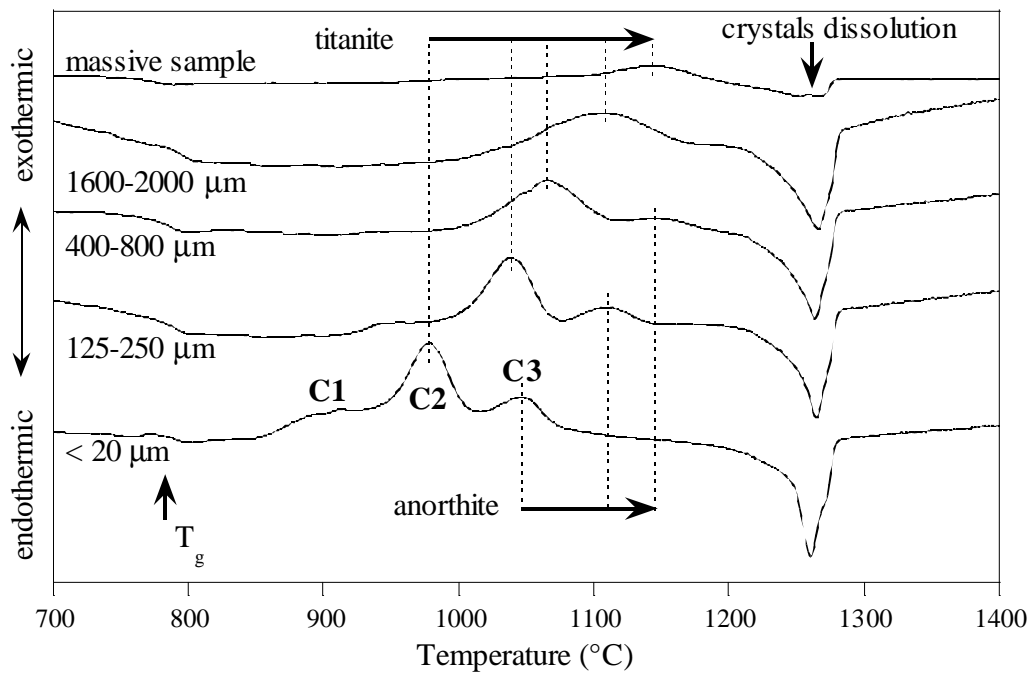


Figure 56

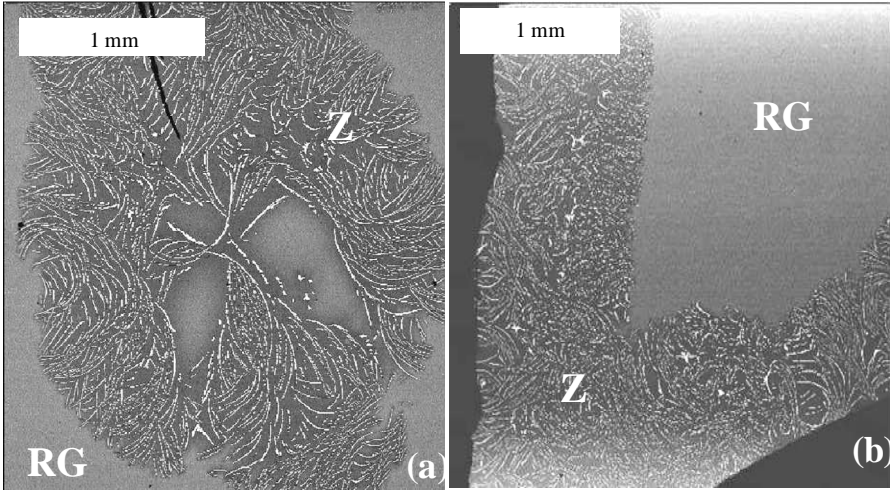


Figure 57

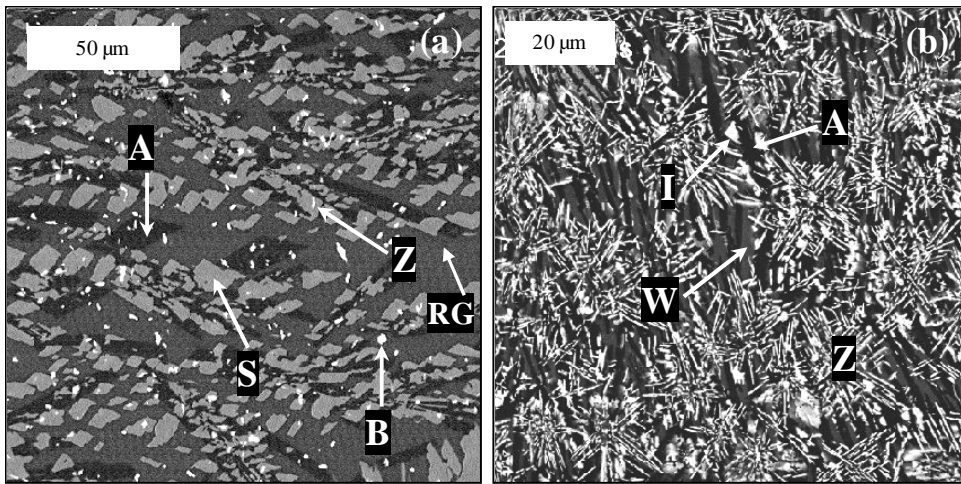


Figure 58

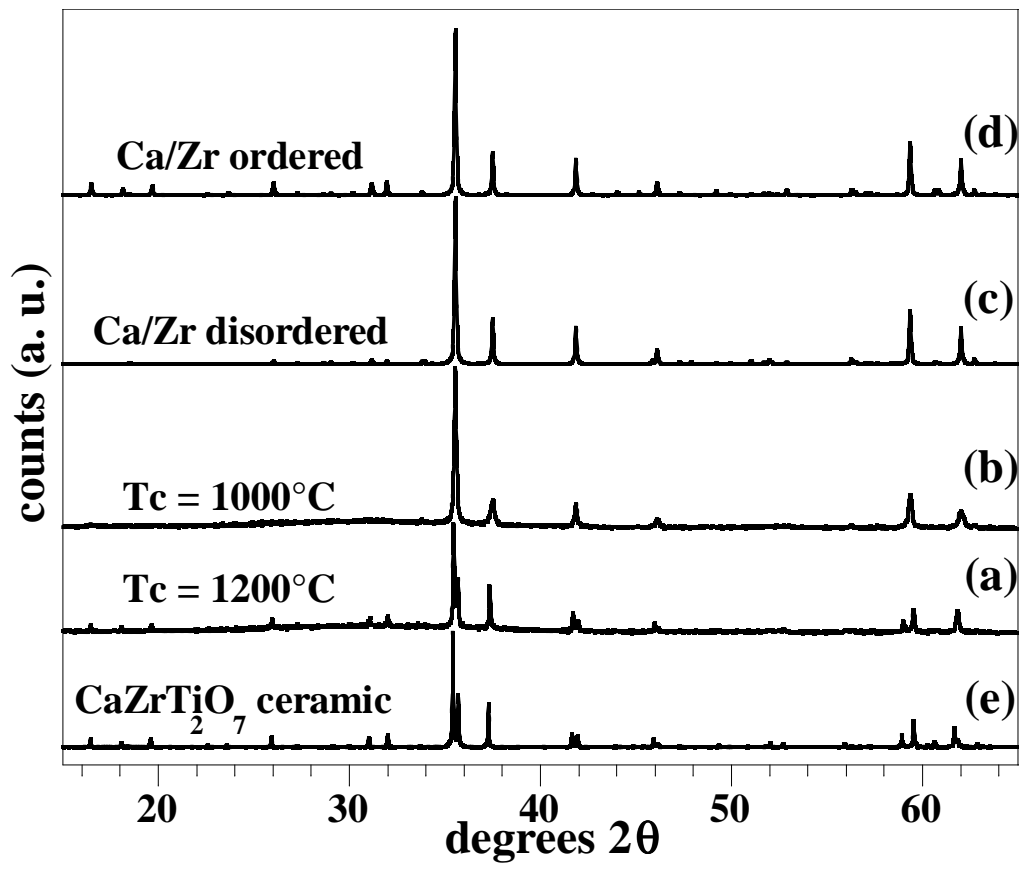


Figure 59

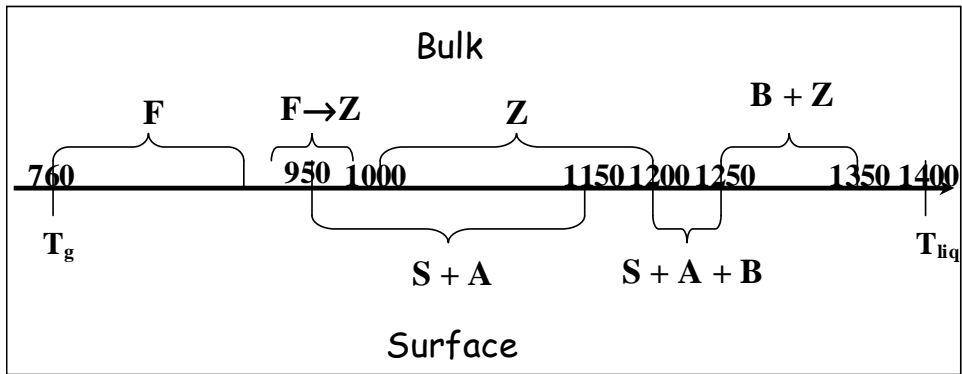


Figure 60

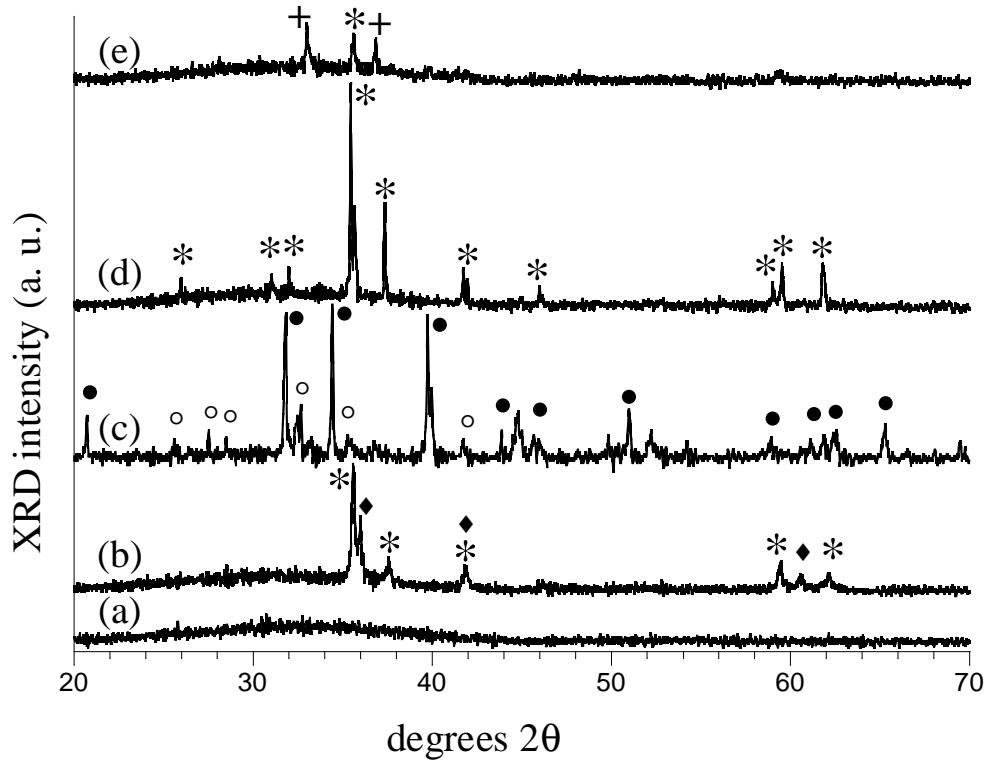


Figure 61

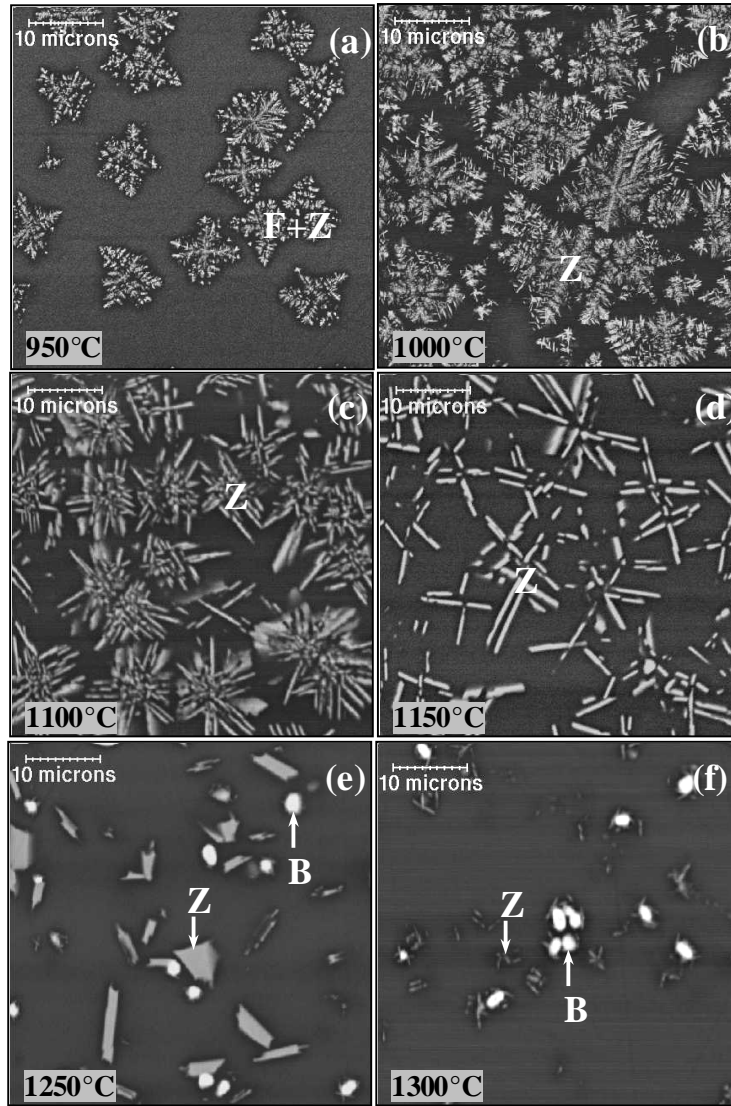


Figure 62

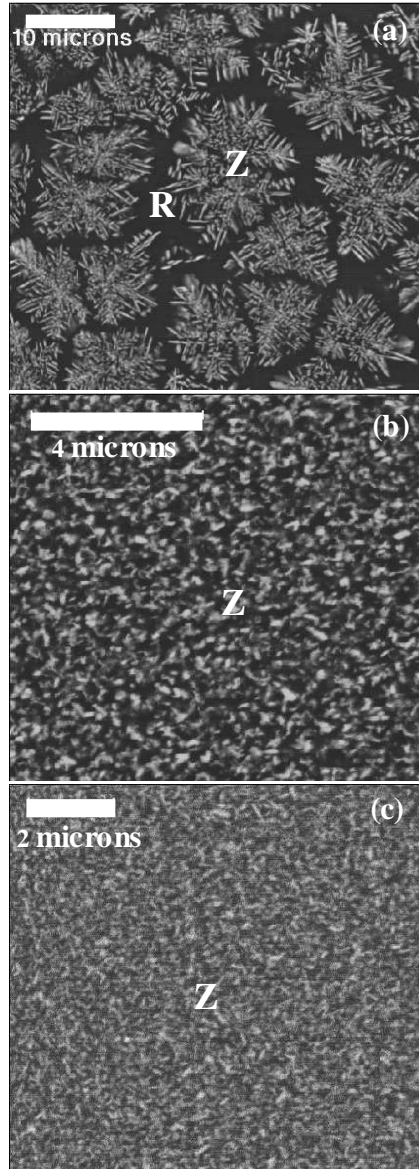


Figure 63

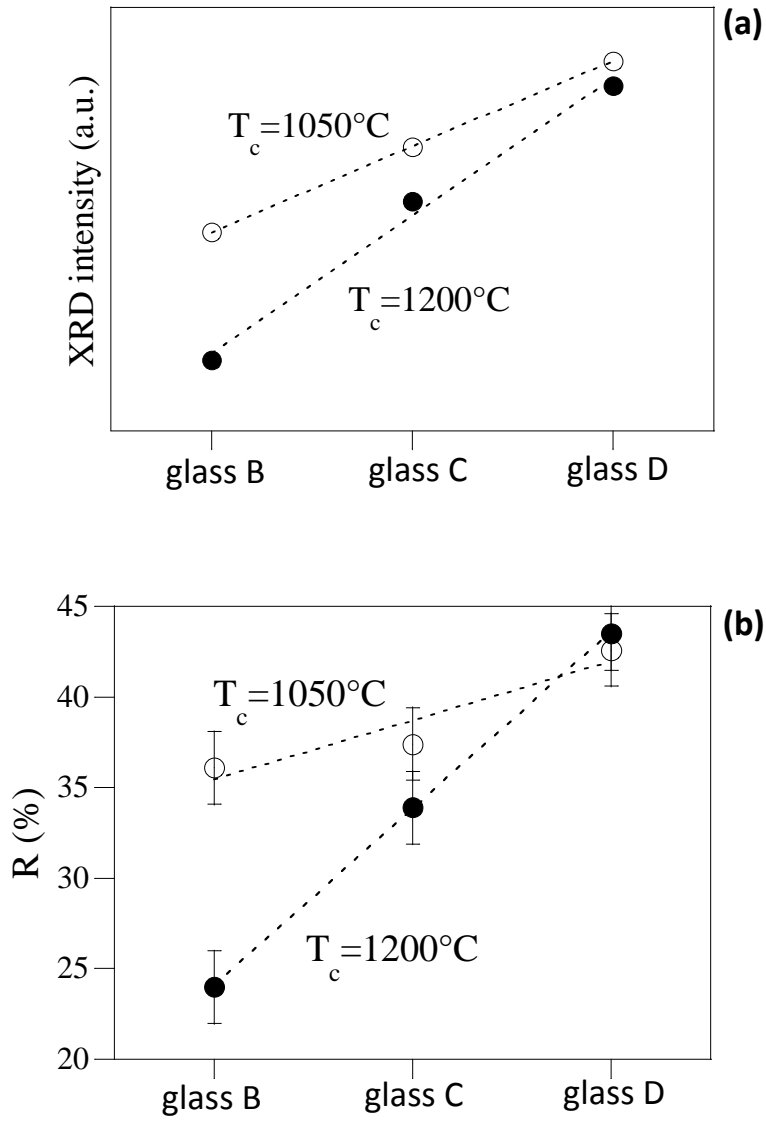


Figure 64

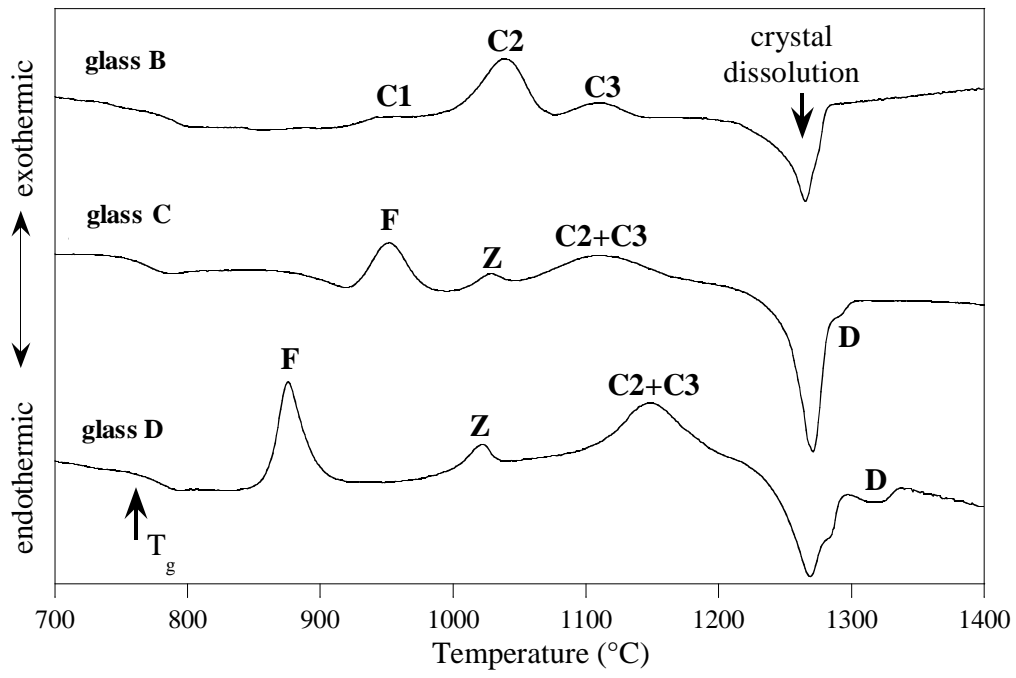


Figure 65

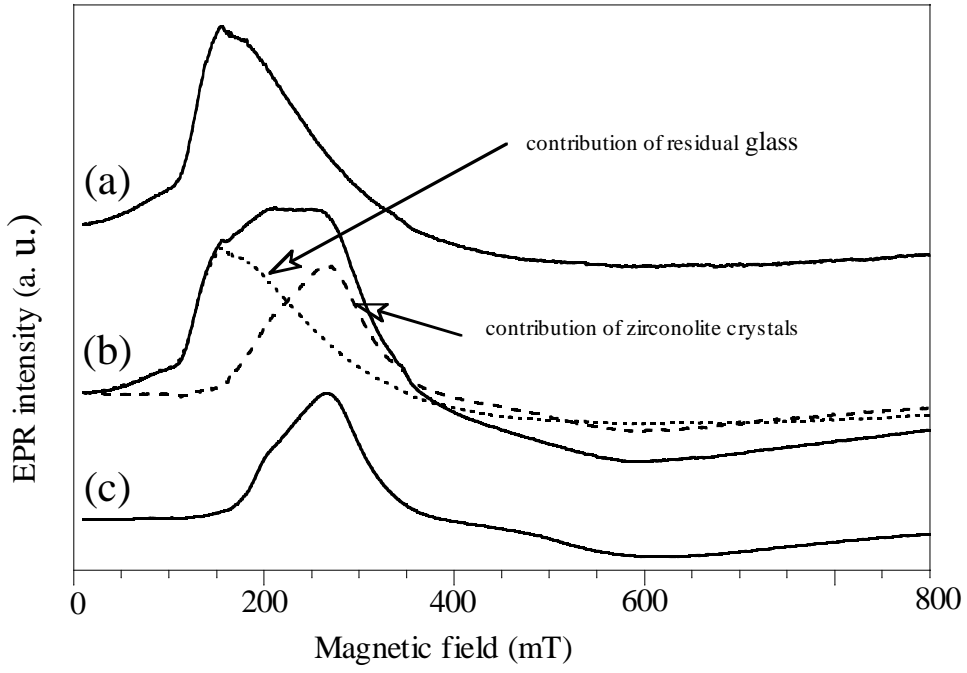


Figure 66

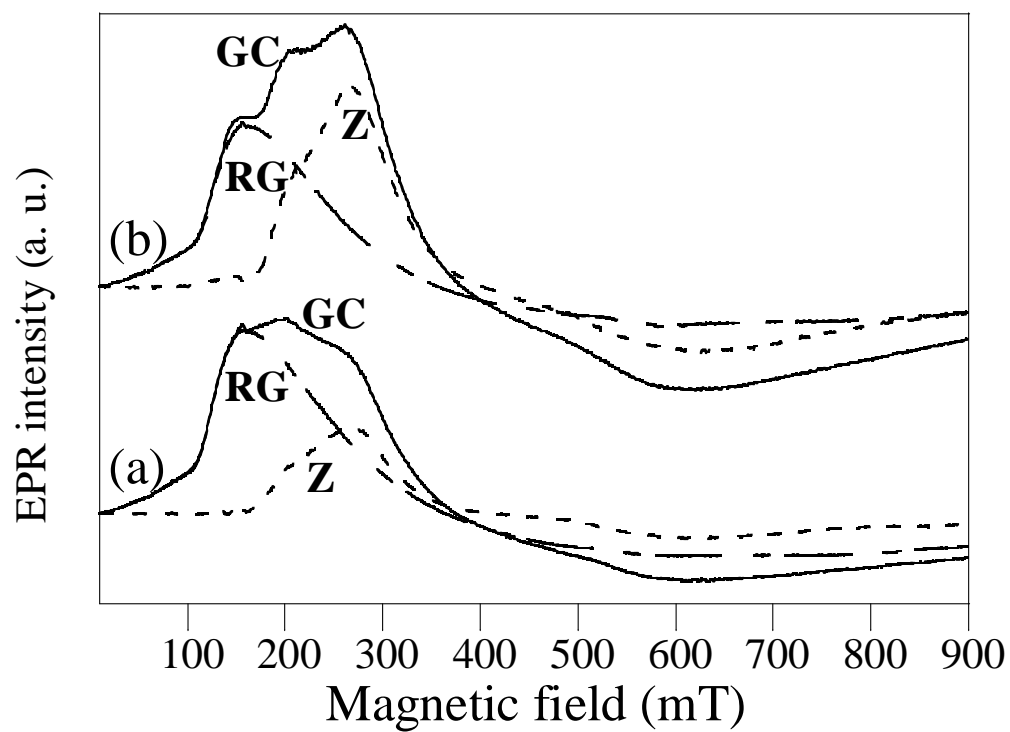


Figure 67

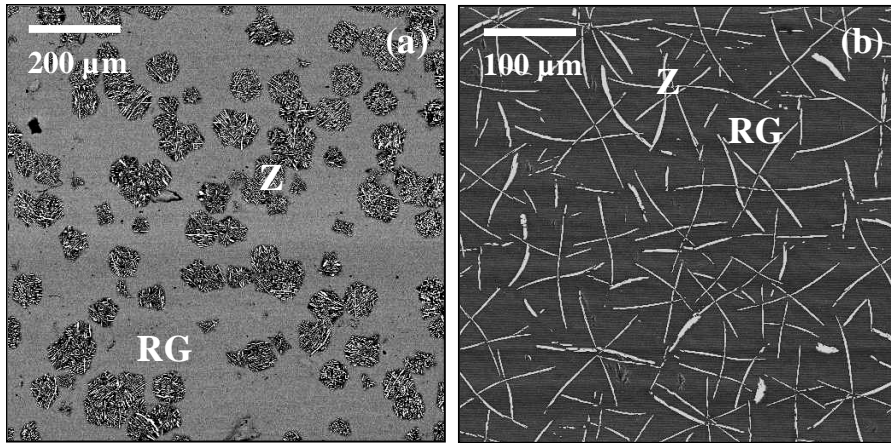


Figure 68

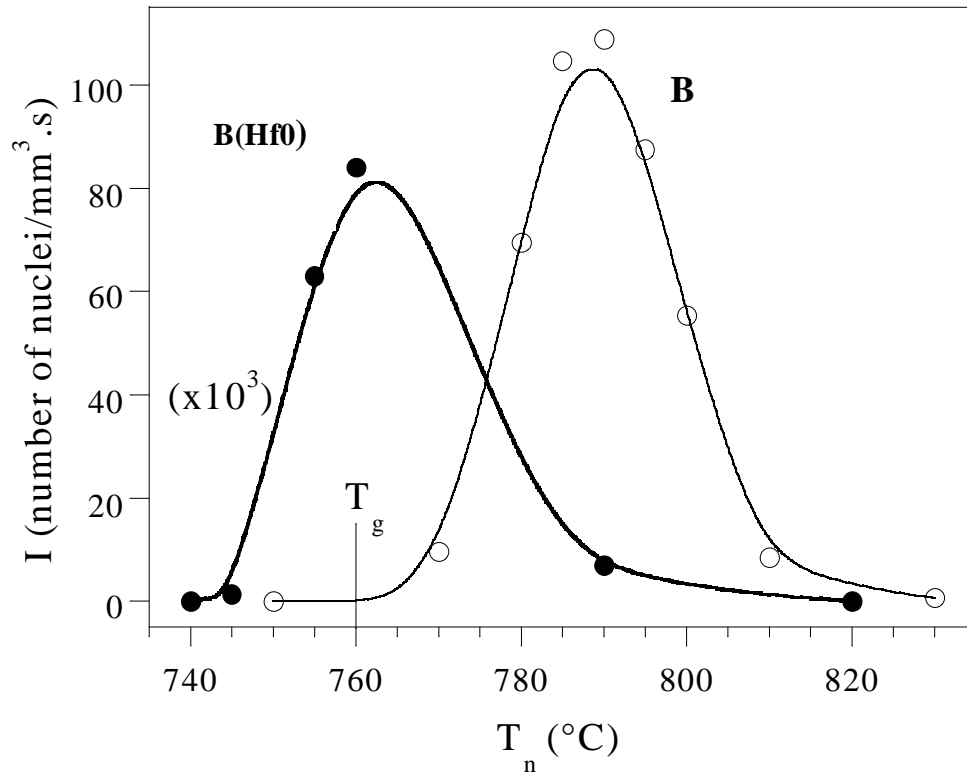


Figure 69

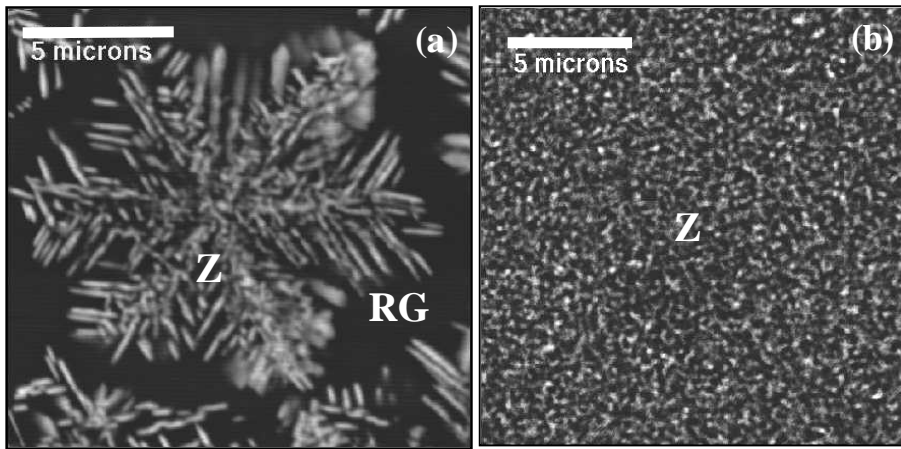


Figure 70

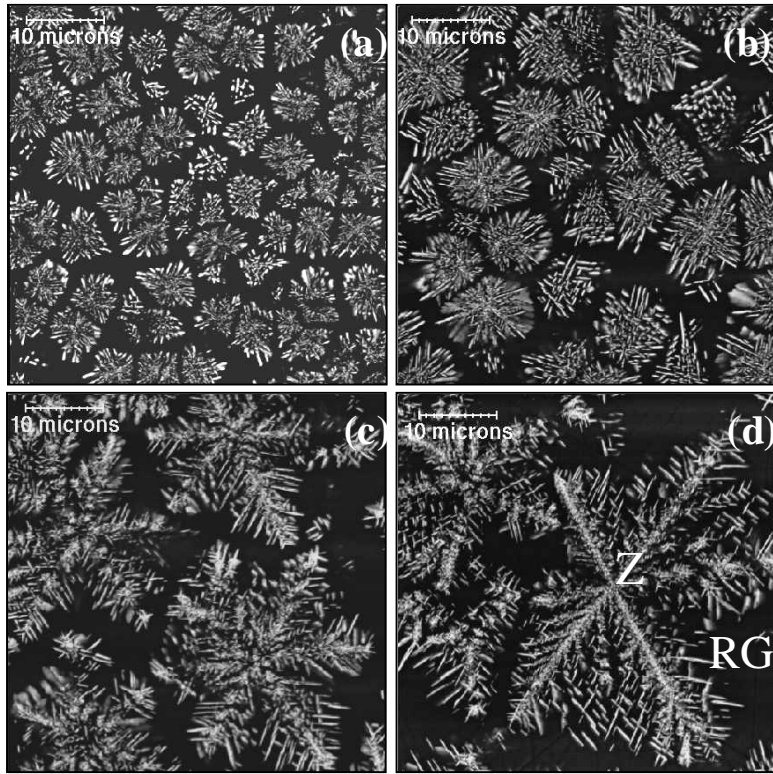


Figure 71

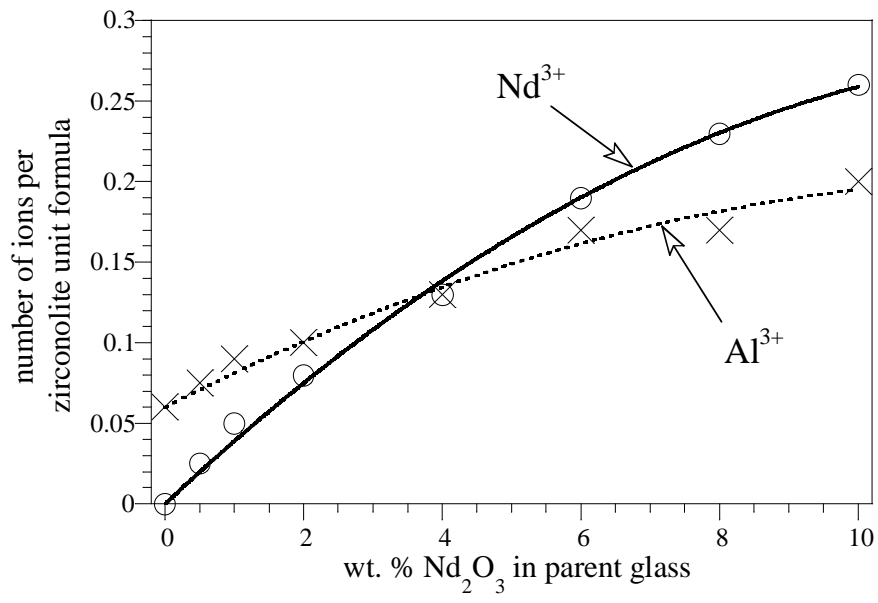


Figure 72

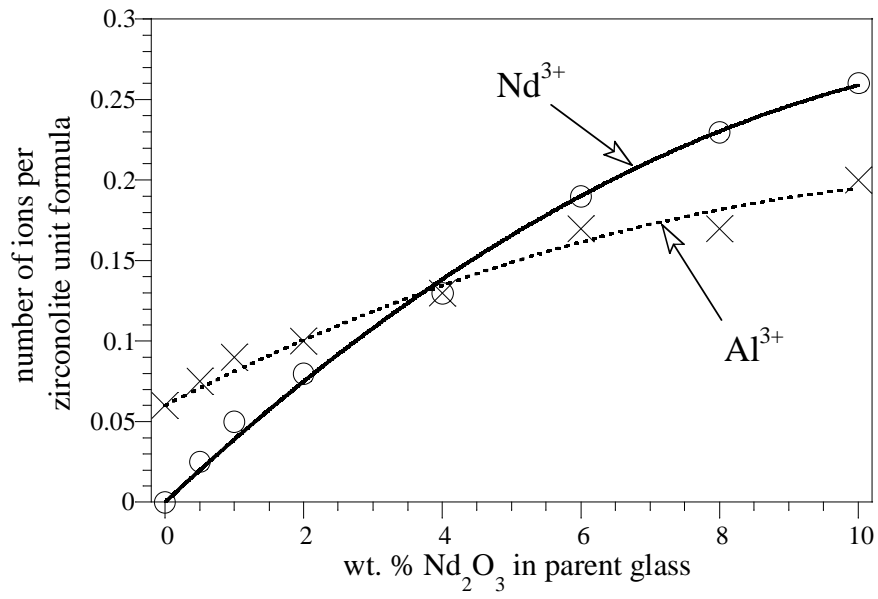


Figure 73

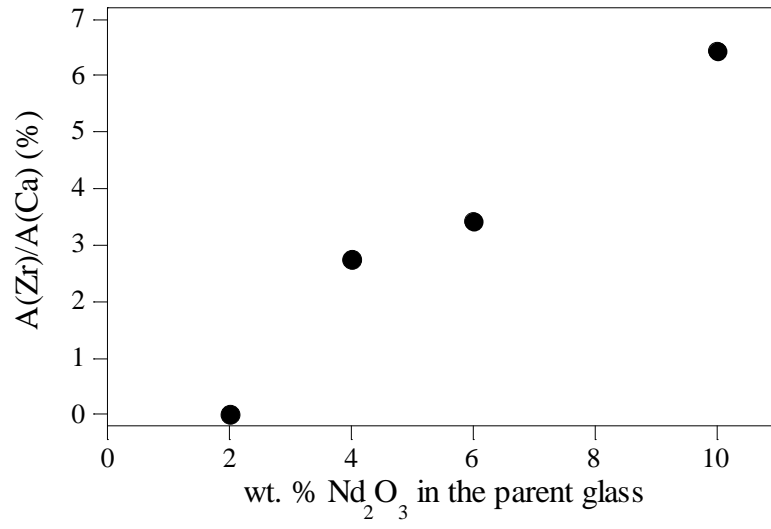


Figure 74

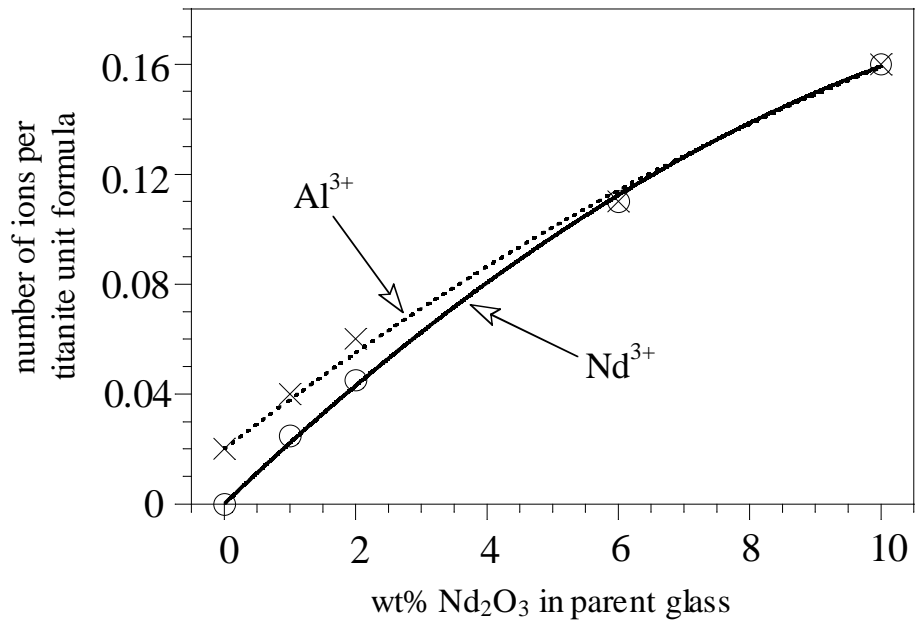


Figure 75

